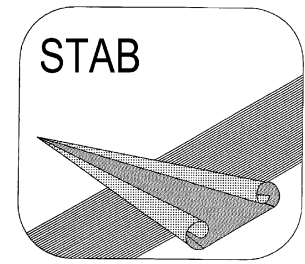**STAB**

J A H R E S B E R I C H T

2024

zum

24. DGLR-Fachsymposium der STAB

13. - 14. November 2024

Regensburg

„Deutsche Strömungsmechanische Arbeitsgemeinschaft, STAB"

INHALT

Mitteilungen der Geschäftsstelle

Die STAB-Jahresberichte werden als Sammlung der Kurzfassungen der Vorträge an die Teilnehmer/innen der abwechselnd stattfindenden Symposien und Workshops verteilt. So erscheint der vorliegende STAB-Jahresbericht 2024 anlässlich des 24. DGLR-Fachsymposiums, das am 13. und 14. November 2024 in Regensburg stattfindet.

Der Bericht enthält 91 „Mitteilungen" über Arbeiten aus den Fachgruppen, die beim Symposium vorgestellt werden. Den „Mitteilungen" ist ein Inhaltsverzeichnis (Seite 14 bis Seite 20) vorangestellt, das nach Fachgruppen gegliedert ist. Innerhalb der Fachgruppen sind die Beiträge alphabetisch nach Autor/in geordnet. Die Beiträge verteilen sich (bezogen auf die Erstautor(inn)en) zu 5 % auf die Industrie, zu 36 % auf Hochschulen und zu 59 % auf Forschungseinrichtungen (DLR, DNW, ISL). Die Autor(inn)en und Koautor(inn)en dieses Berichts sind auf den Seiten 204 bis 206 aufgeführt.

Die Jahresberichte werden nur an den tatsächlich daran interessierten Personenkreis verteilt. Alle Teilnehmer/innen des diesjährigen STAB-Symposiums erhalten ein Exemplar zur Veranstaltung. Darüber hinaus wird der Jahresbericht an die Mitglieder der STAB-Gremien und weitere Interessierte versandt.

Dieser Jahresbericht erscheint in einer Auflage von 150 Exemplaren. Erfahrungsgemäß sind einige Restexemplare bis zum Ende des jeweiligen Jahres verfügbar.

Der jeweils aktuelle Jahresbericht ist auch unter dem unten angegebenen Link als Datei zum Herunterladen verfügbar. Bei Interesse können STAB-Jahresberichte zurückliegender Jahre (ab 1988) bei der STAB-Geschäftsstelle (stab@dlr.de) angefragt werden.

Aktualisierte Informationen über STAB finden Sie auch unter:

STAB - Deutsche Strömungsmechanische Arbeitsgemeinschaft (dlr.de)

Göttingen, im Oktober 2024

Zielsetzungen, chronologische Entwicklung und Organisation

Die Arbeitsgemeinschaft „Strömungen mit Ablösung" (STAB) wurde 1979 auf Initiative der Deutschen Gesellschaft für Luft- und Raumfahrt (DGLR) - Lilienthal-Oberth, e.V. - von Strömungsforschern, Aerodynamikern und Luftfahrtingenieuren des DLR, der Hochschulen und der Industrie gegründet.

Sie entstand aus „dem gemeinschaftlichen Bestreben, die Strömungsforschung in Deutschland generell zu fördern und durch Konzentration auf ein wirtschaftlich und forschungspolitisch zukunftsträchtiges Teilgebiet zu vertiefen" (Auszug aus der Präambel der Verfahrensordnung der STAB).

In Zeiten knapper werdender Budgets bei gleichzeitig massiv steigendem Wettbewerbsdruck sind diese Ansätze notwendiger denn je. Aber auch die öffentlichen Geldgeber setzen diese Kooperationsbereitschaft inzwischen voraus. Da dieser Leitgedanke der STAB inzwischen in anderer Weise verfolgt wird, konzentriert sich die STAB verstärkt auf Fachveranstaltungen.

Die Arbeitsgemeinschaft STAB ist der DGLR als ‚Kompetenznetzwerk' angegliedert.

Auf der Homepage der DGLR ist die STAB zu finden unter:
https://www.dglr.de/vernetzen/fachbereiche/kompetenznetzwerk-stab/

Die STAB vereint alle wichtigen Gebiete der Strömungsmechanik - insbesondere der Luft- und Raumfahrt - aus Grundlagenforschung, Großforschung und Industrie in Deutschland. Die Gründung basierte auf der Idee, Forschungsverbünde aus Industrie, Hochschulen und Großforschung zu einem hochaktuellen Fachthema zu organisieren, das damals als „Strömungen mit Ablösungen" identifiziert wurde. In den Folgejahren wurden weitere strömungsmechanische Fragestellungen aufgegriffen, die STAB zu einem in der Fachwelt bekannten Namen werden ließen. Dabei werden nicht nur die klassischen Themen der Strömungsmechanik angesprochen, sondern auch Probleme aus dem Automobilbau, der Gebäudeaerodynamik, der Verfahrenstechnik, dem Motorenbau usw. diskutiert.

Die Programmleitung hat im November 2000 beschlossen, in Zukunft auf den Zusatz „AG" im Namen zu verzichten.

Die für die Öffentlichkeit relevanten wissenschaftlichen Aktivitäten spiegeln sich in der folgenden chronologischen Entwicklung wider:

DGLR-Symposium „Forschung und Entwicklung auf dem Gebiet der Strömungsmechanik und Aerodynamik in der Bundesrepublik Deutschland"	Bonn, 29.11.-01.12.1978
„Gespräch über Strömungsforschung in Deutschland"	Ottobrunn, 30.01.1979
„Memorandum über zukünftige nationale Zusammenarbeit in der Strömungsforschung, insbesondere der Aerodynamik auf dem Gebiet der Strömungen mit Ablösung"	Oktober 1979
Programmpräsentation anlässlich der BDLI-Jahrestagung	Bonn, 01.07.1980

Programm der Arbeitsgemeinschaft „Strömungen mit Ablösung"	September 1980
Programmpräsentation im Bundesministerium für Forschung und Technologie	Bonn, 19.03.1981
Konstituierung des Kuratoriums und Neuorganisation der Arbeitsgemeinschaft „Strömungen mit Ablösung" (AG STAB)	Köln-Porz, 23.02.1982
Konstituierung von Programmleitung/Programmausschuss	Göttingen, 24.03.1982
Erfassung STAB-relevanter Aktivitäten in der Bundesrepublik Deutschland (Stand Mitte 1981)	April 1982
Fachtagung anlässlich der ILA '82 „Strömungen mit Ablösung"	Hannover, 19.05.1982
Neue Impulse für die Strömungsforschung- und Aerodynamik; Vortrag von H.-G. Knoche, DGLR-Jahrestagung	Hamburg, 01.-03.10.1984
DGLR Workshop „2D-Messtechnik"	Markdorf, 18.-19.10.1988

Symposium

1. DGLR-Fachsymposium	München, 19. - 20.09.1979
2. DGLR- Fachsymposium	Bonn, 30.06. - 01.07.1980
3. DGLR- Fachsymposium	Stuttgart, 23. - 25.11.1981
4. DGLR- Fachsymposium	Göttingen, 10. - 12.10.1983
5. DGLR- Fachsymposium	München, 09. - 10.10.1986
6. DGLR-Fachsymposium	Braunschweig,08. - 10.11.1988
7. DGLR- Fachsymposium	Aachen, 07. - 09.11.1990
8. DGLR- Fachsymposium	Köln-Porz, 10. - 12.11.1992
9. DGLR- Fachsymposium	Erlangen, 04. - 07.10.1994
10. DGLR- Fachsymposium	Braunschweig,11. - 13.11.1996
11. DGLR- Fachsymposium	Berlin, 10. - 12.11.1998
12. DGLR- Fachsymposium	Stuttgart, 15. - 17.11.2000
13. DGLR- Fachsymposium	München, 13. - 15.11.2002
14. DGLR- Fachsymposium	Bremen, 16. - 18.11.2004
15. DGLR- Fachsymposium	Darmstadt, 29.11. - 01.12.2006
16. DGLR- Fachsymposium	Aachen, 03. - 04.11.2008
17. DGLR- Fachsymposium	Berlin, 09. - 10.11.2010

18. DGLR- Fachsymposium	Stuttgart, 06. - 07.11.2012
19. DGLR- Fachsymposium	München, 04. - 05.11.2014
20. DGLR- Fachsymposium	Braunschweig,08. - 09.11.2016
21. DGLR- Fachsymposium	Darmstadt, 06. - 07.11.2018
22. DGLR- Fachsymposium	Präsenzveranstaltung aufgrund der Corona-Pandemie abgesagt
23. DGLR-Fachsymposium	Berlin, 09. - 10.11.2022

Workshop

1. STAB-Workshop	Göttingen, 07. - 08.03.1983
2. STAB-Workshop	Köln-Porz, 18. - 20.09.1984
3. STAB-Workshop	Göttingen, 10. - 11.11.1987
4. STAB-Workshop	Göttingen, 08. - 10.11.1989
5. STAB-Workshop	Göttingen, 13. - 15.11.1991
6. STAB-Workshop	Göttingen, 10. - 12.11.1993
7. STAB-Workshop	Göttingen, 14. - 16.11.1995
8. STAB-Workshop	Göttingen, 11. - 13.11.1997
9. STAB-Workshop	Göttingen, 09. - 11.11.1999
10. STAB-Workshop	Göttingen, 14. - 16.11.2001
11. STAB-Workshop	Göttingen, 04. - 06.11.2003
12. STAB-Workshop	Göttingen, 08. - 09.11.2005
13. STAB-Workshop	Göttingen, 14. - 15.11.2007
14. STAB-Workshop	Göttingen, 11. - 12.11.2009
15. STAB-Workshop	Göttingen, 09. - 10.11.2011
16. STAB-Workshop	Göttingen, 12. - 13.11.2013
17. STAB-Workshop	Göttingen, 10. - 11.11.2015
18. STAB-Workshop	Göttingen, 07. - 08.11.2017
19. STAB-Workshop	Göttingen, 05. - 06.11.2019
20. STAB-Workshop	Göttingen, 16.- 17.11.2021
21. STAB-Workshop	Göttingen, 07.- 08.11.2023

Ein Kurs über „Application of Particle Image Velocimetry, PIV"
findet seit 1993 regelmäßig im DLR in Göttingen statt,
letztmalig am: 18.03. – 22.03.2024

Die Symposiums-Tagungsbände durchlaufen einen Begutachtungsprozess.
Die Bände der letzten Jahre finden Sie hier aufgelistet.

- Notes on Numerical Fluid Mechanics, Vol. 60; Eds.: H. Körner, R. Hilbig; Friedr. Vieweg & Sohn Verlagsgesellschaft mbH, Braunschweig/Wiesbaden, 1997
- Notes on Numerical Fluid Mechanics, Vol. 72; Eds.: W. Nitsche, H.-J. Heinemann, R. Hilbig; Springer-Verlag Berlin Heidelberg
- Notes on Numerical Fluid Mechanics, Vol. 77; Eds.: S. Wagner, U. Rist, H.-J. Heinemann, R. Hilbig; Springer-Verlag Berlin Heidelberg 2002
- Notes on Numerical Fluid Mechanics and Multidisciplinary Design, Vol. 87; Eds.: Chr. Breitsamter, B. Laschka, H.-J. Heinemann, R. Hilbig; Springer-Verlag Berlin Heidelberg 2004
- Notes on Numerical Fluid Mechanics and Multidisciplinary Design, Vol. 92; Eds.: H. J. Rath, C. Holze, H.-J. Heinemann, R. Henke, H. Hönlinger; Springer-Verlag, Berlin Heidelberg 2006
- Notes on Numerical Fluid Mechanics and Multidisciplinary Design, Vol. 96; Eds.: C. Tropea, S. Jakirlic, H.-J. Heinemann, R. Henke, H. Hönlinger; Springer-Verlag Berlin Heidelberg 2008
- Notes on Numerical Fluid Mechanics and Multidisciplinary Design, Vol. 112; Eds.: A. Dillmann, G. Heller, M. Klaas, H.-P. Kreplin, W. Nitsche, W. Schröder; Springer Berlin Heidelberg 2010
- Notes on Numerical Fluid Mechanics and Multidisciplinary Design, Vol. 121; Eds.: A. Dillmann, G. Heller, H.-P. Kreplin, W. Nitsche, I. Peltzer; Springer-Verlag Berlin Heidelberg 2013
- Notes on Numerical Fluid Mechanics and Multidisciplinary Design, Vol. 124; Eds.: A. Dillmann, G. Heller, E. Krämer, H.-P. Kreplin, W. Nitsche, U. Rist; Springer International Publishing Switzerland, 2014
- Notes on Numerical Fluid Mechanics and Multidisciplinary Design, Vol. 132; Eds.: A. Dillmann, G. Heller, E. Krämer, C. Wagner, C. Breitsamter; Springer International Publishing Switzerland 2016
- Notes on Numerical Fluid Mechanics and Multidisciplinary Design, Vol. 136; Eds.: A. Dillmann, G. Heller, E. Krämer, C. Wagner, S. Bansmer, R. Radespiel, R. Semaan; Springer International Publishing AG 2018
- Notes on Numerical Fluid Mechanics and Multidisciplinary Design, Vol. 142; Eds.: A. Dillmann, G. Heller, E. Krämer, C. Wagner, C. Tropea, S. Jakirlic; Springer Nature Switzerland AG 2020
- Notes on Numerical Fluid Mechanics and Multidisciplinary Design, Vol. 151, Eds.: A. Dillmann, G. Heller, E. Krämer, C. Wagner; Springer Nature Switzerland AG 2021
- Notes on Numerical Fluid Mechanics and Multidisciplinary Design, Vol. 154 Eds.: A. Dillmann, G. Heller, E. Krämer, C. Wagner, J. Weiss; Springer Nature Switzerland AG 2024

Vorschau:

22. STAB-Workshop	November 2025
Kurs „PIV"	17.- 21. März 2025

Programmleitung

Prof. Dr. C. Breitsamter
christian.breitsamter@tum.de

(Technische Universität München)
Tel.: 089 289-16137

Prof. Dr. A. Dillmann (Sprecher)
andreas.dillmann@dlr.de

(DLR, Göttingen)
Tel.: 0551 709-2177

Prof. Dr. J. Fröhlich
jochen.froehlich@tu-dresden.de

(TU Dresden)
Tel.: 0351 463-37607

Dr. R. Höld
roland.hoeld@mbda-systems.de

(MBDA Deutschland GmbH,
Schrobenhausen)
Tel.: 08252 99-8845

Dr. G. Heller (Sprecher)
gerd.heller@airbus.com

(Airbus, Manching)
Tel.: 8459-8112582

Prof. Dr. E. Krämer (Sprecher)
kraemer@iag.uni-stuttgart.de

(Universität Stuttgart)
Tel.: 0711 685-63401

Prof. Dr. W. Schröder
office@aia.rwth-aachen.de

(RWTH, Aachen)
Tel.: 0241 80-95410

Prof. Dr. C. Stemmer
christian.stemmer@tum.de

(Technische Universität München)
Tel.: 089 289-16142

Prof. Dr. L. Tichy
lorenz.tichy@dlr.de

(DLR, Göttingen)
Tel.: 0551 709-2341

Fachgruppen[1]	**Sprecher:**
Aeroelastik und Strukturdynamik*	Prof. Dr. L. Tichy (DLR, Göttingen) Tel.: 0551 709-2341 E-Mail: Lorenz.Tichy@dlr.de
Experimentelle Aerodynamik*	Prof. Dr. C. Breitsamter (Technische Universität München) Tel.: 089 289-16137 E-Mail: Christian.Breitsamter@aer.mw.tum.de
Hyperschallaerothermodynamik	Dr. B. Reimann (DLR, Braunschweig) Tel.: 0531 295-3319 E-Mail: Bodo.Reimann@DLR.de und Dr. M. Konopka (Ariane Group GmbH, Bremen) Tel.: 0421 4372-4788 E-Mail: martin.konopka@ariane.group
Multidisziplinäre Optimierung	Dr. M. Hepperle (DLR, Braunschweig) Tel.: 0531 295-3337 E-Mail: Martin.Hepperle@dlr.de und Dipl.-Ing. D. Reckzeh (Airbus, Bremen) Tel.: 0421 538-2136 E-Mail: Daniel.Reckzeh@airbus.com
Numerische Aerodynamik*	Dr. C. Grabe (DLR, Göttingen) Tel.: 0551 709-2628 E-Mail: Cornelia.Grabe@dlr.de
Strömungsakustik*	Prof. Dr. J. Delfs (DLR, Braunschweig) Tel.: 0531 295-2170 E-Mail: Jan.Delfs@dlr.de
Strömungsbeeinflussung	Dr. A. Büscher (Airbus, Bremen) Tel.: 0172 8468 782 E-Mail: Alexander.Buescher@airbus.com
Turbulenz und Transition	Prof. Dr. W. Schröder (RWTH Aachen) Tel.: 0241 80-95410 E-Mail: office@aia.rwth-aachen.de und Prof. Dr. N. Adams (Technische Universität München) Tel.: 089 289-16120 E-Mail: Nikolaus.Adams@tum.de

*assoziierte DGLR-Fachkreise
[1]grundlagenorientiert

Fachgruppen[2]	Sprecher:
Allgemeine Strömungstechnik	Dr. P. Bahavar (DLR, Göttingen) Tel.: 0551 709-2306 E-Mail: Philipp.Bahavar@dlr.de
Aerodynamik bodengebundener Fahrzeuge	Dr. A. Wäschle (Mercedes-Benz AG, Sindelfingen) Tel: 0151 586-26046 E-Mail: alexander.waeschle@mercedes-benz.com
Bio- und Mikrofluidmechanik	Prof. Dr. L. Krenkel (OTH Regensburg) Tel.: 0941 943-9689 E-Mail: lars.krenkel@oth-regensburg.de
Drehflügler	Dr. A. Gardner (DLR, Göttingen) Tel.: 0551 709-2267 E-Mail: Anthony.Gardner@dlr.de
Hochagile Konfigurationen	Dr. R. Höld (MBDA Deutschland GmbH, Schrobenhausen) Tel.: 08252 99-8845 E-Mail: Roland.Hoeld@mbda-systems.de
Transportflugzeugkonfigurationen	Dr. A. Seitz (DLR, Braunschweig) Tel.: 0531 295-2888 E-Mail: Arne.Seitz@dlr.de
Versuchsanlagen	Dr. G. Dietz (European Transonic Wind-tunnel GmbH, Köln) Tel.: 02203 609-110 E-Mail: gd@etw.de
Windenergie	Dr. T. Lutz (Universität Stuttgart) Tel.: 0711 685-63406 E-Mail: lutz@iag.uni-stuttgart.de
Wissenschaftlicher Koordinator	Prof. Dr. C. Wagner (DLR, Göttingen) Tel.: 0551 709-2261 E-Mail: Claus.Wagner@dlr.de

[2]anwendungsorientiert

Stand: Oktober 2024

Verfassen von „Mitteilungen"

Die Anmeldungen zum STAB-Symposium bzw. STAB-Workshop werden bei der jeweiligen Veranstaltung als Bericht/Proceedings an die Teilnehmer/innen verteilt.

Die Mitteilung ist eine zweiseitige Kurzfassung des Beitrags, bei der nur der unten dargestellte Kopf vorgegeben ist.

Mitteilung

Fachgruppe:

Thema/Titel des Beitrags

Autor(inn)en
Institution
Adresse
E-Mail-Adresse

Bitte halten Sie sich bei der Anmeldung zur STAB-Veranstaltung unbedingt an die vorgegebenen zwei Seiten pro „Mitteilung". Tragen Sie bitte keine Seitenzahlen ein.

Der Druck erfolgt weiterhin ausschließlich in schwarz/weiß.

Für Rückfragen steht Ihnen die Geschäftsstelle gerne zur Verfügung:

Tel.: 0551 709 - 2464
E-Mail: stab@dlr.de

Mit freundlichen Grüßen
Ihre Fachgruppenleiter/innen und Ihre Geschäftsstelle

The **CEAS Aeronautical Journal** and the **CEAS Space Journal** have been created under the umbrella of CEAS to provide an appropriate platform for excellent scientific publications submitted by scientists and engineers. The German Aerospace Center (DLR) and the European Space Agency (ESA) support the journals.

CEAS Aeronautical Journal

An official journal of the Council of European Aerospace Societies
ISSN: 1869-5582 (Print), 1869-5590 (Online)
Springer
http://www.springer.com/13272

Editor-in-Chief: M. Fischer (DLR, Cologne, Germany)
Managing Editors: C. Hillenherms, (DLR, Cologne, Germany)
A. Dieball (DLR, Cologne, Germany)
J. Kreikemeier (DLR, Brunswick, Germany)

The journal is devoted to publishing results and findings in all areas of aeronautics-related science and technology as well as reports on new developments in the design and manufacturing of aircraft, rotorcraft, and unmanned aerial vehicles. Of interest are also (invited) in-depth reviews of the status of development in specific areas of relevance to aeronautics, and descriptions of the potential way forward. Typical disciplines of interest include flight physics and aerodynamics, aeroelasticity and structural mechanics, aeroacoustics, structures and materials, flight mechanics and flight control systems, flight guidance, air traffic management, communication, navigation and surveillance, aircraft and aircraft design, rotorcraft and propulsion.

The journal publishes peer-reviewed original articles, (invited) reviews and short communications.

CEAS Space Journal

An official journal of the Council of European Aerospace Societies
ISSN: 1868-2502 (Print), 1868-2510 (Online)
Springer
http://www.springer.com/12567

Editor-in-Chief: H. Dittus (Universität Bremen, Germany)
Managing Editors: A. Dieball (DLR, Cologne, Germany)
W. Kordulla (CEAS, Brussels, Belgium)
J. Steelant (ESA/ESTEC, Noordwijk, The Netherlands)

The journal is devoted to new developments and results in all areas of space-related science and technology, including important spin-off capabilities and applications as well as ground-based support systems and manufacturing advancements. Of interest are also (invited) in-depth reviews of the status of development in specific areas of relevance to space, and descriptions of the potential way forward. Typical disciplines of interest include mission design and space systems, satellite communications, aerothermodynamics (including physical fluid dynamics), environmental control and life support systems, materials, operations, space debris, optics, optoelectronics and photonics, guidance, navigation and control, mechanisms, propulsion, power, robotics, structures, testing, thermal issues, and small satellites.

The journal publishes peer-reviewed original articles, (invited) reviews and short communications.

15. Fachgruppe „Versuchsanlagen"

16. Fachgruppe „Windenergie"

Mitteilung

Fachgruppe: Aerodynamik bodengebundener Fahrzeuge

Wind tunnel calibration methodology for measuring aerodynamic loads
on operational high-speed trains

Alexander Buhr[1], James Bell[1], Lars Siegel[1], Arne Henning[1], Martin Köppel[2],
Matthias Härter[2], Daniela Lauer[2], Mathilde Laporte[3], Robert Winkler-Höhn[3]
[1]German Aerospace Center (DLR), Institute of Aerodynamics and Flow Technology,
Göttingen, Germany, corresponding author: alexander.buhr@dlr.de
[2]DB InfraGO AG, Digitale Schiene Deutschland, Berlin, Germany
[3]German Aerospace Center (DLR), Institute of Vehicle Concepts, Stuttgart, Germany

A reduced-scale wind-tunnel experimental methodology is presented that provides calibration and insight for measurements on an operational high-speed train; the Deutsche Bahn advanced TrainLab (aTL, Figure 1a) [1]. A 5-hole dynamic pressure probe mounted at the front of the aTL is used to determine the incoming flow magnitude and direction. A 1:10 scale wind-tunnel experiment was performed to determine probe corrections to remove the local effects on the probe of the train's head on the incoming flow. A 1:25 scale wind-tunnel experiment was performed to determine drag, side-force and lift polars for the 1st carriage of the aTL (Figure 1b,c). The corrected probe measurements and force calibration provide quasi-steady force estimations (length-scales ≈ train length) of the aTL under real-world operation. A belt of 9 surface-pressure taps around the circumference near the front of the aTL provides insight into the unsteady (length-scales ≪ train length) pressure and forces operational high-speed trains experience. The surface pressure was measured at these locations in both scaled wind-tunnel experiments and at two further positions along the length of the body as well as on the nose of the models for additional insight into the causal flow physics and potential for surface-pressure measurements on operational high-speed trains in the future.

This work is part of the joint project 'KI-MeZIS - AI Methods in Condition Monitoring and Demand-Adapted Maintenance of Rail Vehicle Structures' coordinated by DB AG with the partners DB InfraGO AG, DB AG's AI Factory, DB Systemtechnik, Industrial Analytics GmbH, University of Stuttgart, Institut für Bahntechnik GmbH, MSG Ammendorf and DLR. The project is supported by the BMWK technical programme 'New Vehicle and System Technology', within the framework 'Artificial Intelligence as a Key Technology for the Vehicle of the Future'. The aim of this project is to develop and use an AI-based, onboard monitoring system for operational rolling stock to detect, measure and analyse impact or run-over events as well as aerodynamic loads [1,2]. The output of the monitoring system will be used for strategic maintenance as well as needs-based, cost and energy efficient design of future rolling stock [2].
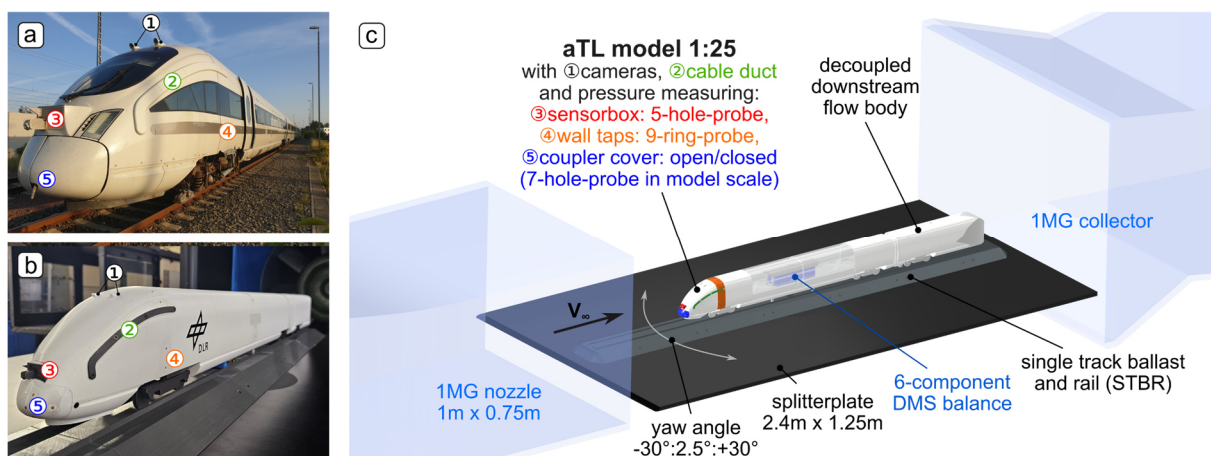
Figure 1: a) advanced TrainLab with sensor systems, b) 3D-printed, 1:25 scale model and c) 1:25 scale setup as measured in the one-metre low-speed wind tunnel Göttingen (1MG).

STAB
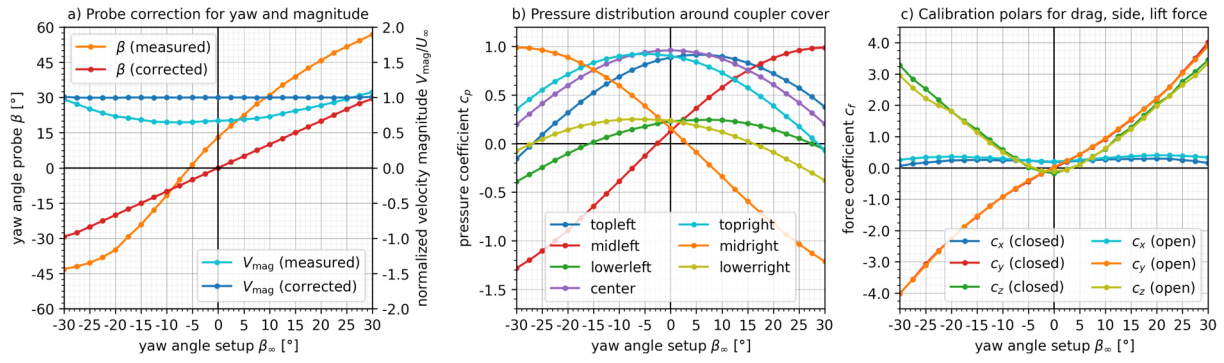
Figure 2: a) measured and corrected probe data for yaw angle and velocity magnitude, b) pressure distribution around coupler cover and c) calibration polars for drag, side and lift force.

The experiments were performed in the one-metre low-speed wind tunnel Göttingen (Figure 1c) at 40m/s wind speed, which corresponds to $Re_h > 10^6$ and respectively $Re_h > 0.4 \times 10^6$ for the 1:10 and 1:25 scale model (related to model height). For each model configuration a yaw angle sweep from -30° to 30° in 2.5° steps was measured. Local effects of specific geometry components of the aTL such as cable duct, sensor box, closed/open coupler cover (Figure 1), were investigated to develop a level of confidence for the robustness for the calibration measurements. The 5-hole probe, the surface pressure taps of the 9-hole belts and 7 additional pressure taps at the coupler cover as well as the total und static pressure of a Prandtl probe in the test section were connected to a 64-channel, 20" WC PSI scanner. The 1:25 scale model was mounted on a 6-component strain-gauge balance (RUAG 196-6I) to measure drag, side and lift forces on the first carriage. The benchmark measurements for the aerodynamic coefficients were performed with reference to the 'Requirements and test procedures for cross wind assessment' (DIN EN 14067-6:2018).

In Figure 2a the correction functions of the 5-hole probe are presented, with measured yaw angle β (orange) and velocity magnitude V_{mag} (cyan), normalized with the freestream wind tunnel velocity U_∞, against the set-up yaw angle β_∞ of the model in the test section. The flow angle $\beta_\infty \leftrightarrow \beta$ and magnitude $\beta_\infty \leftrightarrow V_{mag}$ relationships are not linear due to changing flow displacement around the aTL head geometry for different yaw angles. Neither are symmetric around 0° yaw due to the off-center position of the 5-hole probe to the right side of the aTL nose (Figure 1a,b). Thus, a correction function was derived to determine the 'true' incoming flow conditions β_∞ (red) and U_∞ (blue), which were controlled in the wind tunnel setup. An alternative correction function was determined to be used when the train was operating with an open coupler cover. In Figure 2b the pressure signals of the 7 coupler cover taps are presented. They exhibit changing characteristics with the yaw angle (symmetric to 0° yaw). This indicates that surface pressure taps on the nose region could be a promising alternative to the 5-hole probe. In Figure 2c the drag, side and lift force-coefficient (c_x, c_y, c_z) calibration polars of the aTL's 1st carriage are presented for closed and open coupler cover configurations. For post-processing the full-scale measurements, the probe correction functions are applied to the probe data to determine the oncoming, free-stream (cross-)wind. The force calibration polars are then used to calculate the global aerodynamic loads on the aTL. Within the KI-MeZIS project, the presented results were merged to a database from strain gauge and accelerometer sensor measurements on single aTL surface positions to perform a load spectrum analysis [3]. This analysis can be used to optimize the design and dimensioning of structural components with regard to the required service life or maintenance intervals [2]. The presented methodology could also be used in future high-speed train operation for real-time prediction of aerodynamic loads. This could inform a driver assistance or autonomous system to achieve optimized aerodynamic operation; for improved efficiency and safety.

[1]   Digitale Schiene Deutschland, 'Digital Impact Detection in Railway Operations Collecting data for driverless driving - a ride with the advanced TrainLab', https://digitale-schiene-deutschland.de/en/news/2024/DigitalImpactDetection (25/06/2024).
[2]   Matthias Härter et al., 'KI-MeZIS: Nutzung von künstlicher Intelligenz für die Zustandsüberwachung von Schienenfahrzeugen', 20. Internationale Schienenfahrzeugtagung, Dresden, 18.-20.09.2024.
[3]   Mathilde Laporte et al., 'Methode zur Ermittlung von Betriebslasten bei Schienenfahrzeugen mittels KI-Methoden', 20. Internationale Schienenfahrzeugtagung, Dresden, 18.-20.09.2024.

STAB

Mitteilung

Fachgruppe: Aerodynamik bodengebundener Fahrzeuge

Experimental Investigation of the Flow Field of a Notchback and Estate-Back Full-Scale DrivAer Model with Ground Simulation

Knaus, Lisa*; Haff, Johannes*; Lietmeyer, Christoph*; Weinman, Keith[+]; Fey, Uwe[+]; Ehrenfried, Klaus[+]; Wagner, Claus[+]
*VOLKSWAGEN AG, Berliner Ring 2, 38440 Wolfsburg; [+]Deutsches Zentrum für Luft- und Raumfahrt (DLR), Institut für Aerodynamik und Strömungstechnik, Bunsenstr. 10, 37073 Göttingen, lisa.knaus@volkswagen.de

Hintergrund:
Die zeitgemäße aerodynamische Entwicklung von Kraftfahrzeugen erfolgt in heutigen Automobil- Windkanälen im Maßstab 1:1 und virtuell mit Hilfe von Strömungssimulationen mittels CFD. Zur Validierung der verwendeten CFD-Methoden werden entsprechende Windkanalmessdaten benötigt. Um die Ergebnisse unterschiedlicher CFD-Methoden konsistent vergleichen und einordnen zu können wurde sich auf eine von Heft 2012 vorgestellte generische Fahrzeuggeometrie, das sogenannte DrivAer Modell, verständigt. Das DrivAer Modell hat die geometrischen Proportionen eines PKWs der Mittelklasse und ist modular aufgebaut. Diese Modulbauweise ermöglicht es, verschiedene Karosserieformen darzustellen.
Die für das industrielle Umfeld interessantesten Konfigurationen sind dabei das Stufen- und das Vollheck. Die jeweiligen CFD-Tools müssen in der Lage sein, die durch die verschiedenen Heckformen induzierten Strömungsfelder hinreichend genau abbilden zu können. Um sich möglichst auf den Einfluss der Grundform des Fahrzeugs zu begrenzen, wurde zur Vereinfachung die Fahrzeugkonfiguration mit glattem Unterboden und geschlossenen Kühllufteinein- und auslässen gewählt. Die für die Vergleichbarkeit von Prüfstandsversuch und Straßenfahrt wichtige Raddrehung wird mit berücksichtigt.
Es hat sich bereits gezeigt, dass die Konfiguration mit glattem Unterboden bei der Vollheckvariante zu einem nach oben ausgerichteten Nachlauf mit erhöhtem Luftwiderstand führt. Daher wird zusätzlich der Einfluss einer Spoilerlippe am Ende des Diffusors auf den Nachlauf des Vollhecks untersucht. Im Vergleich zur Änderung der Heckform muss der Einfluss einer solch kleinen Variation der Geometrie ebenfalls von den verwendeten CFD Methoden erfasst werden können und stellt einen weiteren Validierungsfall dar.
Die Verfügbarkeit von Messdaten mit Bodensimulation und drehenden Rädern ist bisher nur eingeschränkt verfügbar und soll durch diese Arbeit ergänzt werden.

Methode:
Die experimentellen Untersuchungen wurdenAero-Akustik-Windkanal der VOLKSWAGEN AG (VW) in Wolfsburg mit einem Versuchsfahrzeug im Maßstab 1:1 durchgeführt. Es handelt sich dabei um einen Windkanal Göttinger Bauart mit einer ¾-offene Messstrecke und einer modernen Bodensimulation. Diese besteht unter Anderem aus einem Laufband-System mit vier individuellen Radantriebseinheiten und einem Mittellaufband, dass die Bewegung der Straße relativ zum Modell simuliert. Zunächst wird die Bodengrenzschicht am Düsenaustritt über die gesamte Düsenbreite abgesaugt. Vor dem Mittenlaufband finden eine erneutes Absaugen der sich wieder aufgebauten Grenzschicht statt. Zusätzlich wird der Impulsverlust über eine konstantes Ausblasen ausgeglichen. Die Windgeschwindigkeit im Plenum wird mit Hilfe der Plenumsmethode geregelt. Der Windkanal verfügt zusätzlich über ein Traversensystem, mit dessen Hilfe unter minimaler Beeinflussung des Strömungsfeldes Messungen im gesamten Plenum automatisiert durchgeführt werden können.
Das Modell besitzt 217 Oberflächendruckbohrungen, die sich unter anderem in der Hauptsymmetrieebene befinden,. Zusätzliche Druckmessstellen befinden sich am Fahrzeugheck mit insgesamt 132 Messstellen am Stufen- und 52 Messstellen am Vollheck.
Die Ergebnisse der Strömungsfeldmessungen basieren auf Totaldruckmessungen mit Rechen unterschiedlicher Ausführung. Alle statischen Druckmessstellen auf der

Modelloberfläche und die Totaldruckrechen wurden über PVC-Schläuche mit piezoresistiven Differenzdruckaufnehmern verbunden. Die Differenzdruckaufnehmer besitzen eine interne Temperaturkompensation und haben bei einem Messbereich von ± 7 kPa laut Hersteller einen Messfehler von ± 0.03 %FS und eine Auflösung von 0.07 Pa. Die Messdaten wurden mit einer Frequenz von 650 Hz und einer Messzeit von jeweils 60 s aufgezeichnet und anschließend zeitlich gemittelt. Der Referenzdruck wurde nahe dem Referenzdruck des Windkanals an der Plenumswand neben der Düse abgenommen.

Ergebnisse:

Der Vergleich der Oberflächendrücke zwischen den beiden Karosserievarianten Vollheck und Stufenheck zeigt einen hohen Grad an Übereinstimmung im vorderen Fahrzeugbereich Erst ab der B-Säule zeigen sich signifikante Unterschiede im Oberflächendruck, die auf die unterschiedlichen Heckformen zurückzuführen sind.

Um die Umströmung der Heckbereiche besser analysieren zu können, werden Oberflächendrücke an zusätzlichen Druckbohrungen auf der Heckscheibe des Stufenhecks analysiert und mit veröffentlichten Ergebnissen aus Messungen mit skalierten Modellen verglichen. Dabei zeigt sich ein hoher Grad an Übereinstimmung.

Zusätzlich werden die gemessenen Grenzschichtverläufe in der Symmetrieebene am Unterboden und auf dem Dach des Modells ausgewertet und präsentiert, zu denen es bisher keine bekannten veröffentlichten Daten gibt. Die Messung der Grenzschicht am Unterboden zeigt, zusammen mit den gemessenen Oberflächendrücken, dass die Strömung der Geometrie gut folgen kann. Nachlaufschnitte in der Symmetrieebene beider Karosserievarianten zeigen die Topologie der Nachlaufgebiete und das deutlich nach oben verschobene Totwassergebiet des Vollheckfahrzeugs. Durch eine Spoilerlippen am Diffusor kann die Nachlauftopologie und damit der Luftwiderstand signifikant beeinflusst werden. Dies zeigt sich in den Strömungsmessdaten in Form eines deutlich symmetrischeren Nachlaufgebiets.

Im Nachlaufgebiet beider Heckvarianten zeigen sich ebenfalls die Wirbelstrukturen aus der Umströmung der A-Säule sowie den Außenspiegeln. Die genaue Vorhersage der Strömungsstrukturen in diesen Bereichen des Nachlaufgebietes ist für die CFD besonders herausfordernd und die Messdatenbasis daher eine wichtige Grundlage für die weitere Validierung. Referenzdaten sind hier wichtig, um die Leistungsfähigkeit von CFD-Tools beurteilen zu können. Bei der Stufenheckvariante hat sich zusätzlich gezeigt, dass es herausfordernd ist, die Ablöseblase auf der Heckscheibe mit der Strömungssimulation richtig vorherzusagen. Die gezeigten Messergebnisse sind daher für die Validierung der Strömungssimulation auch hier eine wichtige Grundlage. Zum Abschluss werden die Vor- und Nachteile von Totaldrucksonden für Strömungsfeldmessungen diskutiert. Mit Ihnen können schnell und einfach Messrechen gebaut und großflächige, relativ fein aufgelöste, Messungen durchgeführt werden. Totaldrucksonden sind robust und können in unterschiedlichsten Rechengeometrien verwendet werden. Der verwendete Messaufbau mit Schlauchverbindungen zwischen Sonden und Druckaufnehmern erlaubt ein schlankes Design der verwendeten Rechen und eine möglichst minimale Beeinflussung der zu messenden Strömung.

Ein Nachteil von Totaldrucksonden ist ihre Sensitivität gegenüber des Anströmwinkels. Ein möglicher Messfehler durch den Anströmwinkel kann durch reine Messungen des Totaldrucks nicht quantifiziert werden. Indirekt kann dies über CFD-Ergebnisse abgeschätzt werden, da hier lokale Geschwindigkeitskomponenten und somit Anströmwinkel bekannt sind. Hier zeigt sich, dass der lokale Anströmwinkel relativ zur Sondenachse in den meisten Bereichen, mit ausreichendem Abstand zum Fahrzeug, klein ist. Dies trifft nicht auf das Rückströmgebiet hinter dem Fahrzeug zu, hier sind Anströmwinkel bis 180° möglich, daher können hier keine Ergebnisse gezeigt werden. Somit ergibt sich ein Auswertefenster bis zu einer unteren Grenze von 20% der Geschwindigkeit der freien Anströmung. Ein weiterer Nachteil ist die Schlauchlänge zwischen Sonde und Druckaufnehmer. Diese führt dazu, dass nur zeitlich gemittelte Daten betrachtet werden können.

Zusammenfassend bietet dieses Paper einen umfassenden Einblick in relevante Strömungsbereiche um das DrivAer Modell. Es zeigt ergänzende Messdaten zu der bereits vorhandenen Datenbasis veröffentlichter Messungen. Der Einfluss dreier Geometrievarianten auf die generelle Nachlauftopologie wird gezeigt und die effektive Verwendung robuster Messmethoden diskutiert.

STAB

Fachgruppe: Aerodynamik bodengebundener Fahrzeuge

The influence of upstream wind variations on the aerodynamic drag of a model cargo train

K. Weinman[*], T.S. Müller, U. Fey, K. Ehrenfried

DLR Göttingen, Institute of Aerodynamics and Flow Technology

Bunsenstr. 10, 37073 Göttingen, Germany

*keith.weinman@dlr.de

DLR NGT-Cargo [1] is a logistics concept using rail as the central mode of freight transport. The concept requires the development of competitive transport systems with respect to operational and associated ecological costs. Within this framework an accurate assessment of the aerodynamic drag under realistic vehicle operating conditions is essential. The air flow about a train is characterized by a large range of energetically significant flow scales which challenge accurate numerical simulation, however CFD methods for certification of trains are now accepted with some restrictions by the transport industry. For example, the EN 14067-6 [2] standard permits evaluation of aerodynamic forces by means of computational fluid dynamics (CFD) simulation for full-scale or reduced model geometries under constant cross-wind conditions. At the present time there are no acknowledged international standards concerned with CFD drag prediction under unsteady on-flow conditions for rail vehicles. It is therefore useful to develop sufficiently accurate CFD models to assist in the study of these flows, particularly with respect to operational cost and safety requirements.

The current work extends an earlier result [3] which compared numerical estimates of drag against wind tunnel measurements. Two approaches are used for the CFD model. Approach D (illustrated in Figure 1) is discussed in [3]. This CFD model uses a computational geometry which closely matches the geometry of the experimental facility. Accurate geometrical descriptions of the wind tunnel nozzle, test section and diffusor sections are used, as well as the active and passive suction devices used in the experiments. A complete description of the 3D geometry of the moving belt, including rollers, is also included in the model. Gaps between the test section environment and the laboratory space, required to correctly manage pressure build-up with an operational moving belt, are also included. Approach C is illustrated in Figure 2. This approach removes many of the modeled components required for Approach D. Only the internal surfaces of the wind-tunnel nozzle and test section are needed. A slip wall boundary condition, due to [4], is applied upstream of the model to mimic the influence of both passive and active suction on the boundary layer approaching the model. The moving belt is modeled as a wind tunnel wall surface patch, under the model, with moving wall boundary conditions. The boundary patches used to mimic the influence of boundary layer suction as well as the moving belt are shown in Figure 2. For both approaches a moving flap system, located approximately in the middle between passive and active suction upstream of the model, is used to control the unsteadiness of the on-flow approaching the model.

After discussion of the CFD validation procedures used in this work, computed aerodynamic drag forces acting on the model under steady and unsteady on-flow conditions are evaluated for both approaches and compared against the experimental measurements. The upstream flap frequencies are varied while holding the bulk wind tunnel velocity constant. RANS approaches are compared against hybrid RANS-LES methods. The meshes used in the current work are designed to properly resolve unsteady velocity fields for these hybrid methods. The influence of the numeric schemes chosen on the solution quality are then reviewed, which allows us to provide a number of provisional recommendations regarding a modeling approach fulfilling a set of relevant objectives.
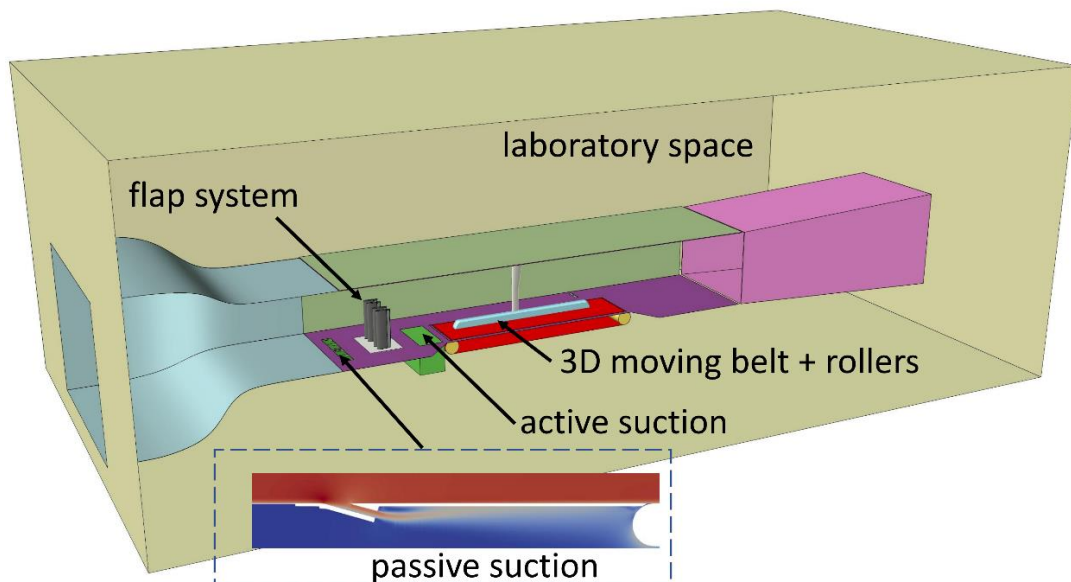
Figure 1: Approach D models the wind tunnel nozzle test section and diffuser embedded inside the laboratory space. The active suction outflow is prescribed as a constant mass flow outlet, while passive suction is provided by a duct system discharging directly into the laboratory space. The outflow from the passive suction system is illustrated in the subfigure above
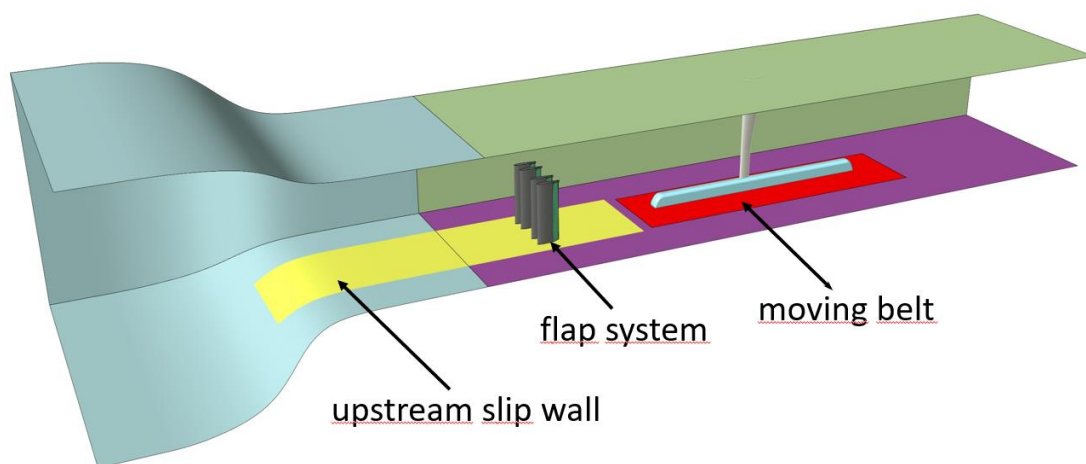
Figure 2: Approach C uses a simplified CFD model including only the wind tunnel nozzle and test section, as well as a simplified moving belt. The effect of suction devices seen in D is mimicked by defining a partial area of the nozzle flow as a slip wall (yellow area). Note that the model and the mounting sword are identical for both approaches

[1] https://verkehrsforschung.dlr.de/en/projects/ngt-cargo,

[2] DIN EN 14067-6:2018, Railway applications – Aerodynamics - Part 6: Requirements and test procedures for cross wind assessment, September 2018

[3] K.A. Weinman and Ehrenfried, K. (2022) *Unsteady inflow effects on model train drag.* In: New Results in Numerical and Experimental Fluid Mechanics XIV, Contributions to the 23rd STAB/DGLR Symposium Berlin, Germany 2022. A. Dillmann, G. Heller, E. Krämer, C. Wagner and J. Weiss (Ed.), Springer, 2024

[4] Wallin, Stefan: Kungliga Tekniska Hoegskolan (private communication)

Mitteilung

Fachgruppe: Aerodynamik bodengebundener Fahrzeuge

Aerodynamische Strömungsphänomene an Radantriebseinheiten in modernen 1:1 Fahrzeugwindkanälen

M. Willmann[1,2], A. Wäschle[1], P. Dannhäuser[1], B. Frohnapfel[2]
[1] Mercedes-Benz AG, Sindelfingen
[2] Institut für Strömungsmechanik (ISTM), Karlsruher Institut für Technologie (KIT)
michael.willmann@mercedes-benz.com

In Fahrzeugwindkanälen kann zur Bodensimulation die 5-Band-Technik verwendet werden. Dieses System besteht aus vier Radantriebseinheiten (RAEs), die für die Raddrehung zuständig sind, und einem Mittenlaufband, das den Großteil des bewegten Bodens zentral unter dem Messobjekt abdeckt. Da die vier RAEs zur Messung der aerodynamischen Kräfte am Fahrzeug Teil der Windkanalwaage sind, kommt es zwischen den RAEs und dem umgebenden festen Boden zu konstruktiv bedingten Spalten, die eine Verbindung des Plenums mit dem Waagenraum schaffen.

Durch den Trend zu breiteren Reifen und dem damit verbundenen, kleiner werdenden Abstand zwischen der Reifenflanke zur Bandkante auf der Innen- und Außenseite, konnte beobachtet werden, dass dieser Abstand einen entscheidenden Einfluss auf die gemessenen Luftkraftbeiwerte hat. Dieser Effekt kann auch bei einer schmalen Bereifung durch die Variation der seitlichen Radposition auf dem RAE-Band provoziert werden. Dabei wird die RAE-Spurweite aus der radzentralen Position verkleinert oder vergrößert, um die Außen- oder Innenseite der jeweiligen Bandkante anzunähern. Durch diese RAE-Änderung können am selben Fahrzeug unterschiedliche Beiwerte gemessen werden. Dabei reagieren nicht alle Fahrzeuge im gleichen Maße sensibel.

Als potenzielle Einflussfaktoren wurden neben der Distanz der Reifenaußenflanke zur Bandaußenkante auch der Einfluss der Längsspaltbreite zwischen RAE und festem Windkanalboden untersucht. Da das Band auf einem Luftlager gleitet, wurde auch die seitliche Luftlagerausblasung berücksichtigt, die durch den Druckausgleich der tragenden Druckluft unterhalb des Bands in das Plenum entsteht. Die Untersuchung des Effekts erfolgte hauptsächlich numerisch. Die Simulationsergebnisse wurden mithilfe von Druck- und Particle-Image-Velocimetry-Messungen in der Radumgebung validiert.

Das Unterdruckgebiet an den Rädern ist bis an die Längsspalte ausgeprägt. Es stellte sich heraus, dass der lokale Druckgradient innerhalb des Spalts, zwischen Plenum und Waagenraum, eine druckgetriebene Sekundärströmung verursacht, welche vor allem bei einer Interferenz mit den Rädern die Radumströmung beeinflusst. Das Verlustgebiet des Reifennachlaufs vergrößert sich und verändert durch die abweichende Fahrzeugumströmung den Heckbasisdruck. Durch die Verkleinerung der RAE-Spurweite, wird die Reifenaußenflanke an die Bandaußenkante angenähert. Der reduzierte Abstand führt ab einem kritischen Distanzmaß zur direkten Interferenz zwischen dem drehenden Rad und der Sekundärströmung. Dies hat einen erhöhten gemessenen Widerstandsbeiwert zur Folge.

Das Strömungsfeld zwischen der angestrebten idealen Straßenfahrt bei vollbewegtem Boden und der Windkanalströmung mit 5-Band-Technik unterscheidet sich vor allem durch die Leckageströmungen maßgeblich voneinander. Daher sollten diese Sekundärströmungen möglichst reduziert werden und für eine präzisere aerodynamische Fahrzeugentwicklung nicht mit den Rädern interagieren. Im Falle der verkleinerten RAE-Spurweite stellte sich auch die Längsspaltbreite als entscheidender Einflussfaktor heraus. Die Variation der Spaltbreite beeinflusste durch die veränderte Spaltquerschnittsfläche den austretenden Massenstrom,

STAB

sodass eine große Spaltbreite den Widerstandsbeiwert des Fahrzeugs durch die energie-reichere Interferenz stets vergrößert.

Die Variation der Luftlager-Ausblasgeschwindigkeiten zeigt, dass höhere Geschwindigkeiten bei kleiner RAE-Spurweite den Widerstandsbeiwert senken. Dies ist darin begründet, dass der verstärkte Querimpuls die austretende, bereits interferierende Störstruktur am Spalt verkleinert und damit die Wechselwirkung mit dem Rad geschwächt wird. Da die Intensität der Luft-lagerausblasung jedoch nicht unmittelbar beeinflusst werden kann, ist die wichtigste Erkenntnis, dass für eine höhere numerische Genauigkeit bei der Abbildung des Phänomens, die Luftlagerausblasung allgemein berücksichtigt werden sollte.

STAB

Comparison of a Strong and a Weak Coupling Scheme for Aeroelastic Computations of the
Dynamic Stall on a Rotor with Double-Swept Blades

Georg Babij
German Aerospace Center (DLR), Institute of Aeroelasticity, 37073 Göttingen
georg.babij@dlr.de

Introduction

High-fidelity aeroelastic simulations of rotor systems are carried out at the Institute of Aeroelasticity at the German Aerospace Center (DLR) by coupling numerical solvers for computational fluid dynamics (CFD) and a multibody system (MBS) with each other, namely the DLR TAU-Code on CFD side as well as Simpack on MBS side. In order to achieve this, data is exchanged between both solvers including in general aerodynamic forces,structural displacements and rigid body motions. In the past, previous simulations utilized a strong coupling scheme which denotes in the terminology used within the rotorcraft community an exchange of data in each physical time step and is mainly suited for time accurate simulations. While seeking for a peri-

*Figure 1: Rotor Test Facility Göttingen
with four-bladed rotor*

odic steady state solution, e.g. a helicopter in forward or hovering flight, the precise simulation of transients is of minor importance and the minimization of wall-clock time in the simulation chain comes to the fore. Without affecting the solvers' algorithms, the latter is achieved first and foremost by reducing the overhead resulting from frequent data exchange and extensive switching between both solvers. Therefore, a weak coupling scheme for rotor sytems between CFD and MBS is presented and applied to a model rotor with double-swept blades. According to the terminology mentioned above, this term denotes an exchange of data from an entire rotor revolution. For one iteration step, TAU calculates aerodynamic forces of an entire rotor revolution on CFD side, whilst a periodic steady state is ensured on MBS side by performing a time integration over multiple rotor revolutions. By this means, transients have been decayed towards the last calculated period which is taken for evaluation of structural displacements and rigid body motions. Against this background, data transfer now takes places in a bundled form. In addition to the aeroelastic simulations with the aforementioned weak coupling scheme, a comparison with a strong coupling scheme is intended. Strongly coupled simulations have already been performed for a model rotor with a double-swept blade in four-bladed configuration [1,2]. They are related to dynamic stall experiments being carried out at the Rotor Test Facility Göttingen (RTG) [3, 4], see Figure 1. The blades measure 541 mm and 72 mm in length and chord at the root, respectively [4]. Due to an axial inflow to the rotor the dynamic stall phenomenon is triggered once per revolution by a sinusoidal variation in pitch angle Θ.

Numerical modelling

Simpack is used to describe the structural dynamics of the entire rotor by means of a multibody system, see Figure 2. In order to take flexible blades into account, their structural displacements are described in a modal representation with an underlying linear elastic material behaviour. Stiffening effects occurring due to centrifugal forces are considered by a geometric stiffness matrix.
With regard to fluid flow, TAU solves the Reynolds-Averaged-Navier-Stokes equations on unstructured grids by means of a vertex-centered finite volume method. Due to the unknown Reynolds stresses turbulence models are applied, such as the SST-k-ω-model according to Menter in this study. Taking into account grid motion and deformation, the Chimera technique as well as the geometric conservation law are utilized. The primary grid contains approximately

13.6 million nodes and consists of a background grid as well as four chimera grids representing the blades.

In order to map data between both differently discretized models, i.e. between the CFD surface grid points and the markers of the MBS substructures, scattered data interpolation methods based on radial basis functions are applied.

Figure 2: Modelling of structural dynamics in Simpack

Numerical investigations and comparison of weak to strong coupling scheme

Several test cases with a rotor speed of f = 23.6 Hz will be presented comprising operating conditions with a collective pitch angle $\Theta_{coll} \in \{17°, 24°, 27°\}$ superposed by a cyclic sinusoidal variation in pitch angle $\Theta_{cyc} \in \{6°, 8°\}$. Thereby, the dynamic stall phenomenon is induced and gradually strengthened which consequently results in increasing non-linearities and hysteresis loops. Both solvers utilize an azimuthal discretization of $\Delta\Psi = 1°$ resulting in a physical time step of approximately $\Delta t \approx 1.177 \cdot 10^{-4}\, s$. Primarily, aerodynamic forces on the blades as well as displacements at their tips are extracted for comparison to previous simulations based on a strong coupling scheme. As shown by a test case representing the onset of dynamic stall with $\Theta_{coll} \pm \Theta_{cyc} = 17° \pm 8°$ in Figure 3, the curves from a hysteresis loop of the integral normal force F_n on one blade and its normal tip displacement w_n are plotted for the strong and weak coupling scheme. Both curves show agreement with each other, although they differ slightly in certain areas. The exact causes are currently being investigated and will be discussed in the final paper.

(a) Normal force F_n over pitch angle Θ

(b) Displacement w_n over pitch angle Θ

Figure 3: Hysteresis curves for strong and weak coupling ($\boldsymbol{\Theta_{coll} \pm \Theta_{cyc} = 17° \pm 8°}$)
Course of time indicated by arrows ↑

References

1. Babij, G.: *Aeroelastic dynamic stall computations of a double-swept blade in a four-bladed rotor configuration*, 48th European Rotorcraft Forum, 2022
2. Babij, G., Müller, M.M.: *Dynamic stall computations of a double-swept rotor blade with rigid and elastic modelling*, 23rd STAB/DGLR Symposium on New Results in Numerical and Experimental Fluid Mechanics XIV. Notes on Numerical Fluid Mechanics and Multidisciplinary Design. Springer, Berlin 2023
3. Schwermer, T., Richter, K., Raffel, M.: *Development of a Rotor Test Facility for the Investigation of Dynamic Stall (2016)*, https://elib.dlr.de/91322
4. Müller, M.M., Schwermer, T., Mai, H., Stieg, C.: *Development of an innovative double-swept rotor blade tip for the rotor test facility Goettingen*. DLRK 2018 Deutscher Luft- und Raumfahrtkongress (Sep 2018), https://elib.dlr.de/122702

STAB

Mitteilung

Fachgruppe Aeroelastik und Strukturdynamik:

Experimental and Numerical Investigation of a Generic Aeroelastic Delta Wing

Konstantin Bantscheff, Christian Breitsamter
Chair of Aerodynamics and Fluid Mechanics, Technical University of Munich,
Boltzmannstr. 15, 85748 Garching bei München, konstantin.bantscheff@tum.de

Introduction

In recent years, advancements in computational capabilities have enabled the development of high-fidelity computational approaches for fluid-structure interactions (FSI). These approaches are crucial for capturing the coupling effects between aerodynamic loads and elastic structures. FSI simulations are particularly important in aircraft aerodynamics when dealing with medium to large deformations, as they account for significant changes in aerodynamic loads compared to a rigid body assumption [1]. Consequently, validating these simulations through experimental analyses is a critical aspect of the aircraft design process. For both simulation approaches and experimental analyses using scaled models is essential to ensure that the structural behavior of the investigated model accurately reflects that of a full-scale equivalent.

Model Design

The focus of this generic wing model investigation lies on the conduction of experimental investigations of an aeroelastically scaled delta wing at high angles of attack. Furthermore, low Mach numbers and steady inflow conditions regarding flap deflections and their effect on the occurring wing deformation is considered. The resulting data is used for validation purposes
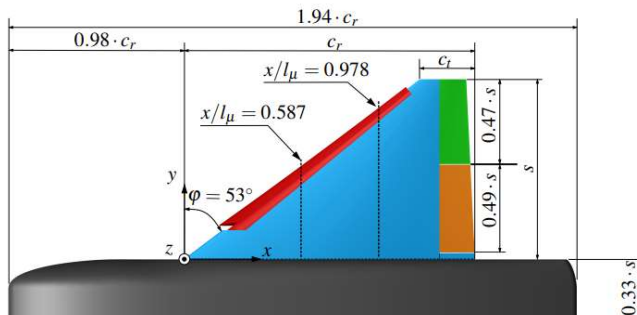
Figure 1: Geometry of the Model53c

regarding computational results. The scaling of the aeroelastic model is conducted according to previous work [2].

For the manufacturing of the scaled wind tunnel model, named Model53c, 3D printing technology is applied. The utilized delta wing model features a leading-edge sweep of $\varphi = 53°$ and a taper ratio of $\lambda = 0.159$. The model is downscaled by a factor of 11.2 with respect to a fictitious full-scale

wing and has a root chord length of $c_r = 0.75\ m$ [3]. A leading-edge slat is deployed at a fixed angle of 20°. The inner and outer trailing edge flaps are screwed to the main wing and can be exchanged by flaps with different deflection angles. Figure 1 shows a sketch of the Model53c geometry and its control surfaces.

Computational Approach

For the simulation procedure, the elasticity of the model is considered. As a result, a two-way FSI simulation is performed by utilizing the ANSYS tools Fluent, transient Mechanical and System Coupling. For the fluid dynamics setup a hybrid RANS-LES modeling approach is used. Specifically, the stress blended eddy simulation (SBES) is applied, where the SST k-ω RANS and LES models are 'blended' by a shielding function on the stress-level [4].

For the structural mechanics simulation, the entire layout of the Model53c, including the interior design, is set up using ANSYS Mechanical. The interface between the CFD simulation and the structural simulation is managed through ANSYS System Coupling. At the beginning of each physical time step, pressure and shear forces from the CFD surface mesh, covering the wing and flaps, are transferred to the corresponding surfaces of the structural mesh. The resulting deformation of the Finite Element Method (FEM) mesh is then communicated back to the CFD surface grid. The deformation of the wing model is propagated into the volume mesh by a

STAB

diffusive smoothing method. This two-way coupling involves multiple consecutive exchange cycles between the two simulations for each time step until the changes in the flow forces and structural displacements on both sides of the data transfer converge.

Detailed transient structural and aerodynamic analyses are performed considering different control surface deflection of the model. A time instant view of the resulting flow field around the wing is depicted in Figure 2, visualizing the vortex structures by applying an iso-surface of the Q-criterion with $Q = 500000 \frac{1}{s^2}$. The simulation at hand is conducted for an angle of attack $\alpha = 20°$ and a dynamic pressure of $q = 500 \, Pa$.

Experimental Analysis

For the experimental investigation in the wind tunnel facility A of the Technical University of Munich the global mean forces and moments are evaluated. Furthermore, multiple accelerometers (PCB 352C22/NC) are installed in the model. This instrumentation setup is utilized to evaluate the local influence of flap deflections on the structural dynamics of the wing. A photogrammetry methodology is applied to examine the global time averaged and transient deformation of the model under multiple operational conditions. The measured time averaged twisting deformation is given in Figure 3 and compared to the aeroelastic simulations. A proper agreement between the simulation approach and the measurements is apparent. Both the simulation and the measurements show a downward twisting of the wing towards the tip, which has a significant influence on the local aerodynamics of the wing with respect to a rigid configuration.
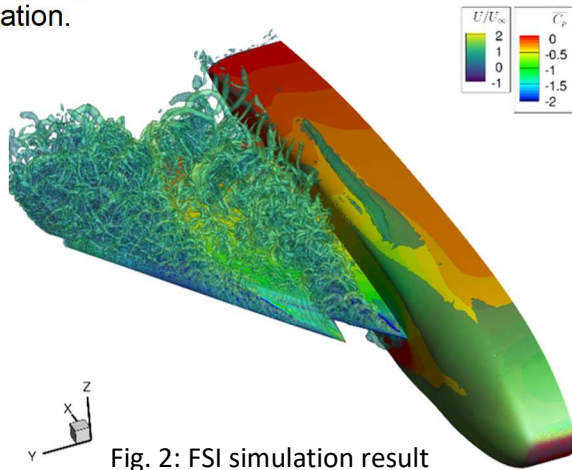
Fig. 2: FSI simulation result for $\alpha = 20°$, $\frac{q}{E} = 0.3 \cdot 10^{-6}$, Q-criterion with $Q = 500000 \frac{1}{s^2}$ and mean pressure coefficient for $t = 0.31 \, s$
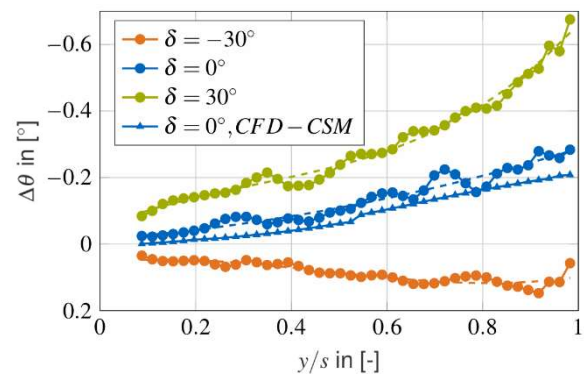
Fig. 3: Wing twist distribution over $\frac{y}{s}$ for three flap deflection angles at $\alpha = 20°$ and $\frac{q}{E} = 0.3 \cdot 10^{-6}$

Acknowledgement

Literaturverzeichnis

[1] C. Reinbold, K. Sørensen und C. Breitsamter, „Aeroelastic simulations of a delta wing with a Chimera approach for deflected control surfaces," *CEAS Aeronautical Journal,* Bd. 13, Nr. 1, pp. 237-250, 2021.

[2] K. Bantscheff und C. Breitsamter, „Dynamic Structural Scaling Concept for a DeltaWing Wind," *Aerospace,* Bd. 10, Nr. 7, p. 581, 2023.

[3] M. Moioli, C. Reinbold, K. Sørensen und C. Breitsamter, „Investigation of Additively Manufactured Wind Tunnel Models with Integrated Pressure Taps for Vortex Flow Analysis," *Aerospace,* Bd. 6, Nr. 10, p. 113, 2019.

[4] F. Menter, „Stress-Blended Eddy Simulation (SBES)—A New Paradigm in Hybrid RANS-LES Modeling," *Springer International Publishing,* pp. 27–37, 2018.

STAB

Mitteilung

Fachgruppe: Aeroelastik und Strukturdynamik

FSTraceInterface: First steps towards coupling `TRACE` with structure solvers

C. Berthold[*], R. Jain[†], I. Huismann[†]

[*]Institute of Propulsion Technology, German Aerospace Center, Linder Höhe, 51147 Cologne, Germany, e-mail: christian.berthold@dlr.de

[†]Institute of Software Methods for Product Virtualization, German Aerospace Center (DLR), Zwickauer Straße 46, 01069 Dresden, Germany
e-mail: ramandeep.jain@dlr.de, immo.huismann@dlr.de

Coupled fluid-structure analysis of turbomachinery blades is becoming increasingly important in order to ensure engine safety, particularly as materials and geometries grow more complex. With increasing complexity of turbomachinery blade row designs, existing one-way coupled methods, as currently used in many industrial design processes, loose their validity. An example being nonlinear damping elements which are used to limit blade vibration amplitudes. Consequently, fully (two-way) coupled simulations accounting for the interaction between fluid and structural fields become important for accurately investigating phenomena such as flutter or forced response of nonlinear blade vibrations. Apart from aeroelastic analysis, also conjugate heat transfer analysis plays an increasingly important role be it for cooling analysis or for the requirement of more precise temperature stress predictions of turbine blades with complex internal cooling channel geometries.

To address this need, a coupling interface, `FSTRACE`, is being developed to integrate the well-established CFD solver `TRACE` with the `FlowSimulator DataManager (FSDM)` library. This integration will enable fluid-structure interaction (FSI) simulations of turbomachinery components using `TRACE` alongside various structural solvers available within `FSDM`, including `CalculiX`, `b2000++ pro`, `Nastran`, and `Ansys`. An additional advantage is that the plugins for `FSDM` already provide functionality accounting for surface mesh deformations, a key requirement in aeroelastic simulations and furthermore interpolation routines are readily available for mapping data between non-matching meshes at the fluid-structure interface.

The current development of `FSTRACE` supports steady conjugate heat transfer (CHT) simulations. The algorithmic pipeline employed for these simulations is depicted in *Figure 1*. The CFD-CSM coupling follows a `Gauss-Seidel` method. Initially, an adiabatic flow solution is computed using `TRACE`, providing an initial surface temperature at the coupling surface. This CFD solution is then utilized by the CSM solver to determine an initial temperature field of the structure. Inside the coupling loop, the surface heat flux, computed by the CFD solver, is passed to the CSM solver. The CSM solver computes an updated temperature field of the structure and the surface temperature is subsequently fed back into the CFD solver and the next coupling iteration is executed. This iterative process continues until the convergence criteria are satisfied. In order to prevent the structural sub-problem to become ill-posed due to a specific choice of boundary conditions (BCs) at the non-interface boundaries, the heat flux (Neumann) BC is relaxed with a Robin BC, yielding a combination of a Neumann BC and a film heat transfer BC.

To verify the implemented interface, a 2D turbine blade is simulated with `FSTRACE` where the structural surface temperature is adjusted by a simple analytical model in order to meet a target heat flux. Subsequently, in order to validate the coupled methodology, a conjugated heat transfer simulation of a plate with finite thickness and a fluid flow on the upper surface is conducted using `FSTRACE` and `CalculiX` (for which also a `FSDM` interface is developed). Finally, to demonstrate the current capabilities of `FSTRACE`, a conjugated heat transfer simulation of a turbine blade with internal cooling is conducted. The converged solution is shown in *Figure 2*.
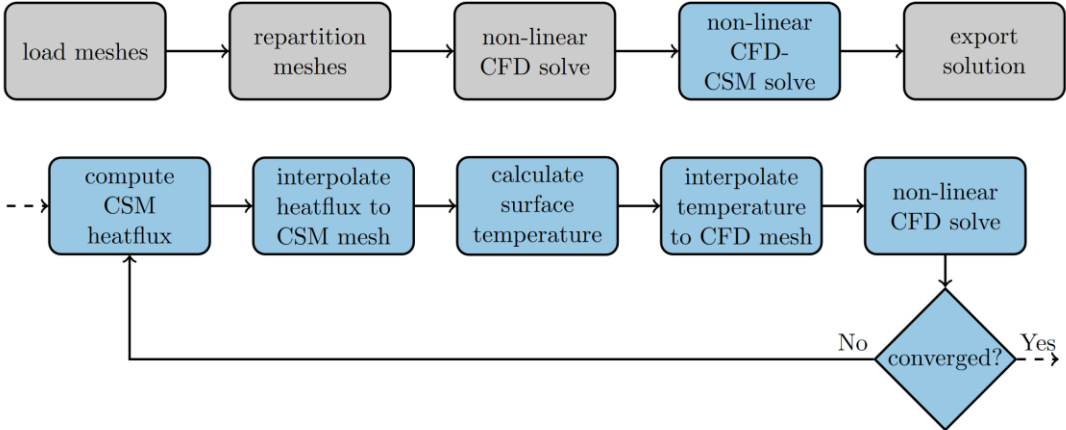
Figure 1: Pipeline for a CFD-CSM coupled simulation in FSDM. The top section illustrates each step involved in executing the FSI simulation, while the bottom section provides a detailed breakdown of the coupling process.
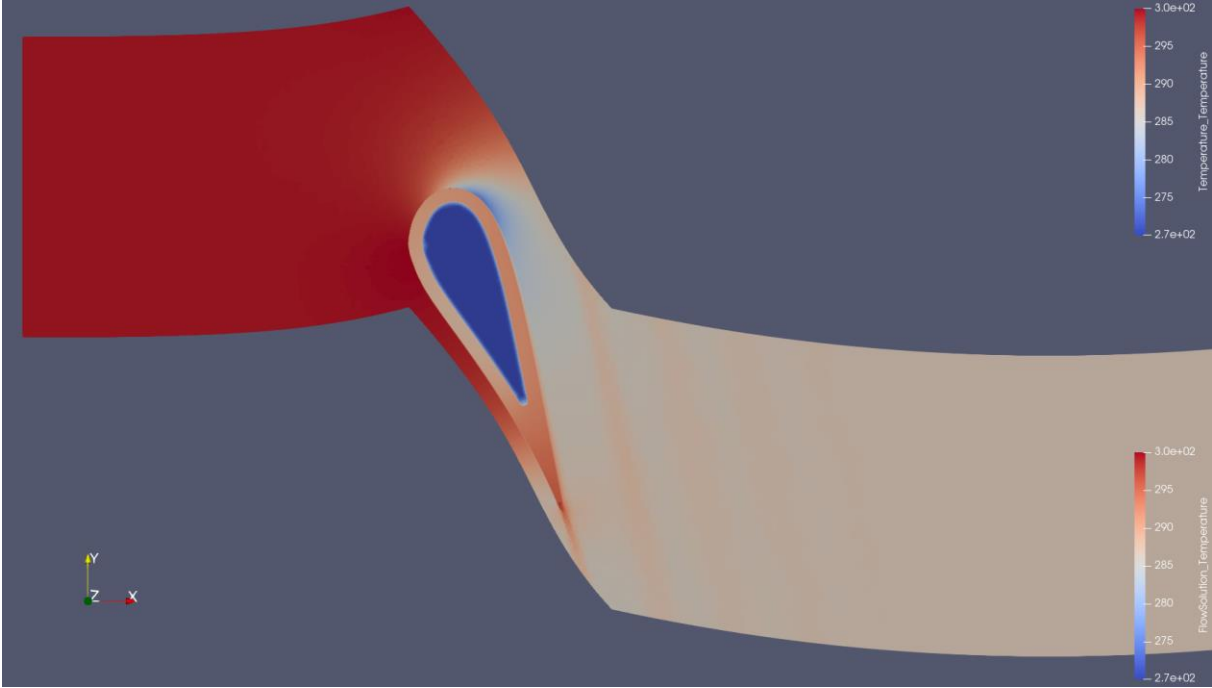
Figure 2: Temperature field solution at 50\% blade height of a CHT turbine blade simulation with an internal cooling channel.

STAB

Numerical simulation of the sloshing behavior
in aircraft hydrogen tanks for different flight maneuvers

A. Goerttler

Institute of Aerodynamics and Flow Technology, German Aerospace Center (DLR)
Bunsenstraße 10, 37073 Göttingen, Germany
Andreas.Goerttler@dlr.de

Introduction

In order to reduce emissions from air traffic by 2050, alternative propulsion concepts must be developed in addition to new aircraft. The combustion of hydrogen or the use of a fuel cell is a promising and environmentally friendly option. However, many issues still need to be solved before liquid hydrogen can be successfully used in aviation, including the safety of storage options, the feasibility of hydrogen propulsion, the development of the refueling infrastructure and other topics.

In addition, the aircraft fuel tanks currently in use, which are located in the aircraft wings, among other places, cannot be used for hydrogen due to the low temperatures required and the thick insulation needed for this. Regardless of the position of the tank, significantly larger cylindrical tanks will be used. This leads to additional problems, as every movement of the aircraft is transferred to the liquid and the long tanks can cause unfavorable sloshing behavior.

Methods

In the DLR project HYTAZER, simulations with the incompressible solver DLR THETA are carried out in this study. The two phases of the cooled hydrogen are considered using the Volume of Fluid (VoF) method [1], which represents either the liquid or the gaseous phase depending on the VoF-value. The CICSAM scheme [2] is used to construct the phase interface.

The simulations are used to calculate the forces and moments for different load cases. For this purpose, various load cases occurring during flight maneuvers are simulated, for example different take-off aborts. Two different tank geometries are used. Both tanks are located behind the passengers in the aircraft. The front tank is cylindrical, while the aft tank tapers conically towards the rear in order to fit into the rear fuselage. In order to analyze the influence of the filling level, five different filling levels are examined.

In addition to a tank without a slosh plate, two different concepts of a slosh plate are examined. These are located parallel to the spanwise direction in the middle of the tank. Furthermore, it is investigated how the longitudinal forces generated by the sloshing fuel differ depending on the fill level and the slosh plate concept.

In addition to the realistic tank geometries, simulations of simple rectangular tanks are also carried out. The focus here is on the effect of sinusoidal excitations of the tank in the longitudinal axis. The exciting frequency is set as a function of the natural frequency of the tank geometry, which mainly depends on the tank length and filling height.

On the one hand, these simulations serve as preparation for a validation experiment on the MAVIS shaking table in order to be able to estimate loads in advance. On the other hand, the tests carried out are recalculated afterwards and the comparison between the experimental and numerical results is used as a validation case.

Results

Figure 1 depicts the x-force for a simulated take-off abort lasting 40 seconds in total. Each line represents a different fill level. There is a consistent oscillation up to 20 seconds, after which the sign of the force changes, since the tank is decelerated at this time point. The higher the fill level, the higher the mean force.

Figure 2 depicts the x-force for a constant fill level of 56%, without and with two additional slosh plate designs. It is evident that the mean force remains unchanged, while the simulations show that the amplitude of the longitudinal forces decreases significantly due to the presence of the slosh plate. However, the frequency of the sloshing motion increases slightly due to the shorter characteristic length.
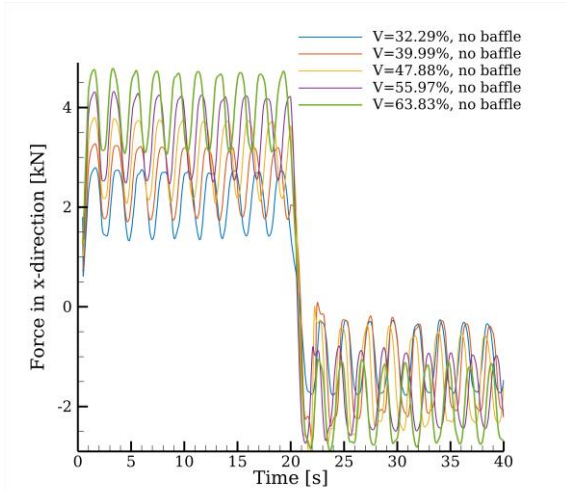
Figure 1: Force in the x-direction for take-off abort for five different fill levels.
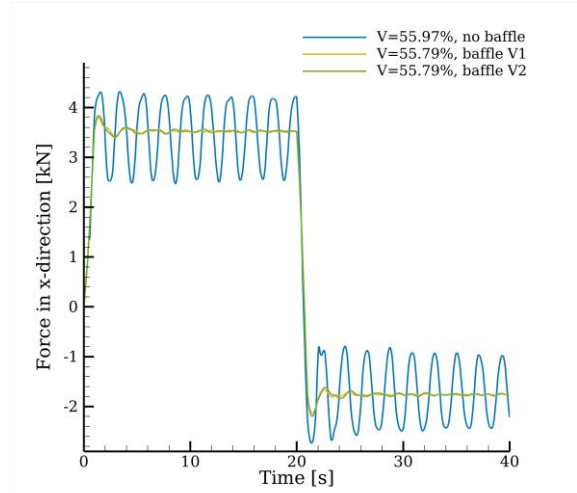
Figure 2: Force in the x-direction for take-off abort for two baffle designs with fill level 56%.

Figure 3 shows the time-varying total forces in the longitudinal direction (x-direction) of a rectangular tank for different excitation frequencies. The forces are already normalized with the maximum force that would occur in a rigid case with the same mass and the same excitation amplitude. Values above 1 indicate therefore a higher force that is triggered by the sloshing of the liquid. This is why this force is called slosh amplification factor in the following.

Figure 4 shows the results of a Fast Fourier Transformation analysis of the forces in the x-direction. There are two main frequencies per case occurring, which mostly reflect the excitation frequency and the natural frequency. However, anomalies occur at excitation frequencies that are very close to the natural frequency.
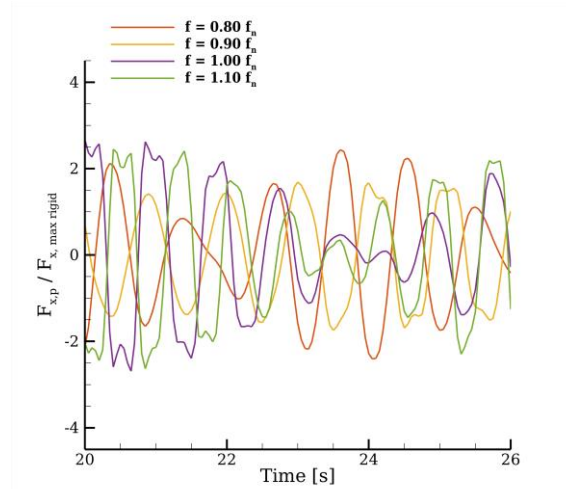
Figure 3: Ratio of the x-force to the expected rigid force for a sinusoidal excitation with different frequencies close to the natural frequency.
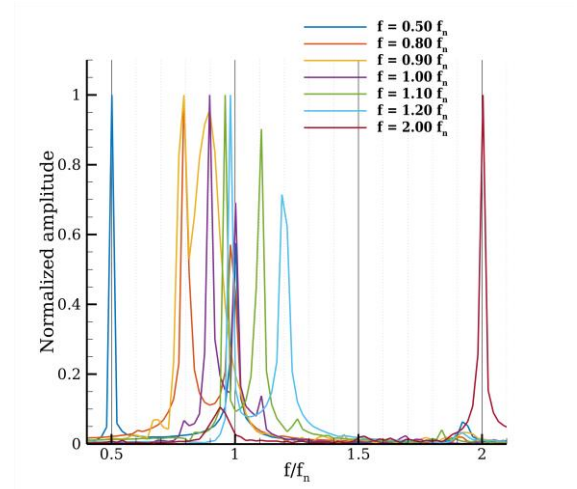
Figure 4: Fast Fourier analysis of the x-force of a simulation with sinusoidal excitation with different frequencies close to the natural frequency.

The final paper will contain a more detailed analysis of the sloshing simulations, with a particular focus on the realistic tank load cases.

References

[1] C.W. Hirt and B.D. Nichols: "Volume of Fluid (VoF) Method for the Dynamics of Free Boundaries", Journal of Computational Physics, 39(1):201–225, 1981. DOI: https://doi.org/10.1016/0021-9991(81)90145-5

[2] O. Ubbink and R.I. Issa: "A Method for Capturing Sharp Fluid Interfaces on Arbitrary Meshes", Journal of Computational Physics, 153(1):26–50, 1999. DOI: https://doi.org/10.1006/jcph.1999.627

STAB

Mitteilung

Fachgruppe: Allgemeine Strömungstechnik

PIV-Messung der Ablenkung eines Atemfreistrahls durch einen Luftvorhang

Andreas Kohl[1,2], Daniel Schmeling[1], Claus Wagner[1,2]
[1]Deutsches Zentrum für Luft- und Raumfahrt e.V. (DLR),
Institut für Aerodynamik und Strömungstechnik, Bunsenstraße 10, 37073 Göttingen
[2]Technische Universität Ilmenau, Institut für Thermo- und Fluiddynamik,
Am Helmholtzring 1, 98693 Ilmenau
E-mail: andreas.kohl@dlr.de

Ein Belüftungskonzept, das in letzter Zeit häufig untersucht wurde, ist der sogenannte Luftvorhang [1,2]: ein planarer turbulenter Freistrahl aus einer rechteckigen Düsengeometrie, der auf eine gegenüberliegende Oberfläche auftrifft und somit eine aerodynamische Barriere erzeugt. Das Konzept birgt das Potential, die Ausbreitung von luftgetragenen Krankheitserregern in Innenräumen zu verringern [1]. Mögliche Einsatzfelder sind Passagierkabinen von Flugzeugen oder Schienenfahrzeugen. Diese sind räumlich stark begrenzt und bieten nur wenig Platz zwischen den Passagieren und dem Strömungsfeld des Luftvorhangs. Ziel dieser Arbeit ist es, die Ablenkung und die Durchdringung eines laminaren Freistrahls, der einen menschlichen Atemimpuls simuliert, durch einen Luftvorhang in Abhängigkeit vom Impulsflussverhältnis γ beider Freistrahlen zu untersuchen. Dieser Ansatz wurde bereits angewandt, um die Stabilität von isothermen Luftvorhängen bei Querströmung mit Hilfe von zweidimensionaler numerischer Simulation zu untersuchen [2]:

$$\gamma = \frac{M_{ac}}{M_{cf}} = \frac{\rho_a \, b_0 \, U_0^2}{\rho_a \, H_0 \, U_{cf}^2} = \frac{b_0 \, U_0^2}{H_0 \, U_{cf}^2} \tag{1}$$

Hierbei ist b_0 die Düsenbreite und U_0 die mittlere Ausströmgeschwindigkeit des Luftvorhangs. U_{cf} gibt die mittlere Strömungsgeschwindigkeit der druckgetriebenen Querströmung durch den Luftvorhang für den Referenzfall (U_0=0) bei inaktivem Luftvorhang an. Die Höhe H_0 in Gleichung (1) bezieht sich auf die Schnittfläche beider Impulsflüsse. In dieser Arbeit wird sie vereinfacht angenommen als der Durchmesser des laminaren Atemfreistrahls an dessen Einlass in das Messvolumen (siehe Abbildung 1). Dieser ist in einem horizontalen Abstand von $5{,}1\, b_0$ auf den Luftvorhang gerichtet und erzeugt somit einen konstanten Impuls senkrecht zur Ausbreitungsrichtung des Luftvorhangs.
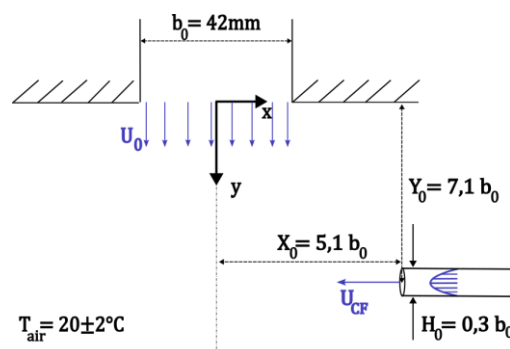
Abbildung 1: 2D-Skizze des Messaufbaus zur Untersuchung der Ablenkung und der Durchdringung des Atemfreistrahles durch den Luftvorhang. Nicht maßstabsgetreu.

In dieser Studie wird der Freistrahl ($Re = 1385$) und somit $U_{cf} = 1.75 \, (\pm 0.1)$ m/s konstant gehalten, wohingegen U_0 und somit die Reynoldszahl des Luftvorhangs Re_{ac} zwischen 900 und 7300 variiert wird. Die sich einstellenden Strömungsfelder werden mittels planarem PIV in der

STAB

Schnittebene ($z = 0$) vermessen und ausgewertet. Die zeitlich gemittelten Felder der zweikomponentigen absoluten Geschwindigkeit $\overline{U}(x,y)$ sind in Abbildung 2 für vier Impulsflussverhältnisse γ dargestellt. In Abbildung 2a) bei γ=0.17 kann der Luftvorhang den Atemimpuls nur leicht in positive y-Richtung ablenken. Wird γ erhöht (Abbildung 2b)), wirkt sich dies auch deutlich auf die Ausbreitungstrajektorie des Atemfreistrahls aus. Diese wird um etwa 60° durch den Impuls des Luftvorhangs nach unten abgelenkt. In Abbildung 2c) beträgt die Ablekung beinahe 90° und zusätzlich wird der Atemimpuls noch deutlicher vor der Mittelachse des Vorhangs (x=0) nach unten abgelenkt. Bei einem Impulsflussverhältnis von 11,61 (Abbildung 2d)) ist kaum noch eine Auswirkung des Atemimpulses auf das gemessene Strömungsfeld des Luftvorhangs erkennbar. Weitere Auswertungen des Strömungsfeldes, auch im Hinblick auf das zeitliche Verhalten, sind Bestandteil des Vollbeitrags dieser Arbeit.
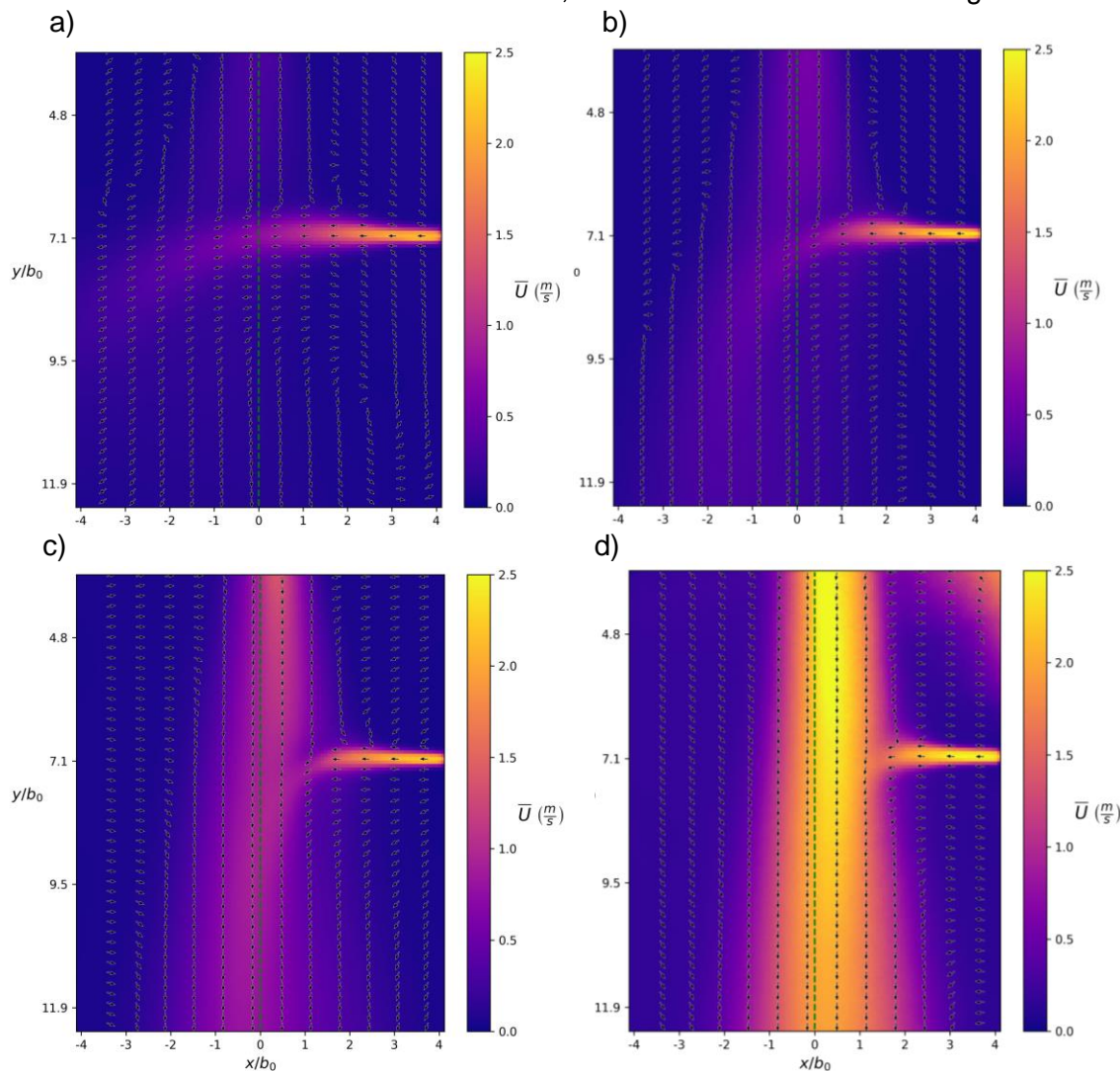
Abbildung 2: Mittlere Strömungsfelder der Interaktionszone beider Freistrahlen bei unterschiedlichen Impulsflussverhältnissen in a) $\gamma = 0,17$, b) $\gamma = 0,65$, c) $\gamma = 3,47$ und d) $\gamma = 11,61$.

Referenzen:

[1] Takamure, Kotaro; Sakamoto, Yasuaki; Yagi, Tetsuya; Iwatani, Yasumasa; Amano, Hiroshi; Uchiyama, Tomomi (2022): Blocking effect of desktop air curtain on aerosols in exhaled breath. In: *AIP Advances* 12 (5), S. 55323. DOI: 10.1063/5.0086659.

[2] Khayrullina, Adelya; Blocken, Bert; Magalhães de Almeida, Maria Odete; van Hooff, Twan; van Heijst, Gert-Jan (2021): Impact of a wall downstream of an air curtain nozzle on air curtain separation efficiency, In: *Building and Environment*, Volume 197, 2021, 107873, DOI:10.1016/j.buildenv.2021.107873.

STAB

Mitteilung

Fachgruppe: Allgemeine Strömungstechnik

Investigating modifications of the heat transfer by velocity boundary conditions in turbulent thermal convection using an off-lattice Boltzmann method

Sai Ravi Gupta Polasanapalli[1,2], Marten Klein[1,2], Heiko Schmidt[1,2]
[1]Lehrstuhl Numerische Strömungs- und Gasdynamik, Brandenburgische Technische Universität (BTU), Cottbus-Senftenberg, [2]Scientific Computing Lab (SCL), Energie-Innovationszentrum (EIZ) Cottbus, Siemens-Halske-Ring 15A,03046 Cottbus.
E-mail : polasana@b-tu.de

Functional surfaces, such as textures and coatings, provide means to passively modify the scalar transfer in technical flows by altering surface energy properties. Mayeed et al. (2016) [1] and Wu et al. (2013) [2] have studied the effect of hydrophobic and hydrophilic surfaces in Rayleigh–Bénard convection. Hydrophobicity can be numerically modeled by prescribing a tailored slip velocity boundary condition. Flows over slippery surfaces are not uncommon, neither in nature [3] nor in industrial applications [4]. The common mathematical property among these applications is to be seen in the utilization of a finite slip length formulation for the boundary condition. A common choice is the Navier slip length, which is the distance between the surface and the imaginary point where the extrapolation of the wall-aligned velocity component becomes zero, see Figure 1(b). A slip length of zero corresponds to a no-slip surface, while an infinite slip length corresponds to a free-slip surface.

In the present study, turbulent Rayleigh–Bénard convection is considered as a canonical problem with fluid confined in a rectangular box with a heated bottom wall, a cooled top wall, and adiabatic side walls. Three-dimensional numerical simulations are performed using lattice Boltzmann method (LBM) [5]. The approach is facilitated by simple geometry and offers efficient upscaling to high Rayleigh number flow regimes with strong thermal forcing. The LBM model is operating in direct numerical simulation (DNS) mode so that full-scale resolution is achieved. The main objective is the investigation of surface slip effects on the heat transfer and the flow organization. The present study serves as a first step towards an even more comprehensive analysis of surface wettability effects in natural convection regimes of wall-bounded flows.

Figure 1(a) shows a schematic of the Rayleigh–Bénard configuration. The computational domain is defined as $H \times H \times H$ in the x, y, and z directions, where H is the edge length of the cubic cavity, serving as the integral spatial scale. The top (bottom) wall is heated (cooled) and has prescribed constant temperature T_h (T_c), where $T_h > T_c$. The vertical side walls are adiabatic surfaces. All walls are subject to different velocity boundary conditions, here no-slip and free-slip. All preliminary simulations discussed below were conducted at $Ra = 2 \times 10^6$ (representing weak turbulence) and $Pr = 4.38$ (water).

Figure 1(c) and 1(d) shows the instantaneous velocity vectors together with the temperature field correspond to the free-slip and no-slip case, respectively. The surface boundary conditions induce substantial changes in both the flow and thermal fields. In the free-slip case, an unsteady single large-scale circulation pattern is evident, evolving in shape and center over time, along with variations in velocity

STAB

magnitude. Conversely, in the no-slip case, a variety of eddy modes become evident, as depicted, and instances of flow reversal are observed. This behavior arises from the fundamental distinction between the two conditions: free-slip surfaces permit tangential fluid motion along the boundary, whereas no-slip surfaces enforce zero fluid velocity at the boundary with a sharp velocity gradient. This high non-linearity in the no-slip case is the primary driver behind the formation of multiple eddy recirculation zones. Consequently, larger velocity fields are observed in the free-slip cases compared to the no-slip surface cases, resulting in a thinner thermal boundary layer thickness that significantly impacts the heat transfer rate. Compared to the all no-slip walls scenario, the heat transfer rate improves by 100% with all walls being free-slip. When only the horizontal walls are free-slip, the rate increases by 48.41%, and when only the side walls are free-slip, it increases by 11.71%.

In our contribution to the STAB workshop, we will present the effect of different surfaces on flow and heat transfer characteristics, taking into account the no-slip, free-slip, and finite-slip lengths of the walls. Following that, the impact of different walls, such as horizontal or side walls, will be discussed separately. Finally, the influence of finite slip length on turbulent characteristics will also be addressed. The work was supported by the North- German Supercomputing Alliance (HLRN) and numerical simulations were carried out on HLRN high-performance computing facilities at Berlin and Göttingen (project ID: bbi00022).
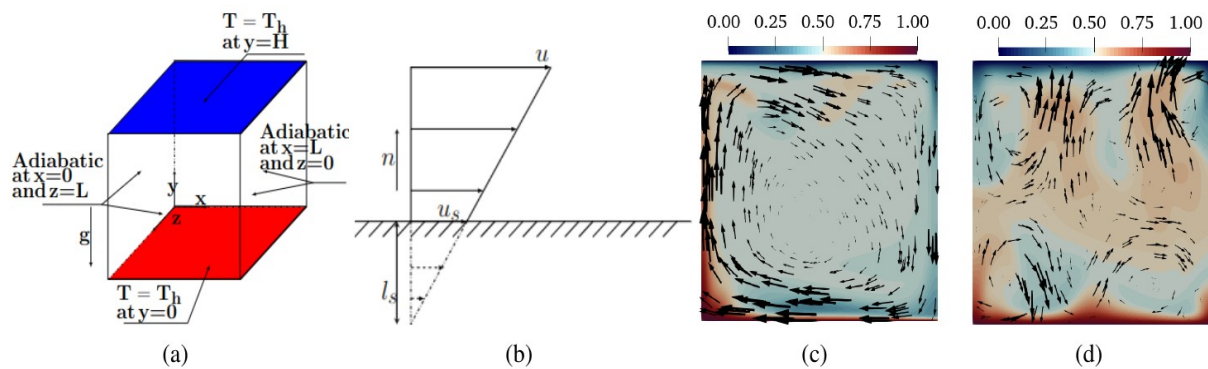
Figure 1: Schematic drawings of (a) the Rayleigh–Bénard set-up and (b) the Navier slip velocity boundary condition with slip velocity u_s and lenght scale l_s given the surface normal n and flow velocity u. In-stantaneous velocity vectors (arrows) and normalized temperature distribution (color shading) on the mid horizontal plane for (c) free-slip and (d) no-slip top and bottom walls.

References

[1] M.S. Mayeed, Patnaik, S. Soumya & R. Mitchell, ASME 2016 IMECE2016. USA: ASME, 2016.

[2] C.H. Wu, Y.S. Huang, L.S. Kuo & P.H. Chen, Int. J. Heat and Mass Transfer **63:** 249–254, 2013.

[3] D.J. Tritton, Nature **257** (5522): 110–112, 1975

[4] C.H. Choi, & C.J. Kim, Phys. Rev. Lett **96**(6): 066001, 2006.

[5] S.R.G. Polasanapalli & K. Anupindi, Phys. Fluids **34** (3): 035125, 2022.

Confluence of Wall Shear Stress and its Relation to Vorticity Surface Flux

Markus Rütten, German Aerospace Center (DLR),
Institute of Aerodynamics and Flow Technology
Bunsenstr. 10, 37073 Göttingen, Germany
markus.ruetten@dlr.de

Introduction

In the last decades the aerodynamic design of aircraft configurations has benefited tremendously from the development of numerical algorithms in modern computational fluid dynamics. Due to these developments the number of design cycles could be significantly increased allowing the investigation of novel ideas and variations whereas the necessary number of wind-tunnel tests could be reduced. Since the design of complicated three-dimensional aerodynamic shapes requires hundreds of shape design variables, most researchers have addressed this challenge by using gradient-based optimizers combined with adjoint methods for computing the gradients, an approach pioneered by Jameson [1]. This is only possible due to the increased availibility of high-performance parallel computing to achieve the targeted objectives [4]. However, during those highly automated computational shape-design processes, the real flow physical mechanisms responsible for lift, drag and flow separation are pushed into the background. Therefore, the present work addresses the relevant surface flow quantities which are interconnected with the local shape contour of the targeted aerodynamic configuration. Based on concepts stemming from vortex dynamics [5] the connection between vorticity, vorticity flux, wall shear stress lines, their curvature and the curvature of the shape of the flow configuration is derived and discussed [2, 3]. In particular, the link of the principle flow pattern behaviour of converging or diverging wall shear stress, for which the term confluence respectively diffluence is coined. The goal of the work is to discuss interrelation of the relevant flow physical quantities with these terms, moreover, focus is laid on exploring potential applications of these quantities in future shape-optimization configuration studies.

Methodology and Results

Following concepts of vortex dynamics the forces acting on the surface of a flow configuration can be calculated by using the surface boundary vorticity flux (BVF) $\vec{\sigma}$ expressed by in-surface quantities:

$$
\begin{aligned}
\vec{\sigma} = \frac{\partial(\mu\vec{\omega})}{\partial n} = \rho\,\vec{n}\times\vec{a} - (\vec{n}\times\nabla_\pi)\,\Pi + \mu\,(\vec{n}\times\nabla_\pi)\cdot[(\vec{\omega}\times\vec{n})\,\vec{n}] \\
+ \mu\left[\nabla_\pi\,(\vec{\omega}\cdot\vec{n}) + \tilde{K}\,(\vec{\omega}\cdot\vec{n})\,\vec{n}\right] + \rho\vec{f}\times\vec{n},
\end{aligned}
\tag{1}
$$

here, including local acceleration $\vec{a} = \frac{D\vec{v}}{Dt}$, external forces $\vec{f}$ and even surface deformation. Herein ρ is the density of the fluid, the term $\Pi = p - (\lambda + 2\mu)\nabla\cdot\vec{v}$ incorporates the pressure p and the compressibility of the fluid assuming a constant dynamic viscosity μ and volume or bulk viscosity λ. The local curvature at a surface point $\vec{r}$ on the surface

S is represented by the curvature tensor $\tilde{K} = -\nabla_\pi \vec{n}$ which links the shape contour with the aerodynamic forces. Further, $\nabla_\pi = [\nabla(.)]_\pi - \vec{n}\left[\frac{\partial(.)}{\partial n}\right]_\pi$ is the wall-tangential gradient operator. Simplifying the BVF equation by investigating only incompressible flows without external forces and applying the wall tangential divergence operator on this equation leads eventually to the source terms of the aerodynamic forces, and a new quantity, the confluence of wall shear stress lines:

$$conf(\vec{\tau}_w) = \nabla_\pi \cdot \vec{\tau}_w - \nabla_\pi \|\vec{\tau}_w\| \cdot \frac{\vec{\tau}_w}{\|\vec{\tau}_w\|}. \tag{2}$$

This quantity allows visualizing the interconnection between the surface topology and wall vorticity fluxes and its impact on force source terms, flow separation and attachment, impressions are shown in Fig. 1. Sudden changes of the confluence is a hint for the neccessity to adapt the surface topology.
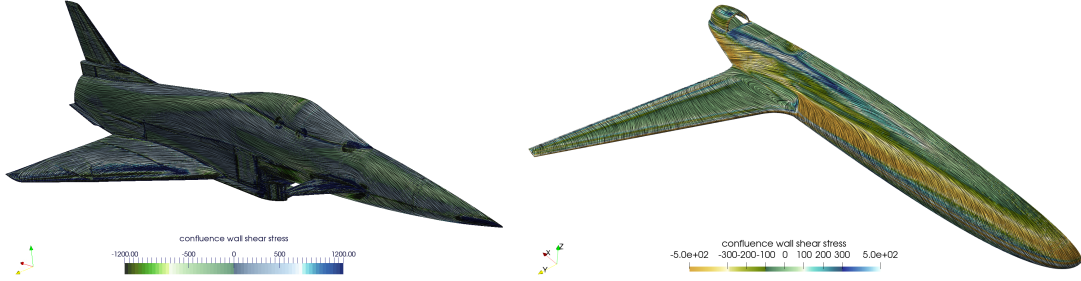
Fig. 1: Visualization of the confluence of wall shear stress as LIC surface flow pattern for the X31 fighter aircraft (left) and flux magnitudes at the surface of a wide body aircraft (right).

Literature

[1] Jameson, A.: Aerodynamic Design via Control Theory. Journal of Scientific Computing, Vol. 3, No. 3, pp. 233–260, 1988

[2] Lighthill, M.J., Introduction of boundary layer theory. In: Rosenhead L. (ed.) Laminar Boundary Layers. Oxford University Press, New York, pp. 46–113, 1963

[3] Panton, R.L.: Incompressible Flow. John Wiley and Sons, 1984

[4] Reuther, J.J., Jameson, A., Alonso, J. J., Rimlinger, M. J., and Saunders, D.: Constrained Multipoint Aerodynamic Shape Optimization Using an Adjoint Formulation and Parallel Computers, Part 1, Journal of Aircraft, Vol. 36, No. 1, pp. 51—60, 1999

[5] Wu, J.Z., Ma, H.Y., Zhou, M.D.: Vorticity and Vortex Dynamics. Berlin, Heidelberg; Springer, 2006

STAB

Mitteilung

Fachgruppe: Allgemeine Strömungstechnik

Particle transport predictions in a generic room: Comparison of URANS and RANS with experiments

Florian Webner[1,2], Andreas Kohl[1,2], Daniel Schmeling[1] und Claus Wagner[1,2]
[1]Deutsches Zentrum für Luft- und Raumfahrt e.V. (DLR)
Institut für Aerodynamik und Strömungstechnik
Bunsenstraße 10, 37073 Göttingen
[2]Technische Universität Ilmenau, Institut für Thermo- und Fluiddynamik,
Am Helmholtzring 1, 98693 Ilmenau
E-Mail: florian.webner@dlr.de

Since the emergence of the COVID-19 pandemic in 2019, aerosol particle transport and infection risk prediction have become of increasing interest. Computational Fluid Dynamics (CFD) offer the possibility to predict the transport of individual particles. However, there are several CFD approaches with different underlying assumptions and computational costs. The Reynolds-Averaged Navier-Stokes (RANS) approach results in a time-averaged flow field and is computationally inexpensive. In contrast, the unsteady RANS (URANS) approach provides transient results at a higher computational cost. This raises the question of which of the two is more feasible for predicting particle transport in occupied, ventilated spaces. Therefore, in this study, we compare the particle transport predictions of a RANS and a URANS approach to experimental data in a simple generic room. Thus, this is a continuation of our previous study [1], where we compared the particle transport predictions of a RANS approach to experimental data in the same room.
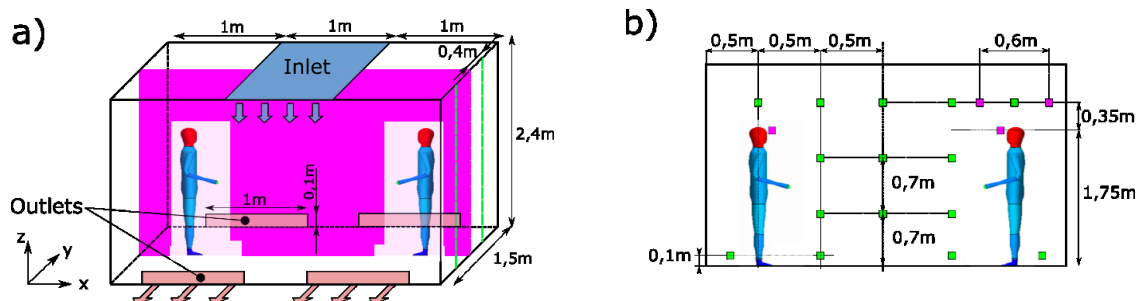
Figure 1: a) Sketch of the generic room used for the experimental and numerical investigations. b) Positions of the aerosol particle sensors on three measurement planes. Green squares indicate the positions of particle sensor on the outward planes (dashed green line in a)), purple squares additional sensor-positions on the middle plane (dashed purple line in a)).

We compare RANS, URANS, and experimental measurements in a generic cuboid room with length, width, and height of 3 m, 1.5 m, and 2.4 m, respectively. Air is supplied from the top with a volumetric flow rate of 25 l/s at a temperature of 17°C and exhausted through 4 passive outlets near the floor (see Fig. 1a). The manikins are heated with a power of 100 W to simulate body heat. A steady, particle-laden stream of 12 l/min is delivered from one of the manikins' mouths to mimic the momentum of human exhalation. To ensure a sufficient signal-to-noise ratio in the experiments, the number of particles released per second is increased to 2×10^7 compared to 2200 particles per second in the CFD. The particle concentration in the room is measured at 47 locations with established particle sensors [2], as shown in Figure 1b). To compare the experimental and numerical results, the particle concentrations in the room are normalized to the particle concentration at the source location (the manikin's mouth). Furthermore, we evaluate the particle concentrations averaged over 200 seconds after a quasi-steady state is established.

STAB

For the CFD, the open source software package OpenFOAM is used. The mesh is refined near the walls and manikins. For both, the RANS and URANS simulations, the turbulent kinetic energy and dissipation are approximated by the k-omega SST model. The particle transport is modeled considering fluid drag, gravity, and random dispersion based on the turbulent kinetic energy. Although the flow field is steady in the RANS case, the particle transport is predicted in a transient manner. We assume that particles are deposited and removed from the domain upon first contact with a wall or manikin. For the URANS approach, the time is iterated by the implicit Euler time scheme and the time step is limited to 90 % of the Courant number. See [1] for more details on the configuration and methodology.

Figure 2 shows a scatter plot of the 47 data points with the normalized particle concentration of the experimental data $C_{n,exp}$ on the x-axis and of the CFD predictions $C_{n,CFD}$ on the y-axis: URANS predictions in blue markers and RANS predictions in orange markers. Additionally, equality is indicated by a black dashed line, meaning that for points closer to the line, the CFD predictions are in better agreement with the experimental measurements. The plot provides two insights: First, the blue markers (URANS) are clustered around the equality line, whereas the orange markers (RANS) are much more scattered, meaning that the URANS predictions are in better agreement with the experimental data. Second, the majority of the markers are within 0.4 % < $C_{n,exp}$ < 0.8 %, meaning that the particle concentration in the room does not vary much according to the experimental measurements. Only two positions show particle concentrations higher than 1 %. Therefore, with the exception of these two points (located in the exhalation jet [1]), the room can be considered as almost well mixed.

Figure 2: Comparison of the predicted particle concentration by RANS and URANS with experimental data at 47 positions.

The average absolute error of the particle concentration compared to the experimental data is almost three times higher for RANS (URANS: 0.087 %, RANS: 0.238 %). Based on the average particle concentration of all measurement points in the experiment of 0.61 %, this translates into average relative errors of 14.2 % and 39.0 % for URANS and RANS, respectively.

The results indicate that unsteady flow structures in the generic room significantly influence the particle transport. Thus, the higher computational cost of URANS allows particle transport predictions at almost three times higher accuracy (14.2 % and 39.0 % relative error for URANS and RANS, respectively). Furthermore, the results show that the considered generic room setup leads to an almost well-mixed room. This information is valuable for assessing whether a well-mixed room assumption is sufficient or whether a CFD calculation is required for future particle transport predictions.

In the full paper, we will discuss the time series of the particle concentration and the fluctuations of the particle concentration over time in RANS, URANS, and experiment.

[1]   Webner et al., Aerosol Spread in a Generic Train Entrance: Comparison Between Experiment and Numerical Simulation, *Notes on Numerical Fluid Mechanics and Multidisciplinary Design*, 2024

[2]   Netherland Aerospace Center (NLR) and National Institute for Public Health and the Environment (RIVM) (2021) "CORSICA final report" NLR-CR-2021-232.

STAB

Mitteilung

Fachgruppe: Bio- und Mikrofluidmechanik

High-resolution flow investigations in native membrane lungs
for understanding shear-induced blood clot formation

Michael Kranz[1,2], Daniel Pointner[1,2], Maria Stella Wagner[3], Matthias Lubnow[4], Karla Lehle[3], and Lars Krenkel[1,2]

[1]Department of Biofluid Mechanics, OTH Regensburg,
Seybothstr. 2, 93053 Regensburg
[2]Regensburg Center of Biomedical Engineering (OTH and University Regensburg)
Seybothstr. 2, 93053 Regensburg
[3]Department of Cardiothoracic Surgery, University Hospital Regensburg,
Franz-Josef-Strauss-Allee 11, 93053 Regensburg
[4]Department of Internal Medicine II, University Hospital Regensburg,
Franz-Josef-Strauss-Allee 11, 93053 Regensburg
michael.kranz@oth-regensburg.de

Extracorporeal membrane oxygenation (ECMO) was developed as a treatment for adults, children, and neonates with severe cardiac or pulmonary disease (1,2). However, despite showing promising patients' outcome, the formation of blood clots within the ECMO membrane lung (ML) can be observed (Figure 1 A). These pose an enormous risk on the critically ill patients.

The ML consists of semi-permeable hollow-fibers which are woven together with delicate warp threads. The fibers are surrounded by the patient's blood and an oxygen-rich gas mixture flows through them. Gas exchange occurs due to a concentration gradient.

It is already known that blood clot formation is triggered by an un-physiological flow regime (1,3). This is manifested in particular by elevated shear rates. We expect their presence of in the vicinity of irregularly arranged hollow-fibers.

Creating a model of the fluid domain of a ML is challenging. In particular, the complex structured warp threads, but also the numerous small hollow-fibers (0.38 mm diameter). Modeling is made particularly difficult by the irregular arrangement of the hollow fibers. In previous tests, it was found that the fibers were partially shifted in the direction of blood flow. Symmetries can only be assumed to a limited extent from this. In addition to the complex geometry of the flow domain, the blood also exhibits a number of significant non-Newtonian effects that can influence the formation of blood clots within the MLs. However, the deposition of blood clots around the hollow fibers in turn affects the geometry of the blood flow domain. In summary, it can be concluded that highly complex fluid mechanical phenomena take place in MLs.

In this study, an unused permanent life support ML (PLS, Getinge, Rastatt, Germany) was utilized as a basis for creation of a native flow domain. The ML was filled with a contrast agent (barium chloride solution) and scanned with a micro-CT (phoenix v|tome|xs 240/180, Baker Hughes Digitals Solution, Hürth, Germany; settings: voltage: 180 kV, current: 190 µA, voxel size: 34,5 µm). This results in a realistic flow domain with native hollow-fiber arrangement. The fluid domain is then segmented (Figures 1 B, C) by the attenuation coefficient of the contrast agent and exported as a STL-file (VG Studio MAX 2022.3, Volume Graphics, Heidelberg, Germany). The resulting three-dimensional blood flow domain was subsequently meshed (Figure 1 D; Centaur 16.0, Surry Hills, Australia) with about 2.5×10^7 nodes for later numerical flow investigations (Figures 1 E, F).

STAB

In our work, we compare different levels of detail of the ML geometry and the influence of realistic blood flow properties and behavior. This means that changes in the local hematocrit distribution within the Fåhraeus-Lindqvist effect on the resulting blood flow field in the relevant subsection of the ML are included.

For the realistic modeling of the blood flow, the Newtonian representation is compared with the well-established Carreau-Yasuda and a multiphase Euler-Euler approach.
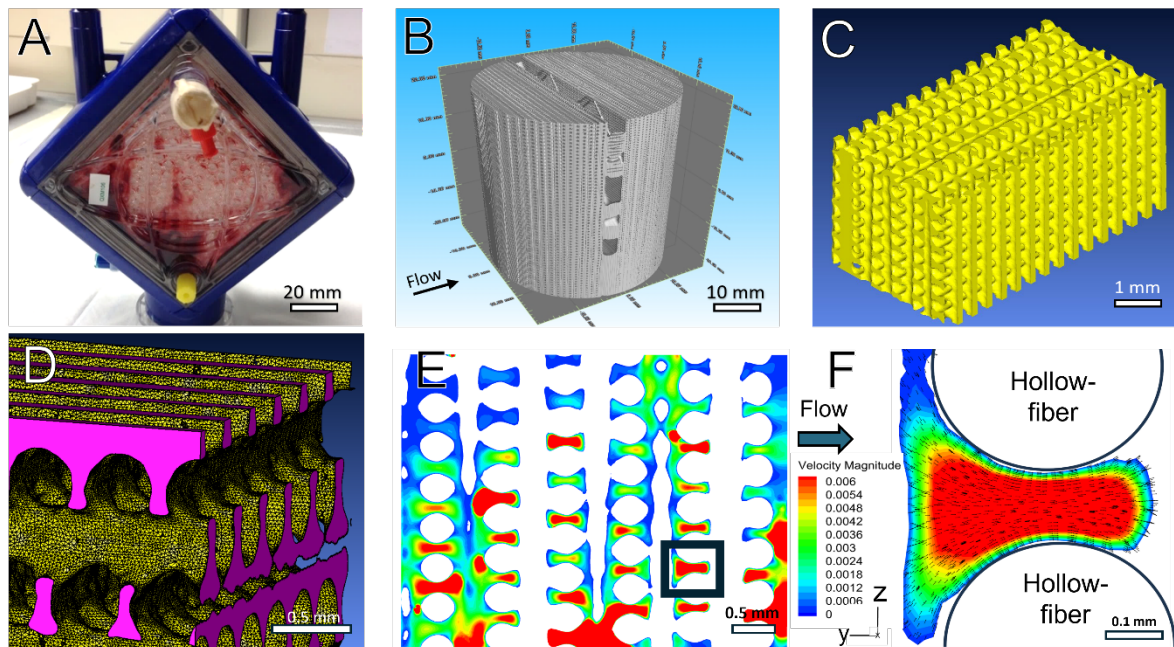
Figure 1: Outline of the process of flow domain creation from the native ML to the numerical flow field in the vicinity of the hollow-fibers. (A) Example of ML with visible blood clot formation. (B) Micro-CT reconstruction of ML. (C) Three-dimensional reconstruction of flow domain within a central section of a ML. (D) Section of highly resolved mesh of flow domain for numerical investigations. (E), (F) Planar visualization of the velocity magnitude at a representative location within the ML; irregular arrangement of hollow-fibers (white) and heterogeneous velocity magnitude visible.

References

1. Wagner MS, Kranz M, Krenkel L, Pointner D, Foltan M, Lubnow M, et al. Computer based visualization of clot structures in extracorporeal membrane oxygenation and histological clot investigations for understanding thrombosis in membrane lungs. Front Med [Internet]. 2024 Jun 19 [cited 2024 Jun 19];11. Available from: https://www.frontiersin.org/articles/10.3389/fmed.2024.1416319

2. Birkenmaier C, Dornia C, Lehle K, Müller T, Gruber M, Philipp A, et al. Analysis of Thrombotic Deposits in Extracorporeal Membrane Oxygenators by High-resolution Microcomputed Tomography: A Feasibility Study. ASAIO J. 2020 Aug;66(8):922–8.

3. Herbig BA, Yu X, Diamond SL. Using microfluidic devices to study thrombosis in pathological blood flows. Biomicrofluidics. 2018 Jul 1;12(4):042201.

STAB

Mitteilung

Fachgruppe: Bio- und Mikrofluidmechanik

Towards Experimental Validation of Models for Shear-Induced Aerosol Generation in
the Human Respiratory System

Johanna Michel, Lars Krenkel

OTH Regensburg, Department of Biofluid Mechanics, Galgenbergstr. 30, 93053 Regensburg
Regensburg Center of Health Sciences and Technology (OTH Regensburg) und
Regensburg Center of Biomedical Engineering (OTH and University Regensburg)
Johanna.michel@oth-regensburg.de

Modeling the propagation of respiratory aerosol has been invaluable for understanding the spread of the Covid19 pandemic. Understanding how and where in the respiratory system these aerosols are formed would give us a way to suppress aerosol generation alltogether. To predict the origin of aerosol particles in the human respiratory system, numerical modelling is necessary as the internal flow inside the airways is highly complex and is not accessible for experimental measurements. Most numerical studies of aerosol generation have focused on shear-induced aerosol generation, which is the most prominent mechanism of aerosol formation in coughing, and were mostly carried out using the volume of fluid method [1], [2], [3] and wall film models [4], [5] such as the eulerian wall film model.

While the volume of fluid method provides a reliable way of modelling the detachment of single particles, it is higly computationally expensive, as the grid elements need to be smaller than the minimum size of predicted particles. The minimum size of respiratory particles of up to 0.01 µm in diameter [6] renders the volume of fluid method not applicable for modeling larger parts of the airways to predict the location of aerosol generation. Wall film models overcome this limitation by being much more computationally efficient. To achieve this, they do not model the formation of individual particles, but treat the wall-film as a property of the surface. Depending on how the flow acts on this virtual surface film, particles are seeded into the flow, which can then be traced using discrete phase modelling.

All the modeling techniques for shear-induced aerosol generation presented above suffer from a lack of validation data. The particle numbers predicted in studies using wall-film models were validated with the number of particles exhaled by test subjects [4], [5]. This however leads to an overestimation of the number of generated particles, due to two reasons. Firstly, aerosol particles are produced in the respiratory system via a multitude of different mechanisms. Secondly, due to the vast size of the human airways and the large scale difference between the individual aerosol particle and the airways, the modelled domain cannot encompass the complete respiratory system because of computational limits. Thus, the number of particles predicted in a model of such a smaller domain should be lower than the total number of exhaled particles. Therefore, validating models of shear-induced aerosol generation with the total number of exhaled particles is not appropriate.

In addition to the lacking validation data, depending on how the wall-film models are implemented, the number of predicted generated particles is dependent of both the mesh resolution and the simulation time step (figure 1). Thus, for predicting shear-induced aerosol generation in the human airways, an improved implementation of these wall-film models based on experimental validation data is necessary.

In this work, we present a method for experimentally determining the data to validate models of shear-induced aerosol generation in the human respiratory system. The presented experimental setup enables measuring how the air shear-flow characteristics, especially the local wall shear stress, and the mucus material properties, including surface tension and viscoelastic properties, influence the quantity and size distribution of generated aerosol. Further, the surface geometry of the film is measured to identify the effect of wave formation on the fluid film.

The left hand side of figure 2 illustrates the experimental setup. The core component is the measurement chamber with a height of 2 mm, where a fluid film is placed on a planar surface

STAB

with a surface area of 1.9 cm^2. To simulate the airflow inside the respiratory system, filtered pressurized air is guided over the mucus mimetic film. Generated particles are measured using an aerosol spectrometer (Resp-Aer-Meter Scientific, Palas GmbH), which records their quantity and size distribution. All connections between components are sealed to prevent inflow of ambient particles. The right hand side of figure 2 shows the quantity of particles formed from a viscoelastic hydrogel as mucus mimetic. The employed volume flow rate through the chamber of 9.5 L/min induces a wall shear stress of 0.17 Pa in the fluid film, which corresponds to breathing. In reference measurements without any mucus mimetic fluid, intruding ambient particles create an average particle flow of 0.78 particles per s. Thus, in these flow conditions and mucus mimetic properties, shear-induced aerosol generation creates an average particle flow of 1.1 particles per second.

The mechanism of shear-induced aerosol generation is based on wave formation on the surface of the fluid film. These waves change the flow geometry, which could influence the air flow characteristics. To record this phenomenon, a tilted laser with light-sheet optics illuminates the measurement chamber in a longitudinal direction (see figure 2, bottom left). A camera placed above the measurement chamber captures the reflection line of the laser plane, which shifts based on the local height of the fluid film. With the same viscoelastic mucus mimetic as above, we observed waves and recorded the velocity of the fluid film.

Using the presented setup, we measure the particle generation under different flow conditions and with different mucus mimetics. As such, we create the data that is necessary to validate the wall-film models for predicting the origin of aerosol particles inside the human respiratory system.
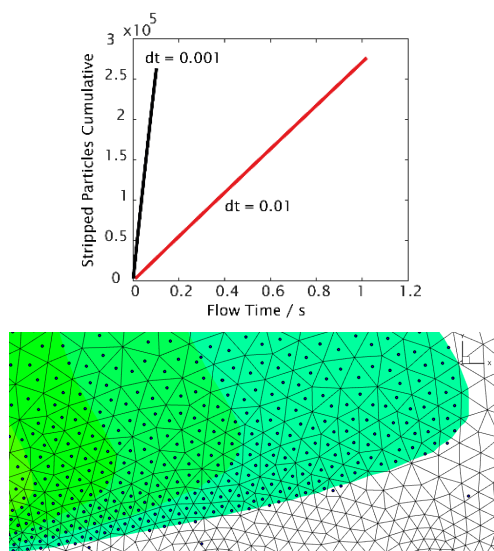
Figure 1: Mesh- and time step dependency of the Eulerian Wall Film model (Ansys Fluent 2023 R2)
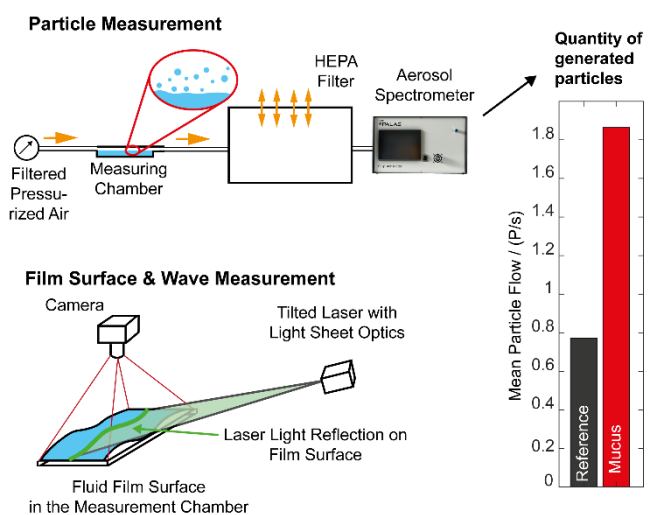
Figure 2: Schematic view of the experimental setup

[1]   R. R. Rajendran and A. Banerjee, "Mucus transport and distribution by steady expiration in an idealized airway geometry," *Med. Eng. Phys.*, vol. 66, pp. 26–39, Apr. 2019, doi: 10.1016/j.medengphy.2019.02.006.

[2]   C. Paz, E. Suárez, J. Vence, and A. Cabarcos, "Analysis of the volume of fluid (VOF) method for the simulation of the mucus clearance process with CFD," *Comput. Methods Biomech. Biomed. Engin.*, vol. 22, no. 5, pp. 547–566, Apr. 2019, doi: 10.1080/10255842.2019.1569637.

[3]   C. Pairetti, R. Villiers, and S. Zaleski, "On shear layer atomization within closed channels: Numerical simulations of a cough-replicating experiment," *Comput. Fluids*, vol. 231, p. 105125, Dec. 2021, doi: 10.1016/j.compfluid.2021.105125.

[4]   N. D. Khoa, K. Kuga, K. Inthavong, and K. Ito, "Coupled Eulerian Wall Film–Discrete Phase model for predicting respiratory droplet generation during a coughing event," *Phys. Fluids*, vol. 35, no. 11, p. 112103, Nov. 2023, doi: 10.1063/5.0174014.

[5]   H. Anzai *et al.*, "Coupled discrete phase model and Eulerian wall film model for numerical simulation of respiratory droplet generation during coughing," *Sci. Rep.*, vol. 12, no. 1, Art. no. 1, Sep. 2022, doi: 10.1038/s41598-022-18788-3.

[6]   M. L. Pöhlker *et al.*, "Respiratory aerosols and droplets in the transmission of infectious diseases," *Rev. Mod. Phys.*, vol. 95, no. 4, p. 045001, Oct. 2023, doi: 10.1103/RevModPhys.95.045001.

STAB

Mitteilung

Fachgruppe: Drehflügleraerodynamik

Evaluation of wind tunnel test data from a helicopter model with novel fuselage geometry and additional passive lift devices

Erik Brehl, DLR, Institute of Flight Systems, Braunschweig, Germany
Erik.Brehl@dlr.de
Oliver Schneider, DLR, Institute of Flight Systems, Braunschweig, Germany
Oliver.Schneider@dlr.de

In the framework of the DLR guiding concept "The Recue Helicopter 2030" a new medium size wind tunnel model was developed from scratch. Two wind tunnel test campaigns were conducted with this new model where a number of new ideas were tested. The basic model setup was tested first in the wind tunnel in 2020. During this campaign the aerodynamic properties of two different fuslages were measured. The reference-configuration represents the state-of-the-art fuselage comparable to the Airbus Helicopter EC135. Furthermore, an optimized design for a conventional rescue helicopter was tested, which is called SZ-1 (scenario 1), see Figure 1. For this campaign the model was equipped with instrumentation in the non-rotating domain. The fixed system instrumentation contains a 6-component main balance for the rotor system, a separated 6-component fuselage balance, three 3-axis accelerometes, pressure sensors in both fuselages (static & dynamic) and additional six channels for a stabilizer balance. No blades and no swash plate actuators were installed.

In 2024 the model was completed with further instrumentation (see [1]). A sophisticated Data Acquistion System (see [2]) was developed for collecting data from the rotating domain and a wireless transmission path for the digitized data. A complete new blade set with instrumentation was manufactured in-house. These carbon blades were equipped with strain gauges (flap, lag, torsion) and dynamic pressure sensors. Sensors for pitch angle and pitch link force measurement were installed as well. The main shaft was instrumented with strain gauges for measuring the shaft moments (Mx, My, Mz). A swash plate with remote controlled actuators was also installed. The actuators can be controlled via a dedicated self developed HMI system at the main pilot station. In the non-rotation domain additional lift devices were added to the model. Two wings were designed and manufactured, which could be mounted optionally at the main model structure. Besides the optimized SZ-1 fuselage (reduced drag) the wings (increased lift) also helped to improve the helicopters performance in forward flight. The further instrumentation in the fixed frame is comparable to the first setup in 2020 (rotor balance, fuselage balance, fuselage pressure sensors, accelerometers, temperature sensors).

Figure 1: New Advanced Fuslage SZ-1

The wind tunnel test has been carried out successfully, where over 1200 test points have been measured during the campaign. The full Paper will describe the evaluation and analysis of wind tunnel test data for a selected number of test points from the test matrix. Due to the fact that two different DAQ systems have been used for rotating and non-rotating sensors the

measuring and data evaluation concept had to be adapted for the new system approach. Also a bunch of new software algorithms had to be implemented in the data evaluation and extraction software. The data for both systems are collected and stored based on the data point number which represents a dedicated test condition from the test matrix. Figure 2 shows the combined lifting force of both wings. ϑ is the angle setting for wing incidence relative to the fuselage incidence angle α of the wind tunnel model. The data were collected for the isolated fuselage without rotor and no rotation (blade stubs installed). A negative force in corresponds to lift. An increased ϑ (wing leading edge upwards) leads to increased lift for the whole the polar until stall occurs at negative α numbers (nose downwards).
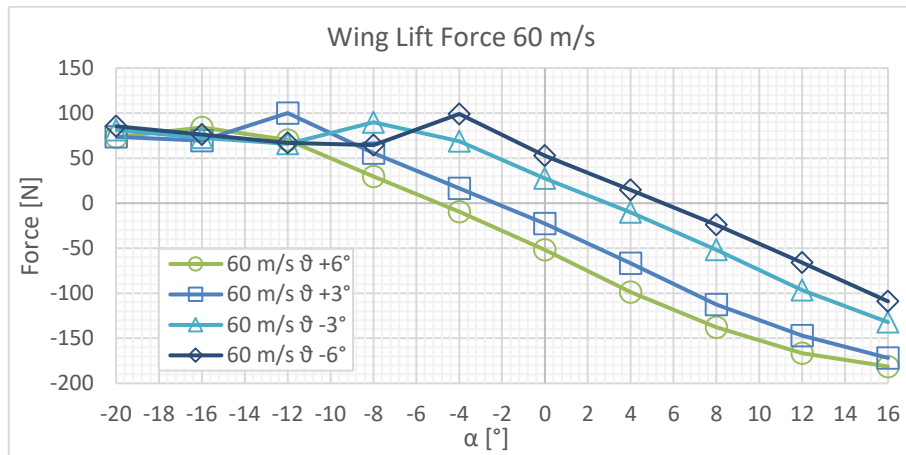
Figure 2: Fixed System Sensor Data – Wing Balance

Figure 3 shows the dynamic pressure sensor data from blade 1Y (№ 1, yellow) for maximum BVI collected by the rotational DAQ at 15 m/s wind speed and 1860 rotor rpm. The Ψ = 0° position is definded as blade in fuselage tail direction. The spinning direction of the rotor is counter clockwise (looked from the top), Figure 3 is a mirrored plot from the bottom. The nomenclature for the shown sensor data is "P70" = pressure sensor at 70% rotor radius, "L" = lower blade side with the following number for the sensor position in percent profile depth (chordwise). The peak at Ψ = 80° is a pressure leap due to an air turbulence which is more present at the blade's leading edge, an indication for noise at that position. Further details will be provided in the full paper.
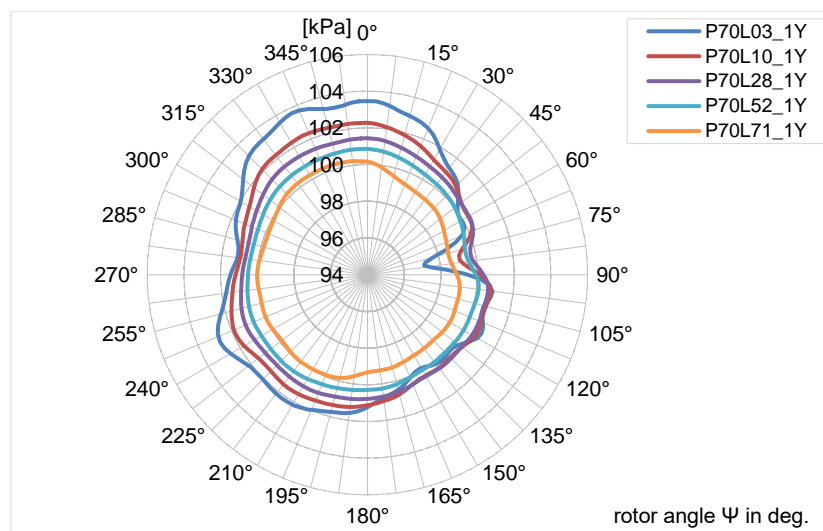
Figure 3: Rotational Sensor Data – dyn. Pressure Sensors

References

[1] Oliver Schneider, "DEVELOPMENT OF A NEW MEDIUM SIZE HELICOPTER WIND TUNNEL MODEL", European Rotorcraft Forum / Marseille, 2024
[2] Erik Brehl, "Rotational Data Acquisition for Rotorcraft Wind Tunnel Models", European Test & Telemetry Conference / Toulouse, 2023

STAB

Mitteilung

Fachgruppe: Drehflügleraerodynamik

Comprehensive Code Modeling Impact on Maximum Thrust, and Beyond, of an Isolated Rotor in Hover: Application of a Free-Wake Method

Berend G. van der Wall
German Aerospace Center, Lilienthalplatz 7, 38108 Braunschweig, Germany
berend.vanderwall@dlr.de

Comprehensive rotorcraft simulation codes are the working horse for design and simulation of a helicopter and its rotor under steady and unsteady operating conditions and also used to predict their limits until rotor stall occurs. Numerical studies date back to the 1970s [1-2], accompanied by experimental work [3-5], but with lack od modeling anc computing capabilities and restrictions in experiments. This paper focuses on the prediction of hovering rotor maximum thrust (due to stall limits) and the thrust & power characteristics when the collective control is further increased. The aerodynamic factors that in parts significantly affect the results for maximum thrust computation are now available in modern comprehensive rotor codes: steady or unsteady aerodynamics, steady or dynamic stall, blade tip losses, curvature flow, yaw angle, downwash model, blade-vortex and fuselage-rotor interaction. The downwash model and tip losses are found as most important factors in general.

This study makes use of the Bo105 40 % Mach-scaled model rotor of DLR and its blade geometry. In order to eliminate blade flexibility effects from aerodynamic effects, the blade is assumed as rigid with only the pitch control degree of freedom. It is a 4-bladed rotor with rectangular blades, 2 m radius, 0.44 m root cutout, 0.121 m chord length and -8 deg/radius linear pretwist with zero twist at 75 % radius.

Aerodynamic parameters investigated with respect to their impact on maximum rotor thrust are the steady stall delay model due to rotation and curvature flow (CF) along chord, the tip loss formulation beginning at a non-dimensional radial coordinate r_{tl}, and especially the rotor induced inflow models (from momentum theory: constant inflow (= Glauert model), from potential theory: nonlinear radial distribution (= Mangler model), from vortex theory (prescribed wake geometry = PW and free-wake geometry = FW). Airfoil coefficients are represented analytically as a function of the Mach number components in chord line direction and normal to it, but also in radial direction to allow for steady stall delay due to CF and yawed flow conditions, but also include compressibility effects. Unsteady aerodynamics include dynamic stall hysteresis in lift, drag and moment and after stall onset also include a vortex shedding model (VS).

Example results for the hover figure of merit FM shown in Figure 1 are computed by a sweep of the collective control angle up to maximum rotor thrust and beyond by up to 10 deg more collective control angle for the various inflow models, combined with different radial begin of the tip loss model. For $r_{tl} = 0.9$ the effect of the steady stall delay due to the CF model is shown in red color. The smaller r_{tl}, the larger the lift loss at the ends of the blade and the smaller the maximum achievable thrust. Steady stall delay introduced by the CF model increases lift capability especially in the inner part of the rotor blade and hence increases the maximum thrust. The radial distribution of the indued inflow is the essential driver for the radial location of stall onset – either inboard first (when small inflow is found inboard and large inflow outboard, as is the case for the Mangler model) which leads to the highest possible thrust amongst the inflow models – or outboard first (with small inflow outboard and larger inboard, as is the case for the Glauert and PW models). The FW model generates an inflow closest to the PW model and its resulting maximum thrust therefore is close to the PW result as well. Experimental data obtained in the wind tunnel with this rotor (albeit with flexible

blades) are indicated by the blue dots; they are confined to moderate thrust values due to re-circulation and turbulence developing in the wind tunnel.
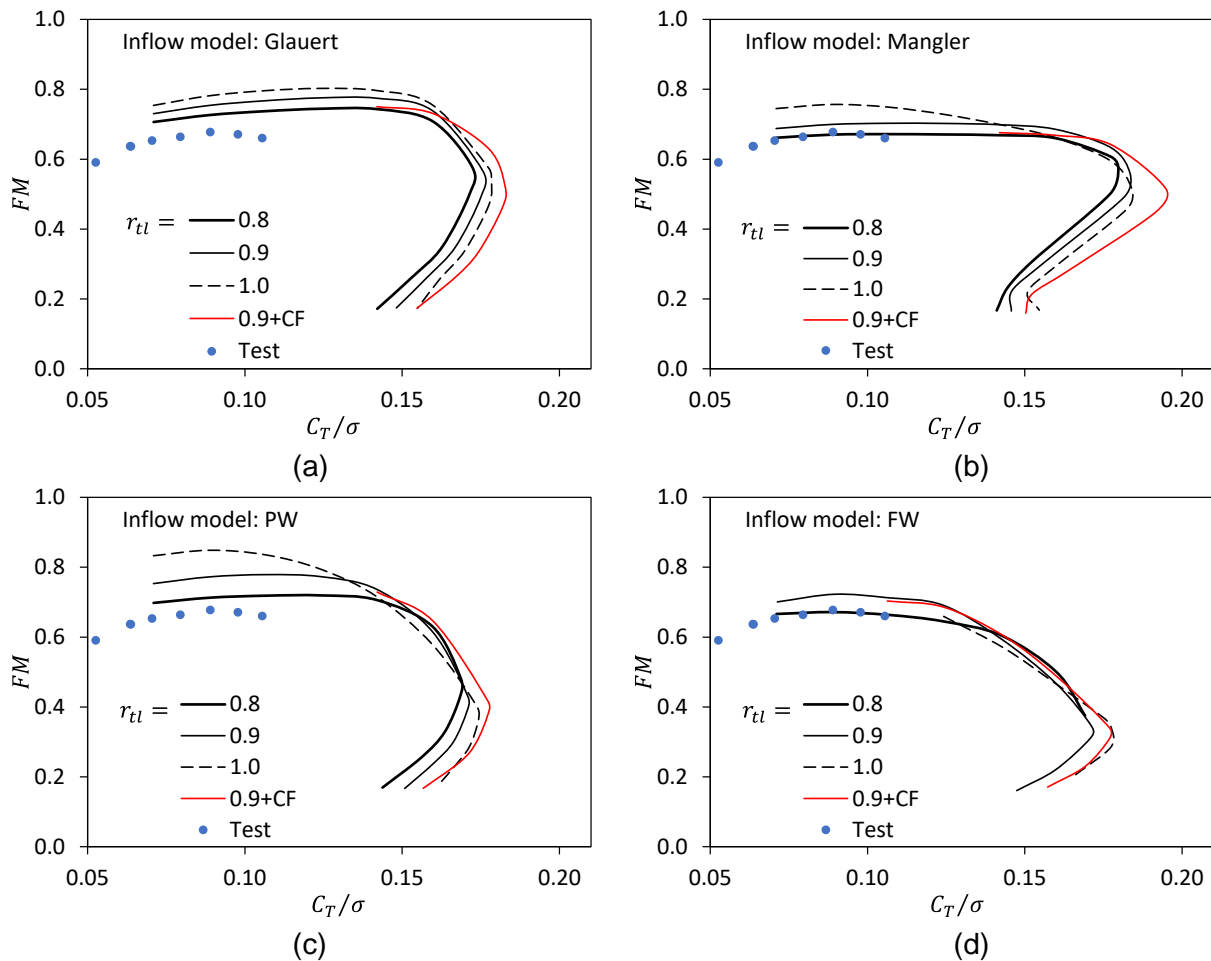
Figure 1: Influence of the inflow model, the tip loss parameter r_{tl} and curvature flow stall delay model CF on the figure of merit in hover. Blue dots: experimental data.

The physical chain from induced inflow distribution, resulting angle of attack distribution, and – in combination with the radial variation of Mach and stall angle of attack – the resulting normal force and moment coefficient distributions that explain the overall rotor stall and maximum thrust characteristics will be given in the final paper.

References

[1] Bellinger, E.D. Analytical Investigation of the Effects of Blade Flexibility, Unsteady Aerodynamics, and Variable Inflow on Helicopter Rotor Stall Characteristics. *Journal of the American Helicopter Society* **1972**, Vol. 17 (3), pp. 35-44. DOI: 10.4050/JAHS.17.35

[2] Landgrebe, A.J., Bellinger, E.D. A Systematic Study of Helicopter Rotor Stall using Model Rotors. In Proceedings of the 30th Annual Forum of the American Helicopter Society, Washington, D.C., 7-9 May 1974.

[3] McCroskey, W.J., Fisher, R.K., Jr. Detailed Aerodynamic Measurements on a Model Rotor in the Blade Stall Regime. *Journal of the American Helicopter Society* **1972**, Vol. 17 (1), pp. 20-30. DOI: 10.4050/JAHS.17.1.20

[4] Amer, K.B., LaForge, S.V. Maximum Rotor Thrust Capabilities, Articulated and Teetering Rotors. *Journal of the American Helicopter Society* **1977**, Vol. 22 (1), pp. 11-12. DOI: 10.4050/JAHS.22.1.11

[5] McHugh, F.J. What are the Lift and Propulsive Force Limits at High Speed for the Conventional Rotor? In Proceedings of the 34th Annual National Forum of the American Helicopter Society, Washington, D.C., 15-17 May 1978.

STAB

Mitteilung

Fachgruppe: Drehflügleraerodynamik

Propeller-Rotor Interaction in Helicopter Air-to-Air Refueling

Berend G. van der Wall
German Aerospace Center, Lilienthalplatz 7, 38108 Braunschweig, Germany
berend.vanderwall@dlr.de

During helicopter air-to-air refueling the rotor of the helicopter engages with several disturbances generated by the tanker aircraft [1,2]. Due to the comparably low maximum speed of helicopters, the tanker aircraft has to fly close to its minimum speed and at low altitude, leaving little margin for the helicopter to its never-exceed speed. This implies the tanker flying with less than its maximum take-off mass, with deflected flaps and with high propeller thrust. A 3D field of the aircraft's disturbances was computed by CFD for motion-based simulator trials of helicopter air-to-air refueling [3]. Helicopters therefore have to sustain position within a volume of large disturbances generated by the aircraft, such as the general wing downwash, strong vortices from the wing tip and either ends of deflected flaps, and the jet or accelerated air within the slipstream of the propellers.

In this paper – based on blade element momentum theory – the impact of the propeller jet on rotor blade aerodynamics is investigated analytically and rotor controls required to re-trim, i.e. integrally reject the disturbance impact on rotor trim, are computed for a typical air-to-air refueling scenario. The problem is sketched in Figure 1.

Figure 1: Sketch of a rotor immersed in the stream tubes of two propellers, or of one propeller with different positions.

As reference example, a tanker aircraft of the size of an A400M is used and as an example helicopter of the size of a CH-53G. The helicopter trim then is for an advance ratio of $\mu = 0.3$, a rotor tilt angle of $\alpha_S = -12$ deg and a thrust coefficient of $C_T = 0.01$; while the propeller slipstream then generates a perturbation of $\Delta\mu = 0.12$ within a width of $\Delta y = 0.45$ in terms of the helicopter rotor radius, and its slipstream center position is denoted by y_p.

Using blade element momentum theory, an analytical solution for integral rejection of the propeller slipstream impact on rotor aerodynamics and its trim is elaborated based on the tangential and normal velocities acting at the revolving blade elements. These components are composed by those of the rotor in undisturbed flow, plus a perturbation caused by the $\Delta\mu$ acting only in the slipstream, i.e. between y_1 and y_2 of the rotor. Then, the rotor thrust and aerodynamic hub rolling and pitching moments can be also expressed by the values of the undisturbed rotor and the perturbations caused by the propeller.

First the undisturbed rotor is trimmed to thrust and zero hub moments, which are textbook solutions for the collective and cyclic control angles. Then the perturbations of the control

angles required to mitigate the propeller perturbations are also elaborated analytically. They are split in two parts: one part acting all over the rotor disk in undisturbed flow; the second part only within the perturbation zone with all the perturbation velocities, which is quite elaborate.

Within the propeller slipstream the blade section lift perturbation ΔC_T contains contributions from the blade twist and undisturbed trim control angles, the perturbation (= re-trim) control angles $\Delta\Theta_{75}$ and $\Delta\Theta_S$ relative to the trim in undisturbed flow, and from the perturbation advance ratio $\Delta\mu$, which also leads to a perturbation in the axial inflow ratio $\Delta\mu_z$ and the induced inflow ratio $\Delta\lambda_i$.

Figure 2 shows a result for the control angles required for the propeller slipstream disturbance rejection in order to keep the rotor trim as in undisturbed flow. Maximum collective $\Delta\Theta_{75}$ and longitudinal cyclic control angles $\Delta\Theta_S$ are required for slipstream positions on the retreating side of the rotor, because the dynamic pressure on the blade is significantly reduced and simultaneously the angle of attack largely modified by the normal inflow component. Contrary, slipstream positions on the advancing side require only marginal control inputs, because the rotor sensitivity to thrust and moments is largely increased by the increased dynamic pressure there. No lateral cyclic control angle is needed due to the symmetry of perturbation lift to the rotor's y axis.
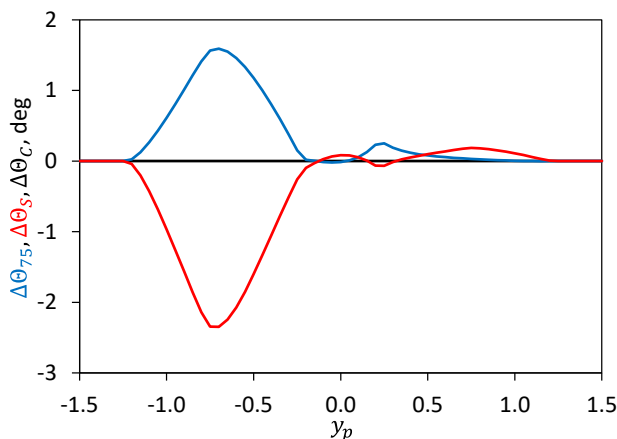
Figure 2: Control angles required to retrim the rotor with the propeller slipstream center position y_p varying across the rotor diameter, advancing side right.

The final paper will include variations of propeller thrust and size, rotor shaft angle of attack and thrust, and flight speed.

References

[1] Dunn, H.P., "The USAF CH-3C Helicopter V/STOL In-Flight Refueling Program and its Operational Uses and Implications," 22nd Annual Forum and Technology Display of the American Helicopter Society Proceedings, Washington, D.C., May 11-13, 1966.
[2] Kashawlic, B.E., Irwin, J.G.III, Bender, J.S., and Schwerke, M., "MH-47G DAFCS Helicopter Aerial Refueling Control Laws," 67th Annual Forum and Technology Display of the American Helicopter Society Proceedings, Virginia Beach, VA, May 3-5, 2011.
[3] Löchert, P., Schmidt, S.O., Jann, T., and Jones, M., "Consideration of Tanker's Wake Flow for Helicopter Air-to-Air Refueling," AIAA Aviation Forum, Virtual, Aug. 2-6, 2021, DOI: 10.2514/6.2021-2561.

STAB

Mitteilung

Fachgruppe: Experimentelle Aerodynamik

Underwater Investigation of Stall Onset on an Elliptic Profile via Temperature-Sensitive Paint

M. Costantini[1]*, B. D. Dimond[1], C. Klein[1], S. Sattler[2], M. Miozzi[3]

[1]DLR, Institute of Aerodynamics and Flow Technology, DLR, Bunsenstrasse 10, D-37073 Göttingen, Germany

[2]TU Braunschweig, Institute of Fluid Mechanics, Hermann-Blenk-Str. 37, D-38108 Braunschweig, Germany

[3]CNR, Institute of Marine Engineering, via di Vallerano 139, I-00128 Rome, Italy

*corresponding author: marco.costantini@dlr.de

Introduction and experimental setup

Elliptic profiles have been the subject of fundamental flow research as "elliptic cylinders" for several decades, including the study of boundary-layer separation and transition [1]. In recent times, elliptic profiles have become relevant also for practical applications, such as canard rotor/wing aircraft [2] and hydrokinetic energy harvesting technologies [3]. In these cases, they are operated at moderate Reynolds numbers, at which their aero/hydrodynamic performance is strongly influenced by flow separation. Information on this crucial phenomenon is therefore of fundamental importance not only for their experimental evaluation, but also for the validation and improvement of the numerical prediction of the involved fluid dynamics.

The onset of stall on an elliptic profile with 16% relative thickness (such as that examined in [2]) is the focus of the present work. The experiments were conducted in the GWB water tunnel of TU Braunschweig [4] on a two-dimensional model with a chord length $c = 0.2$ m. The model installed in the GWB test section is shown in Figure 1 (left). The model upper surface was equipped with a Temperature-Sensitive Paint (TSP) [5] for the global, non-intrusive, time-resolved measurement of the surface temperature distribution. In order to enhance the temperature differences induced by the flow on the surface, the model surface temperature was increased by an internal flow of warm water. The TSP data were acquired over a mid-span region of approx. 0.2×0.3 m^2 at a frequency of 1 kHz. The model was also equipped with a row of pressure taps to measure the surface pressure distribution.

The experiments were performed at two chord Reynolds numbers (Re = 2.5 and 5.0×10^5) for a wide range of angles-of-attack ($-4° \leq$ AoA $\leq 30°$), thus enabling the study of a variety of flow conditions, including laminar-turbulent transition and flow separation. The investigation of transitional phenomena is reported in [6], whereas the present work focuses on pre-stall, stall and post-stall conditions.

Results

The onset of stall on the examined elliptic profile is exemplarily shown for the case at Re = 5.0×10^5 by the surface pressure distributions (Figure 1, right) and the TSP results (Figure 2). Two close angles-of-attack are considered: AoA = 13.0° and 13.2°. As can be seen in Figure 1 (right), the small increase in the angle-of-attack of 0.2° led to a major change in the pressure distribution, indicating the onset of stall. This is elucidated by the instantaneous temperature distributions presented in Figure 2, where the flow is from the left. At AoA = 13.0°, the boundary layer remained attached for most of the profile chord, with turbulent separation limited to the trailing-edge region (wall temperature about 19.5 °C, yellow region with the used color map). At AoA = 13.2°, the surface temperature distributions showed major variations, with the occurrence of large-scale unsteady phenomena within a separated region extending over most of the profile. An example of such phenomena is the appearance of a separated-flow structure resembling a « mushroom slice », which is characteristic as wall signature of stall cells. The final contribution will provide the temporal development of the surface temperature at pre-stall, stall and post-stall conditions, and an evaluation of the onset of stall.
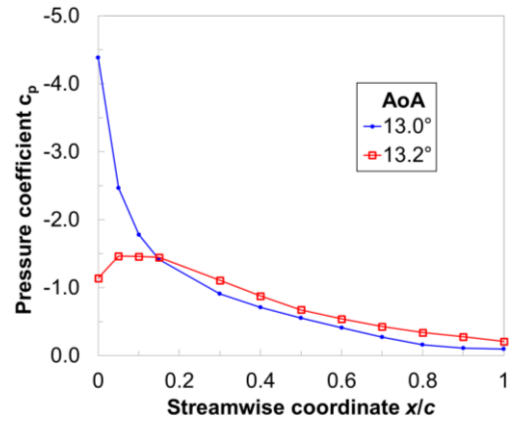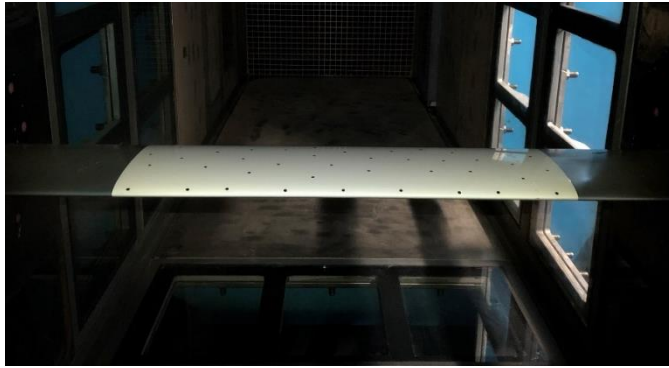
Fig. 1. Left: Elliptic profile model mounted in the GWB test section (view in flow direction). TSP visible as yellow coating. Right: pressure distributions measured on the model upper surface at Re = 5.0 × 10⁵ for AoA = 13.0° and 13.2°.
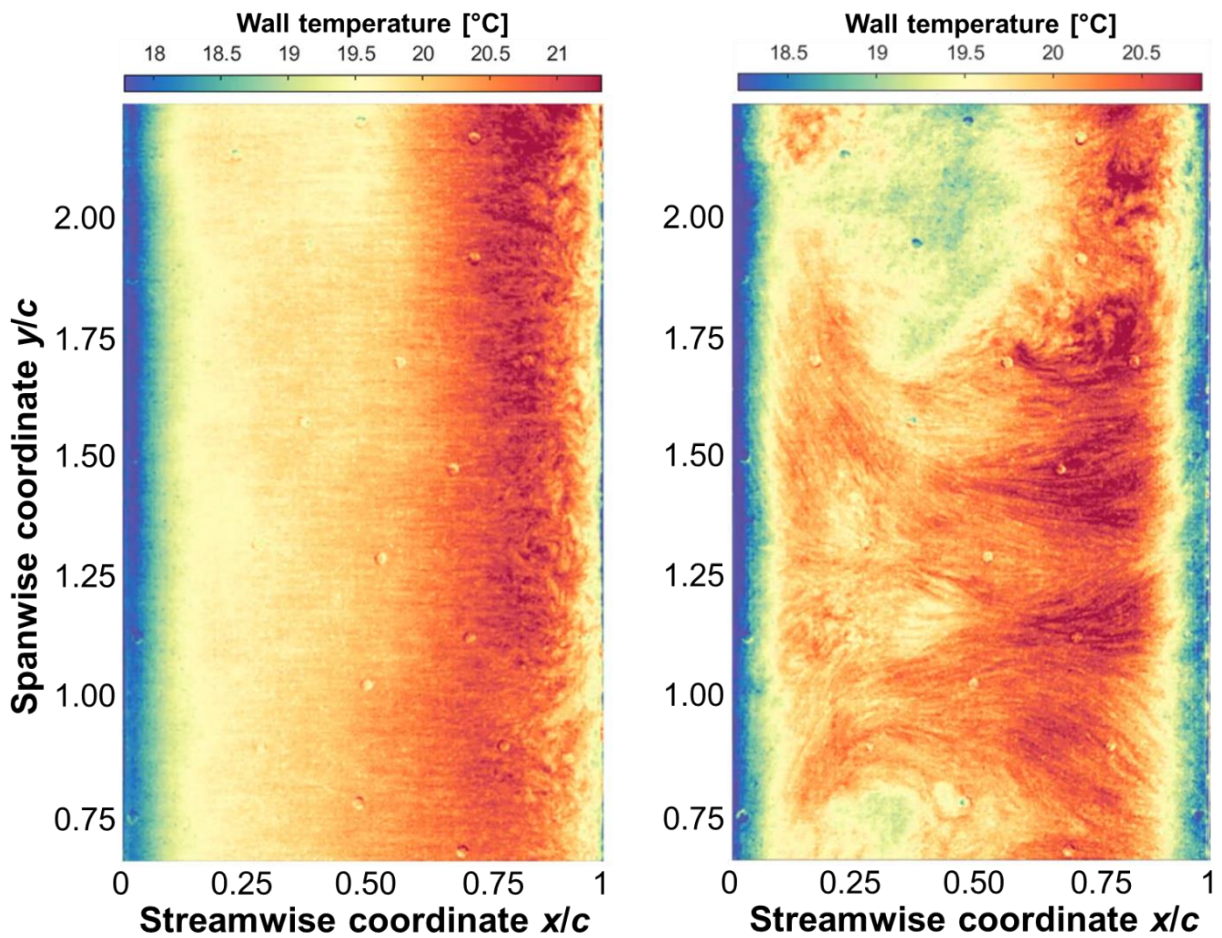
Fig. 2. Instantaneous TSP results on the model upper surface at Re = 5.0 × 10⁵ for AoA = 13.0° (left) and 13.2° (right). Flow from the left.

References

[1] Schubauer G.B. (1939) Air Flow in the Boundary Layer on an Elliptic Cylinder, NACA Rep. No. 652
[2] Kwon K., Park S.O. (2005) Aerodynamic Characteristics of an Elliptic Airfoil at Low Reynolds Number, J. Aircraft, vol. 42(6), pp. 1642-1644.
[3] Kim D., Strom B., Mandre S., Breuer K. (2017) Energy harvesting performance and flow structure of an oscillating hydrofoil with finite span, J. Fluids Structs., vol. 70, pp. 314-326.
[4] Scholz P., Sattler S., Wulff D. (2013): Der Große Wasserkanal "GWB" – Eine Versuchsanlage für zeitauflösende Messungen bei großen Reynoldszahlen, Proc. DLRK 2013, Stuttgart.
[5] Liu T., Sullivan J.P., Asai K., Klein C., Egami Y., (2021): Pressure and Temperature Sensitive Paints, Springer International Publishing.
[6] Costantini M., Dimond B.D., Klein C., Sattler S., Miozzi M. (2024) Transitional Phenomena on an Elliptic Profile, 10th IUTAM Symposium on Laminar-Turbulent Transition, Nagano, Japan.

STAB

Mitteilung

Fachgruppe: Experimentelle Aerodynamik

Messung des Luftwiderstands eines Zugmodells beim Durchfahren eines Tunnels

Klaus Ehrenfried und Daniela Heine

Institut für Aerodynamik und Strömungstechnik, DLR
Bunsenstraße 10, 37073 Göttingen
klaus.ehrenfried@dlr.de

Der aerodynamische Widerstand von Zügen im Tunnel ist gegenüber der Fahrt im Freien deutlich erhöht. Dies gilt insbesondere für neue eingleisige Doppelröhrentunnel mit relativ engem Querschnitt. Bei dem Entwurf von neuen Zügen, die auf Tunnelstrecken eingesetzt werden sollen, ist es daher wünschenswert den aerodynamischen Widerstand vorhersagen zu können. Der Widerstand im Freien kann in Windkanalmessungen an Modellen ermittelt werden, wobei sich zur Erzeugung einer realistischen Strömung im Unterbodenbereich ein laufendes Band unter dem Modell befindet. Die Idee ist es, den aerodynamischen Widerstand im Tunnel mit einem bewegten Modell zu bestimmen, das durch einen Modelltunnel fährt. So ist automatisch eine realistische Relativbewegung zwischen Zug und Tunnel gegeben. In der vorliegenden Arbeit werden entsprechende Untersuchungen in der Tunnelsimulationsanlage Göttingen (TSG) mit einem 16 m langen Modelltunnel und einem Zugmodell im Maßstab 1:25 durchgeführt. Das Modell besitzt einen generischen Kopf. Der Wagenkasten und das Heck entsprechen einem ICE3. Das Modell wird mit Hilfe eines Katapults beschleunigt und bewegt sich dann durch Trägheit ohne Antrieb entlang einer Schienenstrecke durch den Modelltunnel. Dabei wird es durch mechanische und aerodynamische Reibung abgebremst. Die Verzögerung wird gemessen und daraus die Widerstandskraft berechnet. Führt man die Messungen mit unterschiedlichen Geschwindigkeiten durch, können unter der Annahme, dass der aerodynamische Anteil quadratisch und der mechanische linear mit der Geschwindigkeit skaliert, die beiden Anteile getrennt werden. Dabei stellt sich die Frage, wie genau der aerodynamische Widerstand mit der beschriebenen Methode überhaupt bestimmt werden kann. Hier soll daher die Genauigkeit näher betrachtet werden und es soll untersucht werden, von welchen Parametern die Genauigkeit im Wesentlichen abhängt.
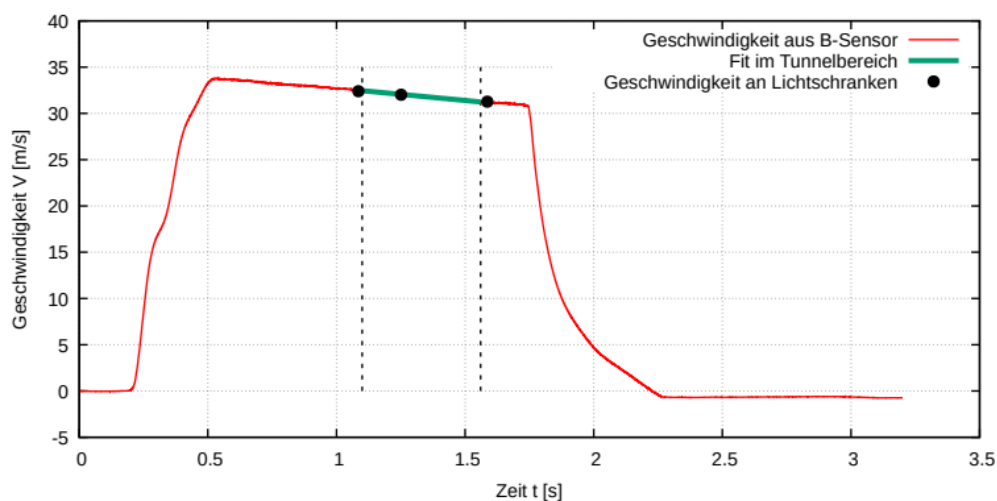
Abbildung 1: Verlauf der Geschwindigkeit des Zugmodells über der Zeit; Rote Kurve: Geschwindigkeit aus Integration der Beschleunigung; Schwarze Punkte: Geschwindigkeit aus den Lichtschrankensignalen; Grüne Linie: Anpassung im Tunnelbereich.

In der vorliegenden Arbeit werden zwei Methoden zur Messung der Verzögerung eingesetzt und miteinander verglichen. Zum einen wird die Beschleunigung direkt mit einem Sensor im Modell gemessen. Die Herausforderung ist dabei, dass der Sensor die relativ hohen Beschleunigungen von 50 g – und mehr – beim Start und beim Abbremsen des Modells verträgt und gleichzeitig Beschleunigungen deutlich unter 1 g zuverlässig messen kann. Die zweite Methode arbeitet mit drei Lichtschranken, durch die das Modell fährt. Zusätzlich ist der Tunnel mit Drucksensoren in der Wand ausgestattet. Um die Messtechnik im bewegten Modell mit der Datenerfassung am Tunnel zu synchronisieren, besitzt das Modell einen optischen Sensor an der Seite. Dieser zeichnet die Signale von beleuchteten Positionsmarkierungen am Ein- und Ausgang des Modelltunnels auf. Weitere Informationen über die eingesetzte Messtechnik sind in [1] zu finden.

In Abbildung 1 ist als Beispiel für eine Versuchsfahrt der Verlauf der Modellgeschwindigkeit über der Zeit aufgetragen. Die rote Kurve wurde aus den im Modell gemessenen Beschleunigungen durch Integration berechnet. Die schwarzen Punkte markieren Geschwindigkeiten, die aus den Signalen der Lichtschranken gewonnen wurden. Die gestrichelten Linien markieren den Zeitbereich, in dem sich das Modell im Tunnel befindet. Bei t = 0.2 s startet das Modell. Es wird in dem Katapult auf ca. 34 m/s beschleunigt. Bei etwa t = 0.5 s verlässt das Modell das Katapult und die mechanische und aerodynamische Reibung bewirken ab da eine stete Verlangsamung. Bei etwa t = 1.75 s fährt das Modell in eine Bremse, wo es in einer Schüttung stark abgebremst wird. Auffällig ist, dass die Geschwindigkeit am Schluss nicht auf null zurück geht, wie man es theoretisch erwarten würde. Das rohe Beschleunigungssignal ist stark verrauscht. Anscheinend akkumuliert sich ein kleiner Fehler bei der Integration einseitig. Auf den ersten Blick passen die mit Hilfe der Lichtschranken ermittelten Werte zu der aus den Beschleunigungsdaten berechneten Kurve. Eine genauere Betrachtung zeigt jedoch auch systematische Abweichungen. Zum Beispiel besitzen die eingesetzten Lichtschranken bauartbedingt eine kleine Unsicherheit, sodass eine befriedigende Genauigkeit erst durch eine Mittelung über mehrere Versuchsfahrten erreicht wird. Die in der Abbildung eingezeichnete grüne Kurve ist eine Anpassung an die Verzögerung im Tunnel. Daraus ergibt sich in dem gezeigten Fall ein Gesamtwiderstand von ca. 12 N. Ungefähr die Hälfte davon macht der aerodynamische Anteil aus.

Parallel zu den experimentellen Untersuchungen werden Berechnungen durchgeführt, die auf einer quasi-eindimensionalen Modellierung der Strömung und der Druckwellen im Tunnel basiert. Die Modellierung benötigt empirische Parameter, die anhand von den gemessenen Wanddruckdaten kalibriert werden. Es wird dann der Verlauf des Widerstands berechnet. Die Ergebnisse zeigen, dass durch hin- und herlaufende Druckwellen erheblichen Schwankungen des aerodynamischen Widerstands im Tunnel auftreten. Die Berechnungen zeigen auch, dass der aerodynamische Widerstand im Tunnel nicht perfekt quadratisch mit der Fahrgeschwindigkeit skaliert.

[1] K. Ehrenfried, D. Heine: Pressure Waves and Flow Induced by a Train in a Tunnel. DOI: 10.1007/978-3-031-40482-5_6, 2023.

STAB

Mitteilung

Fachgruppe: Experimentelle Aerodynamik

Hot-Film Measurements on Rotor Tip Vortices in the High Pressure Wind Tunnel Göttingen (HDG)

Erica Galli [1] [2], Hauke Bartzsch [2], Alex Zanotti [1], Christian Wolf [2], Anthony Gardner [2]

[1] Politecnico di Milano, Piazza Leonardo da Vinci 32, 20133 Milano,
erica.galli@dlr.de
[2] German Aerospace Center, Bunsenstrasse 10, 37073 Göttingen

Introduction

Helicopter blades create helical vortices at the tip of the rotor, so the wake is characterised by a complex three-dimensional velocity field. These vortices affect both the aerodynamic and aeroacoustic performance of the rotor itself, and therefore the study of vortex core size, circulation and vortex pairing for a wide range of vortex Reynolds numbers is of great interest.

Since the study of such vortices presents a challenge both with a numerical approach or with an experimental one on a full-scale helicopter, the High Pressure Wind Tunnel Göttingen (HDG) is employed. Such a facility makes it possible to work with a rotor scale model in a hyperbaric environment in order to obtain vortex Reynolds numbers characteristic of a full-scale helicopter rotor. As the interest of the present work concerns a rotor in a hovering condition and the analysis was carried out in a closed-loop wind tunnel, an optimally sized shield was placed downstream of the test chamber in order to control the inflow velocity of the rotor.

The costant temperature hot-film anemometer technique was chosen for this study because its effectiveness is not affected by the increase in external pressure and provides a very high frequency response, necessary to capture the rapid velocity fluctutations in the small-scale structures that characterize rotor tip vortices.

Experimental Setup

The High Pressure Wind Tunnel Göttingen (HDG) features a 60x60 cm test section, operates in the pressure range of 1-100 bar and a velocity range of 0-35 m/s.

A CAMcarbon Light 12-4.5, mounted on a tube supported by a C-shaped structure, was chosen as the scale rotor for this work. Additionaly, a triggering system on one of the two blades was employed to determine the time delay between the blade passage and the tip vortex measured by the probe in the wake of the rotor.

The hot-film anemometer is installed so that it measures the velocity in the rotor´s axial-radial direction, and is mounted on a traverse system capable of moving both axially and radially with respect to the rotor.

Figure 1: Test section. Rotor with glued dots on blades used to study the effects of boundary layer transition on vortex pairing

As mentioned above, in order to achieve hovering conditions, a screen ensuring a 50% blockage ratio was placed on the first grid downstream of the rotor.

Results

Preliminary analysis was carried out by calibrating the sensor to different external pressures. The result of this calibration is shown in Figure 2. In particular, King's law expresses $E^2 = A + BU^n$ and the interpolation finds a linear trend with the pressure of the coefficients A and n and shows that the coefficient B goes as the square root of the pressure.

Subsequently, the work focused on the analysis of rotor tip vortices. Specifically, to understand their trajectory and vortex pairing, the real-time signal was analyzed, and it was observed where the signal itself exhibited characteristics typical of the vortex region.

Figure 3 displays the velocity recorded by the anemometer during one complete revolution for two blade passages. The dashed line indicates the triggered blade passages.

The data reveals two prominent velocity peaks when the sensor is positioned directly at the edge of the vortex core, where the velocity is at its maximum.

Between the two velocity peaks, there is a sharp local minimum. This minimum arises because, at the center of the vortex core, the swirl velocity is zero, leaving only the translational component.

Consequently, the vortex core size can be estimated by calculating the time interval between the two peaks and multiplying it by the convective velocity.

This size depends on vortex age and Reynolds number and it is compared with analytical vortex models.

Figure 2: Probe calibration curve with changing pressure
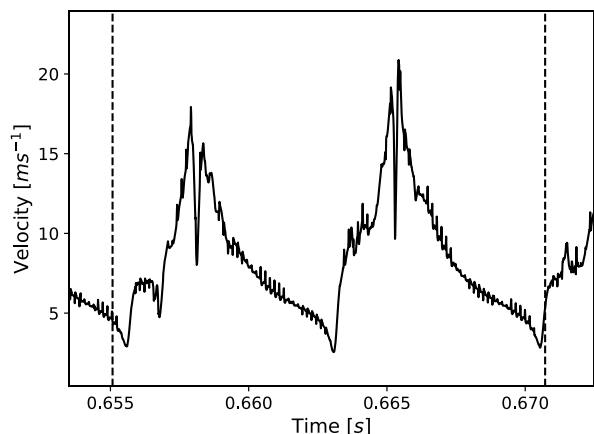
Figure 3: 1 bar hot-film signal at 55° of vortex age

Eventually, by observing the real-time signal, it is possible to gain an understanding of the trajectory of the vortices and their size. The results show that vortices with higher Reynolds numbers decay at lower vortex ages compared to those measured at 1 bar.

References

H. H. Brunn. Hot-Wire Anemometry. Principles and Signal Analysis. Oxford University Press, 1995

J. L. Tangler, R. M. Wohlfeld, and S. J. Miley. An experimental investigation of vortex stability, tip shapes, compressibility, and noise for hovering model rotors. Tech. rep. NASA, 1973

D. W. Boatwright. Measurements of velocity components in the wake of a full-scale helicopter rotor in hover. NTIS, 1972

M. Ramasamy and J. G. Leishman. "A reynolds number-based blade tip vortex model". In: Journal of the American Helicopter Society, Vol. 52 (3) (2007), pp. 214–22
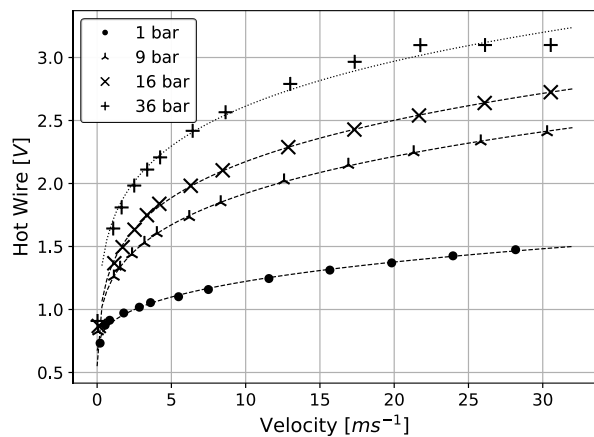
STAB

Mitteilung

Fachgruppe: Experimentelle Aerodynamik

Experimental investigation of the aerodynamics of maple seeds in native free fall and controlled autorotation condition

Lars Krenkel[1,2], Florian Erzinger[1,2], and Markus Rütten[3]
[1]Department of Biofluid Mechanics, OTH Regensburg,
Seybothstr. 2, 93053 Regensburg
[2]Regensburg Center of Biomedical Engineering (OTH and University Regensburg)
Seybothstr. 2, 93053 Regensburg
[3]German Aerospace Center (DLR), Bunsenstr. 10, 37073 Göttingen
lars.krenkel@oth-regensburg.de

Maple seeds exhibit a unique and efficient natural flight mechanism, known as autorotation, which allows them to disperse over wide areas. Understanding the aerodynamics of maple seed flight not only provides insights into natural systems but also has significant implications for the design of small-scale flying devices and drones. The intricate balance between mass distribution, wing morphology, and aerodynamic forces that enables stable autorotation in maple seeds presents a compelling model for biomimetic engineering. Investigating these mechanisms can lead to advancements in fields ranging from robotics to environmental science, where efficient, stable flight at low Reynolds numbers is crucial.

Various working groups have already studied the aerodynamics of maple seeds and identified important aspects. Varshney et al. (2012) investigated the kinematics of falling maple seeds, focusing on the transition from tumbling to stable autorotation. High-speed camera inaging revealed an average fall speed of 0.94 m/s and a rotation speed of 77.9 rad/s for the investigated maple seed species. The study found that even seeds with reduced wing areas could rotate, indicating that the mass moment of inertia, rather than aerodynamic forces, is crucial for autorotation. The seed's asymmetric mass distribution plays a key role in achieving stable rotation. Lee et al. (2014) expanded on this by analyzing the autorotation mechanism using controlled experiments. They observed a higher fall speed of 1.26 m/s and a rotation speed of 133.6 rad/s. Their study identified a leading-edge vortex (LEV) on the seed's upper side, which reduces air pressure and generates lift, slowing the descent. Advanced imaging techniques, including Particle Image Velocimetry (PIV), helped visualising this vortex. Lee and Lee (2016) further explored how the seed's initial position affects its flight dynamics. They found that seeds typically achieve stable autorotation within 660 mm, with the quickest stabilization occurring when the flat wing side is facing downwards. Sohn and Im (2022) focused on the fluid-physical aspects of autorotation through numerical simulations. They emphasized the importance of the seed's mass distribution, noting that the seed base has a density 4.29 times greater than its wing. This difference in density significantly impacts the seed's center of mass and its flight behavior, leading to more accurate modeling of autorotation. This research collectively highlights the critical role of mass distribution and inertia in the stable autorotation of maple seeds.

Despite significant progress in understanding maple seed aerodynamics, several aspects remain unclear. One key area of uncertainty is the precise role of mass distribution and how the seed's varying density influences its stability and flight efficiency. While the importance of the leading-edge vortex (LEV) in generating lift has been established, the detailed dynamics of vortex formation, persistence, and interaction with the seed's rotational motion are not fully understood. Additionally, the transition between tumbling and stable autorotation and the influence of initial conditions on this process need further exploration. The effects of environmental factors, such as wind turbulence and humidity, on seed flight behavior also remain inadequately studied. Addressing these gaps could enhance our understanding of natural dispersal mechanisms and inform the design of more efficient bio-inspired aerial systems.

In order to gain a deeper understanding of the aerodynamics of maple seeds and to obtain additional high-resolution validation data for further numerical investigations (CFD) of vortex systems on maple seeds in autorotation flight, two test rigs have been developed in the Bio-fluid Mechanics Department of the OTH Regensburg, which allow parametric investigations of maple seed flight in native and controlled flight conditions.

In a newly developed free-fall test rig, the native free fall of maple seeds was recorded and analyzed using two high-speed cameras (Photron Fastcams AX 200 mini and UX50) from two perspectives (lateral and vertical from below) at a frame rate of 4000fps. Based on the recorded image data, the angular velocity, the angle of attack and the spatial path of the axis of rotation were analyzed using in-house software. In order to extend the recording time with optimized field-of-view, the lateral camera was mounted on a traverse system, which moves the camera triggered in the direction of fall of the maple seeds.

In a second developed test rig in the form of a controllable vertical laminar air flow, different autorotation states were investigated parametrically under controlled lift, drag and weight force ratios. In this scenario, the flight condition of the maple seeds was also investigated using two high-speed cameras from two perspectives (sideways and vertically from above) in order to examine the angular velocity, the angle of attack and the spatial path of the axis of rotation in detail. In addition, this test facility makes it possible to investigate transient flight conditions with an optimized field-of-view and to carry out supplementary investigations and visualizations using particle image velocimetry and classical or Background Oriented Schlieren (BOS) methods.

In order to provide realistic boundary conditions for later numerical investigations, the maple seeds studied were scanned in high resolution (voxel size of 24 microns) in a micro-CT (Phoenix V|tome|x s) after the test series, the geometry was reconstructed with all important structures in STL format, and the moments of inertia were determined.
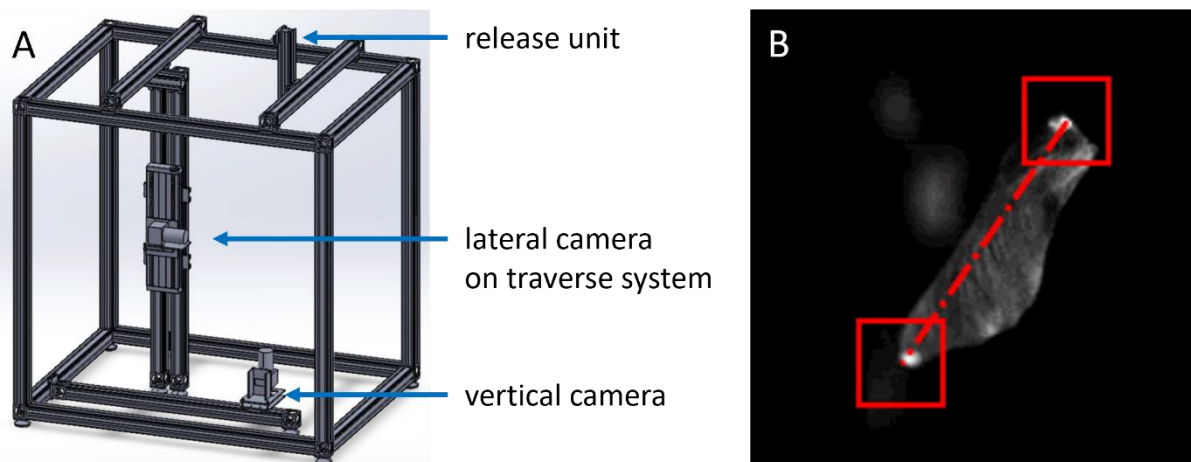
Figure 1: Sketch of the newly developed native free-fall test rig (A) and exemplary image of the autorotation analysis over marked maple seeds in vertical viewing direction (B)

References
1. Varshney, Kapil; Chang, Song; Wang, Z. Jane (2012): The kinematics of falling maple seeds and the initial transition to a helical motion. In: Nonlinearity 25 (1), C1-C8. DOI: 10.1088/0951-7715/25/1/C1.
2. Lee, Sang Joon; Lee, Eui Jae; Sohn, Myong Hwan (2014): Mechanism of autorotation flight of maple samaras (Acer palmatum). In: Exp Fluids 55 (4), S. 1–9. DOI: 10.1007/s00348-014-1718-4.
3. Lee, Eui-Jae; Lee, Sang-Joon (2016): Effect of initial attitude on autorotation flight of maple samaras (Acer palmatum). In: J Mech Sci Technol 30 (2), S. 741–747. DOI: 10.1007/s12206-016-0129-2.
4. Sohn, Myong Hwan; Im, Dong Kyun (2022): Flight characteristics and flow structure of the autorotating maple seeds. In: J Vis 25 (3), S. 483–500. DOI: 10.1007/s12650-021-00812-9.

STAB

Mitteilung

Fachgruppe: Experimentelle Aerodynamik

Hitzdrahtmessungen in sequentiell abgesaugten Grenzschichten

R. von Soldenhoff (Richard.vonSoldenhoff@dlr.de)
P. Weigmann (Paul.Weigmann@dlr.de)
H. Lüdeke (Heinrich.Luedeke@dlr.de)
Deutsches Zentrum für Luft- und Raumfahrt (DLR), Institut für Aerodynamik und Strömungstechnik
Lilienthalplatz 7, 38108 Braunschweig
K. Thamm (k.thamm@tu-braunschweig.de)
Technische Universität Braunschweig, Institut für Strömungsmechanik

Im April sind erneut Windkanalversuche mit Absaugung im DNW-NWB durchgeführt worden (vgl. auch [1]). Im Gegensatz zu früheren Messkampagnen werden mehrfache, sequentielle Absaugbereiche untersucht. Die beiden verwendeten Absaugpaneele bestehen aus laser-geschlitzten Edelstahlblechen mit einer darunterliegenden, 6 mm tiefen Absaugkammer. Sie haben Dimensionen von 1,3 m in Spannweiten- und 0,4 m in Strömungsrichtung. Es werden mehrere Positionen der Absaugbereiche gewählt, sodass die in der Grenzschicht anwach-senden Tollmien-Schlichting-Wellen zunächst über dem ersten Absaugbereich gedämpft werden, danach wieder anwachsen und über dem zweiten Absaugbereich erneut gedämpft werden. Danach wachsen sie weiter an, bis es zur Transition kommt.
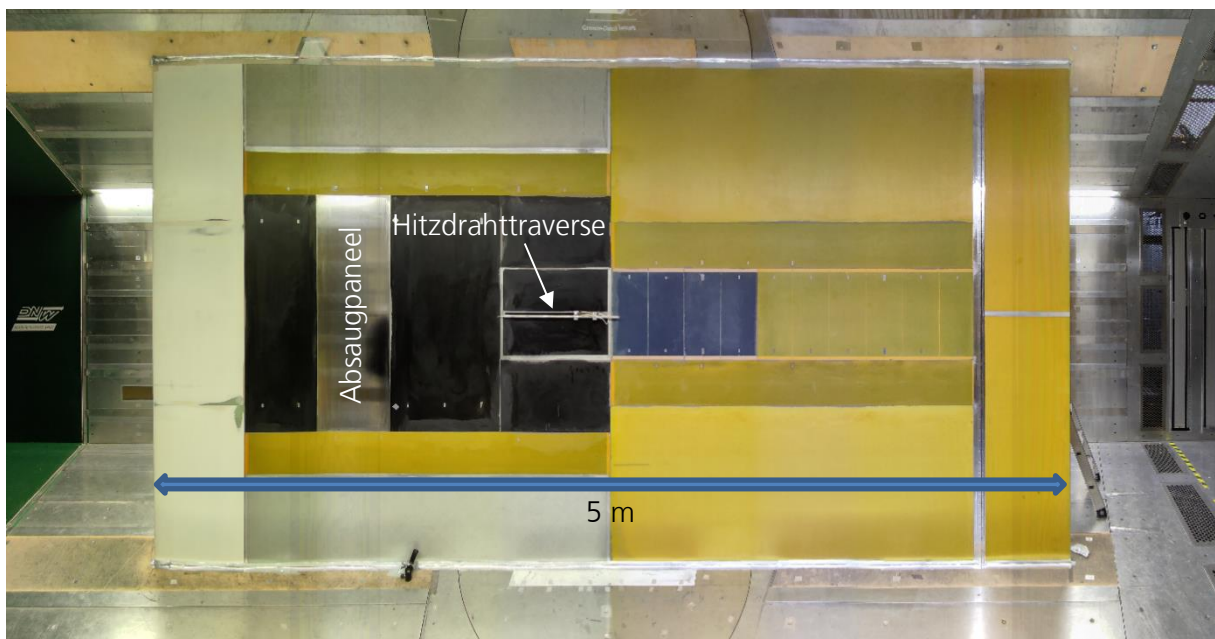
Abbildung 1: Panoramabild des Modellaufbaus mit einem Absaugpaneel und der Hitzdrahttraverse

Neben Infrarotmessungen zur Bestimmung der Transitionslage werden Hitzdrahtmessungen betrachtet. Diese ermöglichen es, sowohl das mittlere Grenzschichtprofil als auch zeitlich aufgelöste Störbewegungen zu messen. Der Hitzdraht ist mittels einer Traverse in Strömungs- und Wandnormalenrichtung verfahrbar aufgehängt. In Abb. 1 ist der gesamte Modellaufbau mit eingebautem Hitzdraht zu sehen. In dieser Konfiguration ist lediglich ein einziges Absaugpaneel eingesetzt. Dabei wird ein Intermittenzphänomen untersucht, welches auftritt, sofern die Absaugung erst bei einer großen Störungsamplitude beginnt.

STAB

Um Grenzschichtprofil und Störbewegung ausreichend auflösen zu können, sind Messpunkte in unmittelbarer Wandnähe erforderlich. Das Herantasten erfolgt bei laufender Messung in 0,1 mm-Schritten unter ständigem Beobachten der Strömungsgeschwindigkeit. So können Punkte bis etwa 0,2 mm Wandabstand angefahren werden.
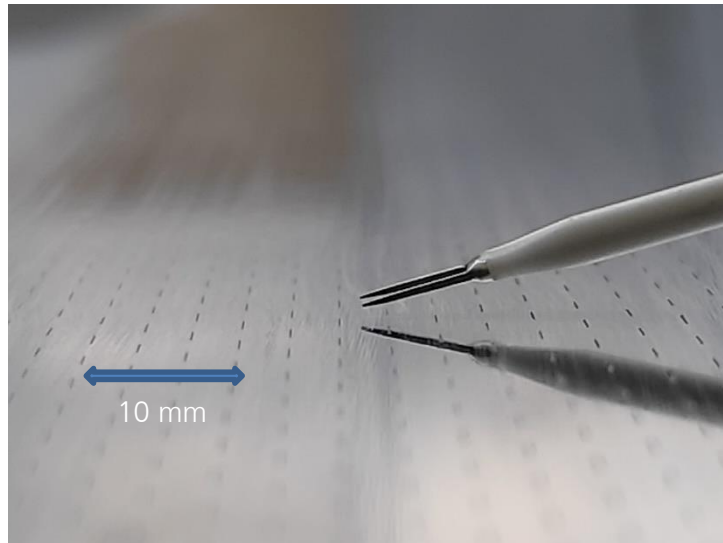
Abbildung 2: Hitzdraht über geschlitzter Absaugoberfläche

Besonderes Augenmerk liegt auf der Dämpfung von Tollmien-Schlichting-Wellen über den beiden Absaugbereichen. Dort werden Messungen in Abständen von 50 mm in Strömungsrichtung ausgewertet und die Störamplituden bestimmt. Abbildung 2 zeigt die Hitzdrahtsonde über einem geschlitzten Absaugpaneel. Die Hitzdrahtdaten werden mit Ergebnissen aus der linearen Stabilitätstheorie verglichen.

Literatur:

[1]   R. von Soldenhoff: Overview of the Wind Tunnel Tests with Suction in the DNW-NWB, in New Results in Numerical and Experimental Fluid Mechanics XIV - Contributions to the 23rd STAB/DGLR Symposium, Berlin. Springer Verlag, 2023

STAB

Mitteilung

Fachgruppe: Experimentelle Aerodynamik

Optische Deformationsmessung zur Lastbeobachtung an einem skalierten Flugversuchsträger

J. Wagner*, T. Kirmse*,
O. Luderer[†] , F. Thielecke[†],
W. Gropengießer[‡], S. Adden[‡]

* German Aerospace Center, Institute of Aerodynamics and Flow Technology,
Bunsenstr. 10, Göttingen, Germany
[†] Hamburg University of Technology, Institute of Aircraft Systems Engineering,
Nesspriel 5, 21129 Hamburg, Germany
[‡] IBK Innovation GmbH & Co. KG, Butendeichsweg 2, Hamburg, Germany
jan.wagner@dlr.de

Zur Lastbeobachtung an Flugzeugflügeln können verschiedene Messgrößen, wie Beschleunigungen, Dehnungen, Druckdaten und Deformationen genutzt werden. Hier wird die Deformation optisch über ein Stereo-Kamera-System erfasst. Dabei kommen zwei verschiedene Messsysteme zum Einsatz:

Die Image Pattern Correlation Technique (IPCT) ist eine etablierte, gut erprobte Methode zur Messung von 2,5D-Flächendeformationen, die auf einer zufälligen Punkteverteilung auf der Fläche basiert. Diese Methode führt zu hohen Genauigkeiten (~ 0,2 Pixel), ist aber rechenintensiv und nicht echtzeitfähig. (Boden et al. 2013)

Dagegen ist eine markerbasierte Messung schnell und effizient und auch mit einer einzelnen Kamera möglich. Die vier Eckpunkte des Markers ermöglichen eine Aussage der Lage im Raum über ein eigenes Marker-Koordinaten-System, allerdings nur an diskreten Punkten. Hier wird eine Weiterentwicklung (Enhanced ArUco Marker) der verbreiteten ArUco-Marker genutzt, die durch den Schachbrett-Rahmen eine bessere Subpixel-Genauigkeit liefern. (Garrido-Jurado et al. 2014; Kedilioglu et al. 2021), siehe Fig. 1. Vorversuche haben gezeigt, dass ein Stereo-Kamera-System eine höhere Genauigkeit gegenüber einer Mono-Kamera Markererkennung aufweist (Kedilioglu et al. 2021).

ArUcoE
Marker

Kamera
Setup über
dem Cockpit
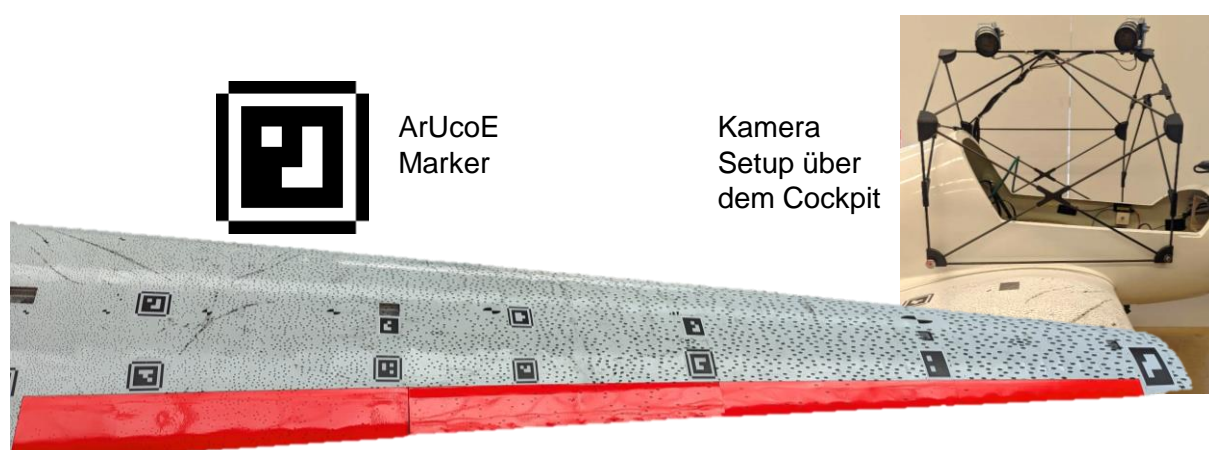
Figure 1: Tragfläche mit IPCT-Muster und ArUcoE-Markern, sowie der Kamera Position über dem Cockpit. Das Messsystem besteht aus 5 Mpx Ximea Kameras und einem Raspberry 5 mit eigender Akkuversorgung über ein UPS HAT.

Bei dem verwendeten Flugzeug handelt es ich um die *AdLoNet-Dimona,* einen skalierten Versuchsflieger der TUHH mit 2,5 m Spannweite und einer Nutzlast von ca. 4 Kg bei 25 Kg

Gesamtgewicht (Luderer et al. 2023), dessen rechter Flügel mit Dehnungsmessstreifen & Beschleunigungssensoren zur Lastenbeobachtung ausgestattet ist

Ziel der Messung ist, beide optischen Systeme miteinander, aber auch mit den restlichen Sensorergebnissen zu vergleichen und ihre Eignung für den Einsatz in Messumgebungen mit starken Beschränkungen hinsichtlich optischer Zugänglichkeit, Bauraum, Gewicht und elektrischer Leistung zu beurteilen.

Literaturverzeichnis

Boden, Fritz; Kirmse, Tania; Jentink, Henk (2013): Image pattern correlation technique (IPCT). In: AIM² Advanced Flight Testing Workshop-HANDBOOK of ADVANCED IN-FLIGHT MEASUREMENT TECHNIQUES. BoD-Books on Demand, Norderstedt, S. 63–85.

Garrido-Jurado, S.; Muñoz-Salinas, R.; Madrid-Cuevas, F. J.; Marín-Jiménez, M. J. (2014): Automatic generation and detection of highly reliable fiducial markers under occlusion. In: *Pattern Recognition* 47 (6), S. 2280–2292. DOI: 10.1016/j.patcog.2014.01.005.

Kedilioglu, Oguz; Bocco, Tomas Marcelo; Landesberger, Martin; Rizzo, Alessandro; Franke, Jorg (2021): ArUcoE: Enhanced ArUco Marker. In: 2021 21st International Conference on Control, Automation and Systems (ICCAS). 12-15 Oct. 2021. 2021 21st International Conference on Control, Automation and Systems (ICCAS). Jeju, Korea, Republic of, 10/12/2021 - 10/15/2021. Piscataway, NJ: IEEE, S. 878–881.

Luderer, O.; Thielecke, F.; Wagner, J.; Kirmse, T.; Gropengießer, W.; Adden, S. (2023): Development and Testing of a Complementary Sensor Network for Robust Estimation of Maneuver and Gust Loads.

STAB

Mitteilung

Fachgruppe: Hochagile Konfigurationen

Numerical Investigations of Vortex-Breakdown Induced Tail Buffet on the DLR-F23 Configuration with Vertical Tail

Patrick Hartl, Matthias Konz, Marc Braune, Holger Mai
DLR – German Aerospace Center
Institute of Aeroelasticity, Department Aeroelastic Experiments
Bunsenstraße 10, 37073 Göttingen, patrick.hartl@dlr.de

Introduction

Modern, high-agility aircraft configurations cover an extensive flight envelope, ranging from high maneuverability at subsonic speeds to high-performance flight conditions in the transonic and supersonic flow regime. The medium to high leading-edge sweep angles of hybrid-delta-wing configurations result in a complex vortical flow field. Even at low angles of attack, the flow separates at the leading edge and generates a vortex. As the angle of attack increases, the leading-edge vortex breaks down, the cross-section of the vortex increases, and an unsteady flow field develops downstream of the breakdown position. Severe pressure fluctuations with distinct frequency contents characterize the flow field and lead to an aerodynamic excitation of the structure of the wing and downstream located elements such as the vertical tail. The excitation of the vertical tail through the unsteady flow field leads to significant structural fatigue.

DLR-F23-T Configuration

At the DLR Institute of Aeroelasticity, a new hybrid-delta-wing configuration with a vertical tail (VT), the DLR-F23-T, was developed based on the existing DLR-F23 model [1]. The DLR-F23 half-span wind tunnel model consists of a triple-delta wing with an ogival cosine-chined forebody. The configuration is divided into three wing segments. The front wing part, comparable with a leading-edge vortex controller (LEVCON), has a medium leading-edge sweep of $\varphi_1 = 45°$, followed by a wing midsection (strake) with a high leading-edge sweep of $\varphi_2 = 75°$ and the main wing section with the same leading-edge sweep as the front section, $\varphi_3 = \varphi_1$. The vertical tail has a height of $h_{VT} = 0.170 \, m$ with a root chord of $c_{r,VT} = 0.270 \, m$ and a tip chord of $c_{t,VT} = 0.070 \, m$. It has a leading-edge sweep of $\varphi_{VT,LE} = 45°$ and a trailing-edge sweep of $\varphi_{VT,TE} = 10°$. The VT is oriented parallel to the model x-axis with a dihedral angle of $\nu_{VT} = 30°$.

Numerical Setup

The numerical simulations presented in this study are performed with the compressible flow solver DLR-TAU-Code. The computational meshes are generated with the software CENTAUR. The prism grid consists of 34 layers with a stretching factor of 1.24 and with a height of the first cell of $1.5 \cdot 10^{-6} \, m$, leading to $y^+ < 1$ on the whole surface. In the context of a mesh convergence study, five different meshes were evaluated and as a result the fine mesh with 34.4 mio. points was selected. The simulations are conducted with a physical time-step size of $\Delta t = 2.5 \cdot 10^{-6} \, s$. The unsteady CFD simulations were performed with URANS and IDDES [2] as turbulence approaches. For the URANS simulations, the one-equation Spalart-Allmaras turbulence model (SA) in its negative formulation and rotation correction (SA-neg-RC) is used. Based on the lack of scale separation between coherent unsteadiness and stochastic turbulence, there are concerns about whether URANS can reliably predict the relevant unsteady flow features. For this reason, IDDES simulations are conducted on the URANS basis of the k-ω-SST turbulence model.

Results

The results presented in this paper are based on simulations conducted at a Mach number of $Ma_\infty = 0.55$ and a Reynolds number of $Re_{l_\mu} = 2.31 \cdot 10^6$ and with an angle of attack of $\alpha = 24°$. The CFD simulations are performed on the rigid model without consideration of fluid-structure interactions. Figure 1a shows the results of the IDDES simulation with the isosurfaces of the Q-

STAB

criterion, colored with the non-dimensional axial velocity u/U_∞. The inboard vortex (IBV) develops on the forebody. The midboard vortex (MBV) forms at the LEVCON and the strake. The outboard vortex (OBV) is generated at the leading edge of the main wing. Figure 1b shows the root-mean-sqare (rms) values $c_{p,rms}$ of the pressure fluctuations on the wing and the vertical tail. The highest pressure fluctuations are identified in the area of the vortex breakdown of the MBV and at the leading edge of the vertical tail. Figure 2 shows the root bending moment of the vertical tail. The absolute value of the mean value of the root bending moment is 4.110 Nm for IDDES and 3.684 Nm for SA-neg-RC. Compared to the slight differences in the mean value, a significant deviation can be seen in the rms value. IDDES shows much higher oscillation amplitudes, and the rms values are five times higher than the ones obtained using SA-neg-RC. Both methods predict comparable PSD peaks for the root bending moment in the frequency domain. The predominant excitation occurs at a reduced frequency of $k = 0.91$ $(449.2\ Hz)$ for IDDES and $k = 0.83$ $(410.2\ Hz)$ for SA-neg-RC. These quasi-periodic oscillations arise from a helical mode instability (HMI) of the breakdown flow. On the principle of reduced frequency as a similarity parameter, a value in the range of $k = 1.0$ is given in the literature for the excitation due to the HMI [3].
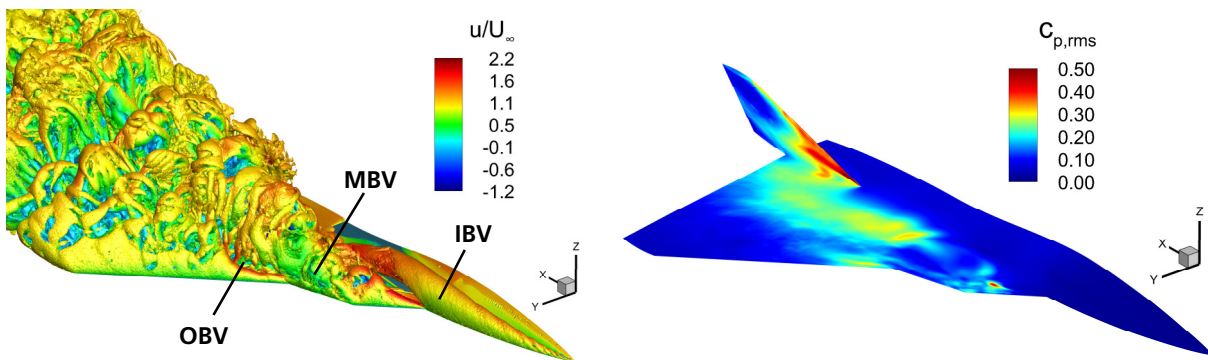
Figure 1a: Isosurfaces of the Q-criterion, colored with the non-dimensional axial velocity u/U_∞

Figure 1b: Rms values $c_{p,rms}$ of the pressure fluctuations on the wing and the vertical tail

Figure 1: Results of the IDDES-Simulation for $\alpha = 24°$, $Ma_\infty = 0.55$, $Re_{l_\mu} = 2.31 \cdot 10^6$
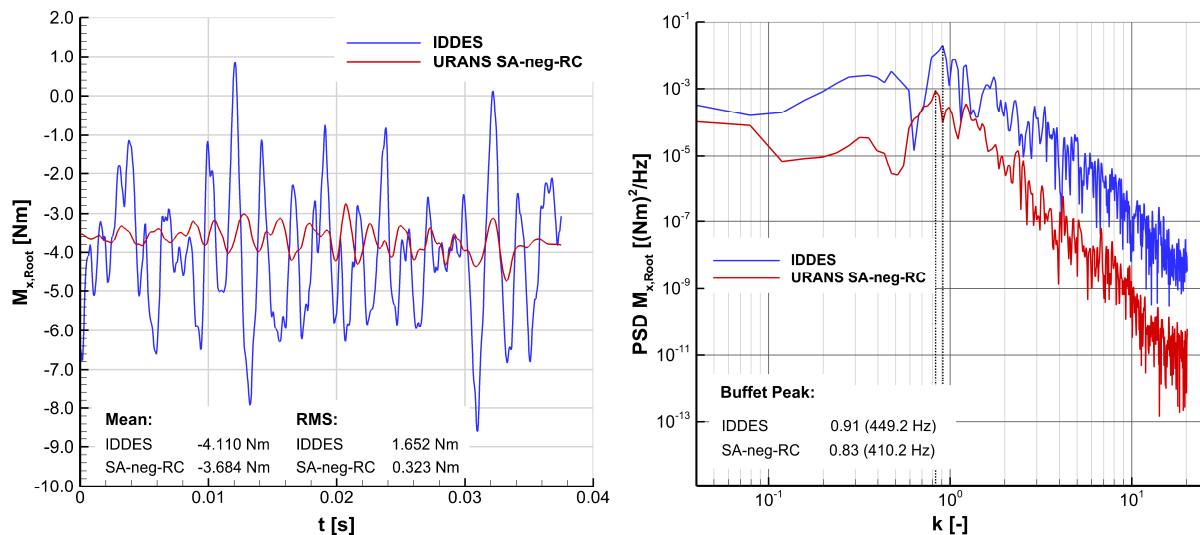
Figure 2: Vertical tail root bending moment $M_{x,Root}$ for $\alpha = 24°$, $Ma_\infty = 0.55$, $Re_{l_\mu} = 2.31 \cdot 10^6$

References

[1] J. Zastrow, F. Oberdieck, U. Henne, C. Klein, "Numerical and Experimental Investigations on the DLR-F23 Combat Aircraft Wind Tunnel Model," *33rd Congress of the International Council of the Aeronautical Sciences*, ICAS 2022, 4.-9. September 2022, Stockholm, Schweden, ISBN: 978-171387116-3

[2] M. L. Shur, P. R. Spalart, M. K. Strelets, A. K. Travin, "A hybrid RANS-LES approach with delayed-DES and wall-modelled LES capabilities, " In: *International Journal of Heat and Fluid Flow,* 29(6), pp1638-1649, 2008. doi: 10.1016/j.ijheatfluidflow.2008.07.001

[3] I. Gursul, "Review of Unsteady Vortex Flows over Slender Delta Wings, " In: *Journal of Aircraft*, 42.2, pp 299-319, 2005. doi: 10.2514/1.5269

STAB

Mitteilung

Fachgruppe: Hochagile Konfigurationen

Limits of quasiconical symmetry in 3D shock-boundary layer interaction at a single fin on a flat plate

Wieland Lühder
DLR Göttingen, Wieland.luehder@dlr.de
Erich Schülein
DLR Göttingen, Erich.Schuelein@dlr.de

Introduction : Quasiconical symmetry in 3D-STBLI

Three dimensional shock-wave turbulent boundary layer interactions (3D-STBLI) of a single fin, mounted on a flat plate, are investigated. This configuration is known to create a quasi-conical flowflield, where most flow properties solely depend on the conical angles and not on the distance to the virtual conical origin (VCO) [1]. The prerequisite for this symmetry is the plane compression
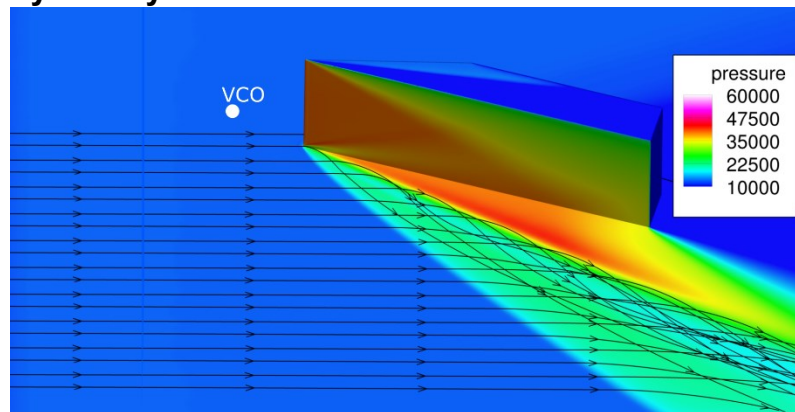
Figure 1: RANS distribution of wall pressure [Pa] in the interaction region of a single fin and streamlines within the boundary layer on the incoming flow forming a separation vortex. (Mach 3, $\beta = 16°$, $Re_1 = 45 \times 10^6$/m)

shock, which is generated at a semi-infinite sharp fin in an inviscid flow. This symmetry is known to be broken for viscous fluids in the vincinity of the leading edge of the fin, resulting in an «inception region». Furthermore, the finite height on the fin causes a deformation and weakening of the shock front, which propagates downstream to the plate surface, as can be seen in Fig. 1. Between those two effects lies an alleged zone of conical symmetry. This symmetry was demonstrated to exist for the lambda shock system (main shock, separation shock and rear shock) with conical shadowgraphy [2] as well as for the surface pressure distribution. Several other flowfield quantities are assumed to follow this symmetry in recent publications (like [3]), although this has not yet been explicitly proven.

Using experimental methods to measure wall shear stress and heat flux distributions, we can now quantitatively investigate the deviations from a perfect conical symmetry. This helps to prove several assumptions of quasiconical behaviour right, suggest corrections or assume uncertainities of the quasiconical approach.

Experimental Methods

The experiments were conducted at the Rohrwindkanal Göttingen (RWG), which is a Ludwieg tube facility. The experiments were conducted at Mach numbers of 3 and 5 for a constant unit Reynolds number of $Re_1 = 45 \times 10^6$/m. Two alternative fin geometries were tested on the rotating insert of the model, varying the fin angle β and leading edge radius R in discrete steps. Wall pressure, wall shear stress and heat flux on the flat-plate surface were measured in the RWG in three separate test campaigns. Figure 2 (left) shows an image of the fin inclined at $\beta = 16°$ on the turntable, which is equipped with 211 pressure taps for measuring the wall pressure distribution. The skin-friction

coefficient C_f was measured with oil film interferometry (OFI). A typical OFI-interferogram can be seen in Fig. 2 (center). The inverse determination of the skin friction coefficient from the thin film equation [4] requires knowledge of the change in the oil film thickness distribution over time from an OFI test as well as the path of the limiting streamlines, which are obtained in a separate wind tunnel run. Each wind tunnel experiment only yields a small evaluable area and several data sets need to be combined to obtain a nearly complete 2D distribution of wall shear stress amplitude and direction. Finally, the heat flux was measured using quantitative infrared thermography (QIRT), whereby the temporal development of the model surface temperature (Fig. 2, right) is documented and processed.
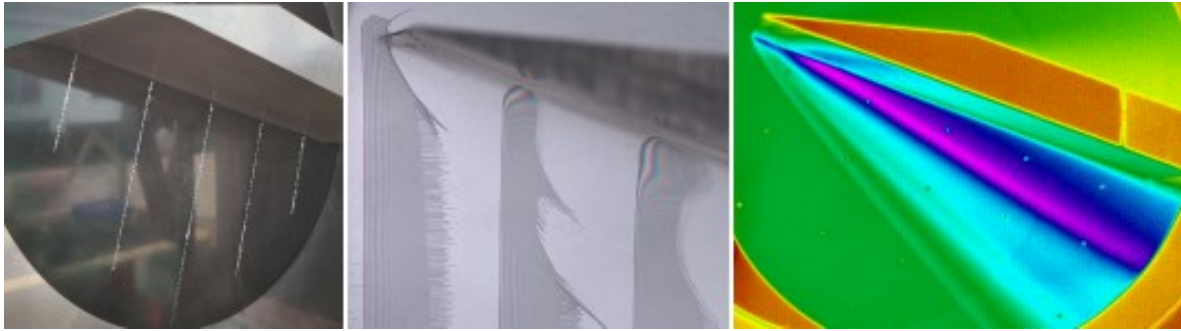
Figure 2: Three experimental methods, consisting of pressure taps (left), Oil film Interferometry (center) and quantitative infrared thermography showing the model surface temperature (right).

Sample Results

Figure 3 shows the normalised peak values of the wall pressure, the skin friction coefficient C_f and the Stanton number St along the conical rows as a function of the distance to the fin leading edge x'. The inception region can be clearly seen as a steep climb of the Stanton number (red line) up to $x' = 65$ mm in this configuration. But even at higher distances no perfectly constant values are measured, as is typically assumed within the quasiconical symmetry. Furthermore, this behavior changes with the model geometry. In the case of Mach 3, the quasiconical symmetry is not preserved near the rear edge of the fin and the peak values tend to decrease. At a Mach number of 5, the measured values stay nearly constant for a longer distance but the impact of a changed geometry of the leading edge is very strong. A blunt leading edge of the fin with curvature radius of only 0.8 mm can double the size of the inception region.
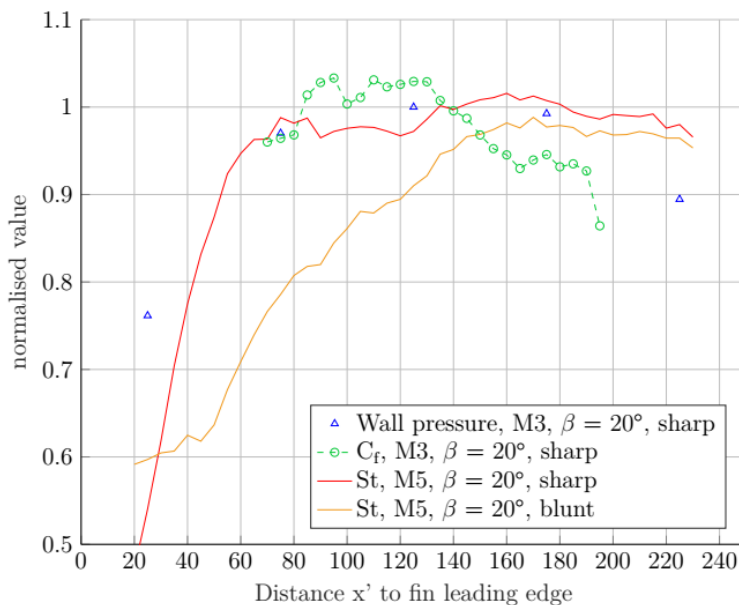
Figure 3: Sample results of peak values of the wall pressure, friction coefficient (both at Mach 3) and Stanton number (at Mach 5) over the distance to the fin leading edge.

Literature

[1] Adler, M. C., and Gaitonde, D. V. Flow similarity in strong swept shock/turbulent-boundary-layer interactions. *AIAA Journal 57*, 4 (2019), 1579– 1593

[2] Alvi, F., and Settles, G. Structure of swept shock wave/boundary-layer interactions using conical shadowgraphy. In *21st Fluid Dynamics, Plasma Dynamics and Lasers Conference* (1990), American Institute of Aeronautics and Astronautics.

[3] Baldwin, A., Mears, L., Alvi, F., Kumar, R., and Naughton, J. Effect of swept shockwave boundary-layer interaction strength on surface skin friction. *AIAA Journal 61*, 4 (2023), 1608–1622

[4] Brown, J., and Naughton, J. The thin oil film equation. *No. NAS 1.15:208767* (1999)

STAB

Mitteilung

Fachgruppe: Hochagile Konfigurationen

Experimental and numerical investigation of the vortical flow on the transonic missile LK6E2

Christian Schnepf, Sebastian Weiss, Ulrich Henne, Erich Schülein,
DLR, Institut für Aerodynamik und Strömungstechnik (AS),
Bunsenstraße 10, 37073 Göttingen, christian.schnepf@dlr.de

Introduction

A key requirement for modern subsonic, transonic and supersonic interceptor missiles is high maneuverability. This requirement is associated with high angle of attack maneuvers, resulting in large flow separations and vortical flow. The vortices that form can have a crucial influence on the aerodynamic characteristics of the missile and lead to non-linear aerodynamic behaviour. Nevertheless, an exact numerical prediction of the flight performance in this non-linear range is a desired goal for future missile design. But it is precisely in this area that RANS methods sometimes still do not show sufficient accuracy. This study addresses a transonic test case for which standard RANS simulations do not correctly predict a vortex-induced break in the rolling moment coefficient with increasing total incidence σ. Figure 1 shows the corresponding rolling moment development for a Mach number of M = 0.85 and a fixed roll angle of λ = 45°. The break at σ > 16.0° is the result of a non-simultaneous transformation of leading edge vortices that form on two wings of the four wings of the missile. The geometry studied is the LK6E2 transonic missile (Fig. 1, left side). LK6E2 is the result of an internal design study of the DLR for high maneuverable transonic missiles. The LK6E2 and the associated test case was already investigated in the NATO STO Task Group AVT-316 [1], but the comparisons between CFD and experiment was based solely on aerodynamic coefficients. This study also includes data from pressure sensitive paint measurements [2] (PSP) and Oil film interferometry measurements [3] (OFI) which is compared with the results of numerical simulations.
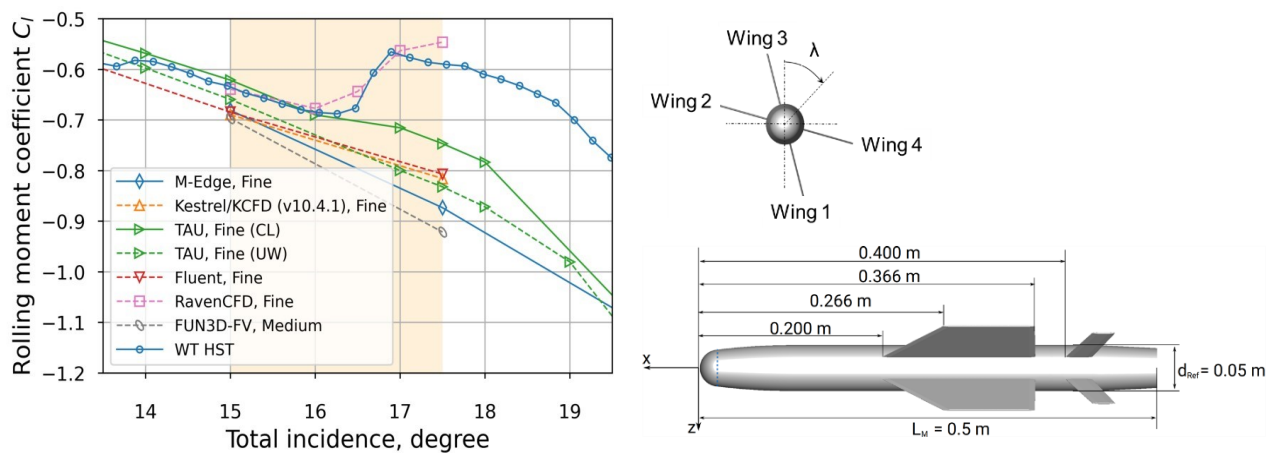
Figure 1 Comparison of numerical predicted data and wind tunnel data (WT HST) for the test case LK6E2 for a Mach number of M = 0.85 and a Reynolds number of 500,000 *Fehler! Verweisquelle konnte nicht gefunden werden.* **(left plot). Outer mould line of the LK6E2 (right plot).**

Tools and Method

The numerical simulations have been carried out with DLR's finite volume flow solver TAU. TAU solves the Reynolds-averaged Navier-Stokes equation on hybrid grids. In this study the standard Menter SST turbulence model was used to closure the system of equation. All the simulations have been conducted with the finest grid of the family of grids as defined in [1].

The optical flow measurements have been carried out in the Transonic Wind Tunnel Göttingen (DNW-TWG) for a Mach number of 0.85 and a roll angle of 45°.

Results

Figure 2 shows the visualization of the wall shear stress lines on wing 2 and wing 4 on the right-hand side and the corresponding pressure distribution on the left-hand side. Both results clearly indicate that the flow separation and the development of the vortical flow over the wings are different between both wings shown. On wing 2, the OFI data reveals that a leading edge vortex forms from the shear layer separating at the leading edge. Downstream of the reattachment line of this vortex, the flow continues in longitudinal direction of the wing. A second flow separation at the trailing edge is not observable. The aforementioned leading edge vortex is clearly reflected in the pressure distribution on the left side of Fig. 2. In contrast, the pressure distribution on wing 4 shows a kind of pressure plateau in the first half of the wing. A footprint of a leading edge vortex is not identifiable. Compared to wing 2, the pattern of the wall shear lines on wing 4 is also completely different. There is no sign of a vortex at the leading edge. Instead a kind of recirculation can be observed, which takes place in the plane of the wing. Combining the results of the two measurements methods provides clear evidence that the leading edge vortex on wing 4 disappears for $\sigma > 15.0°$. This agrees with the result of a RANS simulation with RavenCFD which is able to predict the break in the rolling moment [1].
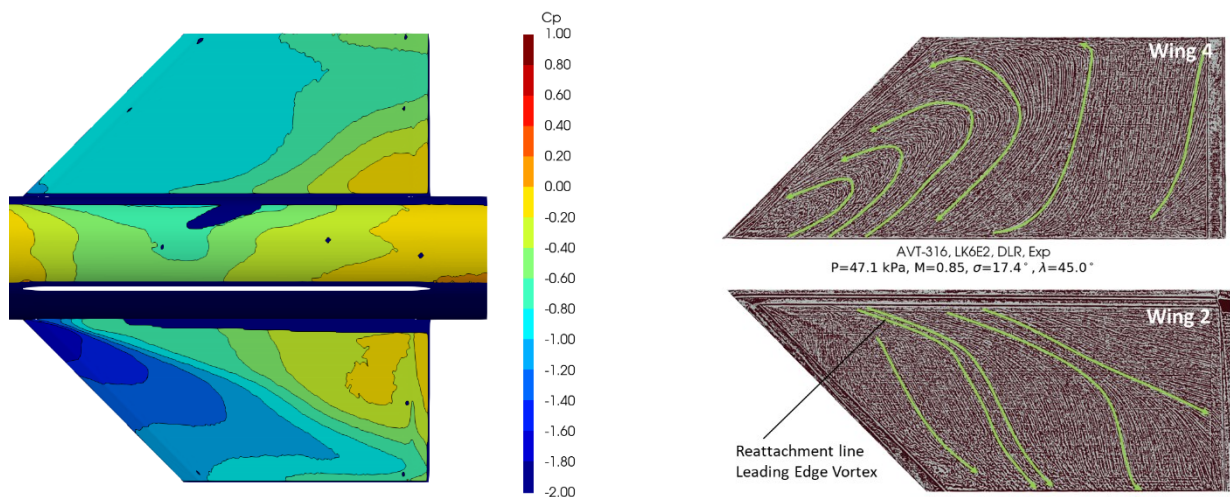
Figure 2 Pressure distribution (PSP) and visualization of the wall shear stress lines (OFI) for M = 0.85 and σ = 17.5°.

Outlook

In the final paper the development of the flow with increasing σ will be analyzed for a total incidence range of $14.0° < \sigma < 20.0°$ based on the data of the optical flow measurements. This data will be compared with data of numerical simulations and the differences that exist are highlighted. It is shown that in the range of $15.0° < \sigma < 20.0°$ the transformation of the leading edge vortex on wing 4 is not always correctly predicted by standard RANS simulations.

[1]   NATO STO, "Vortex Interaction Effects Relevant to Military Air Vehicle Performance", STO-TR-AVT-316, 2024.

[2]   Henne, U., Yorita, D., and Klein, C., "Application of Lifetime-Based Pressure-Sensitive Paint for Transonic Tests on a Generic Delta Wing Planform," New Results in Numerical and Experimental Fluid Mechanics XII: Contributions to the 21st STAB/DGLR Symposium, Darmstadt, Germany, 2018, Springer, 2020, pp. 287–296

[3]   Lunte, J., Schnepf, C., and Schülein, E., "Optical wall shear stress measurements on the leeward side of a delta wing," 2018 Aerodynamic Measurement Technology and Ground Testing Conference, 2018, p. 3806.

STAB

Mitteilung

Fachgruppe: Hochagile Konfigurationen

Development of Leading-Edge Vortices in Subsonic and Transonic Conditions

E. Tangermann, E. Schmidt, K. Rajkumar and M. Klein
Universität der Bundeswehr München, 85577 Neubiberg
eike.tangermann@unibw.de

Delta wing configurations typically gain significant lift from a system of vortices emanating from their swept leading edges. The present work investigates the development of these vortices along the wing with a focus on the effect by shocks in transonic flow based on data from numerical simulation. To separate the impact of the shocks from other phenomena occurring in the vortex dynamics, the flow will be assessed in subsonic (*Ma=0.5*) as well as transonic (*Ma=0.85*) conditions, where only the latter features shocks embedded in the vortex system.

The underlying geometry is a generic delta wing configuration proposed by Airbus D&S for the investigation of phenomena occurring on multiple delta shaped planforms [1]. They comprise a double and a triple delta planform where the wings are flat plates with a sharpened leading edge. The flow is primarily investigated at an angle of sideslip of *β=5°*, which leads to a strongly asymmetric vortex system. Previous work by the authors has identified the development of features in the transonic flow field at different angles of attack up to and beyond vortex breakdown [2] and observed the transient interaction between shock and vortex breakdown [3]. Including subsonic flow results in the present work allows for a better characterisation of shock-induced effects.

All numerical simulations have been performed using the TAU flow solver [4] by the German Aerospace Centre (DLR). Turbulence has been modelled using the kω-SST turbulence model. Since the investigation covers various cases with varying angles of attack (*α=16°-32°*), a scale-resolving approach would not have been feasible. Further, within [3] the kω-SST model has been shown to produce sufficiently accurate results for the present configuration in the context of the present evaluation.

| Ma = 0.5 | Ma=0.85 |

Fig. 1 Triple delta at *α = 20°*. Iso-surface from *Q* (grey) and density gradient as indication of shocks (coloured by *Ma*).

STAB

| Ma = 0.5 | Ma=0.85 | Ma = 0.5 | Ma=0.85 |
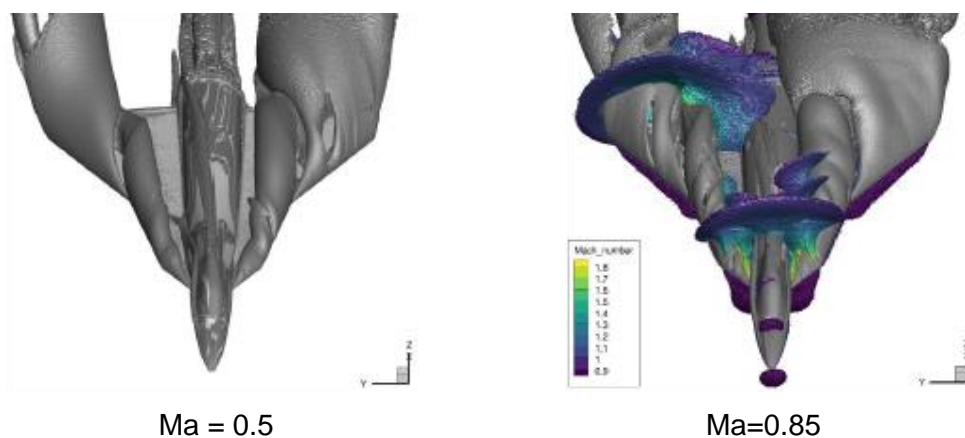
Fig. 2 Double delta at $\alpha = 20°$. Iso-surface from Q (grey) and density gradient as indication of shocks (coloured by Ma).

Fig. 3 Double delta at $\alpha = 20°$. Pressure coefficient on the surface, left: Ma = 0.5, Right: Ma = 0.85, AoA = 20°

Around $\alpha=20°$ the vortex breakdown occurs only above windward wing for both planforms. Figures 1 and 2 visualise the vortex system by showing iso-surfaces from Q-criterion. In the transonic case several shocks can be seen, which are indicated by surfaces of high density gradient. As expected, the shocks destabilize the vortices up to breakdown. This can also be seen in the surface pressure plot of Figure 3, where downstream of the shock front the vortex footprints are weaker and wider than in the subsonic case. Nevertheless, the locations of vortex breakdown often remain comparable between both Mach numbers.

For a more quantitative description of the vortex behaviour, the final paper will feature profiles of the development along the vortex core line. The impact of the turbulence within the vortex on the axial velocity will be discussed as well as source terms of vorticity and their effect on the velocity field. The comparison between subsonic and transonic cases will then allow to quantify the actual impact of shocks and other compressible effects and distinguish between them and other effects of vortex dynamics.

References

[1] Hitzel, S.M., Winkler, A., Hövelmann, A. (2020). Vortex Flow Aerodynamic Challenges in the Design Space for Future Fighter Aircraft. In: Dillmann, A., Heller, G., Krämer, E., Wagner, C., Tropea, C., Jakirlić, S. (eds) New Results in Numerical and Experimental Fluid Mechanics XII. DGLR 2018. *Notes on Numerical Fluid Mechanics and Multidisciplinary Design*, vol 142. Springer, Cham. doi:10.1007/978-3-030-25253-3_2

[2] Di Fabbio, T., Tangermann, E., Klein, M. (2023). Analysis of the vortex-dominated flow field over a delta wing at transonic speed. *The Aeronautical Journal*, *127*(1317), 1851–1868. doi:10.1017/aer.2023.30

[3] Rajkumar, K., Di Fabbio, T., Tangermann, E., M. Klein (2024). Physical aspects of vortex-shock dynamics in delta wing configurations. *Physics of Fluids,* 36 (6): 066112. doi:10.1063/5.0213122

[4] Gerhold, T. (2005). Overview of the Hybrid RANS Code TAU. In: Kroll, N., Fassbender, J.K. (eds) MEGAFLOW - Numerical Flow Simulation for Aircraft Design. *Notes on Numerical Fluid Mechanics and Multidisciplinary Design (NNFM)*, vol 89. Springer, Berlin, Heidelberg. doi:10.1007/3-540-32382-1_5

STAB

Mitteilung

Fachgruppe: Hyperschallaerothermodynamik

Comparison of Different Fidelity Approaches for the Coupled Aerothermodynamic Heating of High Lift Reentry Vehicles

Fynn Barz, Marius Franze

Institute of Aerodynamics and Flow Technology, Spacecraft, German Aerospace Center (DLR), Lilienthalplatz 7, Braunschweig, 38108, Lower Saxony, Germany, fynn.barz@dlr.de

Abstract

In the present study, the influence of different fidelity flow solvers and structure models on the aerothermodynamic heating of high lift reentry vehicles (HLRV) is investigated. The study is carried out on a generic blunt leading edge waverider (WR) configuration, see Figure 1. The heating of the structure is calculated by the strong coupling between the flow solver and the structure solver. The calculations are carried out for the forced flight along a generic reentry trajectory. The high-fidelity reference data are provided by a coupled simulation of the commercial structure solver Ansys and the DLR flow solver TAU [1]. The low-fidelity solutions are performed by fast engineering methods. The differences of the heating along the trajectory are analyzed.

Introduction

HLRV are of increasing interest during the last years. The reason is their maneuverability and the ability to fly at high Mach numbers over a long duration of time. Hence, such configurations are not only interesting for the transportation purpose but also from a defense perspective. Furthermore, they are a suitable geometry for the testing of multidisciplinary optimization due to the description of the geometry by just a few parameters.

In recent years, the high-fidelity calculations of reentry vehicle became state of the art. Also, the multidisciplinary coupling of high-fidelity solvers was performed more frequently. However, these methods need a high computational effort and create a massive amount of data. These facts make them less attractive for multidisciplinary optimization due to the number of calculations needed. For this reason, low-fidelity solvers are needed within multidisciplinary optimizations to reduce the parameter space for the high-fidelity optimizations. The low-fidelity solvers are much faster, but the accuracy of the results can highly lack validity depending on the mission and geometry. Therefore, this investigation gives detailed insight into the differences between the high-, and low-fidelity multidisciplinary solution for a generic HLRV. This knowledge enables the optimizer in the multi-fidelity optimization process to decide when a higher-fidelity solver needs to be conducted.
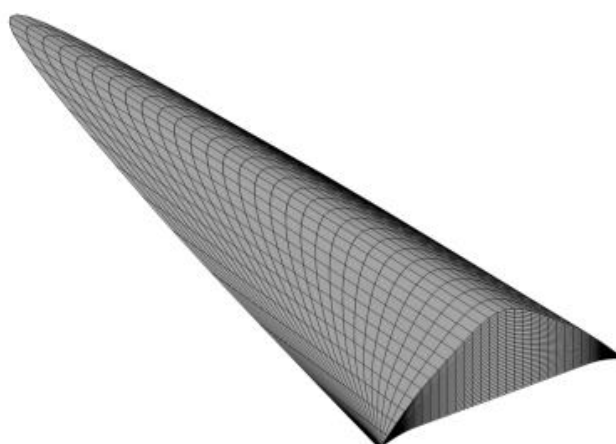
Figure 1: The generic waverider configuration.

Mission

The generic trajectory is depicted in Figure 2. The flight starts with the separation from the motor. Afterwards, the vehicle flies a dipping reentry followed by cruise phase in 30km height with a Mach number of 10.
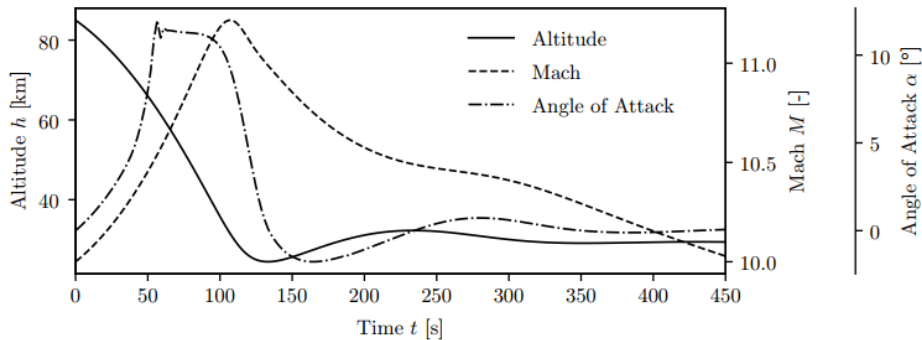
Figure 2: The generic reentry trajectory.

Numerical Setup

The computation is performed in the FlowSimulator [2] framework, which is a simulation environment developed by the DLR. The environment enables to perform high-performance computations due to its foundation, the FSDataManager. The FSDataManager keeps all data needed for the simulation in RAM and manages the partitioned data in parallel computations. Thus, the only files written on disc are for calculation restart or the final results. Within the FlowSimulator, all tools are controlled via a Python layer which allows for fast setup of simulations. Herein, the CoNF^{2}aS^2 module serves as a control program for multidisciplinary simulations. The module provides simulation parameter for every solver, initializes the solvers, runs the calculations and governs the exchange of data between the solvers.

The low-fidelity flow solution is calculated by the Kaufman matching point method [3]. This method incorporates the modified Newtonian method and the shock expansion method. The modified Newtonian methods is used for the leading edge region. At the matching point, the pressure gradients of the both methods are the same. From this point, the shock expansion method is used downstream. The combination of the methods enables the calculation of configurations with detached shocks. The heat transfer in the blunt leading-edge region is described by the empirical relation of the flow around a cross flow cylinder. Downstream, the Eckert reference enthalpy method combined with solutions of the boundary layer equations for the flat plate are conducted.

The structure solver is a finite element one-dimensional heat conduction solver. The heat conduction equation is hereby solved for every surface element in its normal direction. In the normal direction, stacks of different materials can be described. This leads to a simplified model of the structure and thermal protection system of the vehicle.

References

[1] D. Schwamborn, T. Gerhold and R. Heinrich, "The DLR TAU-Code: Recent Applications in Research and Industry," *ECCOMAS CFD, Eggmond aan Zee, The Netherlands,* 2006.

[2] M. Meinel and G. Einarsson, " The FlowSimulator Framework for Massively Parallel CFD Applications," *PARA, Reykjavik, Island,* 2010.

[3] L. G. Kaufman, "Pressure Estimation Techniques for Hypersonic Flows Over Blunt Bodies," *Journal of Astronautical Sciences,* 1963.

STAB

Mitteilung

Fachgruppe: Hyperschallaerothermodynamik

Hypersonic Ablation Modeling using DSMC

Lennart Bott, Christian Stemmer

Lehrstuhl für Aerodynamik und Strömungsmechanik, Technische Universität München,
Boltzmannstr. 15, 85748 Garching b. München
Christian.Stemmer@tum.de

Ablative phenomena are investigated for rarefied flows at the Chair of Aerodynamics and Fluid Mechanics (Technical University of Munich) using the Direct Simulation Monte Carlo (DSMC) code SPARTA (Stochastic PArallel Rarefied-gas Time-accurate Analyzer.

Spacecraft usually reenter the planetary's atmosphere at hypersonic speeds and are exposed to severe aerothermodynamic loads during their descent. Ablative thermal protection systems (TPSs) are used to protect the payload by dissipating kinetic energy from the vehicle through ablative processes such as melting, sublimation, and chemical reactions. Most numerical models investigate the interaction of the hypersonic flow with the ablating surface within the continuum regime at the point of peak heating [1, 2]. However, assuming accurate surface and flow conditions is still challenging as ablative processes are already present at much higher altitudes for rarified flows. The continuum assumption may be locally or globally violated, as shown for the flow over a flat plate at two different atmospheric altitudes of H = 50 km (Mach 15) and H = 70 km (Mach 25) with a 2D, $\sin^2$-shaped obstacle by Song and Stemmer [3]. Hence, particle methods like DSMC based on the Boltzmann equation must be employed to accurately model the non-equilibrium characteristics of the flow [4, 5].

To investigate ablation for such large Knudsen number flows on a macroscopic (capsule size) scale, preliminary work was done in Bott *et al.* [6], expanding SPARTA's ablation model developed by Borner and Plimpton [7, 8]. A scaling factor model was proposed, achieving a phenomenological ablation description but falling short of reproducing ablation rates observed in experiments. Also, a strong dependence of the calculated ablation rate on the chosen DSMC-simulation parameters was detected. Recent work was devoted to solving those problems by developing a material-based ablation model for SPARTA, using the specific latent heat h_{lat} of the material. In addition, the integral form of the heat-balance equation is employed to couple the particle flow to the ablating surface, making the kinetic energy of the particles the decisive criterion for ablation.

Fig. 1 shows the ablation of a square with the new material-based model in time with the flow left to right. A surface recession with a high local resolution (grid cell level) is modeled, calculating the highest ablation rates at the leading edge of the square and almost no ablation at the upper and lower side, as well as the wake-flow facing surface. Also, the dependency of the ablation-rate on the DSMC-simulation parameters is eliminated by the new approach, as shown exemplarily for the grid-cell size and the length of a timestep in Fig. 2 and 3. In addition, ablation rates of the same magnitude as observed in plasma tunnel experiments by Löhle *et al.* [9] for the reentry of the Japanese Hayabusa capsule at an altitude of H = 78.8 km and Mach number of Ma = 41.1 are obtained and will be shown.
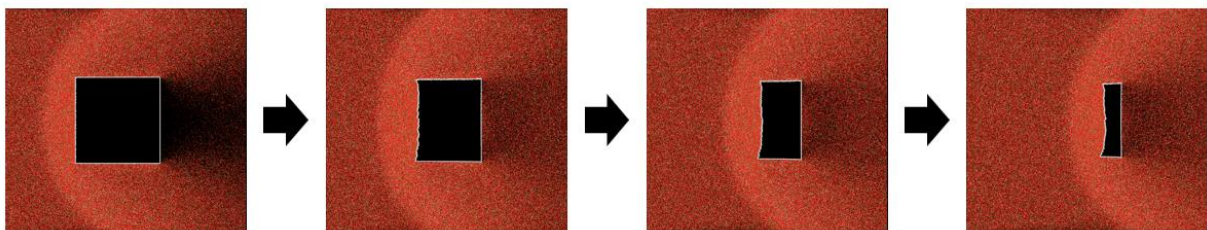
Fig. 1: Ablation of a square in time employing the material-based ablation model; Flow from left to right
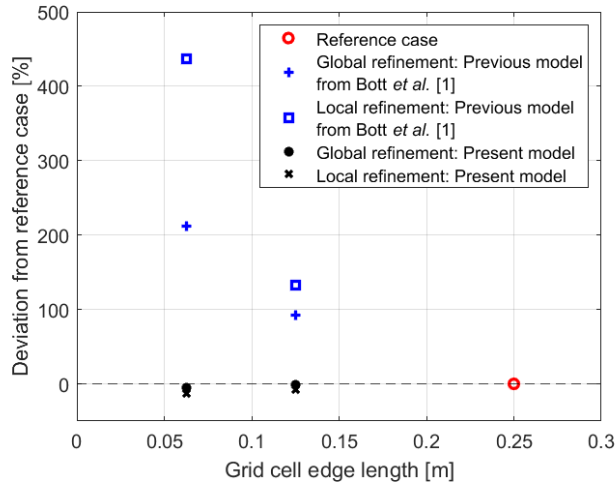
Fig. 1: Ablation rate dependency on the grid cell size
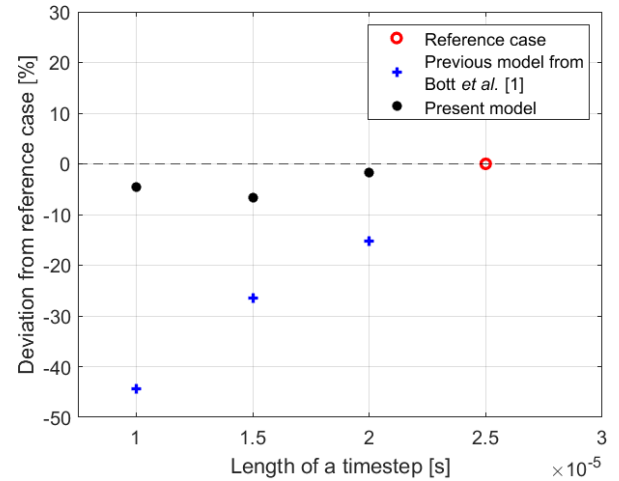
Fig. 2: Ablation rate dependency on the timestep length

References

[1]   Daniele Bianchi, Francesco Nasuti, and Emanuele Martelli. "Navier-Stokes Simulations of Hypersonic Flows with Coupled Graphite Ablation". In: Journal of Spacecraft and Rockets 47.4 (2010), pp. 554–562. issn: 0022-4650 1533-6794. doi: 10.2514/1.47995.

[2]   Alexandre Martin and Iain D. Boyd. "Strongly Coupled Computation of Material Response and Nonequilibrium Flow for Hypersonic Ablation". In: Journal of Spacecraft and Rockets 52.1 (2015), pp. 89–104. issn: 0022-4650 1533-6794. doi:10.2514/1.A32847.

[3]   Song Chen and Christian Stemmer. "Modeling of Thermochemical Nonequilibrium Flows Using Open-Source Direct Simulation Monte Carlo Kernel SPARTA". In: Journal of Spacecraft and Rockets 59.5 (2022), pp. 1634–1646. issn: 0022-4650 1533-6794. doi: 10.2514/1.A35359.

[4]   John D. Anderson. Hypersonic and high temperature gas dynamics. AIAA, 1989.

[5]   Iain D. Boyd and Thomas E. Schwartzentruber. Nonequilibrium gas dynamics and molecular simulation, volume 42. Cambridge University Press, 2017.

[6]   Lennart Bott, Song Chen, and Christian Stemmer. DSMC Study of Hypersonic Ablation Using SPARTA. 2nd International Conference on Flight Vehicles, Aerothermodynamics and Re-entry Missions & Engineering (FAR). 2022.

[7]   S. J. Plimpton, S. G. Moore, A. Borner, A. K. Stagg, T. P. Koehler, J. R. Torczynski, and M. A. Gallis,. (2019). Direct simulation Monte Carlo on petaflop supercomputers and beyond. *Physics of Fluids*, *31*(8).

[8]   Arnaud Borner, Krishnan Swaminathan-Gopalan, Kelly A. Stephani, and Nagi N. Mansour. Detailed DSMC surface chemistry modeling of the oxidation of carbon-based ablators. AIP Conference Proceedings. Conference Paper. 2016. doi: 10.1063/1.4967612.

[9]   S. Loehle, T. Hermann, and F. Zander. "Experimental assessment of the performance of ablative heat shield materials from plasma wind tunnel testing". In: CEAS Space Journal 10 (2018), pp. 203–211. issn: 1868-2502.

STAB

Mitteilung

Fachgruppe: Hyperschallaerothermodynamik

DNS of an oblique-breakdown transition in an oblique-shock/ flat-plate-boundary-layer interaction flow

Jan Niklas Kuhnlein[1], Alexander Theiß[1], Christian Schnepf[1], Christian Stemmer[2]
[1] DLR Göttingen, Institut für Aerodynamik und Strömungstechnik, Abteilung Hochgeschwindigkeitskonfigurationen, Bunsenstraße 10, 37073 Göttingen
[2] Lehrstuhl für Aerodynamik und Strömungsmechanik, Technische Universität München, Boltzmannstr. 15, 85748 Garching bei München
jan-niklas.kuhnlein@dlr.de

Introduction: At the intake of scramjet or ramjet engines and at control surfaces of missiles, complex shock wave/boundary-layer interactions (SWBLI) in the hypersonic and supersonic flow regime occur. The SWBLI significantly influences the flow topology and causes large heat loads in the vicinity of the impinging shock. This is particularly pronounced, when the boundary layer in the interaction region is in a state of laminar-turbulent intermittency [1]. In this study, Direct Numerical Simulations (DNS) are carried out for a SWBLI on a flat plate for oblique shock wave angles of 12.4° and 13.0° impinging on the plate from above (see fig. 1). A first mode oblique breakdown transition scenario is forced in the simulations by disturbing the boundary-layer flow upstream of the SWBLI. The objective of this study is to investigate and analyze the streamwise development of the relevant eigenmodes of this disturbance. Furthermore, the influence of the disturbance on the skin friction and the heat transfer rate at the wall of the SWBLI is of particular interest.

Methods: The DNS are conducted using the finite-volume flow solver Navier-Stokes Multi-Block (NSMB), which has been successfully utilized in previous DNS studies of hypersonic SWBLI [2]. A fourth-order central scheme is chosen for spatial discretization. Explicit time integration with a three stage Runge-Kutta method is used.
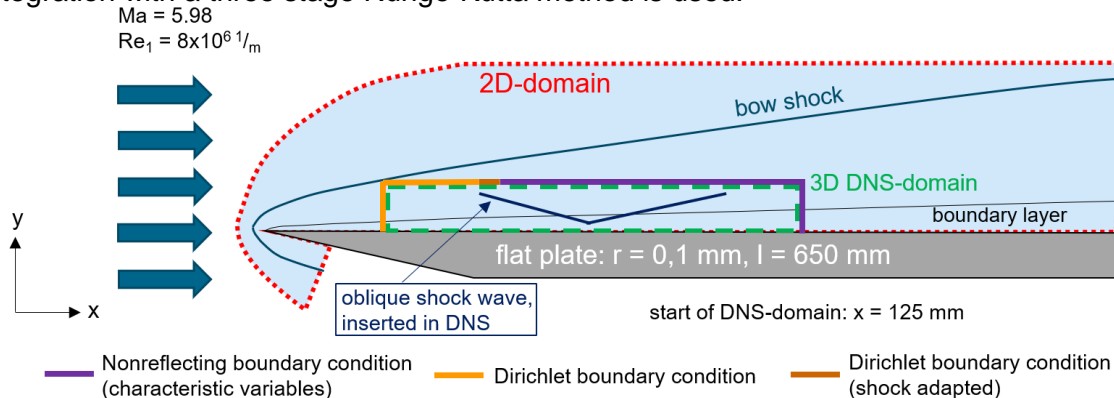
Figure 1: Sketch of the computational domains and boundary conditions: 2D-grid (dashed) and DNS-grid (dotted).

First, a two-dimensional (2D) baseflow solution for the flat-plate boundary-layer flow without shock at Mach number $Ma = 5.98$ and unit Reynolds number $Re_1 = 8 * 10^6 \, 1/m$ is computed on a domain including the leading edge with radius of $r = 0.1 \, \text{mm}$. Second, a restricted domain is used for the three-dimensional (3D) DNS to save computational costs (see fig. 1). Profiles of the flow variables are required for the Dirichlet inflow boundary condition on the left and upper faces upstream of the shock. These values are obtained from the 2D-baseflow solution. The oblique shock wave is introduced into the DNS in the upper left Dirichlet boundary condition by a discontinuity in the flow variables according to the Rankine-Hugoniot equations. A non-reflective boundary condition is applied downstream of the shock at the upper right side of the restricted domain and at the outflow. Periodic boundary conditions are applied in the spanwise direction. Transient perturbation modes are superimposed on the mean-flow values of the inflow boundary condition to force transition. The introduction and streamwise development of the forcing modes have been validated with solutions of Parabolized Stability Equations (PSE) in a previous study [3]. In this study, PSE analyses for the base flow without SWBLI

are conducted to find the suitable forcing modes for an oblique breakdown scenario. The highest growth rates throughout the streamwise dimension of the domain for the oblique first modes are found at a frequency of $f = 9\,\mathrm{kHz}$ with a spanwise wavenumber of $\beta = 230\,1/\mathrm{m}$. In a first step, simulations are carried out on an existing domain to verify the procedure for generating an oblique breakdown scenario. This domain has smaller spanwise extent resulting in a spanwise wavenumber of $\beta = 490\,1/\mathrm{m}$ and thus a smaller growth rate. Two oblique first modes are imposed in opposite spanwise direction to trigger the oblique breakdown scenario. The maximum amplitude of the perturbation modes is scaled to approximately $3.8\,\%$ of the freestream density. The results of this preliminary investigation are presented below.

Preliminary Results: To illustrate the flow features of the DNS, the magnitude of the density gradient is shown in fig. 2. The boundary-layer thickness increases significantly at the position of the SWBLI. A separation bubble occurs between $x \approx 0.15\,\mathrm{m}$ and $x \approx 0.325\,\mathrm{m}$. In the boundary layer downstream of this separation bubble, small spanwise structures develop, which begin to break down at the end of the DNS domain. In order to analyze the development of different spanwise and temporal modes of the described process, the Fast Fourier Transform (FFT) is used. The results are presented in the final paper.
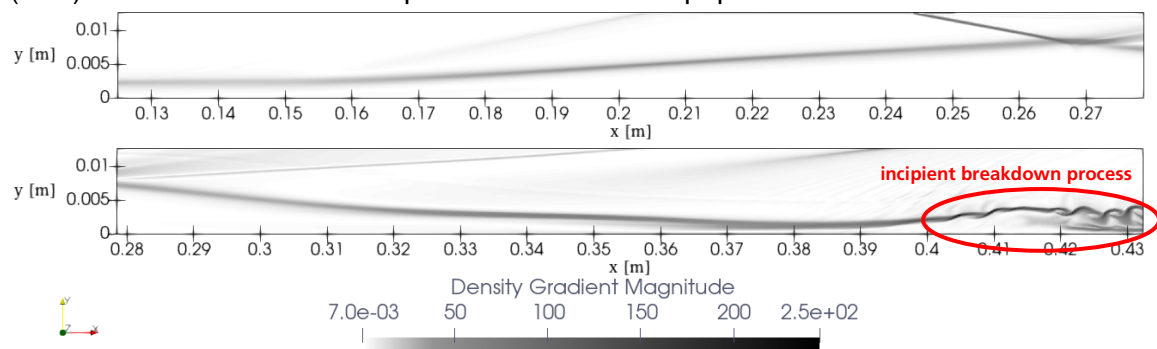
Figure 2: Density gradient magnitude (pseudo-schlieren) on a cut plane at z = 4.5 mm for the 13° shock angle case.

The evolution of the Stanton number St along the streamwise direction is shown in fig. 3. The simulation data shown are mean values (averaged in time and in spanwise direction). Analytical solutions for the laminar and turbulent (Van Driest II transformation [4]) boundary layer are included as a reference. Upstream of $Re_x = 1.1 * 10^6$, the DNS data agree very well with the laminar solution. Downstream of $Re_x = 2.2 * 10^6$, a steep increase in St can be observed, which is caused by both the pressure increase due to the shock and the incipient transition process. The overshoot of St has not reached its maximum yet, indicating, that the transition process is not finished within the DNS domain.
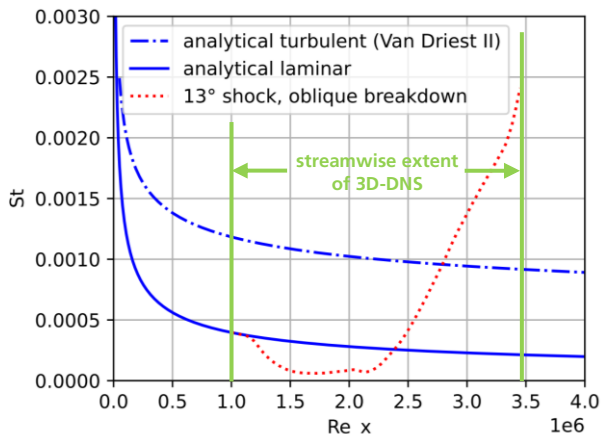
Figure 3: Stanton number development in streamwise direction for the 13° shock angle case.

Between $Re_x = 1.1 * 10^6$ and $Re_x = 2.2 * 10^6$, the effect of the separation bubble is visible. In the final paper, results will be presented for an extended domain to investigate the whole transition process. The spanwise extent of the domain will also be adapted to match the most amplified spanwise wave number determined from PSE.

[1] Lunte, J. und Schülein, E. (2019). *Heat transfer amplifications in transitional shockwave/boundary-layer interactions*, AIAA 2019-3440. AIAA Aviation 2019 Forum. https://doi.org/10.2514/6.2019-3440

[2] Giuseppe Chiapparino, Christian Stemmer, *Numerical investigation of a Mach 6 hypersonic laminar flow on two-dimensional cold-wall compression corners with controlled surface roughness*, International Journal of Heat and Fluid Flow, Volume 94, 2022, 108937, https://doi.org/10.1016/j.ijheatfluidflow.2022.108937

[3] Kuhnlein, J.N., Theiß, A., Schnepf, C. and Stemmer, C. (2023). *Vorstudien zur DNS einer transitionellen Plattengrenzschicht mit schräg einfallendem Verdichtungsstoß mittels NSMB*, STAB-Jahresbericht 2023 - Proceedings of the 21st STAB-Workshop 2023 in Göttingen

[4] Van Driest, E.R., *The problem of aerodynamic heating*, Institute of the Aeronautical Sciences, 1956.

STAB

Mitteilung

Fachgruppe: Hyperschallaerothermodynamik

Parametric grid fin design study for the T3 vehicle within SALTO

Jens Neumann
German Aerospace Center (DLR)
Institute of Aerodynamics and Flow Technology
Spacecraft Department
Lilienthalplatz 7, 38108 Braunschweig
j.neumann@dlr.de

1. Introduction

The reuSable strAtegic space Launcher Technologies & Operations (SALTO) project, funded by the European Union, aims to increase the technological maturity of reusable launchers in Europe. As part of this project the pre-design of the Themis T3 demonstrator is being analysed and improved. The T3 is a notional reusable first stage. Its aerodynamic control surfaces are to be designed as grid fins within the framework of SALTO.

The concept of grid fins was first described in 1985 by Belotserkovsky et al. [1]. They are becoming increasingly relevant for reusable launchers and promise to be a good solution for these vehicles due to several reasons. Grid fins show good efficiency over a wide range of flight speeds, especially in the supersonic and subsonic regime. They show a delayed stall behaviour and are effective at high angles of attack compared to regular fins. Grid fins require comparably low hinge moments and they can be folded to reduce drag during ascent.

On the T3 vehicle the grid fins will unfold for the descent phase. During this time, they have to fulfil two primary tasks: Enable efficient trim and controllability of the vehicle during the aerodynamic phases. Once these requirements have been met, the design should be improved with regard to other criteria. These include primarily the reduction of mass. In this study, a systematic overview of various geometrical parameters is given concerning their influence on the control forces generated along the trajectory, as well as their effects on the mass of the grid fin. The parameters will be compared to a baseline configuration.

Other factors such as the aerodynamic drag that arises when folded during ascent, aerothermal loads or structural integrity are also relevant for the grid fin design, but are not analysed further in this study.

2. Methodology

To evaluate different grid fin designs CFD studies were performed. The DLR Navier-Stokes solver TAU [2] was used for these calculations. This second-order finite-volume flow solver was used, while applying a one-equation Spalart-Allmaras eddy viscosity model [3]. The AUSMDV flux vector splitting upwind scheme was used for the entire trajectory.

The simulations only consider the grid fin to reduce computational costs. The influence of the remaining vehicle was ignored, as it is assumed that its influence has a similar effect on all of the investigated geometries.

3. CFD Results

An excerpt of the overall results is shown in this section. One of the gouverning parameters in grid fin design is the internal cell spacing s. In Figure 1 three different geometries are compared to the baseline grid fin. The spacing s is varied between 50%, 133% and 200% of the baseline value. Additionally, the cell numbers in y and z direction N_y and N_z were changed, to keep the

original width and height of the grid fin mostly constant. The figure shows the Mach numbers plotted against C_{fy}, the force coefficient in y direction. The investigated Mach numbers cover most of the descent trajectory ranging from supersonic, transonic to subsonic speeds. The deflection angle of the grid fin is 10°.

Using 0.5s shows lower C_{fy} values for all Mach numbers analysed. Therefore, this geometry does not lead to an improvement in aerodynamic controllability. Doubling the spacing, results in lowered C_{fy} in the subsonic and supersonic regime, when no flow choking is present. It increases the resulting force for transonic speeds and for Ma=1.45 and Ma=1.79 (the flow is strongly choked for these two trajectory points). The same increase, but less pronounced can be seen for 1.33s. It also shows a smaller decrease at subsonic and high supersonic velocities.

The 0.5s version increases the weight of the fin by 83.6%, while the 1.33s and 2s versions reduce it by 18.8% and 40.5% respectively.
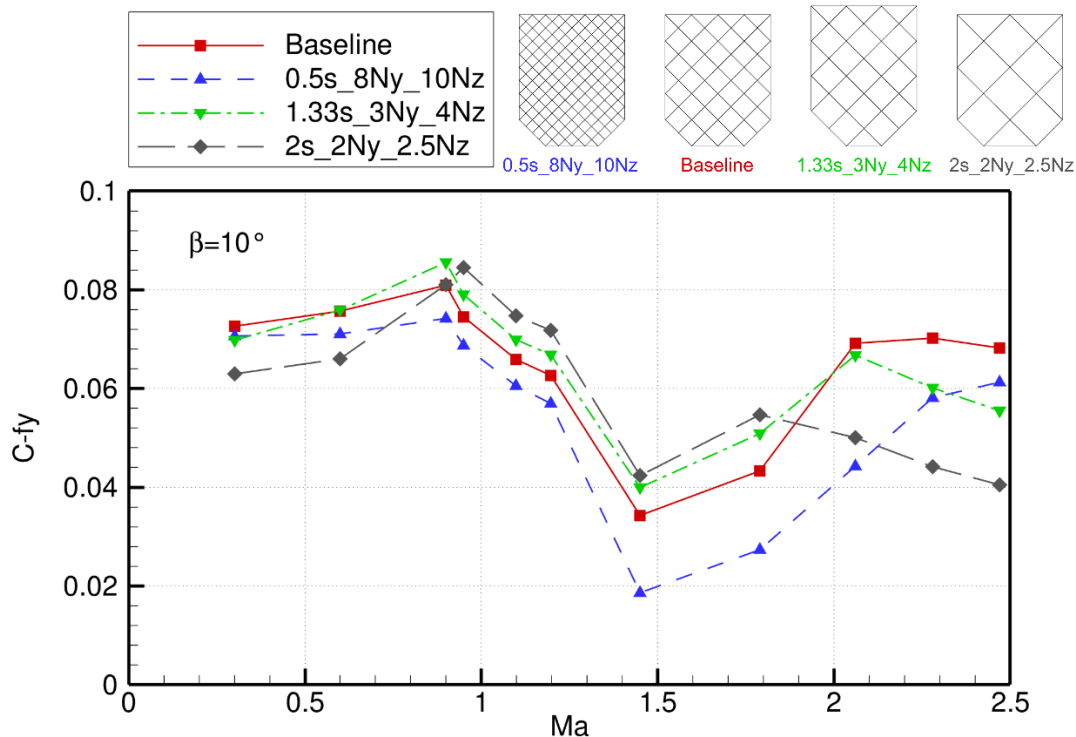
Figure 1: C_{fy} over Ma for different cell spacings s, while keeping outer dimensions approximately the same.

Acknowledgements

Literature:

[1] Belotserkovskiy, S., Odnovol, L.A., Safin, Y.Z., Tyulenev, A., Frolov, V. and Shitov, VA. Keshete-chatye krylaya (lattice wings). Machine Translation, Wings with Internal Framework, FTD-ID (RS)-1289-86, Foreign Technology Division, February 1987, pp 10–96.
[2] Langer, S., Schwöppe, S., Kroll, N.: The dlr flow solver tau - status and recent algorithmic developments. AIAA Paper 2014-0080 (2014)
[3] Spalart, P. R., Allmaras, S. R., A One-Equation Turbulence Model for Aerodynamic Flows, AIAA-92-0439, 30th Aerospace Sciences Meeting and Exhibit, Reno, USA, 1992, 6-9 January. DOI: 10.2514/6.1992-439.

STAB

VALIDATION OF NUMERICAL MODELS FOR HYPERSONIC CONTINUUM FLOW ANALYSIS

Philip Seitz[1], Martin Konopka[2]

ArianeGroup GmbH, Airbus-Allee 1, 28307 Bremen, [1]philseitz@gmx.de [2]martin.konopka@ariane.group

1. ABSTRACT

Reynolds averaged Navier-Stokes and Newton method computations are performed for reentry bodies in hypersonic continuum flow. The present work intends to validate high fidelity CFD models for equilibrium and non-equilibrium chemistry in hypersonic continuum flow at atmospheric reentry, and compare them to the predictions of the Newton method model STRAT. The Equilibrium and a non-equilibrium chemistry models are reviewed against the EURASTROS reference case from literature using the CFD solver TAU. Those simulations aim to reproduce the capsules' aerodynamic coefficients, as well as the heat flux and pressure distributions over the capsule's surface. So far, results are available for the equilibrium chemistry configuration, presenting consistent results for the aerodynamic coefficients at a maximum deviation of 0.89% for the lift coefficient. Larger deviations of up to 63.17% are found for the heat flux distribution. This is expected to result from a laminar-turbulent transitional flow configuration and shall be examined in more detail for the final version of this work. Further work includes the evaluation of the non-equilibrium chemistry model and the Newton model on the EURASTROS reference case. In addition to the EURASTROS reference case the chemical equilibrium, the non-equilibrium, and the Newton model are further compared on a representative test case of a 2D cylinder for a range of load points common for reentry trajectories. Special focus thereby is on the accurate modeling of wall heat transfer and identifying possible limitations of the models. The results are reviewed against a reference case from literature.

2. INTRODUCTION

Rising demand for space services recently lead to a renewed interest in hypersonics due to aspects of reusability. Given an increasing launch cadence along with aspects of sustainability, such as space debris mitigation, the benefits of a reusable system come to prevail over an expendable design. For this reason, ArianeGroup is expanding its capabilities in the modeling of hypersonic flow fields. The hypersonic flow regime is defined by the increasing dominance of thermochemical effects in the flow field, causing perfect and ideal gas models to predict inaccurate results with increasing Mach number. As the assessment of thermal loads and aerodynamic flight stability is a major factor in the development of hypersonic vehicles, those aerothermodynamic effects influence the entire vehicle concept. ArianeGroup is using and developing models of varying complexity applicable to hypersonic flow conditions. The purpose of this work is to review three of those models, the DLR Tau code with equilibrium chemistry, the DLR Tau code with non-equilibrium chemistry, and an in-house Newton method model. The equilibrium and non-equilibrium chemistry models are incorporated in the DLR Tau code computational fluid dynamics (CFD) solver, providing detailed solutions on aerodynamic stability and aerothermodynamic loads. The DLR TAU solver uses a RANS turbulence modeling and a hybrid meshing approach. On the other hand there is the in-house Newton method solver STRAT, allowing for less time-consuming predictions of thermomechanical loads based on the local surface inclination method and approximate correlations for the stagnation point heat flux. Once validated, those tools can be applied to research questions of varying demand for accuracy and flexibility, depending on the respective state of development. This work aims to compare and validate the three described numerical models for application in hypersonic continuum flow and identify limitations of their applicability. The models are validated on the reference case of the EURASTROS capsule presented by Marquardt et al. [1], with focus on reproducing flow field in terms of wall pressure and heatflux distribution, as well as the capsule's aerodynamics. Further, all models are compared on a representative reference case of a 2D cylinder, allowing for validating the models against the reference data presented by [2].

So far, validation of the equilibrium (Case 1) and the non-equilibrium chemistry model (Case 2) are in progress. Both are set up as 3D Reynolds-averaged Navier-Stokes (RANS) simulations in the FVM solver TAU using either the Spalart-Allmaras or Menter SST turbulence models. The equilibrium chemistry of Case 1 is set up as a reduced 5-species air model in form of a pre-generated database. This database stores pre-calculated fluid properties and viscous transport coefficients in a range of temperatures and densities for the respective species N_2, O_2, NO, N and O. For Case 1, similar to the reference case, the flow is assumed to be fully turbulent and a radiative equilibrium boundary condition with an emissivity of ϵ = 0.8 is used. The freestream properties of the farfield boundary condition are shown in **Table 2-1**.

Table 2-1: Case 1 – Flow configuration for validation of equilibrium chemistry model from [1]

Case	α	h	Ma	v_∞	p_∞	T_∞	ρ_∞
Case 1	-25°	40700m	6.80	2162m/s	254Pa	253K	0.0035kg/m^3

The geometry is meshed with a hybrid tetrahedral and prism grid, which is sequentially adapted until the wall heat flux distribution approaches a grid independent solution. All adaptations were converged to a minimum achievable density residual and a heatflux increment, both improving with increasing number of adaptation. The solution obtained for inviscid flow field, including the shock layer, thereby closely coincide the results obtained by Marquardt et al. et al. [1] as shown in **Figure 2-1**.
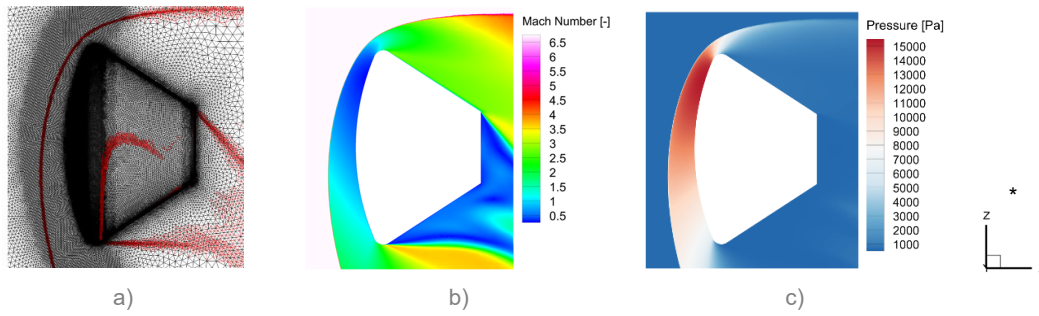
Figure 2-1: Validation Case 2 – Symmetry plane contours of a) mesh refinement b) Mach number c) pressure

The capsule is flying at a stable trim AoA of α=-25deg with the CoG shifted off axis by Δx=0.91m and Δz=0.1443m as measured from the coordinate origin at the center point of the heatshield. The reference length and reference surface result to the capsules diameter L_{ref}=3.5m and the projected front area S=9.621m^2. Evaluation of the aerodynamic coefficients c_L and c_D in **Table 2-2** shows reasonable consistency with the reference values, indicating towards correct representation of the capsules aerodynamics. Both pitching moment coefficients are fairly close to the theoretical value of $c_{m,y}$=0 for a stable trim point. Larger deviations are discovered for the stagnation point heatflux distribution. The stagnation point heatflux predicted by the Case 1 simulation exceeds the reference value derived from Marquardt et al. [1] by 59.36%. This deviation is found to be dependent on the turbulent flow configuration and the chosen viscous wall boundary condition. When considering the local Reynolds number on the heatshield, the load point exhibits laminar-turbulent transitional flow on the heatshield. However, no transition model is employed in the current study.

Table 2-2: Case 1 – Evaluation of aerodynamic coefficients and wall heat flux

	Reference	Case 1	Relative Error
$c_{m,y}$	-7.61×10^{-2}	2.912×10^{-3}	–
c_L	0.449	0.453	+0.89%
c_D	1.204	1.207	+0.25%
q_{STAG}	55000W/m^2	87648W/m^2	+59.36%

For the final version of this work, the wall heat transfer modeling of the equilibrium chemistry model thus is assessed in more detail by reviewing different wall conditions and comparison with analytical correlations by Tauber [3]. In addition, the non-equilibrium chemistry model for Case 2 is set up in order to reproduce the corresponding reference data presented by Marquardt et al. [1]. For the non-equilibrium chemistry model, a thermal equilibrium condition is assumed due to the limitation of the current work to the continuum flow regime. This allows for defining the non-equilibrium chemistry model by the number of mass equations to be solved and one temperature prescribing the thermodynamic degrees of freedom. Both cases are compared with the results of the Newton solver STRAT, allowing to review its predictions in terms of aerodynamic coefficients and aerothermal loads. The final version of the work concludes with a detailed study on the effects of thermochemistry on the wall heat transfer, comparing the equilibrium, non-equilibrium and the Newton method model on a representative 2D cylinder. The analysis is performed for multiple load points consistent with Virey et al. [2], allowing to further validate the obtained results. Therefore, the analysis are performed in multiple representative trajectory points as outlined in **Table 2-3**.

Table 2-3: Case 3 – Trajectory points for comparison of equilibrium, non-equilibrium and Newton method model

Case 3	h	Ma	v_∞	p_∞	T_∞	ρ_∞
Trajectory Point 1	70000m	20.30	60000m/s	5Pa	217.45K	7.00×10^{-5}kg/m^3
Trajectory Point 2	50000m	12.13	4000m/s	76Pa	270.65K	7.98×10^{-4}kg/m^3
Trajectory Point 3	30000m	6.63	2000m/s	1172Pa	226.65K	1.80×10^{-2}kg/m^3

The corresponding simulations are based on a similar setup with the preceding simulations in order to follow a consistent scheme throughout the validation process. This includes a RANS turbulence modeling approach and a hybrid tetrahedral and prism mesh that is adapted until the change in wall heat flux is considered negligible. As of special importance for non-equilibrium chemistry, also the influence of the wall catalysis model shall be investigated. The performed validation studies, combined with this final comparison over three additional trajectory points, shall allow for stating the range of applicability for each model and identify possible inconsistencies.

3. REFERENCES

[1] P. Marquardt, M. Fertig, T. Reimer and A. Gülhan, "EURASTROS capsule design and re-entry analysis," European Conference for Aeronautics and Space Sciences (EUCASS), 2022.

[2] C. Virey, J. Collinet and P. Brenner, "A review of industrial numerical methods for the simulation of hypersonic flight," in *57th 3AF International Conference on Applied Aerodynamics*, Bordeaux, 2023.

[3] M. E. Tauber, "A Review of High-Speed, Convective, Heat-Transfer Computation Methods," NASA Ames Research Center, Moffett Field, CA, 1989.

Mitteilung

Fachgruppe: Multidisziplinäre Optimierung

Parametric Aerodynamic Shape Optimization with Latent Diffusion

Long Chen, Jan Rottmayer, Tobias Kortus, Emre Özkaya,
Nicolas R. Gauger, Yinyu Ye

Chair for Scientific Computing, University of Kaiserslautern-Landau (RPTU)
Institute for Computational & Mathematical Engineering, Stanford University

{long.chen, jan.rottmayer, emre.oezkaya, nicolas.gauger}@scicomp.uni-kl.de
tobias.kortus@rptu.de
yinyu-ye@stanford.edu

Introduction

We present a data-informed parametric aerodynamic shape optimization method with latent diffusion. Generative models have shown success in shape design applications, where these models are often used as novel shape parameterization methods. We take a different perspective: instead of introducing new parameterization methods that substitute existing approaches, we empower existing approaches through a latent diffusion process. The construction of our method is based on the fact that virtually any shape parameterization method that maps between parameter space and shape space can be considered as a shape en/decoder. In this work, we demonstrate our method using aerodynamic shape optimization of airfoils. We use the Hicks-Henne method (HHM) for shape parameterization, the UIUC airfoil database as training data, SU2 as the CFD solver, and Bayesian Optimization as optimizer.

Method

We train a denoising diffusion model and use DDIM sampling for the reverse diffusion process G to generate HHM parameters x from coordinates z in the latent space,

$$G(z) = x.$$

Let X_G denotes the set of Hicks-Henne parameters generated by G,

$$X_G := \{x \mid x = G(z), z \in Z\},$$

where Z is some bounded set in the latent space. The figure below shows an illustration of X_G, possibly a manifold, that is embedded in the full Hicks-Henne parameter space X.
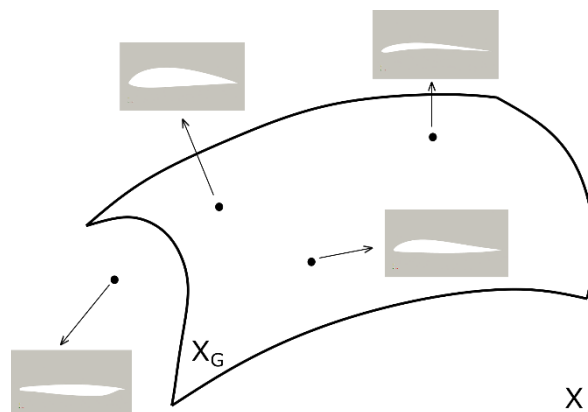

Fig 1: Illustration of a parameter manifold X_G embedded in the HHM parameter space X. Arrows denote the shape decoding processes.

We formulate a data-informed parametric shape optimization problem as

$$\begin{aligned} \min \quad & f(x), \\ \text{s.t.} \quad & c(x) \leq 0, \ x \in X_G, \end{aligned}$$

STAB

where $f\colon \mathbb{R}^n \to \mathbb{R}$ is the objective function, $c\colon \mathbb{R}^n \to \mathbb{R}^m$ are the constraints. The above optimization can be viewed as a Riemannian optimization, where the optimization variables are constrained to lie on a manifold. To solve the problem, we use the Bayesian Optimization method, which shows to be practical when the problem dimension is moderate. Specifically, we use BoTorch due to its strong support for GPUs. The function evaluations and mesh deformations are carried out using the open-source software SU2.

By using an existing parameterization method as the en/decoder, the effort required to integrate our method into existing design workflows is minimal compared to other generative model-based approaches. Moreover, rigorous comparisons between parameterization methods with and without generative models are possible, since the diffusion process does not change the parameter dimension. Finally, our proposed method has the potential for parametric design applications that are not limited to shape optimization.

Results

A key question to the practical usefulness of our proposed method is whether the manifold constraint can capture aerodynamically efficient shapes that are unseen in the training data. Our computational experiments provide an affirmative answer to this question. We demonstrate this using a constrained optimization problem under the flow condition of a Mach number of 0.8, and an angle of attack of 2.31°,

$$\min \quad Cd(x),$$
$$\text{s.\,t.} \quad Cl(x) \geq 0.5, \;\; t \geq 0.105, \;\; x \in X_G,$$

where t is the thickness of the airfoil. We perform RANS simulation with the Spalart-Allmaras turbulence model.
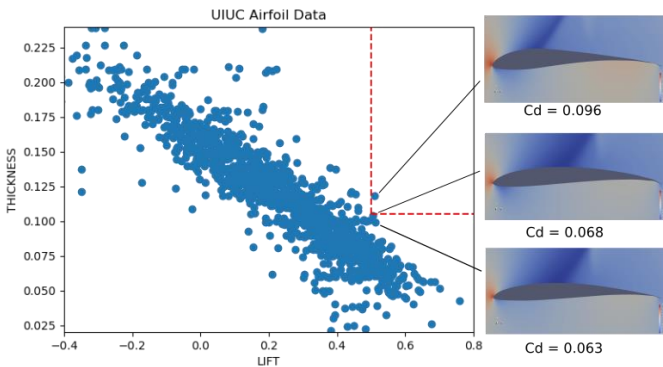
Fig 2: UIUC database airfoils evaluated in the design flow condition.

Fig 3: Optimized shape with diffusion constraint. Cl =0.50, t = 0.105, Cd = 0.038

Figure 2 shows sample evaluations of airfoils from the UIUC database, with the red lines representing the constraint boundaries. The constraints are set to be challenging, as only one training sample falls within the feasible set (top airfoil of figure 2). We also plot the flow solutions of two other samples that have the least constraint violations. Figure 3 shows the optimized shape using the presented method: it has a very different shape from the training samples on figure 2, and the drag is significantly reduced (0.038 compared to 0.068 and 0.063).

Outlook on Final Paper

We will present more extensive computational studies with different training data, diffusion architectures, and optimizations. Comparisons with other generative models, such as generative adversarial networks (GANs), are in progress. Investigations of the loss landscape with respect to the latent variables are of interest.

Literature

[1] Economon, Thomas D., et al. "SU2: An open-source suite for multiphysics simulation and design." *AIAA Journal* 54.3 (2016): 828-846.
[2] Ho, Jonathan, Ajay Jain, and Pieter Abbeel. "Denoising diffusion probabilistic models." *Advances in neural information processing systems* 33 (2020): 6840-6851.

STAB

Mitteilung

Fachgruppe: Multidisziplinäre Optimierung

Adjoint-based aerodynamic shape optimization with free laminar-turbulent transition

Daniela Gisele François[1], Andreas Krumbein[2]
[1,2] DLR, Institut für Aerodynamik und Strömungstechnik, C²A²S²E
[1]Lilienthalplatz 7, 38108 Braunschweig,
[2]Bunsenstraße 10, 37073 Göttingen
[1]daniela.francois@dlr.de

Introduction:
Aerodynamic shape optimization plays a critical role in aircraft design in order to achieve the desired operational performance. In this context, adjoint methods are already a common practice to efficiently compute the gradients of the predefined figure of merit, subjected to geometrical and physical constraints, that indicate the direction of the required shape modification to attain the optimal design. Laminar-turbulent transition is usually neglected during these processes to avoid the complications of adding the external modules that are usually needed to compute the transition prediction. However, the increased demand for cost-efficient aircraft designs and the growing awareness for global warming effects have shifted the attention towards natural laminar flow (NLF) aircraft designs [1], where transition becomes relevant. Optimization processes based on fully turbulent solvers may lead to very underoptimized NLF configurations. In addition, transition may also have a noteworthy impact on configurations with shock or flow separation, where its location affects the strength and location of both flow phenomena. The current availability of transition transport models (TTM) for predicting transition without the need of external modules, could enable considering this effect also in inverse design processes. Therefore, the design capabilities of the discrete adjoint solver of the DLR TAU code was extended to account for free transition effects by integrating the DLR γ TTM which was successfully coupled to the negative S-A turbulence model in [2].

Numerical Method:
The optimization problem consists in finding the design variables that minimize the figure of merit. This is,

$$\min_D I(W, X, D)$$

under the constraint

$$R(W, X, D) = 0,$$

where I is the cost function such as lift (L) or drag (D), W is the vector of flow variables, X is the mesh node coordinates, D is the vector of design variables, and R is the discretization of the flow governing equations. Since $R(W, X, D)$ and its derivative with respect to D are zero for all D, the derivative dI/dD, which indicate the minimization direction, can be found from the derivative of the Lagrangian, dL/dD, where

$$L = I + \Lambda^T R.$$

The adjoint vector Λ^T is computed by the adjoint solver by solving the linear adjoint equation,

$$\left(\frac{\partial R}{\partial W}\right)^T \Lambda = -\left(\frac{\partial I}{\partial W}\right)^T.$$

To consider free transition predicted by the DLR γ TTM coupled to the negative S-A turbulence model, the flow variables vector is extended to include the transition controlling variable γ, $W = [\rho\ u\ v\ w\ p\ \tilde{v}\ \gamma]^T$, and the same for R to include its transport equation R^γ, $R = [R^\rho\ R^u\ R^v\ R^w\ R^p\ R^{\tilde{v}}\ R^\gamma]^T$, where $R^{\tilde{v}}$ was also corrected according to the modifications of the coupling strategy. For further details on the implementation of the adjoint method and the DLR γ TTM the authors refer to [2,3].

STAB

Results:

The first validation results of the implementation of the DLR γ TTM into the adjoint solver of the DLR TAU code for shape design considering free transition was performed on the RAE2822 airfoil at M = 0.72, Re_c = 23·10^6, and Tu = 0.1%. Three design points, based on the lift coefficient (C_L = 0.27, C_L= 0.98, C_L = 0.33), were arbitrarily selected for the optimization. The optimization meant to minimize drag at constant lift by minimizing *I = -L/D*, while C_L is kept constant throughout the optimization process by adjusting the angle of attack, then $\alpha = \alpha(D)$. The shape parametrization is performed by a Hicks-Henne function with 9 design points on the upper and the lower surface of the airfoil, and the geometry volume reduction was constrained to avoid an excessive reduction of the airfoil thickness during the optimization. The optimization was performed for each design point independently and for a multi-point design by applying a weighted sum of the three design points. Figure 1 shows that the outcomes of the optimization processes result in configurations that actually improved their performance in accordance to the design conditions. The single-point optimized geometries return the larger reduction in drag at their design condition, although their performance may worsen for the off-design points (e.g. Opt. pt. 3 at the design points 1 and 2). On the other hand, the multi-point optimized geometry produces an overall better performance at expense of a slightly reduction of the drag drop compared to the single point design at the specific design points. In the final paper, it will be presented a full description of the optimization processes and mechanisms, as well as a detailed investigation of the benefits of considering transition during the optimization.
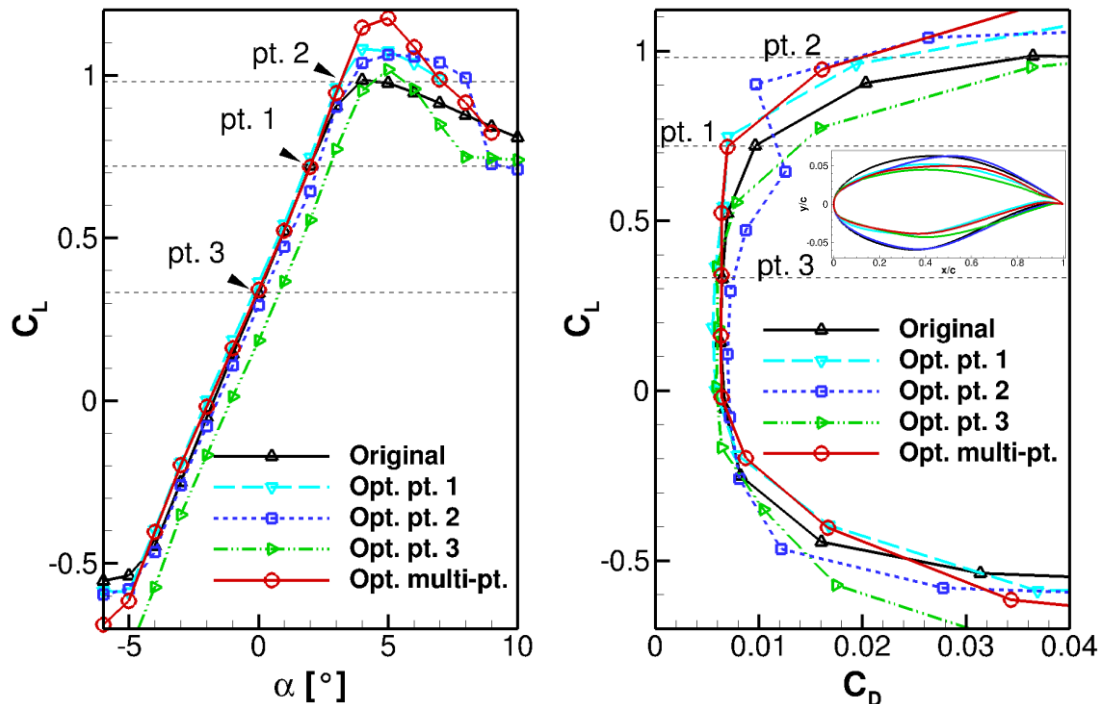
Figure 1: Comparison of Aerodynamic polars between the initial geometry (original), the single point optimized geometries (Opt. pt. 1,2, and 3), and the multi-point optimized geometry (Opt. multi-pt.).

Reference:

[1] Green, J. E., "Laminar Flow Control - Back to the Future?", 38th Fluid Dynamics Conference and Exhibit, AIAA Paper 2008-3738, 2008. https://doi.org/10.2514/6.2008-3738

[2] François, D. G., Krumbein, A., "On the Coupling of a γ-based Transition Transport Model to the Negative Spalart-Allmaras Turbulence Model", 56th 3AF International Conference on Applied Aerodynamics, FP36-AERO2022-francois, 2022.

[3] Brezillon, J. und Dwight, R. (2005) *Discrete Adjoint of the Navier-Stokes Equations for Aerodynamic Shape Optimization.* EUROGEN 2005, 2005 Sep 12-14, Munich, Germany.

STAB

Mitteilung

Fachgruppe: Multidisziplinäre Optimierung

Multidisciplinary Design Methods for Fixed-Wing UAVs and the Application to the Air Cargo Challenge 2024

Jannik Frank, Yannick Schäfer, Tjalf Stadel and Gregor Zwickl
Universität Stuttgart / Akamodell Stuttgart e.V.,
Pfaffenwaldring 35, 70569 Stuttgart, jannik.frank@akamodell.de

Introduction

With the rising market for unmanned aerial vehicles (UAVs), the development of advanced design methods is becoming increasingly important [1]. Traditional approaches, focused either on aerodynamics or payload, are insufficient when no precise Top Level Aircraft Requirements are given. This work presents a design methodology for a fixed-wing UAV developed for the Air Cargo Challenge 2024, where the design payload mass as well as the aircraft geometry are degrees of freedom. Design parameters must be selected to maximize one overall figure of merit, in this case the competition scoring. Therefore, a holistic approach of combined aerodynamic, structural, propulsive and trajectory optimization is required [2]. Instead of numerical optimization, extensive parametric studies are employed to determine sensitive parameters and identify global optima, thereby maximizing UAV performance. The application and validation of this method are demonstrated through Akamodell Stuttgart's successful participation in the Air Cargo Challenge (ACC) 2024. In the competition, takeoff distance, maximum payload, efficiency, and top speed of a UAV with a specified propulsion system are considered in the scoring [3]. Due to conflicting requirements of these aspects, trade-off studies at an overall aircraft design level are necessary. This paper describes the methodology and its validation with literature, wind tunnel tests, and flight test data of previous aircraft. Finally, the flight performance of the ACC 2024 aircraft designed with this methodology is compared to the calculated values, resulting in good agreement.
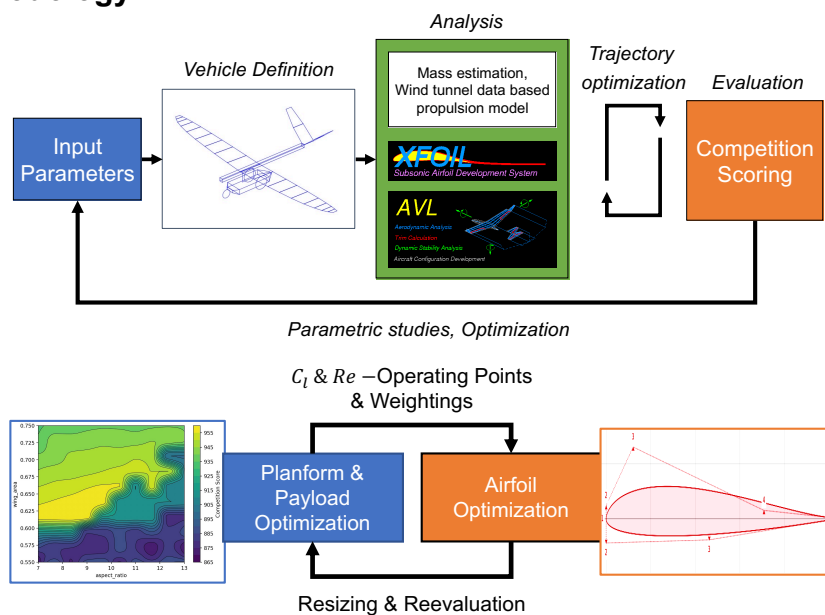
Design Methodology

Fig. 1: Design workflow: Overall aircraft sizing and iterative airfoil optimization

The design tool used conducts a recalculation for a given aircraft geometry, calculating flight performance, and evaluating it based on the calculated score according to the competition

regulations. The aerodynamic model is based on a combination of AVL [4] and XFOIL [5]. Drag of additional components is estimated with handbook methods and calibrated using wind tunnel data. Wind tunnel tests were also conducted to determine the thrust for the specified propulsion system for different propellers as a function of the airspeed. The described models are used to determine the relevant flight performance according to the competition regulations. The parameters describing the vehicle were minimized to a significant set of design variables, allowing for parametric studies to be conducted and the impact on the competition score to be investigated. In addition to the geometric parameters, the feasibility of a retractable Fowler flap and retractable landing gear was examined. This required weighing the additional mass against drag reduction and the increase in maximum lift coefficient and analyzing the impact on the optimized overall aircraft. Once a sensible parameter combination of payload, wing area, aspect ratio, propeller, and catalog airfoil was determined, the design was further optimized in a second iteration. Here, the wing geometry and airfoil were iteratively optimized. Airfoil optimization was conducted using Xoptfoil-JX [6], following a design-by-polar approach. Optimization focused on operating points (in terms of Reynolds number and C_l combinations) according to the optimized mission trajectory, resulting directly from the design tool. Additionally, the weighting of individual operational points was determined through sensitivity studies of the airfoil performance on the competition score.

Flight Testing

Using the described methodology, an appropriate configuration was selected, and an optimized parameter set was determined. The result was a design with retractable landing gear and moderate wingspan with comparably low aspect ratio, featuring a relatively thin airfoil with 7% relative thickness, a high maximum lift coefficient, and low drag in the tailored laminar bucket. The model was then constructed using lightweight composite materials and successfully tested in the competition. Figure 2 shows the good agreement of calculated and measured flight performances.
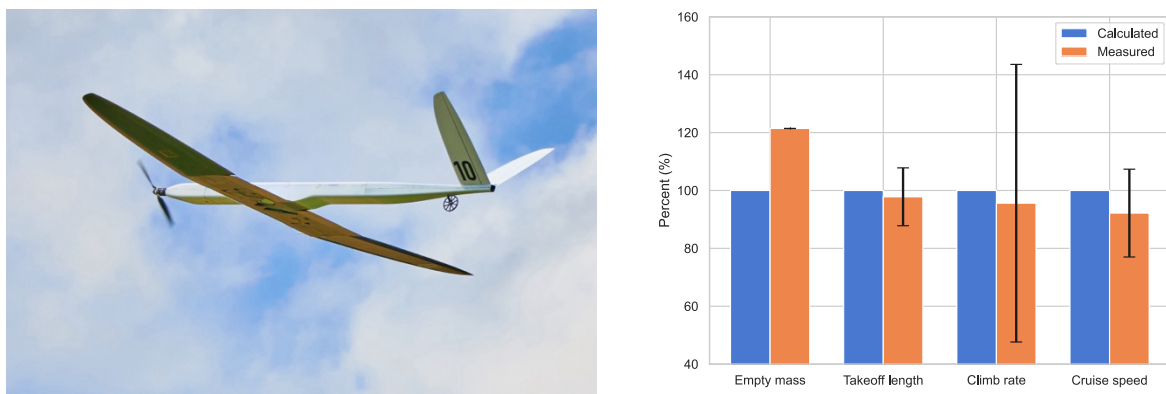
Fig. 2: Aircraft in flight (left) and its performance comparison (right)

Literature

[1] R. Austin, Unmanned Aircraft Systems: UAVS Design, Development and Deployment, John Wiley & Sons, 2011.

[2] N. Matos und A. Marta, „Concurrent Trajectory Optimization and Aircraft Design for the Air Cargo Challenge Competiton,“ *Aerospace,* 2022.

[3] ADDI, „Air Cargo Challenge 2024 Participation Handbook,“ 2024. [Online]. Available: https://aachen-drone.com/wp-content/uploads/2024/05/Rules-ACC24-v1_3.pdf.

[4] M. Drela, „AVL,“ 2024. [Online]. Available: https://web.mit.edu/drela/Public/web/avl/.

[5] M. Drela, „XFOIL: An Analysis and Design System for Low Reynolds Number Airfoils,“ *Low Reynolds Number Aerodynamics: Proceedings of the Conference Notre Dame, Indiana, USA,* pp. 1-12, June 1989.

[6] J. Günzel, „Xoptfoil-JX,“ 2022. [Online]. Available: https://github.com/jxjo/Xoptfoil-JX.

STAB

Mitteilung

Fachgruppe: Multidisziplinäre Optimierung

Hybrid B-Spline-Targets Airfoil Parametrization with a Direct Link to CAD-based Aircraft Geometry

Časlav Ilić[†], Patrick Wegener

German Aerospace Center (DLR)
Institute of Aerodynamics and Flow Technology, Lilienthalplatz 7, 38108 Braunschweig
[†]Corresponding author, `caslav.ilic@dlr.de`

In the field of aircraft aerodynamic and multi-disciplinary design, especially where formal optimization methods are involved as well, there is a neverending quest for the most problem-suitable parametrized description of airfoils. With advent of computer-based design (CAD), it became possible to reperesent airfoils by higher-order polynomial-basis curves, such as b-splines or NURBS. For rubber-like deformation of basic shapes, a popular parametrization method is FFD [3]. More tuned to airfoil shape requirements are PARSEC [4] and CST [2].

Aerodynamically and structurally significant airfoil geometric quantities include thickness, camber distribution, nose radius, trailing edge thickness, or curvature distribution. Some of the mentioned parametrization methods do not, by themselves, represent any of those quantities (b-splines, NURBS), while other make some effort to do so (PARSEC, CST). All these methods are also *explict* methods, where for the given set of inputs, the output shape (discretized airfoil surface points) is computed by direct application of a set of formulas.

In this work instead an *implicit* airfoil parametrization method is proposed, called hybrid b-spline-targets (HBT). Assuming a CAD system (here Dassault CATIA) provides standard b-spline curves, within that system the airfoil lower and upper surface may be represented by b-splines. The design parameters within the CAD system are thus the coordinates of the b-spline control points. Externally to the CAD system, a system of equations is solved, that performs an invertible (bijective) transformation between the CAD control-point coordinates on the one side, and the significant set of airfoil geometric quantities on the other side. Specifically, overall thickness, nose radius, and separate camber and thickness distribution parameters are considered. Internal unknowns in the system are coefficients to a set of "bump" functions (not entirely unlike test functions in a finite-element method). Thus, a human designer or an optimization algorithm can use the significant airfoil geometric quantities directly as design parameters, while losslessly maintaining the quality of the geometry representation provided by the CAD system. In the full paper the mathematical construct will be shown in detail.

In a recent work by the authors [1], the HBT parametrization was applied to improving wing design of the DLR-F25 configuration. This configuration was developed within the LuFo VI-2 project VirEnfREI funded by the German Ministry for Economic Affairs and Climate Action (BMWK). It was important that any improvement in performance, i.e. lift-to-drag ratio, were not detrimental to structural weight, through modified section overall thickness or spanwise load distribution, or to high-lift characteristics, through modified nose radius. Thus only the thickness distribution offsets were set as design parameters, of which there were 9 for each of the 6 selected wing sections, resulting in a total of 54 parameters. A 10 million point mesh of the DLR-F25 wing-body-HTP configuration was generated by the commercial ANSA mesh generator (fig. 1). The flow and discrete-adjoint gradients were computed by the DLR TAU flow solver. The optimization algorithm was SNOPT. Initial and optimized configurations are compared on figures 2, 3, and 4. While thickness and nose radius were fixed by construction, the spanwise load distribution (fig. 3) changed very little, due to fixed camber shape. This small change is a pure non-linear, transonic effect, which would not be detected by linear aerodynamic methods (such as used e.g. for computing design loads for structural sizing).

In the final paper this result will be compared to a more conventional optimization, where the design parameters will be directly the b-spline control point coordinates (19 per wing section, for a total of 114 parameters), and the thickness, nose radius, and camber shape test points will be presented as explicit equality constraints to the optimization algorithm (10 per section, for a total of 60 constraints).
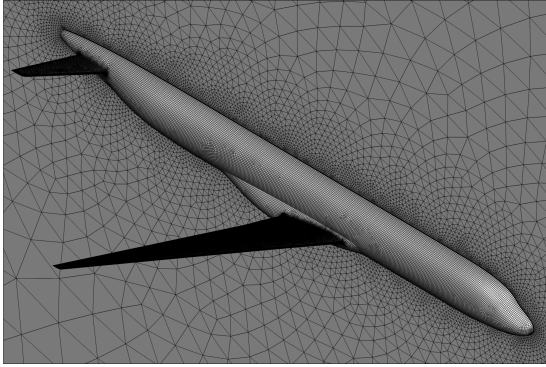
Figure 1: Hybrid-unstructured mesh of the wing-body-HTP DLR-F25 configuration.
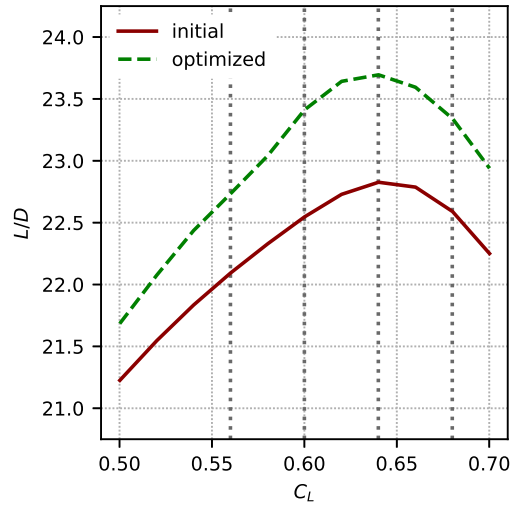
Figure 2: Lift-to-drag polars.
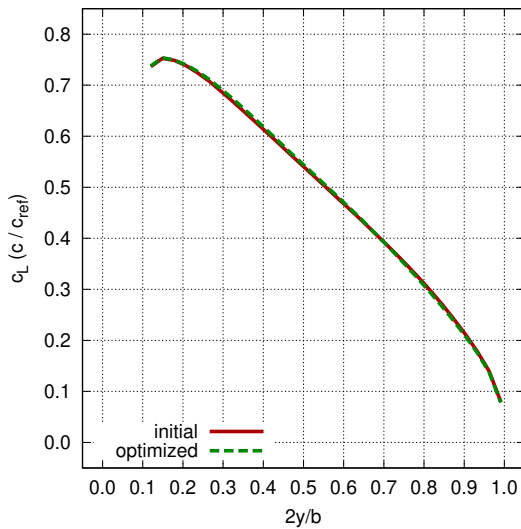
Figure 3: Spanwise load distribution.
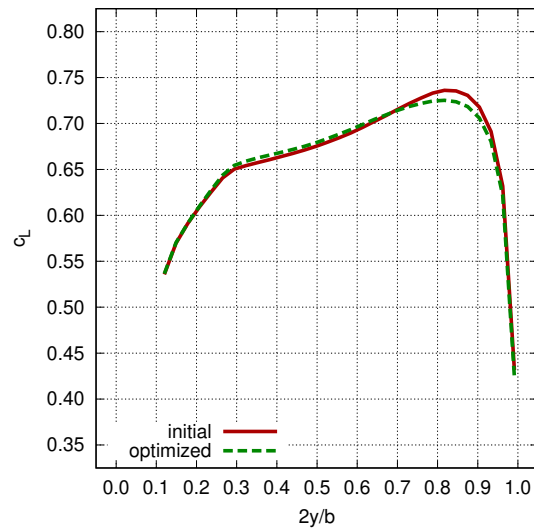
Figure 4: Spanwise lift coeff. distribution.

References

[1] C. Ilic, P. Wegener, J. Ruberte Bailo, J. Himisch, S. Geisbauer, T. Wunderlich, and M. Abu-Zurayk. Phased high-fidelity aerodynamic design from scratch of a very high-aspect ratio narrow-body airliner. In *AIAA Aviation 2024*, 2024.

[2] B. M. Kulfan and J. E. Bussoletti. "Fundamental" parametric geometry representations for aircraft component shapes. In *11th AIAA/ISSMO Conference*, 2006.

[3] A. Ronzheimer. Shape based on freeform deformation in aerodynamic design optimization. In *ERCOFTAC Design Optimization International Conference*, 2004.

[4] H. Sobieczky. Parametric airfoils and wings. *Notes on Numerical Fluid Mechanics*, 68, 1998.

Mitteilung

Fachgruppe: Multidisziplinäre Optimierung

Generalized Derivative Enhanced Surrogate Modeling Framework
for Aerodynamic Design Optimization

Emre Özkaya, Nicolas R. Gauger
Chair for Scientific Computing, University of Kaiserslautern-Landau (RPTU)
{emre.oezkaya, nicolas.gauger}@scicomp.uni-kl.de

Introduction

We present a derivative-enhanced Gaussian Process Regression (GPR) surrogate model designed for aerodynamic design optimization. The proposed model incorporates arbitrary directional derivatives of an objective function alongside the functional values during model training. By leveraging this additional derivative information, the surrogate model is better equipped to capture the true tendencies in the data, effectively mitigating the issue of over-exploration commonly encountered in the Bayesian optimization framework. This approach ensures more accurate and reliable predictions, ultimately enhancing the efficiency of the optimization process.

Method

The starting point is the generic design optimization problem, where an expensive objective function must be minimized or maximized, subject to box constraints on the design variables and inequality constraints that may also be costly to evaluate. With advancements in algorithmic differentiation, it is often possible to utilize tangent or adjoint solvers capable of evaluating gradient vectors or directional derivatives for the objective function and/or some constraints. However, due to technical limitations, this derivative information may not always be available for the objective function or certain constraints. Therefore, it is crucial to develop a method that can adapt flexibly to these scenarios, ensuring robust and efficient optimization even when complete derivative information is not accessible.

The proposed method builds upon the Gaussian Process Regression (GPR) model, also known as Kriging, by incorporating derivative information into the training process. Unlike the well-known Gradient Enhanced Kriging method [1], which relies on full gradient information, the new approach utilizes directional derivatives at selected samples. This choice significantly reduces the size of the correlation matrix, thereby decreasing the computational burden during model training. Additionally, the new method results in much better-conditioned matrices, which enhances the robustness of the model. For the Bayesian optimization process, which is established in Efficient Global Optimization (EGO) framework, we integrate the derivative-enhanced model with a trust region strategy to mitigate overfitting and prevent the optimization algorithm from getting trapped in local minima. A similar strategy is used in classical Bayesian optimization with only functional values in the training data [2].

Results

The proposed method was evaluated on a modified version of a generic aerodynamic shape optimization problem available in the SU2 framework [3]. The test case involves minimizing the drag of a NACA0012 airfoil under transonic flow conditions, with constraints on lift and cross-sectional area. The airfoil shape is parameterized using Hicks-Henne bump functions applied to both the suction and pressure sides to generate deformed shapes. The gradients

STAB

of the drag coefficient with respect to the shape parameters were computed using the discrete adjoint solver in SU2.

During the Design of Experiments (DoE) phase, 300 samples were used to generate the training data for drag, lift, and cross-sectional area. At this stage, all computations were performed using the classical solver without the adjoint approach. These DoE samples are represented by blue dots in the accompanying figure, where the x-axis shows the negative drag coefficient (-CD) and the y-axis shows the lift coefficient (CL) of the samples generated during the process. Additional samples generated by the Efficient Global Optimization (EGO) algorithm are indicated by orange dots. The lift constraint, specified to be slightly lower than the lift of the initial airfoil (0.72), is shown as a green dashed line in the figure.

The optimization process achieved a significant reduction in drag (from 0.01344 to 0.00209) while maintaining lift and cross-sectional area above the specified limits of the inequality constraints. Due to the selective local search strategy within the trust region, only 32 adjoint evaluations were necessary during the optimization. All other samples were generated using the primal solver, which incurs a lower computational cost.
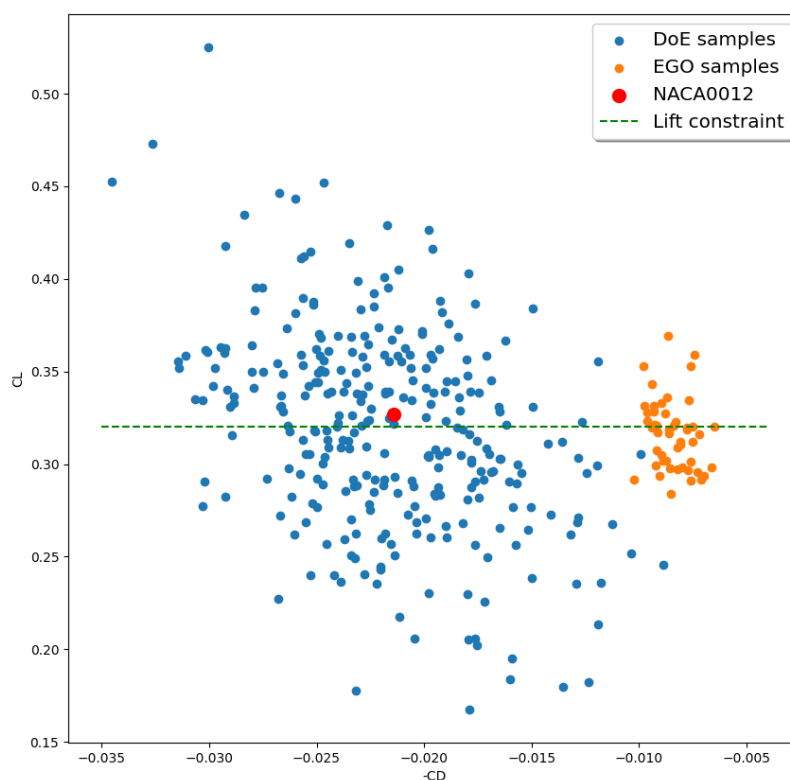
Literature

[1] Zhong-Hua Han, Stefan Görtz, Ralf Zimmermann, Improving variable-fidelity surrogate modeling via gradient-enhanced kriging and a generalized hybrid bridge function, Aerospace Science and Technology,Volume 25, Issue 1, 2013, Pages 177-189, https://doi.org/10.1016/j.ast.2012.01.006.

[2] David Eriksson, Michael Pearce, Jacob Gardner, Ryan Turner, Matthias Poloczek, 2019. Scalable Global Optimization via Local Bayesian Optimization. Proceedings of the 33rd International Conference on Neural Information Processing Systems, Article No.: 493, Pages 5496 – 5507.

[3] https://su2code.github.io/tutorials/Inviscid_2D_Unconstrained_NACA0012/

STAB

Mitteilung

Fachgruppe: Multidisziplinäre Optimierung

Sobolev Training for BNN Surrogates in Efficient Global Optimization

Jan Rottmayer, Long Chen, Emre Özkaya and Nicolas R. Gauger

Chair for Scientific Computing, RPTU Kaiserslautern-Landau
Paul-Ehrlich-Str. 34, 67663 Kaiserslautern, Germany
{jan.rottmayer, long.chen, emre.oezkaya, nicolas.gauger}@scicomp.uni-kl.de

Introduction

This paper presents a gradient-enhanced neural network surrogate model specifically designed for aerodynamic shape optimization (ASO). Bayesian Neural Network (BNN) surrogates propose a solution to the scaling problem found in the commonly used Gaussian Process (GP) surrogates. Leveraging recent advances in adjoint solvers, we integrate Bayesian Neural Network (BNN) surrogates with Sobolev Learning [1], allowing the incorporation of derivative information to enhance surrogate training efficiency.

In this work, we analyse the predictive capabilities of the gradient enhanced BNN model on a shape deformation dataset, generated using SU2, and demonstrate the utility of our approach in Efficient Global Optimization [2] for an ASO problem.

Methods

BNNs extend the standard neural network ansatz by introducing model uncertainty typically through a prior on the parameter space of the neural network. A practical approach involves using the well-established dropout mechanism to achieve an approximate Bayesian formulation. In the adapted dropout, each neuron (or unit) in a layer is retained with a probability p independently of other neurons during both training and inference. For a given layer l the dropout mask $D^{(l)}$ is a binary vector where each element follows a Bernoulli distribution. The model's prediction is defined through an empirical distirbution obtained from T forward passes with independent dropout masks, essentially approximating the true posterior through Monte-Carlo sampling. This, so called Monte-Carlo dropout prediction, can be seen as predicting with sub-networks sharing weights.

Contrary to classical learning approaches for neural networks, we consider a gradient enhanced approach using Sobolev spaces. Sobolev Learning minimizes a loss function that considers both function values and their first-order derivatives, enhancing model training. Let L denote the loss function, m the NN model parametrized by θ and d be the design space dimension. Then, the standard empirical error minimization:

$$\sum_{i=1}^{N} \left\{ L\big(m(x_i|\theta), f(x_i)\big) \right\}$$

is adapted to account for derivative errors:

$$\sum_{i=1}^{N} \left[L\big(m(x_i|\theta), f(x_i)\big) + \sum_{j=1}^{d} L\left(\nabla_j m(x_i|\theta), \nabla_j f(x_i)\right) \right]$$

enabling the model to match the target function's derivatives as well. This adaptation can also be seen as regularization in the standard formulation when introducing a weighting term in front of the derivative error.

In combination, the proposed model has the potential to lower the training costs, specifically in the high-data regime, while extending training to include possibly available derivatives. Further,

STAB

due to the natural connection between BNN and GP models [3], the replacement in the EGO framework is straight forward. Furthermore, the proposed gradient enhancing for BNNs avoids the poor scalability of gradient enhanced GP models, thus making them more suitable for high-dimensional design problems.

Numerical Results

We setup a dataset consisting of 1800 RAE shape design samples. In each experiment, we sub-sample the dataset to get train data and take the remainder as test data. We train a GP, BNN and BNN with Sobolev learning on the training data, evaluate predictions on test data and repeat the experiment 10 times to assure resistance to outliers. The Gaussian Process model uses a typical Matern 5/2 kernel function and is tuned with maximum likelihood estimation (MLE). Furthermore, both BNN models use the same multi-layer perceptron skeleton consisting of two hidden layers of dimension 64, a dropout probability of 0.4 on the last hidden layer and SiLU activation. The number of training iterations for the BNN models is kept constant.
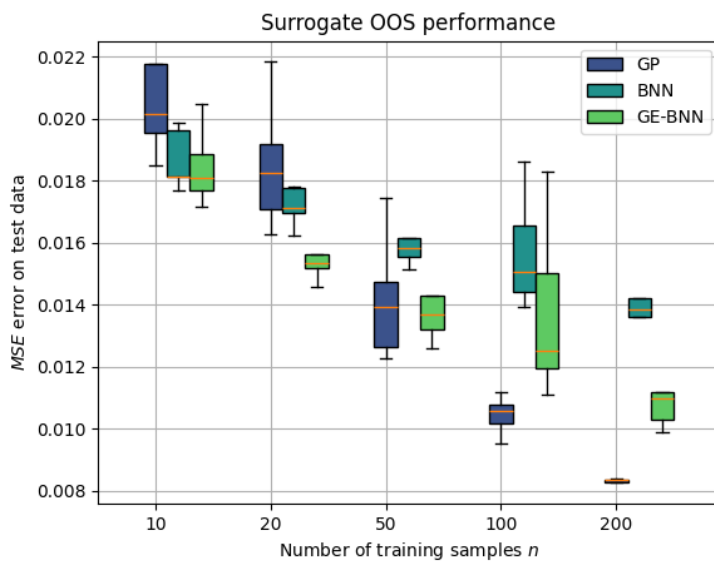

Figure 1: Surrogate out-of-sample (OOS) benchmark for RAE shape deformation dataset.

Figure 1 shows the results of the surrogate benchmark. In low-data scenarios, the BNN and GE-BNN models outperformed the classical GP model, although the overall performance of all models was comparable. With increasing number of training samples, the performance of the GP model overtakes the GE-BNN and BNN models, which is attributed to the lack of increase in training iterations for the neural network models. Additional investigations are necessary to draw definitive conclusions. Overall, all three models exert similar performance, which fortifies its potential utilization in EGO due to the superior scaling properties of both, the BNN and gradient enhanced BNN surrogate.

Full Paper Outlook

We plan to present results from an ASO problem, focusing on RAE shape optimization under transonic conditions, utilizing the SU2 flow solver and RANS simulations. We will also add comparisons to the widely used GEK model and the respective optimization traces and expand on the model comparison to allow more detailed analysis on the scalability prospect.

Literature

[1] Czarnecki et.al., "Sobolev Training for Neural Networks", arXiv:1706.04859
[2] Jones, D.R., Schonlau, M. & Welch, W.J. Efficient Global Optimization of Expensive Black-Box Functions. Journal of Global Optimization 13, 455–492 (1998). https://doi.org/10.1023/A:1008306431147
[3] Wilson, A. G., and Izmailov, P., "Bayesian deep learning and a probabilistic perspective of generalization," Proceedings of the 34th International Conference on Neural Information Processing Systems, Curran Associates Inc., Red Hook, NY, USA, 2020.

STAB

Mitteilung

Fachgruppe: Numerische Aerodynamik

A Simplified Actuator Line Implementation for the DLR TAU-Code

Mário Firnhaber Beckers, Michael Schollenberger and Thorsten Lutz
University of Stuttgart, Institute of Aerodynamics and Gas Dynamics (IAG),
Wankelstraße 3, 70563 Stuttgart, Germany
mario.firnhaber-beckers@iag.uni-stuttgart.de

In the research field of aerodynamic propeller-wing interactions, both steady-state and unsteady effects can be observed. Steady-state interaction effects are the result of mean flow interactions, e.g. the propeller thrust accelerating the flow leading to increased dynamic pressure inside the slipstream and thus to increased lift of wing segments located inside the slipstream [1]. These effects can be captured well with steady-state simulations and propeller models like the Actuator Disk (ACD) model [2]. The unsteady interaction effects mainly result from the unsteady slipstream of the rotating propeller blades (featuring effects such as blade tip vortices), which can be reproduced in CFD simulations by either directly resolving the rotating blades inside the simulation or by modelling the unsteady forces. Different methods are available to model the unsteady propeller forces, but the Actuator Line (ACL) model is likely the most common. In wind turbine research this model has been extensively applied, e.g. by Mikkelsen [3]. Simply put, in the ACL model the rotor reaction forces are calculated only for specific lines that each represent one individual blade. The forces are then introduced locally into the flow as volumetric force terms, generally with a smoothing function to avoid large discontinuities.

In 2020, Schollenberger [4] implemented a boundary condition based ACL into the DLR TAU-Code [5]. At its core it is a modification of the ACD model implemented into TAU by Raichle [2]. However, this modification which follows common ACL approaches is quite complicated code-wise and can lead to problems in a high performance computing environment. In the proposed paper a new ACL implementation for the TAU-Code is presented and validated. The new implementation is also a modification of the ACD, however a comparatively simple one that makes greater use of the existing ACD functions as a basis (as well as the existing overall TAU framework) and consists of only two fundamental changes, visualized in Figure 1: 1) the implementation of a rotating "mask" to highlight the discrete blades and 2) the use of mean flow variables instead of the time-accurate flow variables to determine the local flow angle used in the calculation of the force reaction.
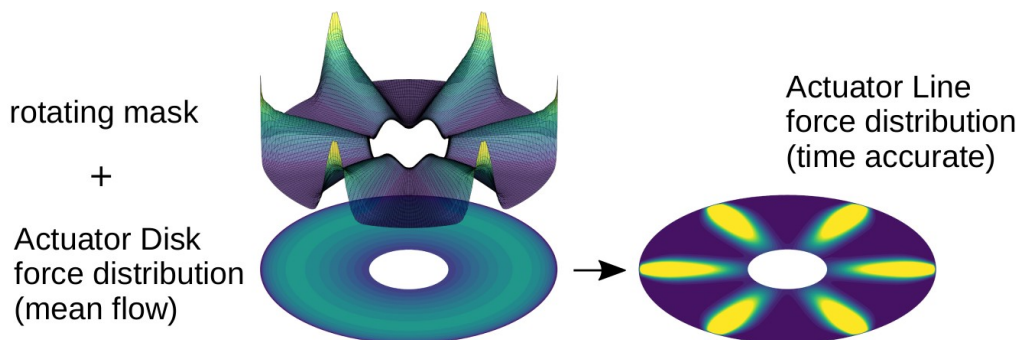

rotating mask

+

Actuator Disk
force distribution
(mean flow)

Actuator Line
force distribution
(time accurate)

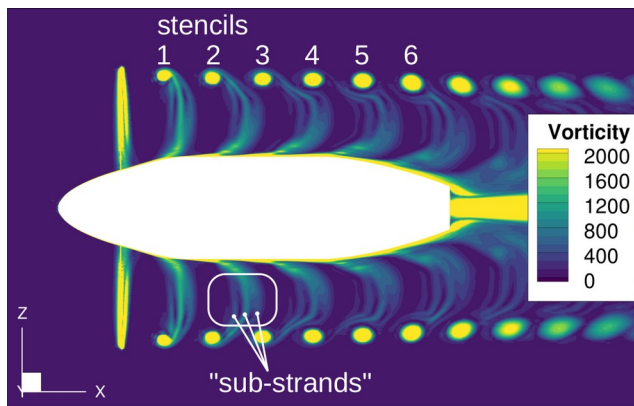Figure 1: Visualization of the principle of the simplified ACL implementation.

STAB

Figure 2: Propeller slipstream vorticity. Stencils of blade tip vortices crossing the Y=0 plane (1-6, one per blade) and division of blade wake into „sub-strands" highlighted.
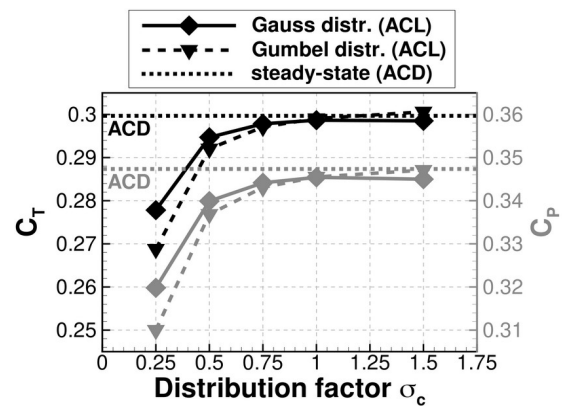
Figure 3: Influence of ACL distribution factor and function (Gauss / Gumbel): Thrust coefficient C_T in black and power coefficient C_P in grey. Steady-state ACD results for reference.

Figure 2 shows the vorticity inside the slipstream obtained in a simulation with the new ACL implementation, showcasing the ability to capture the unsteady blade tip vortices and the blade wake. A preliminary parameter study was carried out in order to determine parameter sensitivities and initial best practices for the new ACL implementation. The distribution factor σ_c, shown in Figure 3 alongside the distribution function, was found to be the parameter with the strongest impact. Additionally, the flow averaging interval, the time step, the circumferential resolution were varied.

The full paper will feature a direct comparison between the new ACL implementation and the existing one. They will be compared with respect to the obtained results of the integral coefficients, the unsteady slipstream as well as the computing performance. Both implementations are applied in test cases from Nederlof [6], which allows for additional validation due to the included phase-averaged flow field data of the slipstream.

Acknowledgments

References

[1]   Veldhuis LLM (2005) Propeller wing aerodynamic interference. PhD thesis, Delft University of Technology

[2]   Raichle A, Melber-Wilkending S, Himisch J (2007) A New Actuator Disk Model for the TAU Code and Application to a Sailplaine with a Folding Engine. vol 96, DOI 10.1007/978-3-540-74460-3 7

[3]   Mikkelsen R (2004) Actuator disc methods applied to wind turbines. PhD thesis

[4]   Schollenberger M, Lutz T, Krämer E (2020) Boundary Condition Based Actuator Line Model to Simulate the Aerodynamic Interactions at Wingtip Mounted Propellers. pp 608–618, DOI 10.1007/978-3-030-25253-3 58

[5]   Schwamborn D, Gerhold T, Heinrich R (2006) The DLR TAU-Code: Recent Applications in Research and Industry. URL https://elib.dlr.de/22421/

[6]   Nederlof R, Ragni D, Sinnige T (2022) Experimental investigation of the aerodynamic performance of a propeller at positive and negative thrust and power DOI 10.2514/6.2022-3893

STAB

Mitteilung

Fachgruppe: Numerische Aerodynamik

Turbulence-resolving simulations of a coaxial jet based on Reynolds stress modelling

Marius Herr, Axel Probst
DLR, Institut für Aerodynamik und Strömungstechnik
Bunsenstraße 10, 37073 Göttingen, marius.herr@dlr.de, axel.probst@dlr.de

Introduction

In the present work, the flow of a coaxial engine with an inner, heated core stream and a surrounding cold bypass stream is simulated at transonic flow conditions using a scale resolving simulation technique. The rotationally symmetric engine geometry has a central body and an industrially relevant short cowl engine exhaust design (cf. Fig. 1.). It originates from the CoJeN (Computation of Coaxial Jet Noise) project, funded by the European Union, which generated a database for coaxial jet flows. This database is used to benchmark our own results. Our work is funded by the German research organisation (DFG) and is part of the research unit FOR2895. One aim of the research unit is to simulate transonic flow about a transport aircraft configuration with an Ultra High Bypass Ratio engine and jet streams. We are particularly interested in whether and how an engine jet influences the dynamics of transonic shock fronts and whether it can trigger shock oscillations about the wing that are critical to flight safety (shock-buffet). As a preliminary step for the full aircraft-engine configuration with jet streams (for which no experimental data will be available), the present work is aimed to qualify and validate our method on a generic coaxial jet flow.
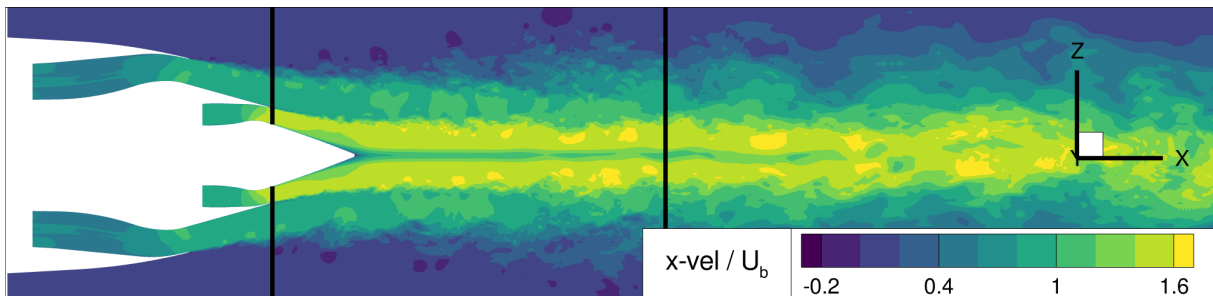
Figure 1: *Slice with streamwise velocity snapshot from an RSM-IDDES simulation of the co-axial CoJeN jet. The velocity is normalized with the nozzle exit velocity of the bypass stream U_b. The black lines indicate the profile positions of Figure 2.*

The complexity of unsteady transonic flow phenomena around the target aircraft configuration (not part of this publication) requires a turbulence resolving simulation technique for preferably accurate numerical results. Since direct numerical simulation (DNS) and even large eddy simulations (LES) are computationally not manageable for the simulation of the entire configuration, we selected a more affordable hybrid RANS/LES technique which is based on the IDDES approach. Due to the complex corner regions at the engine-pylon as well as pylon wing intersections, a sophisticated RANS background model based on Reynolds stress modelling is employed [1]. This RSM-based IDDES has already been successfully applied to the same aircraft configuration with through flow nacelles [2]. In this work, the RSM-IDDES method is for the first time applied to a realistic engine flow with jet.

Proceeding and Results

As can be seen in Figure 1, the engine jets are prescribed within the engine at two annular boundaries. There, total pressures and total temperatures for the core and bypass jets are specified independently of each other. Furthermore, the turbulent intensity is also specified at the engine boundaries on the basis of experimental reference data. The latter is in contrast to

other publications in this field, in which a definition of the boundary condition of the turbulent intensity is either not given or not calibrated with the aid of experimental reference data [3].
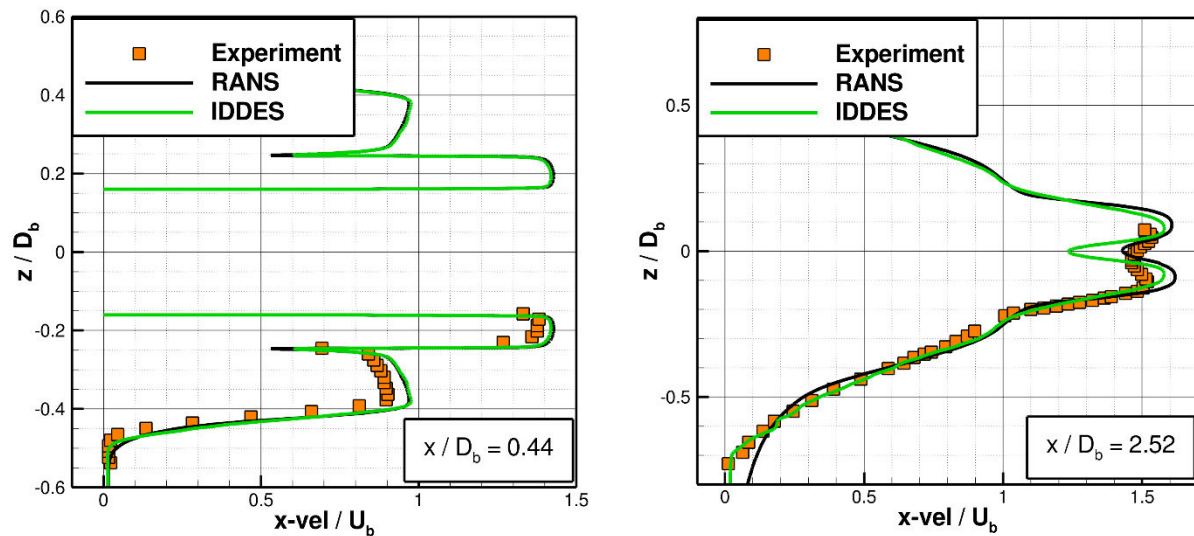

Figure 2: *Radial normalized x-velocity profiles of the jet at two different x – positions for a RSM - RANS and a temporal averaged RSM-IDDES solution with reference data [3].*

A hybrid mesh with 55 million points was constructed for the turbulence resolving simulations. Structured, highly resolved mesh regions are located in the vicinity of the engine as well as in the area of the jet flow, while an unstructured, coarse mesh is present in the far field. The local cell size is locally limited to 1/20 of the local geometric length scale (nozzle or jet diameter), which corresponds to the common LES meshing criterion for free shear flows. For the rotationally symmetric mesh, 450 points are used in circumferential direction, resulting into isotropic cells at the trailing edges of the engine and thus providing high resolution in these critical areas. Concerning the modes of the IDDES method, the DDES mode is active in the area of the engine close to the wall in such a way that the turbulent boundary layers are treated in RANS mode. Downstream of the trailing edges, the IDDES method automatically switches to LES mode. Starting from the trailing edges, the LES mode spreads out in a wedge shape in the direction of flow so that the entire flow is rapidly captured by LES.

Figure 2 presents radial velocity profiles at two positions in streamwise direction (see also Figure 1) of RSM - RANS and RSM - IDDES solutions. The early profile at $x / D_b = 0.44$ (D_b : bypass diameter) demonstrates very good agreements with experimental data [3] for both simulations. For a position further downstream, the agreements of both simulations are still acceptable. However, the IDDES simulation features a distinct drop in velocity in the wake region of the central body. In the final paper, it will be demonstrated that this drop can be attributed to a lack of turbulent mixing in the respective wake flow which can be avoided by the appropriate use of local, synthetic turbulence injection. Additionally, the publication will contain a detailed description and analysis of the different scale-resolving simulations and their sensitivities, providing velocity and Reynolds stress profiles and their comparison to experimental data at various positions.

References

[1] HERR, Marius; RADESPIEL, Rolf; PROBST, Axel. Improved Delayed Detached Eddy Simulation with Reynolds-stress background modelling. Computers & Fluids, 2023, 265. Jg.,S. 106014.

[2] SPINNER, Sebastian, et al. Scale Resolving Simulation of Wing Lower Surface Buffet Effects Induced by the Installation of a UHBR Nacelle. In: AIAA AVIATION FORUM AND ASCEND 2024. 2024. S. 4264

[3] YAN, Jianping, et al. Computation of Jet Noise using a Hybrid Approach. In: 13th AIAA/CEAS Aeroacoustics Conference (28th AIAA Aeroacoustics Conference). 2007. S.3621.

STAB

Mitteilung

Fachgruppe: Numerische Aerodynamik

Robustness, accuracy and efficiency of the discontinuous Galerkin spectral element method under local mesh refinement in an industrial CFD solver

Miquel Herrera, Ralf Hartmann

German Aerospace Center (DLR),
Institute of Aerodynamics and Flow Technology,
Lilienthalplatz 7, 38108, Braunschweig

miquel.herrera@dlr.de, ralf.hartmann@dlr.de

The aerospace industry is interested in scale-resolving simulations (SRS) with shortened time to solution. Work is underway at the DLR to develop a "rapid SRS" process chain, which combines: 1) automatic mesh generation, 2) immersed imposition of boundary conditions, 3) use of wall models, and 4) the discontinuous Galerkin spectral element method (DGSEM).

We consider the split-form DGSEM with Legendre-Gauss-Lobatto collocation points on tensor-product elements. This method is promising for large eddy simulation (LES) as it combines:
 1) robustness, both in theory (in the sense of entropy stability) and in practice,
 2) high resolving efficiency[1] for smooth solutions,
 3) high throughput that reduces only moderately (linearly) with increasing design order.
In the present work, we want to investigate to what extent each of these three properties is retained when the DGSEM is applied to geometrically nonconforming meshes.

Our interest in nonconforming DGSEM is two-fold. Firstly, so that we can apply it to automatically generated Cartesian meshes obtained by recursive refinement of cells near solid boundaries in an octree fashion. Secondly, because we want to employ DGSEM also on locally refined curvilinear hexahedral grids in order to efficiently resolve localized solution features such as vortex structures, shear layers or shock waves.

We have extended the DGSEM already available in the CFD software by ONERA, DLR and Airbus [4] (CODA[2]) to support nonconforming pairs of elements by means of the mortar method [3]. We currently have two variants of this approach implemented, depending on whether the least-squares projections to/from mortars are approximated using the collocated quadrature rule of the DGSEM basis itself (we refer to this variant as *Lobatto mortar*), or using the more accurate Legendre-Gauss rule (*Gauss mortar*). A third variant, based on [1], is currently in development and we plan to include it in the comparisons in the final article.

For a first assessment of robustness, we simulate a uniform flow. The domain is the $[-5,5]^3$ cube, with periodic boundary conditions on all 6 sides. The initial condition is given by the primitive state vector (density, velocity vector, pressure) $= (0.7, 0.2, 0.3, -0.4, 1.0)$. We solve the Euler equations (i.e. there is no physical dissipation) using the 7-stage, 3rd order explicit Runge-Kutta time scheme from [5, section 3.3.3] and a time step size of 0.02. We employ the quadratic nonconforming mesh in Figure 2, obtained by applying the following mapping before local refinement:

$$\tilde{x} = a \cos(\omega x) \cos(3\omega y) \sin(4\omega z),$$
$$\tilde{y} = a \sin(4\omega x) \cos(\omega y) \cos(3\omega z),$$

STAB

$$\tilde{z} = a \cos(3\omega x) \sin(4\omega y) \cos(\omega z),$$

where $\omega = \pi/10$ and $a = 10/15$.

We compare two numerical surface fluxes: the central flux of Chandrashekar and the upwind flux of Roe with no entropy fix. The discretization is DGSEM of 5th order. We employ the Chandrashekar flux as numerical volume flux in both cases. Figure 1 shows the results obtained with CODA, and compares them with those obtained using exactly the same numerical methods in the open-source research solver FLUXO [2]. For both mortar method variants combined with a diffusive surface flux, the solution remains equal to the initial one for all times. For the nondissipative central surface flux, neither of the mortar method variants is stable. For the Gauss mortar variant, however, the error growth is slower and divergence occurs later than for the Lobatto one. This behavior is also observed with the FLUXO code.

In the full paper, our intention is to use the inviscid Taylor-Green vortex test case [2] to assess robustness and accuracy in a more challenging problem.
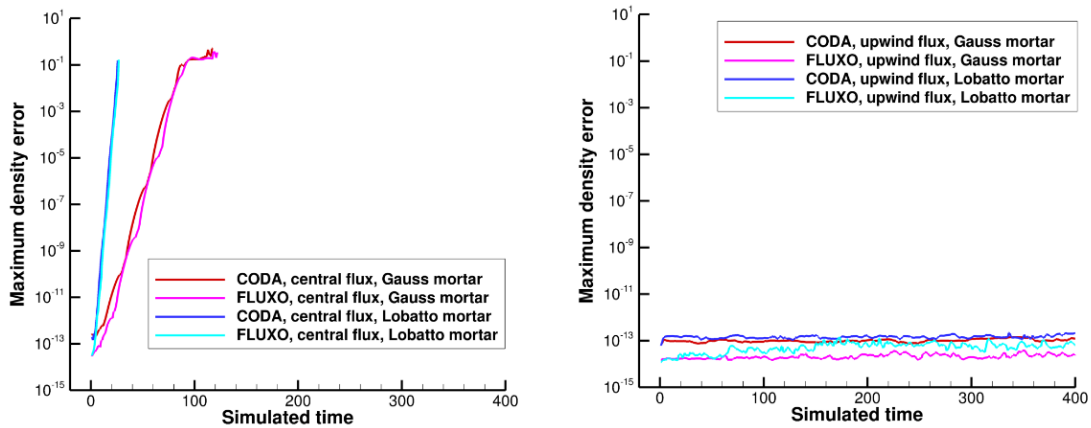
Figure 1: Largest difference in density with respect to the initial condition over all collocation points in the mesh over time. Left: Chandrashekar surface flux. Right: Roe surface flux.
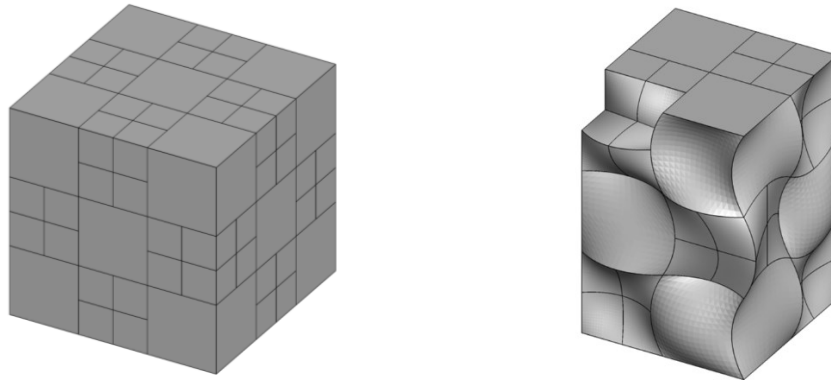
Figure 2: The mesh used to obtain the results in Figure 1. Left: full view. Right: cutaway view.

References

[1] J. Chan, M. J. Bencomo, and D. C. Del Rey Fernández, "Mortar-based Entropy-Stable Discontinuous Galerkin Methods on Non-conforming Quadrilateral and Hexahedral Meshes," *J Sci Comput*, vol. 89, no. 2, p. 51, Nov. 2021, doi: 10.1007/s10915-021-01652-3.

[2] G. J. Gassner, A. R. Winters, and D. A. Kopriva, "Split form nodal discontinuous Galerkin schemes with summation-by-parts property for the compressible Euler equations," *Journal of Computational Physics*, vol. 327, pp. 39–66, Dec. 2016, doi: 10.1016/j.jcp.2016.09.013.

[3] D. A. Kopriva, S. L. Woodruff, and M. Y. Hussaini, "Computation of electromagnetic scattering with a non-conforming discontinuous spectral element method," *Int. J. Numer. Meth. Engng.*, vol. 53, no. 1, pp. 105–122, Jan. 2002, doi: 10.1002/nme.394.

[4] T. Leicht *et al.*, "DLR-Project Digital-X - Next Generation CFD Solver 'Flucs,'" in *Deutscher Luft- und Raumfahrtkongress 2016*, Feb. 2016. [Online]. Available: https://elib.dlr.de/111205/

[5] T. Toulorge and W. Desmet, "Optimal Runge–Kutta schemes for discontinuous Galerkin space discretizations applied to wave propagation problems," *Journal of Computational Physics*, vol. 231, no. 4, pp. 2067–2091, Feb. 2012, doi: 10.1016/j.jcp.2011.11.024.

STAB

Mitteilung

Fachgruppe: Numerische Aerodynamik

Entropy-stable fluxes for high-order Discontinuous Galerkin simulations of high-enthalpy flows.

Georgii Oblapenko[1], Arseniy Tarnosvkiy[2], Moritz Ertl[3], Manuel Torrilhon[4]

[1]Applied and Computational Mathematics, RWTH Aachen, 52062 Aachen, oblapenko@acom.rwth-aachen.de

[2]Applied and Computational Mathematics, RWTH Aachen, 52062 Aachen, arseniy.tarnovskiy@rwth-aachen.de

[3]Insitute of Aerodynamics and Flow Technology, German Aerospace Center (DLR), 37073 Göttingen, moritz.ertl@dlr.de

[4]Applied and Computational Mathematics, RWTH Aachen, 52062 Aachen, mt@acom.rwth-aachen.de

Accurate simulations of high-enthalpy reacting multi-species flows are a crucial component of the research and development cycle for design of new spacecraft [1]. As available computing power increases, so does the range of physical phenomena that can be modelled. At the same time, development of new numerical methods that are able to fully leverage modern computing architectures is a crucial part of CFD development [2]. Discontinuous Galerkin (DG) methods possess many properties that make them the preferred approach for future CDF solver development: 1) higher-order solution representation 2) low numerical dissipation 3) less stringent requirements on grid-shock alignment 4) improved computational efficiency due to data locality.

One of the desired properties of numerical schemes is entropy conservation [3,4], as it helps ensure stability of the resulting scheme. Within the Discontinuous Galerkin Spectral Element Method (DGSEM), this requires entropy-conservative numerical volume and surface flux
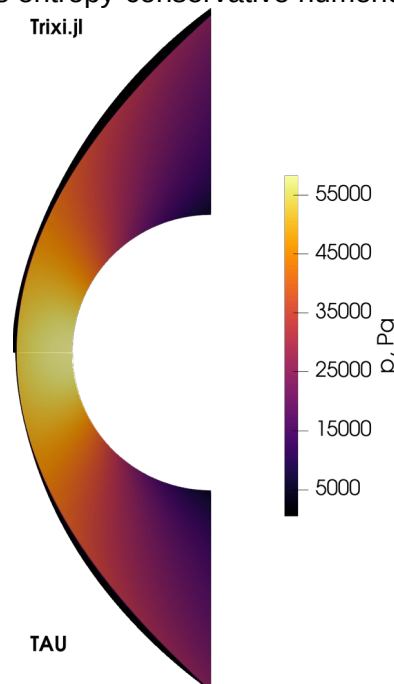

Figure 1: Pressure field for supersonic flow of calorically perfect gas around a cylinder.

STAB

functions [5]. Whilst for calorically perfect gases the derivation of such flux functions is relatively straightforward [6], for flows where the internal energies are temperature-dependent, most approaches rely on simplified models for the internal energies and specific heats [7,8], which either reduces the range of applicability of such models, or requires precomputation of curve fits. In [9] a more generic approach to computation of entropy-conservative fluxes for flows with temperature-dependent energies was proposed, which relies on linear reconstruction of energies and specific heats from tabulated values.

In the present work, the approach developed in [9] is leveraged for high-order DG simulations of reacting multi-species flows. Comparisons to the DLR TAU solver [10] are carried out for two-dimensional reacting flows in order to verify the developed approach and assess its performance.

Preliminary results show excellent agreement between solutions obtained with the TAU solver and the developed approach as implemented in the Trixi.jl framework [11] for the case of a calorically perfect gas, as seen on Fig. 1 for the case of an inviscid Mach 10 flow around a cylinder.

1. Karl, S., & Bykerk, T. (2024). Sustainable space technologies—Strategies toward a predictive aerothermal design of re-useable space transportation systems. *Review of Scientific Instruments*, *95*(2).
2. Slotnick, J. P., Khodadoust, A., Alonso, J., Darmofal, D., Gropp, W., Lurie, E., & Mavriplis, D. J. (2014). *CFD vision 2030 study: a path to revolutionary computational aerosciences* (No. NF1676L-18332).
3. Tadmor, E. (2003). Entropy stability theory for difference approximations of nonlinear conservation laws and related time-dependent problems. *Acta Numerica*, *12*, 451-512.
4. Chan, J. (2018). On discretely entropy conservative and entropy stable discontinuous Galerkin methods. *Journal of Computational Physics*, *362*, 346-374.
5. Fisher, T. C., & Carpenter, M. H. (2013). High-order entropy stable finite difference schemes for nonlinear conservation laws: Finite domains. *Journal of Computational Physics*, *252*, 518-557.
6. Ranocha, H. (2018). Comparison of some entropy conservative numerical fluxes for the Euler equations. *Journal of Scientific Computing*, *76*(1), 216-242.
7. Gouasmi, A., Duraisamy, K., & Murman, S. M. (2020). Formulation of entropy-stable schemes for the multicomponent compressible Euler equations. *Computer Methods in Applied Mechanics and Engineering*, *363*, 112912.
8. Peyvan, A., Shukla, K., Chan, J., & Karniadakis, G. (2023). High-order methods for hypersonic flows with strong shocks and real chemistry. *Journal of Computational Physics*, *490*, 112310.
9. Oblapenko, G., & Torrilhon, M. (2024). Entropy-conservative high-order methods for high-enthalpy gas flows. *arXiv preprint arXiv:2403.16882*.
10. Hannemann, K., Schramm, J. M., Wagner, A., Karl, S., & Hannemann, V. (2010). A closely coupled experimental and numerical approach for hypersonic and high enthalpy flow investigations utilising the HEG shock tunnel and the DLR TAU code. *VKI/RTO Lecture Series, RTO-EN-AVT-186 Aerothermodynamic Design, Review on Ground Testing and CFD*.
11. Ranocha, H., Schlottke-Lakemper, M., Winters, A. R., Faulhaber, E., Chan, J., & Gassner, G. J. (2021). Adaptive numerical simulations with Trixi. jl: A case study of Julia for scientific computing. *arXiv preprint arXiv:2108.06476*.

STAB

Mitteilung

Fachgruppe: Numerische Aerodynamik

Development and assessment of an Immersed Boundary Method in an unstructured flow solver for steady and scale-resolving simulations

Roberto Sanchez-Ortiz[1], Jesús Miguel Sánchez Gil[2], Axel Probst[1], Axel Schwöppe[2]

DLR, Institute of Aerodynamics and Flow Technology

[1]Bunsenstraße 10, 37073 Göttingen, Roberto.SanchezOrtiz@dlr.de, Axel.Probst@dlr.de

[2]Lilienthalpl. 7, 38108 Braunschweig, Jesus.SanchezGil@dlr.de, Axel.Schwöppe@dlr.de

This paper presents the implementation and assessment of an Immersed Boundary Method (IBM) in the CFD software by ONERA, DLR, Airbus (CODA). The main advantage of this approach is the fully automatic generation of hexahedral, non-body-fitted meshes, which overcomes an often-encountered bottleneck in industrial CFD and is therefore sometimes called *Rapid-CFD*. While most implementations of this approach rely on dedicated Cartesian solvers or on the Lattice-Boltzmann method, we extend an unstructured compressible flow solver by IBM capabilities, enabling a wide range of both steady (RANS) and unsteady (e.g. scale-resolving) applications. Many IBM approaches found in the literature, e.g. [1], [2], rely on significant modifications to the solver and even the fluid-model equations. In contrast, the method of ONERA in [3], [4] is a geometric approach where the equations are left untouched and accuracy is achieved by a specific hole-cutting algorithm to define the immersed boundary. While the original method is applied to a Cartesian solver, this paper adopts the method for the unstructured solver CODA, using the hole-cutting algorithm and grid generation of Cassiopée [5]. The grid generation was originally based on an Octree algorithm required for Cartesian solvers, but was abandoned in favor of a new approach based on a (flow-independent) adaptive mesh refinement (AMR) method developed by ONERA in Cassiopée. This approach uses a nonconforming isotropic refinement process that starts with a uniform Cartesian grid and refines it based on the distance to the object. The result is an unstructured grid of isotropic hexahedrons with hanging nodes and a computational boundary nonconforming to the wall, as can be seen in Figure 1. This new approach presents up to 4 times fewer elements than the equivalent Octree-based grid without loss of accuracy, as the refinement areas are more optimally distributed, and proves to be more suitable for an unstructured solver such as CODA.
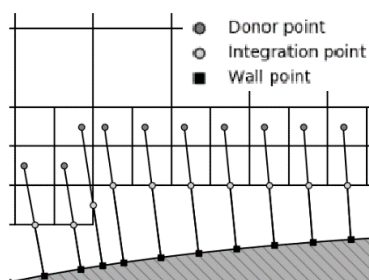
Figure 1. Schematic view of a grid with an immersed boundary close to the object (hatched area) with wall point (square), integration point at the face center (light circle), and donor point (dark circle).

The immersed boundary condition consists of three points aligned in a straight line perpendicular to the wall geometry (wall, integration and donor point). The solution at the donor point, interpolated as a linear reconstruction, is used to solve the wall model of Musker [6], and provides the boundary layer profile for the computation of the state at the integration point of the boundary. The boundary condition is then weakly imposed as usual in CODA, assuming constant density and constant pressure. The immersed boundary method was tested in RANS simulations of the ONERA M6 wing on a grid with 30 million elements. As shown in Figure 2, the pressure distribution reproduces the reference solution of a body-fitted mesh with good accuracy, especially for the grid with a cell size near the wing of 0.001 with respect to the root chord, and also predicts the shock wave position consistently.

STAB

Figure 2. Pressure distribution of the ONERA M6 wing at stage 0.44, 0.65 and 0.8 (from left to right) of the semispan for the body-fitted solution (circles) and the immersed boundary method (solid line) for two different grid refinements.

As a scale-resolving simulation test case, the *Boeing Rudimentary Landing Gear* is computed with wall modeled LES using the WALE sub-grid model and wall functions on a grid with 15 million elements. Figure 3 shows the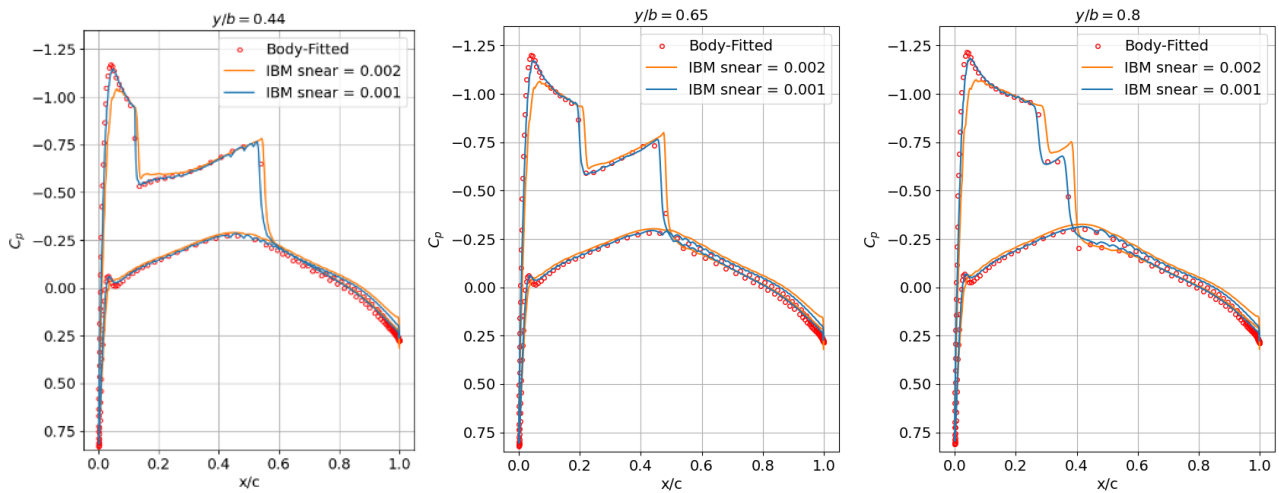 resolved eddy structures with a Q-criterion snapshot on top of the IBM grid. Other numerical studies include the simulation of a periodic channel with a body-fitted grid, validating the wall modeled LES capabilities in CODA.
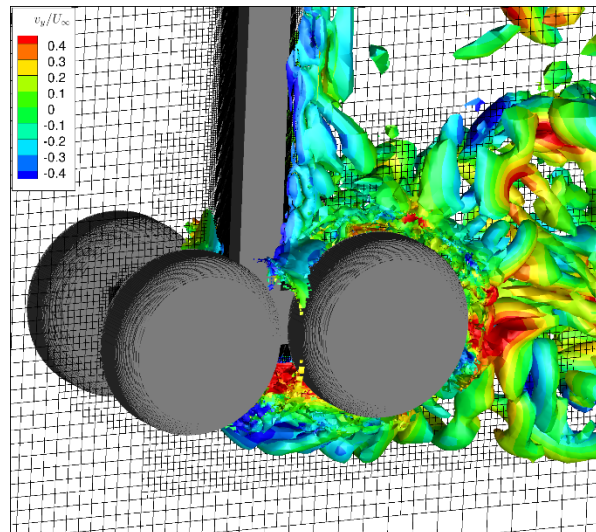
Figure 3. Q-criterion colored by the normalized lateral velocity in the wall-modelled LES simulation of the Boeing Rudimentary Landing Gear using the present IBM approach.

Bibliography

[1] F. Capizzano, "Turbulent Wall Model for Immersed Boundary Methods," *AIAA Journal*, vol. 49, no. 11, pp. 2367–2381, Nov. 2011, doi: 10.2514/1.J050466.

[2] Y. Tamaki and T. Imamura, "Turbulent Flow Simulations of the Common Research Model Using Immersed Boundary Method," *AIAA Journal*, vol. 56, no. 6, pp. 2271–2282, Jun. 2018, doi: 10.2514/1.J056654.

[3] T. Renaud, C. Benoit, S. Peron, I. Mary, and N. Alferez, "Validation of an immersed boundary method for compressible flows," in *AIAA Scitech 2019 Forum*, in AIAA SciTech Forum. , American Institute of Aeronautics and Astronautics, 2019. doi: 10.2514/6.2019-2179.

[4] B. Constant, S. Péron, H. Beaugendre, and C. Benoit, "An improved immersed boundary method for turbulent flow simulations on Cartesian grids," *Journal of Computational Physics*, vol. 435, p. 110240, Jun. 2021, doi: 10.1016/j.jcp.2021.110240.

[5] C. Benoit, S. Péron, and S. Landier, "Cassiopee: A CFD pre- and post-processing tool," *Aerospace Science and Technology*, vol. 45, pp. 272–283, Sep. 2015, doi: 10.1016/j.ast.2015.05.023.

[6] A. J. Musker, "Explicit Expression for the Smooth Wall Velocity Distribution in a Turbulent Boundary Layer," *AIAA Journal*, vol. 17, no. 6, pp. 655–657, Jun. 1979, doi: 10.2514/3.61193.

STAB

Fachgruppe: Numerische Aerodynamik

Numerical investigation of wall curvature effect on air cooling lines with tilted heat exchanger for Electrified Aero Engines

Prabhjot Singh[1], Sebastian Merbold[2]

[1,2] Institute of Electrified Aero Engines, German Aerospace Centre (DLR), Cottbus (Germany)

[1]prabhjot.singh@dlr.de, [2]sebastian.merbold@dlr.de

Heat exchangers (HEx) are critical components in the thermal management systems of electrified aero engines, known for their extensive heat transfer surfaces. In the case of fuel-cell electric systems heat rejection at low working temperatures is required, resulting in high weight demands and significant drag impact, reducing the overall efficiency. Accurately computing the air flow for these complex structures is a significant challenge. This study employs a transient Large Eddy Simulation (LES) of air flow in cooling lines and modeling heat exchangers using porous media approach (by the use of Darcy-Forchheimer equation [1]). The solver used is self-adapted pisoFoam solver, pisoTempFoam, which incorporates heat transfer in this simulation. An offset fin heat exchanger configuration with variable upstream and downstream regions (relative to HEx) cros-section is investigated, utilizing available experimental data to determine the coefficients and subsequently calculate the pressure drop across the heat exchanger for the porous model [2][3]. By employing porous media assumption, the simulation of heat exchangers is simplified, capturing essential flow characteristics without the computational overhead typically associated with detailed geometric modeling. The primary objective of this study is to optimize geometric designs for enhanced thermal management and flow efficiency. In order to reduce the overall cross-sectional blockage of the cooling line, the heat exchanger (HEx) is tilted within the duct. Due to the flow redirection, guidance features (like configuring upstream and downstream regions relative to HEx) need to be applied to mitigate flow separation effects. Initial simulations performed in two dimensions focus on evaluating pressure drops and flow separations, providing essential data for optimizing upstream and downstream regions (relative to HEx) configurations. This involves systematically studying the effects of wall curvature before and after the tilted heat exchanger (HEx). The upstream and downstream regions cross-sections depend on the tilting angle of the HEx. Figure 1 depicts different configurations for the wall curvature radius (r_i) for upstream and downstream regions, where we have heat exchanger oriented at an angle (α) and slip flow is at angle (β) to the downstream cros-section of HEx.
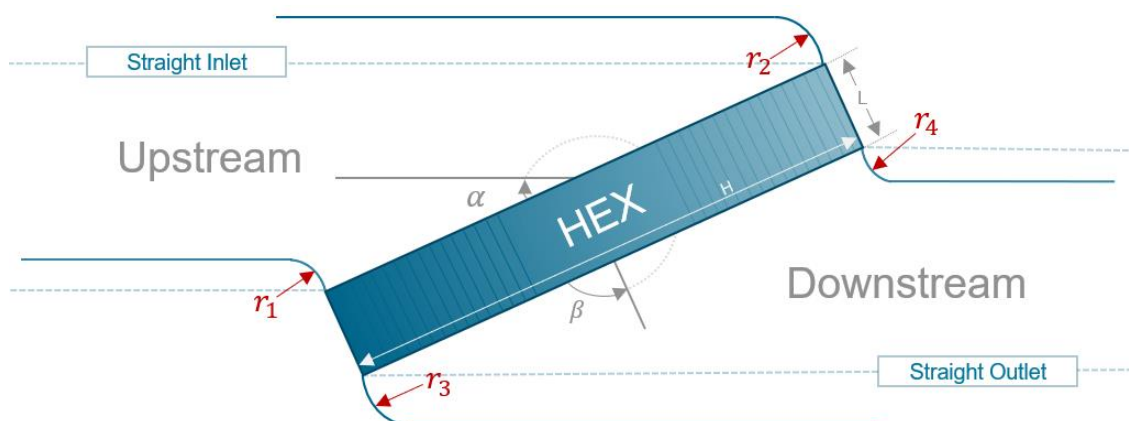
Figure 1 : Sketch of the geometric configuration of air cooling line with tilted heat exchanger of lateral length L. The radii (r_1, r_2, r_3, r_4) represent the upstream and downstream wall curvatures relative to the HEX and 'α'as the angle of alignment.

The wall curvature radius (r_i) ranges from 0 to 2 times the lateral length (L) of HEx, measuring 0.286 meters in our example. The study evaluates results based on different parameters and in context to this

study, also depicts greater pressure drop and drag due to flow stagnation and reverse flow issues along the edges. Figure 2(a) and 2(b) depicts two different configurations for the upstream and downstream regions where we have heat exchanger oriented at an angle of 24 degrees, measuring 0.286 meters in lateral length (L) and 1.8 meters in height (H) (for this presented case only).

a)

b)
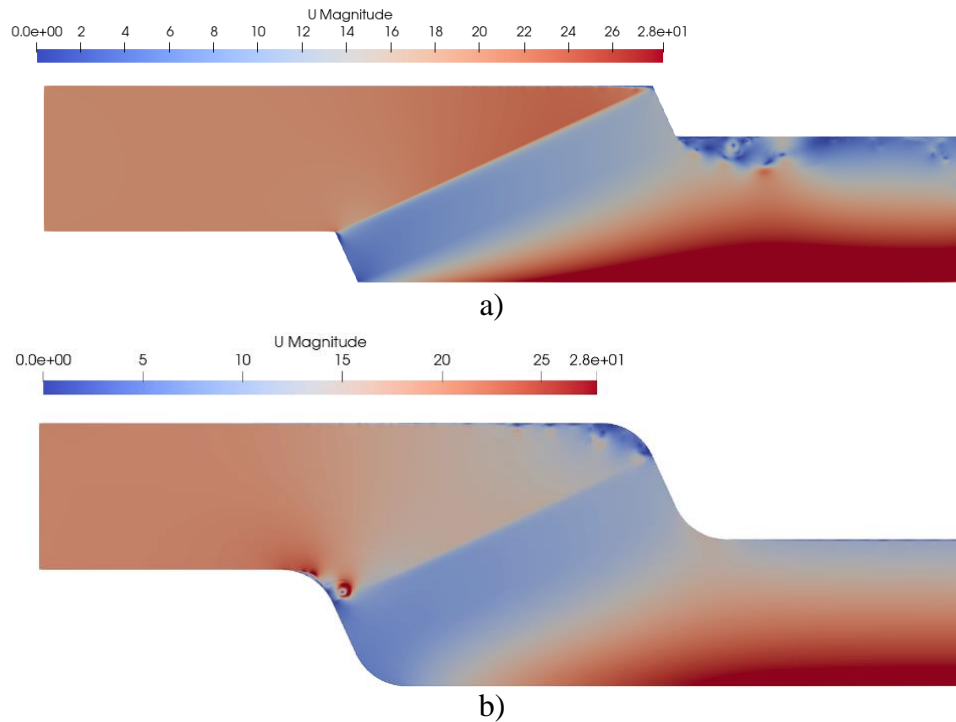
Figure 2 : Instantaneous velocity contours for a) sharp edged case (r_i=0) and b) wall curvature case (r_i= L)

Figure 2 (a) depicts a design with a sharp edges in the upstream and downstream regions, where flow separation is observed at the downstream. In contrast, Figure 2(b) depicts a configuration with same wall curvatures at upstream and downstream ends, exhibiting flow separation upstream to the HEx but achieving separation-free flow downstream. A systematic analysis of altering the wall curvature radii is presented to find optimal configurations to improve the uniformity of the flow at the Heat exchanger and to reduce the induced drag by flow separation. Furthermore, three-dimensional Large Eddy Simulations (LES) using pisoTempFoam solver are performed for configurations with a low tendency toward flow separation.

References :
1. Wang, L., Cardenas, M. B., Wang, T., Zhou, J. Q., Zheng, L., Chen, Y. F., & Chen, X. (2022). The effect of permeability on Darcy-to-Forchheimer flow transition. Journal of Hydrology, 610, 127836.
2. Dong, J., Chen, J., Chen, Z., & Zhou, Y. (2007). Air-side thermal hydraulic performance of offset strip fin aluminum heat exchangers. *Applied Thermal Engineering*, *27*(2-3), 306-313.
3. Kim, D. U., Son, J. Y., Kim, T. K., & Kim, Y. W. (2020). Friction correlation of an offset strip fin modeled as porous medium for application to a geothermal heat exchanger. *Geothermics*, *87*, 101873.

STAB

Mitteilung

Fachgruppe: Numerische Aerodynamik

The physics of spanwise gaps between lifting and control surfaces: An analysis using RANS and hybrid RANS/LES methods

Larissa B. Streher[1], Axel Probst[2]
German Aerospace Center, Institute of Aerodynamics and Flow Technology, Lilienthalplatz 7, 38108 Braunschweig, Germany
German Aerospace Center, Institute of Aerodynamics and Flow Technology, Bunsenstraße 10, 37073 Göttingen, Germany
{larissa.streher;axel.probst}@dlr.de

Aircraft control surfaces are aerodynamic devices that dynamically alter the geometry of flight vehicles, consequently influencing unsteady aerodynamic loads. Originally designed for stability and control purposes, these aerodynamic devices have been exploited by active control systems more recently. These systems collect data on the state of the aircraft and the surrounding atmospheric flow and strategically deploy the control surfaces to alleviate the loads on the air vehicle. Designing such systems is, however, non-trivial as the loads on aircraft with moving control surfaces must be accurately predicted using numerical methods during the early design phase of new aircraft.

A key challenge in the prediction of the loads when deploying control surfaces is modeling moving control surfaces while also considering the small gaps present between lifting and control surfaces. These gaps introduce complex flow phenomena, increasing vorticity and noise, and significantly impacting the overall aerodynamic efficiency (see Liggett and Smith [1, 2]).

As the presence of streamwise gaps leads to an increase in drag and subsequent decrease in overall aerodynamic efficiency (see Liggett and Smith [1, 2]), these gaps are usually sealed in real-life configurations. On the other hand, sealing the spanwise gaps is a geometrically complex task that is still under research, with current efforts focusing on the utilization of wing morphing technologies.

Due to difficulties in sealing spanwise gaps, this study investigates the influence of such gaps on the aircraft aerodynamics, a topic that is not yet fully understood. Here, we investigate the complex flow physics introduced by spanwise gaps using the benchmark active controls technology model (BACT) experimentally studied by NASA (see Bennett et al. [3]). The BACT model consists of a NACA0012 wing with the presence of upper and lower spoilers, as well as a trailing edge control surface. In this work, only the trailing edge device and the spanwise gaps between this device and the lifting surface are considered (see Fig. 1). Various control surface deflection angles and free-stream conditions are studied. Additionally, we use both Reynolds-average Navier-Stokes (RANS) and hybrid RANS/large-eddy simulation (LES) approaches to model turbulence, given the sensitivity of vorticity to the applied numerical schemes and the difficulty of RANS models to correctly predict large-scale separation.

The differences in flow circulation obtained with the RANS and hybrid RANS/LES turbulence approaches are investigated in detail using the BACT configuration. Specifically, this study reveals that the presence of spanwise gaps induces unstable detached shear layers that roll up into vortices at the beginning of the spanwise gap (located at the same streamwise position as the leading edge of the control surface). This behavior is similar to that observed with streamwise gaps, as described by Deck [4] and Khorrami et al. [5]. Additionally, large counter-rotating streamwise vortices are formed within the inner and outer spanwise gaps of the trailing edge control surface, as illustrated in Fig. 2. These vortices move downstream, significantly affecting the wing's wake. The orientation of these streamwise vortices depends on whether the control surface is deflected upwards or downwards, while their vorticity magnitude is also influenced by the free-stream conditions and the employed turbulence modeling approach.

STAB

Ultimately, this study deepens the understanding of spanwise gap flow physics, providing essential insights that are pivotal for the design of advanced active control systems for future aircraft.
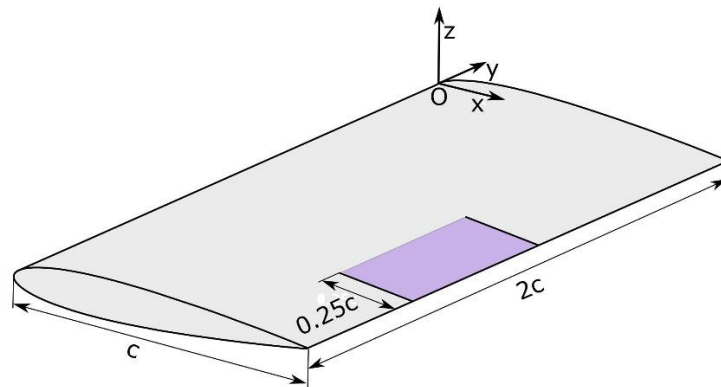

Figure 1: BACT configuration with trailing edge control surface (in pink). The chord length is c = 406.4mm. Spanwise gaps of l_y = 0.8mm are present between the lifting surface (in light gray) and the trailing edge device. The streamwise gap is not considered in this work.
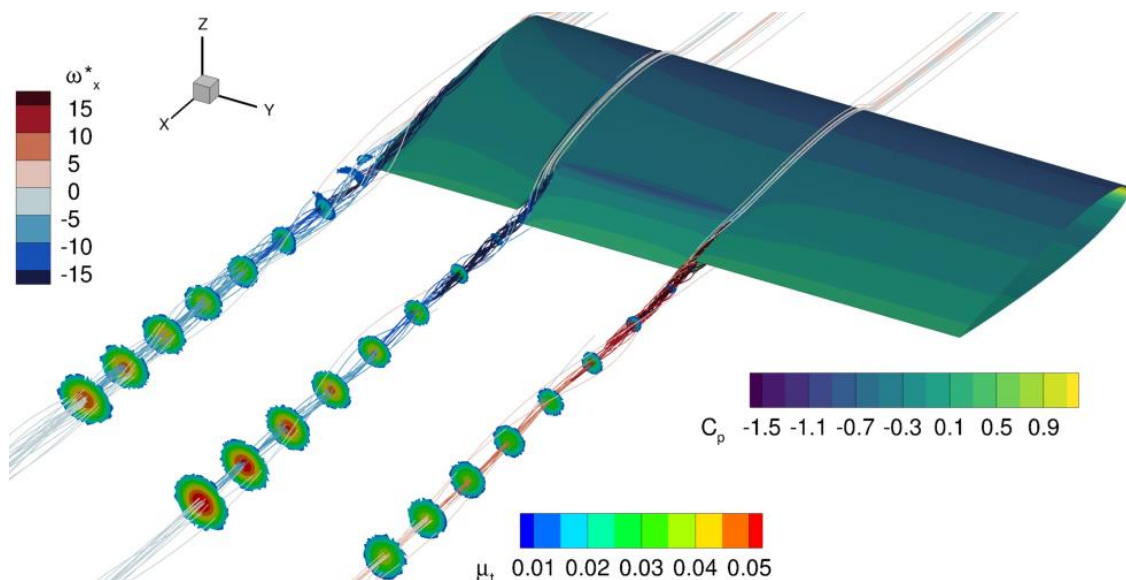
Figure 2: BACT configuration with the trailing edge control surface deployed by 10.3° and simulated using a RANS model. The colormap on the wing surface represent the pressure coefficient distribution, whereas the streamtraces illustrate the streamwise vorticity and the isosurfaces on the wake represent the turbulent eddy viscosity.

[1] Liggett, N. and Smith, M.J. (2013). The physics of modeling unsteady flaps with gaps. *Journal of Fluids and Structures*, 38:255-272.

[2] Liggett, N. and Smith, M.J. (2013). Study of gap physics of airfoils with unsteady flaps. *Journal for Aircraft*, 50(2):643-650.

[3] Bennett, R.N., Scott, R.C., and Wieseman, C.D. (2000). Test case for the benchmark active controls model: Spoiler and control surface oscillations and flutter. In *Verification and validation data for computational unsteady aerodynamics, Report of the Applied Vehicle Technology Panel (AVT) Task Group AVT-010, RTP Technical Report 26,* pages 201-224.

[4] Deck, S. (2005). Zonal-detached-eddy simulation of the flow around a high-lift configuration. *AIAA Journal*, 43:2372–2384.

[5] Khorrami, M., Choudhari, M., Singer, B., Lockard, D. and Streett, C. (2003). In search of physics: the interplay of experiment and computation in slat aeroacoustics. In: *41st AIAA Aerospace Sciences Meeting and Exhibit*, Reno, NV.

STAB

Mitteilung

Fachgruppe: Numerische Aerodynamik

Coupled CFD-FM Wing Unfolding with Chimera

Finn Wilden, Mareike Semprich

MBDA Deutschland GmbH, Hagenauer Forst 27, 86529 Schrobenhausen,

finn.wilden@mbda-systems.de, mareike.semprich@mbda-systems.de

During the launch of a cruise missle the unfolding process of the wing is a critical maenuver which therefore brings increased risk for flight-testing. To reduce this, a method was developed to simulate the unfolding process using a coupled CFD flight mechanics (CFD-FM) approach. The method uses Tau's 6DoF libraries [1] and the Chimera method [2].

As a simple cruise missile test configuration with trapezoidal swept wings and cuboid with rounded edges as a fuselage is used in a parasol configuration. The wings are not geometrically connected to each other to enable the folding process without the bodies colliding. There is a gap of at least half an airfoil thickness between the wing and fuselage. As flight conditions $\mathrm{Ma} = 0.8$ and $\mathrm{Re} = 4.4e6$ are used with an angle of attack of 0°.

The Chimera mesh contains of a fuselage mesh as the background mesh (with farfield), and two wing meshes as sub-meshes (only nearfield). Prior to the Chimera mesh a classical mesh was set up to verify sufficient discretization parameters with a grid convergence study to be then transferred to the Chimera meshes. In addition local refinement in all meshes was necessary to ensure enable the reliable finding of Chimera interpolation partners. This is crucial for the quality of the CFD with a Chimera mesh [3] and was found to be a major task in the creation of a valid setup. A mesh convergence study was also conducted for the Chimera grid setup to verify its meshing parameters. Also simulation results of both meshes (Classix and Chimera) were compared to ensure sufficient quality of the Chimera setup.

Taus *automatic hole cutting* method [4] is applied to automatically determine the interpolation regions during the simulations. Taus implicit backward Euler is used with $\mathrm{CFL} = 0.5$ and the UPWIND scheme in conjunction with AUSMDV and the Menter-SST 2003 turbulence model. The timestepsize is set to $\Delta t = 0.0005\,s$ and Taus Cauchy convergence is applied to save computational time. For the CFD-FM coupling procedure a threshold of 10^{-3} is utilized.

Taus 6DoF libraries enable to initialize each body that lays in its own Chimera sub-mesh as an individual flight mechanics object an thus has all six degrees of freedom. The FM-solver then calculates the movement of each body in space based on the acting aerodynamic forces and additional external forces which can be defined in the Tau-Python code. In addition, the mass and the moments of inertia of each body must be defined before the simulation. [5]

In the developed method both wings are initializes as FM-objects, but five of the six degrees of freedom are locked, so that only a rotation around the z-axis is possible. The fuselage is currently not initialized as a separate FM-object, as it is part of the background mesh. Therefore, the unfolding process of the wings can be simulated in a coupled manner, but the FM-response behavior of the entire missile cannot. The forces acting on the wings and on the entire missile can thus be used for evaluation of the FM-response behavior.

An external, constant torque $M_{z,Motor}$ is applied to the wings to drive the wing. This accelerates the wings and unfolds them against the direction of flow. When the wings reach the target unfolding angle of $\phi = 0\,°$ (correspons to a leading edge sweep of $\varphi = 40\,°$) the wings are stopped by a stop moment $M_{z,Stop}$ produced by a supercritically damped spring-damper system so that they reach an end position without oscillation. In superposition with the acting aerodynamic Moment $M_{z,aero}$ this results in a total moment on the wing:

$$M_z = \begin{cases} M_{z,aero} + M_{z,Motor} & \text{for } \phi > 0\,° \\ M_{z,aero} + M_{z,Motor} + M_{z,Stop} & \text{for } \phi \leq 0\,° \end{cases}$$

Figure 1 and Figure 2 show exemplary results of the coupled wing unfolding simulation. In these the entire unfolding process took a total time of $t_U = 0.1125\,s$. Figure 1 shows that, in order to start the unfolding process in a steady state, a settling ($t/t_U < 0$) time is simulated first. At $t/t_U = 0$, the degree of freedom of the wing rotation around z is released and the external motor torque is applied. As the aerodynamic counter-moment increases only slightly, the acceleration of the left wing is nearly constant until the stop acts, so that the wing

speed increases linearly and the unfolding angle quadratically. When $\phi = 0\,°$ is reached, the [4] spring-damper systems stops the wing quickly with a large counter-torque so that it reaches a stationary final state without oszillation. The duration of the stopping process is 0.0205 s.
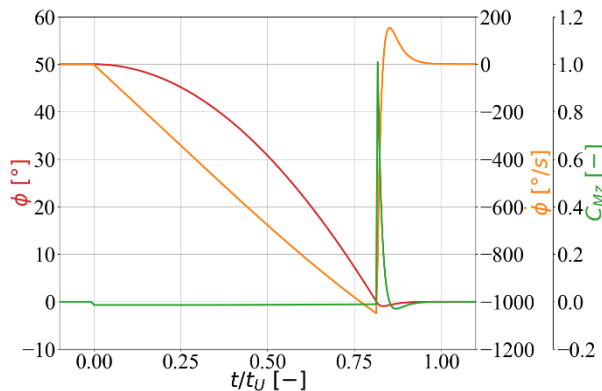

Figure 1: Wing unfolding angle ϕ, wing angular velocity $\dot\phi$ and total wing moment coefficient C_{Mz} over the dimensionless unfolding time t/t_D
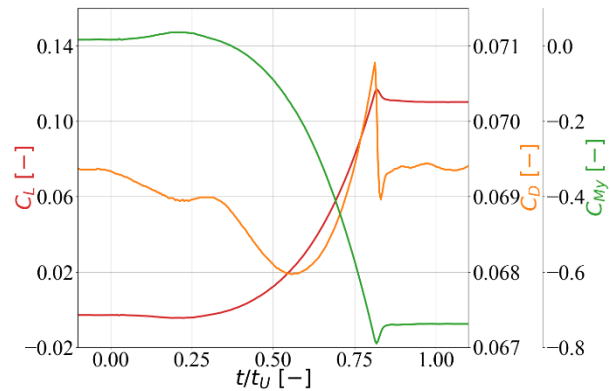
Figure 2: Aerodynamic coefficents acting on the missile over the dimensionless unfolding time t/t_D

Figure 2 shows the FM reaction of the whole missile based on the change of the aerodynamic coefficients. Up to the effect of the stop at $t/t_U = 0.818$ there is a progressive increase in lift and the pitching moment drops progressively, which was to be expected. When the stop is reached, an extreme point is reached because the relative velocity at the wings is at its maximum. After that, the coefficients quickly approach their stationary limit value. The development of the drag coefficient, on the other hand, is more subject to change, since drag changes on the wings and on the fuselage are superimposed. For $t/t_U > 0.818$ it can be seen that the drag fluctuates during and after the deceleration process. This is due to an oscillation of the pressure field around the wings caused by their very rapid deceleration. The oscillation of the pressure field also has an effect on the lift and pitching moment, but cannot be seen in Figure 2 because the mean value is significantly larger than the oscillation amplitude.

Some parameters of the unfolding process were varied as part of the study: Motor torque, stop stiffness, angle of attack and turbulence model. The methodology developed confirmed fundamental correlations (e.g. a higher motor torque leads to a shorter unfolding time) and could thus be established. In addition, limits were identified e.g. the selected time step size limits the maximum usable stiffness of the stop system due to the explicit nature of the CFD-FM coupling.

The application of the developed method to a real missile is still pending. For this the creation of the Chimera mesh is particularly challenging, as the gaps between the fuselage and wings are smaller than in this test case. An extension of the approach by using an own submesh for the fuselage so that the whole missile can react flight mechanically to influences on the overall system due to the unfolding process is planned and already foreseen in the Tau-Python setup. But this approach is only practical if the missile also contains of a tail unit and can hence maintain a stable flight condition. The developed methodology is also to be transferred to the deployment of fins.

[1] D. Schwamborn, T. Gerhold and R. Heinrich, "The DLR TAU-Code: Recent Applications," DLR, Delft, NL, 2006.

[2] J. A. Benek, F. C. Dougherty and J. L. Steger, "Chimera: A Grid-Embedding Technique," Arnold Engineering Development Center, Air Force Systems Command, 1986.

[3] H. Hadzic, "Development and Application of Finite Volume Method for the Computation of Flows Around Moving Bodies on Unstructured, Overlapping Grids," TUHH, 2006.

[4] F. Spiering, "Development of a Fully Automatic Chimera Hole Cutting Procedure in the DLR TAU Code," *New Results in Numerical and Experimental Fluid Mechanics, volume 132,* pp. 585-595, 2016.

[5] R. Heinrich, L. Reimer and A. Michler, "Multidisciplinary simulation of maneuvering aircraft," Portsdown West, UK, 2011.

STAB

Mitteilung

Fachgruppe: Strömungsakustik

Fast non-empiric stochastic methods for aircraft surface pressure fluctuations to predict interior and exterior noise excitations

G.G. Ramasawmy[1], R. Ewert[2], C.K. Appel[3], J.W. Delfs[4]
Deutsches Zentrum für Luft- und Raumfahrt e.V. (DLR)
Institut für Aerodynamik und Strömungstechnik
Abeteilung Technische Akustik
Lilienthalplatz 7, 38108 Braunschweig

This work is concerned with the prediction of the excitation of aircraft cabin noise from tightly integrated propulsion systems. One major contributor to surface pressure fluctuations at the aircraft fuselage originates from the radiated jet noise near field. Two other contributing noise sources to be mentioned are, i), direct turbulent boundary layer related excitations, and ii) engine fan noise.

As part of the collaborative research project SYNTRAC, different propulsor configurations and their impact on fuselage excitation are studied with numerical simulation. The concepts—among others—comprise a rear fuselag mounted propulsor and a V-tail pylon mounted rear propulsor. Aircraft configurations featuring conventional under-wing jet engine installation are not considered since the propulsors are mounted away from the aircraft's fuselage which would result in a focus on the integration aspects of engine, pylon and wing.

Computational aeroacoustics (CAA) is a crucial step in assessing and minimizing the relevant noise source contributions already in the design phase. It is planned to use scale resolving wall modelled LES based methods to study the cabin noise excitation of jet noise.

However, simulation times specifically for full scale configurations are still too high to be applicable within an aeroacoustics optimization loop. Chances are that the number of data points directly deducable from a set of high-fidelity predictions are too small to be sutiable for surrogate modeling, so that the latter at least has to be supported by some simplified but physics based modeling to enable a sufficient fine grained prediction of the noise features together with significantly reduced simulation times.

The results reported in this work focuses on hybrid CAA methods with stochastic noise source models as a class of physics based simulation method that offer great promise to rapidly and accurately predict the impact of noise sources on the aircraft at desired low computational cost and as such enables aeroacoustics optimization.

Simulation results discussed in this work are based on the Fast Random Particle-Mesh method (FRPM) that synthesizes different turbulent noise sources [1].

---
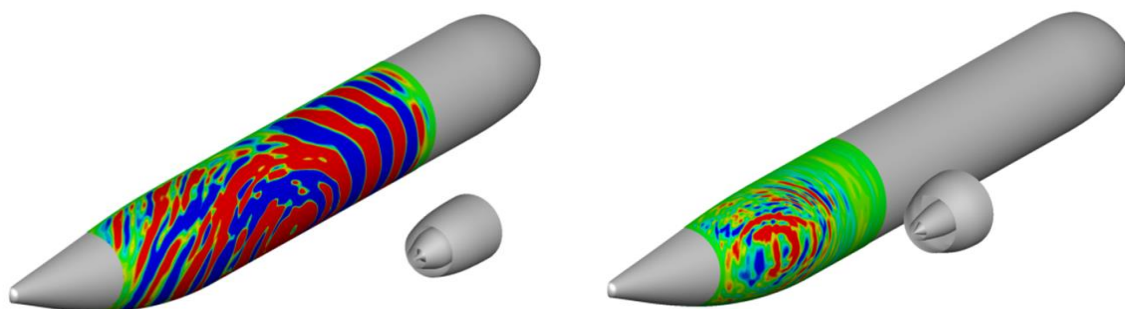
[1] geervan.ramasawmy@dlr.de

[2] roland.ewert@dlr.de

[3] Christina.Appel@dlr.de

[4] Jan.Delfs@dlr.de

STAB

Figure 1: Fuselage pressure fluctuations from FRPM, conventionally (left) and UHBR nozzle (right).

Promising results have been reported for the jet based excitation of cabin noise [2]. For this work a primal stochastic realization of the Tam & Auriault jet mixing noise model has been applied. However, the application of the Tam & Auriault model for the pylon-propulsor concept requires to include furtheron the effect of near-field installation effect on pressure fluctuations in some ongoing work. With regard to the modeling of surface pressure fluctuations from synthetic turbulence, good results were demonstrated [3].

Several improvements for more complex application have been accomplished and will be presented at the symposium. Specifically, in the project UHBR2NOISE, DLR has worked together with Airbus on boundary layer noise modelling at high pressure gradients for the non-cylindrical fuselage area. The FRPM method has been used for the generation of synthetic turbulence and the resulting hydrodynamic surface pressure fluctuations.

Based on TAU CFD-RANS solutions of the averaged flow field on the fuselage, the unsteady turbulent time-dependent velocity fluctuations are realized with standard FRPM according to the RANS flow variables. Statistical parameters of the synthetic turbulence fulfill the specifications from RANS very precisely. This means that the mean-square of velocity fluctuations are suitable proportional to the turbulent kinetic energy distribution of RANS, and the integral length scale and time scale of the synthesized turbulence locally comply with corresponding values derived from turbulent dissipation or turbulent dissipation rate values from RANS two-equation closure.

The transient surface pressure for each time step is determined from the velocity fluctuations by solving a Poisson problem. The transient surface pressure then defines the vibro-acoustic excitation. The synthetic turbulence fluctuations are realised on an auxiliary grid. The realised 1-D spectrum of the turbulence is Gaussian, i.e. the course following the plateau shows a progressive drop to higher wave numbers and does not correspond to a Kolmogorov power law with a -5/3 drop in the energy cascade.

The existing method was significantly expanded and improved for use in the cockpit area and fuselage areas with pressure gradients and convective flow acceleration to e.g. give a better representation of spatial anisotropy effects.

An overview of the results accomplished for three different regions at the fuselage in comparison with simplified analytical modeling and results from flight measurements will be presented at the symposium.
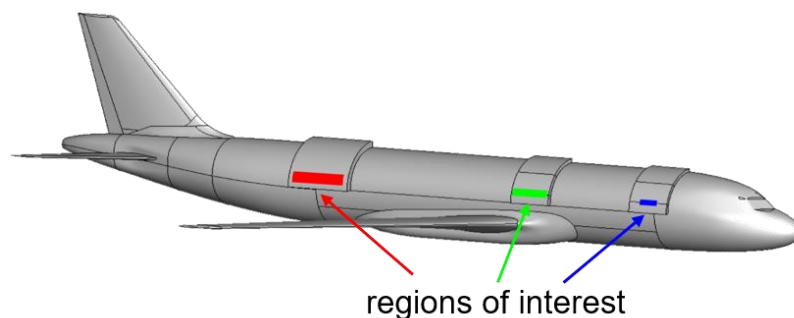

regions of interest

Figure 2: Three different simulation domains considered for fuselage surface pressure excitation.

[1] R. Ewert, J. Dierke, J. Siebert, A. Neifeld, C. Appel, M. Siefert, O. Kornow, CAA broadband noise prediction for aeroacoustic design, Journal of Sound and Vibration, Volume 330, Issue 17, 2011, Pages 4139-4160, https://doi.org/10.1016/j.jsv.2011.04.014.

[2] C. Blech, C. Appel, R. Ewert, J.W. Delfs, S.C. Langer, Numerical prediction of passenger cabin noise due to jet noise by an ultra–high–bypass ratio engine, Journal of Sound and Vibration, Volume 464, 2020, https://doi.org/10.1016/j.jsv.2019.114960.

[3] Hu, N., Reiche, N., Ewert, R. (2017). Simulation of turbulent boundary layer wall pressure fluctuations via Poisson equation and synthetic turbulence. Journal of Fluid Mechanics, 826, 421-454. doi:10.1017/jfm.2017.448

STAB

Mitteilung

Fachgruppen: Strömungsakustik

Characterizing Airflow Turbulence in the Aeroacoustic Wind Tunnel Braunschweig (AWB) using Turbulence Grids

Sparsh Sharma[a], Alexandre Suryadi, Michaela Herr

Institute of Aerodynamics and Flow Technology, German Aerospace Center (DLR), Germany

[a] Corresponding author: Lilienthalpl. 7, 38108 Braunschweig; sparsh.sharma@dlr.de

This paper extends previous research [1, 2] on grid-generated turbulence and its effect on airfoil leading-edge noise by incorporating both numerical and experimental analyses. Building upon the foundational study, which used Large Eddy Simulation (LES) to investigate turbulence effects on a NACA0012 airfoil, this research introduces comparative experimental results. Two distinct grid configurations and two airfoil profiles, NACA0012 and NACA66-006, are studied to provide a more comprehensive understanding of inflow turbulence and leading-edge noise. Measurements will be conducted in the Acoustic Wind Tunnel Braunschweig (AWB) [3], as illustrated in Figure 1a, to enable rigorous validation of numerical simulations against experimental data. Furthermore, the full paper will detail the procedures for generating and measuring grid-generated turbulence and will assess the aerodynamic and aeroacoustic characteristics of the selected airfoils. By combining numerical simulations with practical experiments, this study aims to characterize the grid-generated turbulence in the AWB.

Measurements will be conducted with the turbulence grids placed between the nozzle throat and exit, as shown in Fig. 1a. The grid is characterized by its mesh size (M) and bar width (d), as visually depicted in Fig. 1b. In the current investigation, three bars with a square cross-section of $d \times d$ are planned, where $d = 20$ mm, 30 mm and 40 mm. The implementation of the grid allows for a spacing between bars of multiples of $M = 80$ mm. Hotwire anemometry will be used to classify the turbulence downstream of the grids and line microphone arrays to investigate the effect of inflow turbulence to the leading-edge noise

The numerical simulations were conducted using the Large Eddy Simulations (LES) suite of OpenFOAM [4]. The computational setup involved using the incompressible solver $pimpleFoam$, based on the factorised finite volume method (for a detailed description, please refer to [2]). A
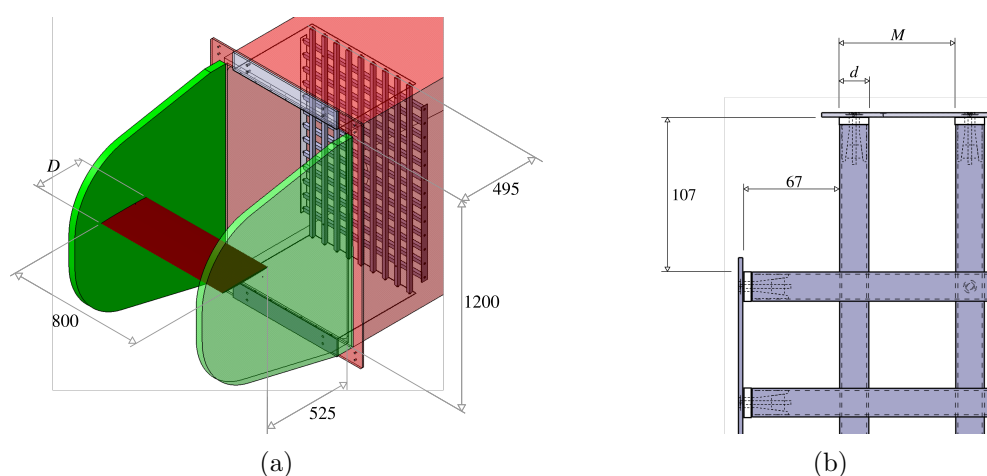

$$(a) \qquad\qquad\qquad (b)$$

Figure 1: Schematic of the implementation of the grid-generated turbulence in the AWB: (a) the AWB nozzle with the grid-turbulence generator, side walls and the wing section downstream and (b) a representative turbulence grid (not to scale).
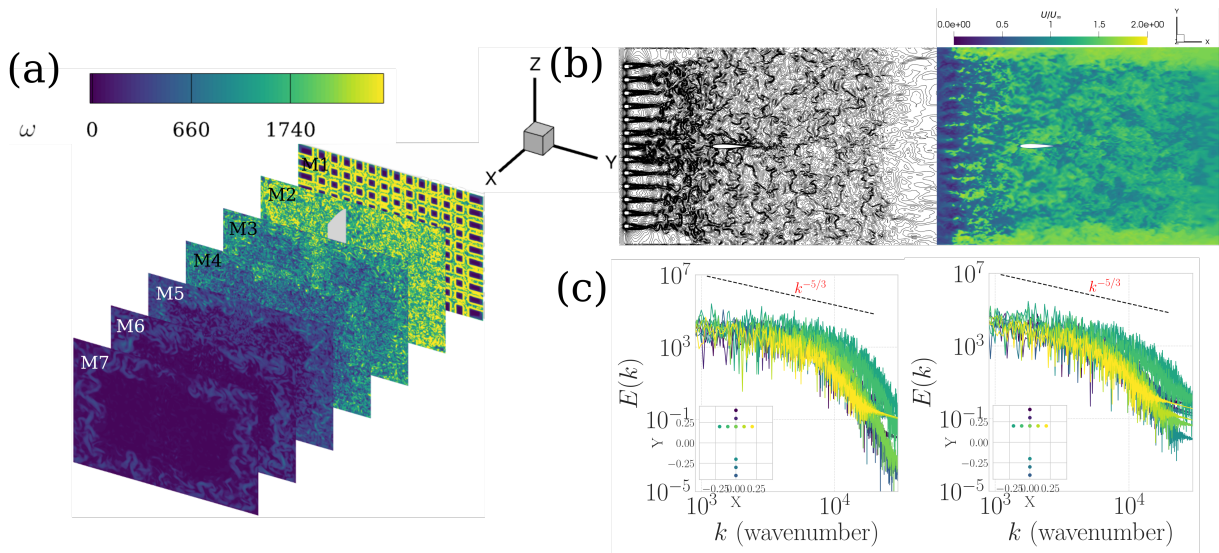
Figure 2: (a) Contour plots depicting the instantaneous vorticity field ω at streamwise locations, (b) velocity field downstream the grid in (x, y)-plane, and (c) energy spectra of streamwise and normal velocity fluctuations (dashed line indicates the characteristic Kolmogorov scaling $k^{-5/3}$ in the inertial subrange.)

three-dimensional computational domain is established, extending 10 times the airfoil chord length ($10c$) upstream from the leading edge of the airfoil to the velocity inlet boundary and 30 times the chord length ($30c$) downstream to the pressure outlet. The upper and lower boundaries of the domain are defined as symmetry boundaries and are both situated at a distance of $10c$ from the airfoil chord line. Figure 2a displays the vorticity field contours, ω, obtained at seven monitoring planes in the $(x - y)$ plane, designated M1 to M7 at selected streamwise locations. These contours offer valuable insights into the evolution of the flow. As anticipated, distinct wakes are evident behind the grid, highlighting the intermittent nature of the flow field. Nevertheless, as the distance downstream from the grid bars increases, the flow field transitions towards homogeneity and reduced spatial intermittency. Fig. 2b shows the instantaneous velocity contours in spanwise mid-plane. The structures, shed by the grid elements, are convected downstream, merge relatively quickly. Fig. 2c shows the energy spectra, $E(k)$, of streamwise and normal velocity fluctuations downstream of the turbulence grid at different probe locations seen in the inset. Here, k is the longitudinal wavenumber, defined as $k = 2\pi f/U$, where f is the frequency and U is the velocity. The numerical results are compared with the classical Kolmogorov scaling $k^{-5/3}$, which is expected for the inertial subrange.

References

[1] S Sharma, A Suryadi, and M Herr. Assessment of Turbulence Modeling in Navier-Stokes Simulations for Grid-Generated Turbulence and Airfoil Interaction. In *30th AIAA/CEAS Aeroacoustics Conf. (2024)*, Rome, Italy, jun 2024.

[2] S Sharma and M Herr. Efficient Prediction of Turbulent Inflow and Leading-Edge Interaction Noise Using a Vortex Particle Method with Look-up Table Approach. *J. Phys. Conf. Ser.*, 2767(2):022059, jun 2024.

[3] M Pott-Pollenske and J Delfs. Enhanced Capabilities of the Aeroacoustic Wind Tunnel Braunschweig. In *14th AIAA/CEAS Aeroacoustics Conf.*, Vancouver, British Columbia, Canada, may 2008.

[4] H. G. Weller, G. Tabor, H. Jasak, and C. Fureby. A tensorial approach to computational continuum mechanics using object-oriented techniques. *Comput. Phys.*, 12:620–631, 11 1998.

STAB

Mitteilung

Fachgruppe: Strömungsakustik

Acoustic measurements and time-resolved traffic-noise simulations in the Graefekiez

Lars Siegel[1] and Tobias Müller[1]

[1]German Aerospace Center (DLR), Institute of Aerodynamics and Flow Technology, Göttingen, Germany, corresponding author: lars.siegel@dlr.de

Within the framework of the Graefekiez project [1], noise measurements were carried out for several weeks at fixed locations within the Graefekiez in Berlin. The aim was the local assessment of long-term noise emissions in urban agglomerations and the evaluation of the corresponding impact on the residents' quality of life. The on-site measurements are compared to time-resolved traffic-noise simulations in order to investigate the impact of traffic-noise emissions in comparison to other sources of urban noise pollution.

To carry out the measurements, data acquisition systems were installed on the street-facing façade of three selected buildings. Using these data acquisition systems, the sound signal at the probe locations was recorded using condenser microphones (type: SoundID Reference, Fa. Sonarworks) in accordance with the ISO 1996-2 standard [2]. The recorded signal was amplified using an audio interface (type: Audio 1, Fa. Swissonic), which also supplied the 48V phantom power for the microphones, and processed using a connected mini PC (type: DL20N V2, Fa. Shuttle). The "fast" (1/8 second) averaged sound pressure level was calculated directly from the incoming sound signal, so that no raw data needed to be stored in compliance with national privacy policies. The measurement was carried out continuously for 24 hours per day during the full measurement campaign, which lasted from August 1st, 2023 until March 14, 2024. Using LTE adapters connected to the data acquisition systems, the measurement process was continuously remotely monitored and adjustments to the measurement procedure were made whenever neccessary.

The three diagrams on the right side of Figure 1 show the average of the measured sound pressure level Leq at the three probe locations during a time span of 24 hours. The averaging was performed for a set of 24h signals spanning a time frame of several weeks. The averaged sound-pressure levels at the three probe locations display a number of quantitative similarities, which are discussed in detail.

In addition to the measurements, the traffic noise has been simulated in the area around the probe locations. The simulation is based on a time-resolved noise-mapping technique, which combines the microscopic traffic simulation SUMO [3] with a ray-tracing approach which is based on the CNOSSOS-EU directive [4]. On the left side of Figure 1 the weighted day-evening-night sound-pressure level L_{DEN} is shown, as obtained from the time-resolved traffic-noise simulation. The combination of the measurements and the traffic-noise simulation allows for a qualitative comparison of the results and to estimate the impact of noise sources which are not part of the road traffic. Furthermore, the results provide a number of interesting perspectives for further developments which can be applied in various European cities.
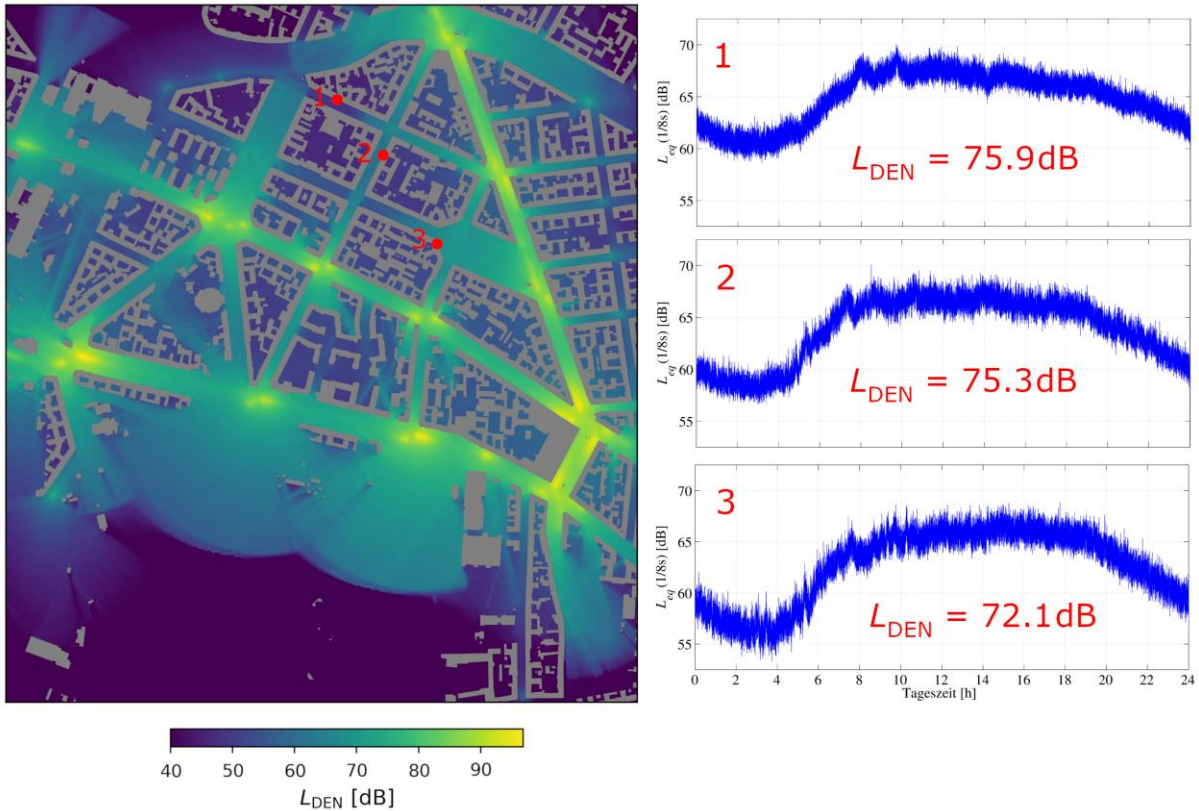
STAB

Figure 1: Left – day-evening-night sound pressure level L_{DEN} obtained from the time-resolved traffic-noise simulation in the area around the three probe locations; Right – sound-pressure level L_{eq} at the three probe locations during a period of 24 hours averaged over samples spanning a time frame of several weeks and the corresponding L_{DEN}.

[1] https://www.berlin.de/ba-friedrichshain-kreuzberg/politik-und-verwaltung/aemter/strassen-und-gruenflaechenamt/strassen/mobilitaetswende/artikel.1428814.php
[2] ISO 1996-2 Acoustics – Description, measurement and assessment of environmental mnoise – Part 2: Determination of sound pressure levels (2017-07).
[3] Pablo Alvarez Lopez, Michael Behrisch, Laura Bieker-Walz, Jakob Erdmann, Yun-Pang Flötteröd, Robert Hilbrich, Leo hard Lücken, Johannes Rummel, Peter Wagner, and EvamarieWießner. Microscopic traffic simulation using SUMO. In The 21st IEEE International Conference on Intelligent Transportation Systems. IEEE, 2018.
[4] S. Kephalopoulos, M. Paviotti, and F. Anfosso-Lédée. Common Noise Assessment Methods in Europe (CNOSSOS-EU). Publications Office of the European Union, 2012.

Mitteilung

Fachgruppe: Strömungsakustik

Flow Separation Noise Sources

Alexandre Suryadi[a], Michaela Herr

Institute of Aerodynamics and Flow Technology, German Aerospace Center (DLR), Germany

[a] Corresponding author: Lilienthalpl. 7, 38108 Braunschweig; alexandre.suryadi@dlr.de

The DLR Impulse project SAFER[2] aims to develop a machine learning model for the detection of turbulent boundary layer separation induced by an adverse pressure gradient. Whereas identifying turbulent separation itself remains a challenging topic, it is also necessary to classify the noise penalty to the degree of flow separation. This paper investigates the flow separation noise of a 2.1 m span NACA 64-618 wing model installed in the 3/4-open anechoic test section of the Low-Speed Wind Tunnel Braunschweig (NWB) of the German-Dutch Wind Tunnel (DNW), figure 1a. The same figure shows the phased microphone array with 140 LinearX M51 1/2" microphones and 10, 1/2" Bruel&Kjær free-field microphones were distributed equally facing each side of the blade model as sketched in figure 1b. Aerodynamic parameters were measured using a load balance installed under the floor of the test section and, additionally, 5 spanwise distributed static pressure taps, totaling 281, monitor the model's pressure distribution. Three boundary layer states were measured (1) naturally transitioning (*Clean*) and forced transition (*Trip*) with 0.4 mm high zig-zag tapes at two positions: (2) at 5% local chord length (c) on the suction side (SS) and 10%c pressure side (PS), and (3) at 25%c SS and 10%c PS. Aerodynamic forces and far-field noise were measured at wind tunnel speeds of $U_0 = 44, 52, 60, 70, 80$ m/s and at 12 angles-of-attack from $\alpha = 0°, 2°, 4°, 5.5°, 9°, 10°, 13°, 16°, 18°, 20°, 21°, 23°$. Note that α corresponds to the geometric angle of attack, and no angle correction is made here.
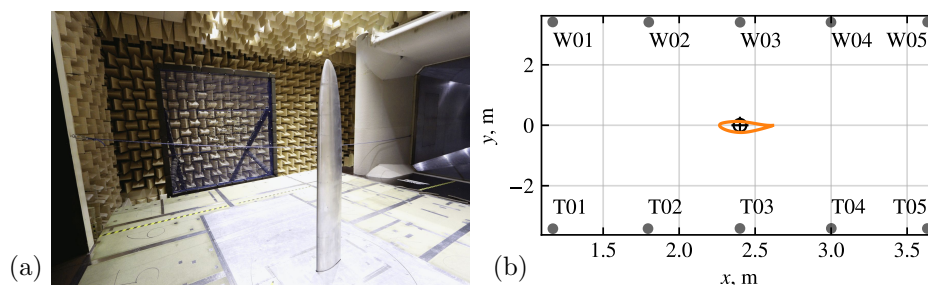

Figure 1: (a) Experimental setup in the NWB and (b) a sketch of the free-field microphone positions: (W01···5; T01···5) around the model. The flow is from left to right.

Analysis of the far-field noise using the coherent output power (COP) method [1] produces a large coherence, γ, and a phase angle, θ, around π within a frequency range that characterizes trailing-edge noise as shown in figure 2. It follows from the coherence identity that the measured far-field noise spectrum can be discriminated into its coherent, i.e. COP, and incoherent parts in figure 3a. With increasing α, the coherent part has a maximum that shifts to a lower frequency, whereas the incoherent part has increasing relevance at higher frequency. Their scaling with the Mach number, Ma, is shown in figure 3b. The coherent part scales according to $Ma^{\approx 5}$ of an edge radiated noise [2] and the incoherent part scales with $Ma^{>5}$ from $\alpha \geq 9°$. Sound localization with the phased microphone array shows that the incoherent part consists of the tip noise at a high frequency and noise at an intermediate frequency that seems to be detached from the edge. These sound maps are shown in figure 4.

The present result shows that the elements of flow separation noise consist of a low-frequency edge-radiated noise that can be modeled using a turbulent wall-pressure model [3] and a mid-frequency noise that is, seemingly, detached from the edge. So far, the modeling of the latter is not fully understood. The full paper will present the methodology, aerodynamic results, and noise source localization.
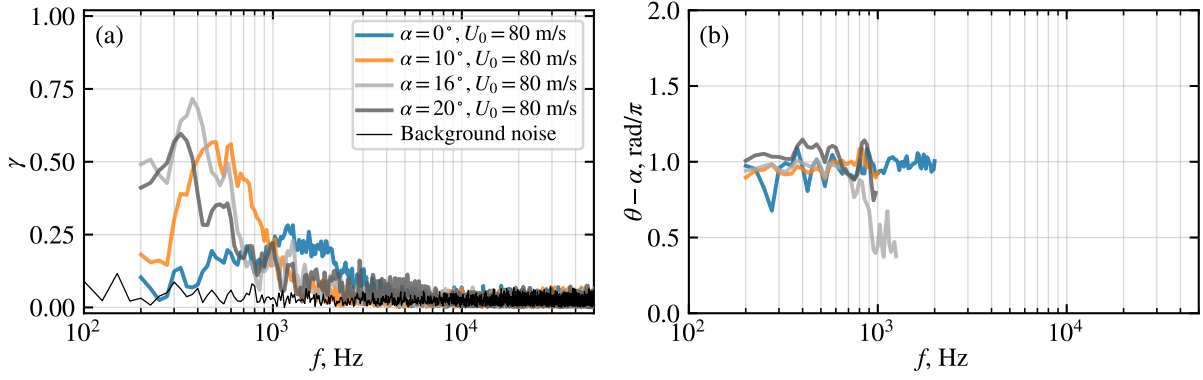
Figure 2: (a) Coherence spectra and (b) phase angle spectra of 4 αs (*Trip* 05/10) and the background noise of the wind tunnel.
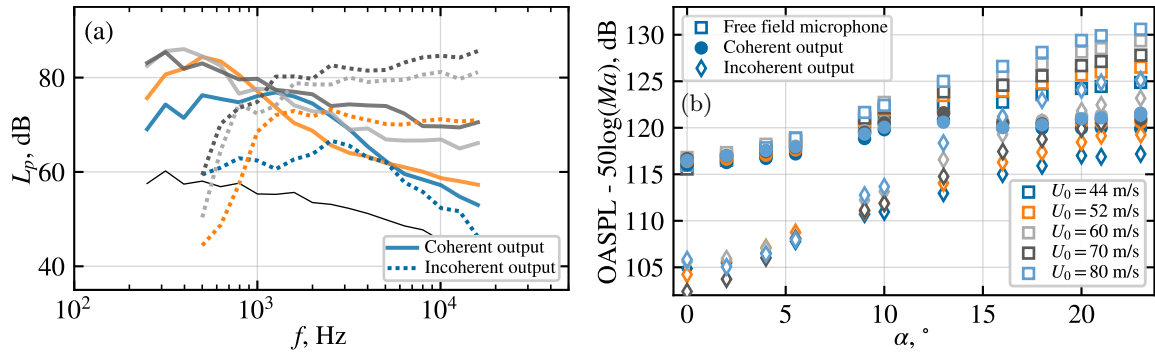

Figure 3: (a) One-third octave band spectra, the line color follows the legend in figure 2a and (b) OASPL vs α.
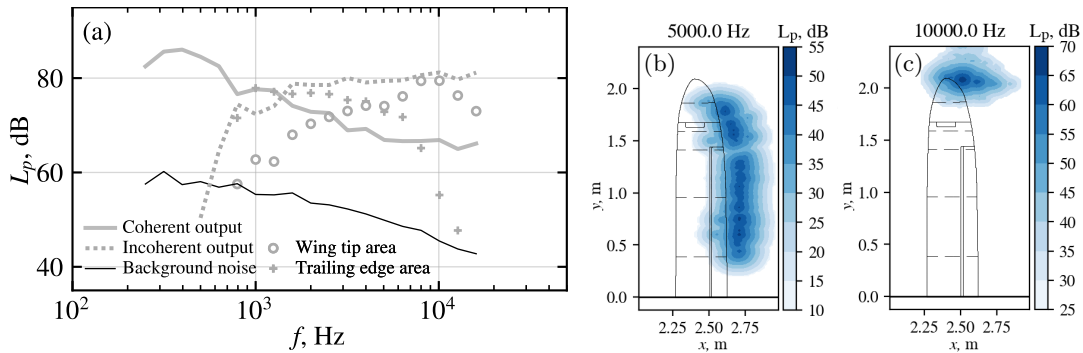
Figure 4: Noise source maps of the NACA 64-618 wing model, $\alpha = 16°$ and $U_0 = 80$ m/s: (a) breakdown of the noise spectrum, (b) around the trailing edge and (c) around the tip at a selected frequency.

References

[1] Florence V. Hutcheson and Thomas F. Brooks. Measurement of Trailing Edge Noise Using Directional Array and Coherent Output Power Methods. *International Journal of Aeroacoustics*, 1(4):329–353, 2002.

[2] J. E. Ffowcs Williams and L. H. Hall. Aerodynamic sound generation by turbulent flow in the vicinity of a scattering half plane. *Journal of Fluid Mechanics*, 40(04):657, 1970.

[3] Alexandre Suryadi. Prediction of Trailing-Edge Noise for Separated Turbulent Boundary Layers. In A. Dillmann, G. Heller, E. Krämer, C. Wagner, C. Tropea, and S. Jakirlić, editors, *New Results in Numerical and Experimental Fluid Mechanics XII*, volume 142 of *Notes on Numerical Fluid Mechanics and Multidisciplinary Design*, pages 769–779. Springer, Cham, 2018.

Mitteilung

Fachgruppe: Strömungsakustik

Broadband noise simulation of small coaxial rotor configurations

Jianping Yin

German aerospace center DLR, Institut für Aerodynamik und Strömungstechnik Institution,Departtment Helicopter, Lilienthalplatz 7, 38108 Braunschweig,jianping.yin@ dlr.de

1. Introduction

In the development of a multirotor propulsion system for Urban Air Mobility vehicles (UAM) or for small-scale drones, noise may become a potential major barrier to market success as the rising concern for environmental issues and increasingly stringent noise regulation. Similar to the rotorcraft, the main sources of the noise from the multirotor system consists of rotor tonal and broadband noise. In contrast to the rotorcraft, broadband noise may become a dominant noise source for rotors with low tip Mach number or disturbed rotor inflow, which is the case in multirotor configurations. The contributions of the broadband noise, especially in the multirotor configurations, has not been studied extensively. To further understand the noise radiation and propagation for multirotor system configurations, the GARTEUR Action Group HC/AG-26 [ref.1] is established. The present studies are part of the activities conducted within this group.

2. DLR methodologies and multirotor model

Broadband noise is a stochastic noise source. A direct computation of broadband noise from turbulent boundary layers (BL) using CFD or CAA still requires a very significant effort, especially for the rotor configurations. DLR broadband noise code (BbaN) [ref.2] was derived according to Brooks, Pope, and Marcolini airfoil self-noise prediction model (BPM model) [ref.3]. The accuracy of predictions depends on a number of factors including the accuracy of the BL module used, how well the aeroacoustic scaling is determined and effects of flow unsteadiness. To overcome some of the limitations, an approximate boundary layer analysis based on the inviscid potential flow solution from DLR's Unsteady Panel Method (UPM) was applied. The tonal noise is obtained utilizing a coupled simulation of the UPM-Code and the DLR Ffowcs-Williams-Hawkins APSIM-Code. This process chain has already been successfully applied to a number of propeller and helicopter investigations [ref.4,5]. Therefore, validations in this work focus on the BbaN with the experiment data. The predictions will be analyzed and compared with the test results. This paper will focus on the results from the numerical and wind tunnel activities conducted by DLR.

The multirotor experimental data for acoustics were obtained in DLR's Acoustic Wind tunnel in Braunschweig (AWB). In this paper, the data acquired with 13 inches diameter (D=330.2 mm) and 7 inches (177.8 mm) pitch beechwood rotors from the German small propeller manufacturer Xoar Electric (Xoar PJN BW 13x7 rotor) is used. The rotor rig was designed to extend the capabilities of the facility to meet the requirements of simultaneous measurements of multiple rotors under hover and forward flight conditions, e.g. Figure 1. Using this setup, several rotor configurations can be investigated; isolated, coaxial, and tandem with vertical and lateral offset. A coupled simulation utilizing the DLR UPM-Code with BL-modelling for flow field computations and the BbaN code for a subsequent computation of the

broadband noise emissions was performed.

3. Results and discussion

Figure 2 left shows an example of the comparisons of 1/3 Octave spectrum with experiment for a coaxial rotor configuration in hover at two microphones. Both the numerical simulation (BbaN) and test indicate that tonal noise is the dominant source for the frequencies below 8000Hz while above 8000Hz the broadband noise is dominant. The comparison shows a very good agreement when using the BbaN method. In contrast the results using the original BPM do not capture the shape of the broadband noise indicating that the BL information provided by the BPM model is not suitable for this rotor. In the final paper, the comparisons between the simulation and experimental results will be extended. The details of the method for the broadband noise and the pros and cons will be discussed.
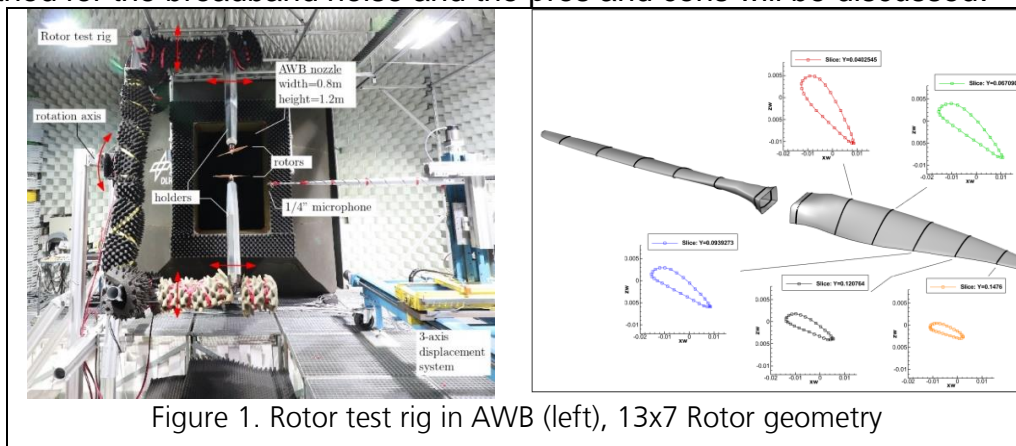

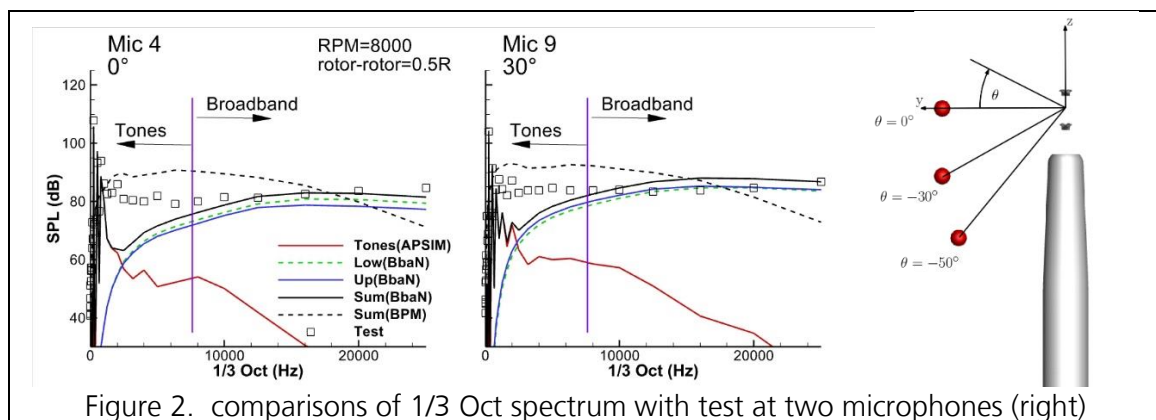Figure 1. Rotor test rig in AWB (left), 13x7 Rotor geometry

Figure 2. comparisons of 1/3 Oct spectrum with test at two microphones (right)

Literatur:

[1] Yin, J., De Gregorio, F., Petrosino, F., Rossignol, K-S, Schwarz, T., Cotte, B., Brouwer, H., Clero, F., Mortain, F., Reboul, G., Zanotti, A., Vigevano, L., Gibertini, G., Bernardini, G. Schmähl, M., Kaltenbach, HK., Pagliaroli, T., Keßler, M., Barakos, G., Ragni, D., Testa, C.: Noise Radiation and Propagation for Multirotor System Configurations. In: Terms of Reference for the GARTEUR Action Group HC/AG-26, December 2021

[2] Yin, J.: DLR BROAD BAND NOISE CODE (BbaN), in DLR-Projekt URBAN-Rescue, D4.2.2c, 2023

[3] Thomas F. Brooks, D. Stuart Pope, and Michael A. Marcolini, "Airfoil Self-Noise and Prediction", NASA Reference Publication 1218, July 1989.

[4] Rossignol, K.-S., Yin, J., Rottmann, L.: Investigation of Small-Scale Rotor Aeroacoustic in DLR's Acoustic Wind Tunnel Braunschweig, in 28th AIAA/CEAS Aeroacoustics 2022 Conference., Southampton, UK, 2022

[5] Rossignol, K.-S., Yin, J., De Gregorio, F., Visingardi, A., Ceglia, G., Barbarino, M., Petrosino, F.: Aeroacoustics of Small Contra-Rotating Co-Axial Rotors in Hover and Forward Flight, in 30th AIAA/CEAS Aeroacoustics 2024 Conference, Rom, Italy.

Mitteilung

Fachgruppe: Strömungsbeeinflussung

Numerical Study for Active Flow Control on High-Lift Configurations by Oscillating Dropped-Hinge Flaps

Paloma García-Guillén, Johanna Kärner, Christian Breitsamter
Chair of Aerodynamics and Fluid Mechanics, Technical University of Munich,
Boltzmannstr. 15, 85748 Garching bei München, p.garcia-guillen@tum.de

Enhancing the operational efficiency of modern transport aircraft is essential for achieving future goals in environmental and economic sustainability within the aviation sector. The emission reduction objectives established by the ACARE Flightpath 2050 [1] provide a foundational framework for these efforts and underscore the need for innovations in aircraft design and performance. In the field of aerodynamics, a key area of focus is the optimization of flight-relevant systems such as high-lift devices. Various technical measures are employed that passively or actively influence the airflow to increase lift. Classic methods for passive flow control include high-lift devices such as slats and flaps. However, there is a growing focus on active flow control (AFC) systems, and the investigation of unsteady flow behavior on lift generation has become a pivotal topic for many scholars. These concepts can alleviate adverse effects related to the aeromechanics of lifting surfaces, such as by delaying stall in fixed-wing aircraft. Building on this capability, the potential to enhance the maximum lift coefficient by using oscillating flaps is addressed.

Within the DFG project *Active Flow Control through Oscillation of a Dropped-Hinge Flap*, the use of oscillating adaptive dropped-hinge flaps (ADHF) is investigated experimentally and numerically. Modern fly-by-wire aircraft already provide the architecture that allows for periodic oscillation of the flaps when integrated with an adapted actuator concept. Ruhland and Breitsamter [2] conducted numerical studies showing that an oscillating dropped-hinge flap (DHF) can significantly influence the separation topology of the flow. Flow separation could be suppressed beyond the maximum static flap deflection angle. However, understanding the associated flow physics needs further detailed basic investigations.

The current paper introduces a study on a high-lift configuration of a generic transport aircraft featuring an oscillating ADHF, which includes a single-segment flap and a slat as high-lift devices. The geometry studied is a rectangular wing with quasi-two-dimensional flow. First, numerical studies with steady deployed high-lift systems are conducted to identify the parameter space and for later comparative analysis. Subsequently, the factors influencing the performance of the high-lift system with harmonic flap oscillations are determined. Free design parameters in this study include the reduced frequency k and the amplitude $\Delta\delta$ of the oscillation. The focus is set on assessing how these parameters impact the boundary layer topology, gap flow, and aerodynamic properties such as lift, drag, and pitching moment coefficients. The hinge point position of the ADHF is fixed to minimize the number of independent influencing factors. Subsequently, the identified operating point is used for a detailed analysis of specific system parameters, such as flap gap and overlap. Herein, characteristic flow regions are selected from the numerical data for detailed analysis.

In addition, the influence of the Reynolds number is investigated. For a fundamental understanding of the unsteady flow and separation topologies on the ADHF, numerical investigations are conducted under typical wind tunnel conditions at low Reynolds numbers of $Re = 0.5 \cdot 10^6$ and $Re = 2 \cdot 10^6$. In further investigations, numerical simulations will be analyzed and validated using experimental data. Furthermore, the current investigations are conducted for a Reynolds number of $Re = 30 \cdot 10^6$ to simulate realistic flight conditions of modern transport aircraft.

STAB

The numerical flow simulations are conducted using the ANSYS Fluent flow solver, employing unsteady Reynolds-averaged Navier-Stokes (URANS), as well as hybrid URANS and large-eddy simulation (LES) approaches. The dynamic mesh motion feature enables the flap's oscillation. All required CFD meshes are generated with the ANSYS ICEM CFD meshing tool.

A validation of the numerical setup for steady deployed high-lift systems is performed through comparison with experimental C_P-data from investigations by Lin and Dominik on the NASA high-lift research airfoil [3], as shown in Fig. 2. The quasi-two-dimensional flow field is simulated at a Reynolds number of $Re = 16 \cdot 10^6$, a Mach number of $Ma = 0.2$, and an angle of attack of $\alpha = 20°$ using a hybrid URANS-LES approach. The used block-structured mesh depicted in Fig.2 comprises approximately 15 million cells.
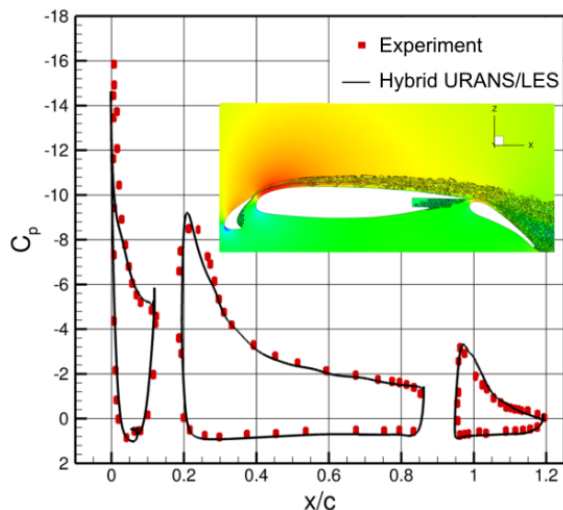

Figure 1: Comparison between experimental data from pressure measurements by Lin and Dominik [3] and numerical data from URANS/LES Simulations of the NASA high-lift research airfoil ($Re = 16 \cdot 10^6$, $Ma = 0.2$, $\alpha = 20°$).
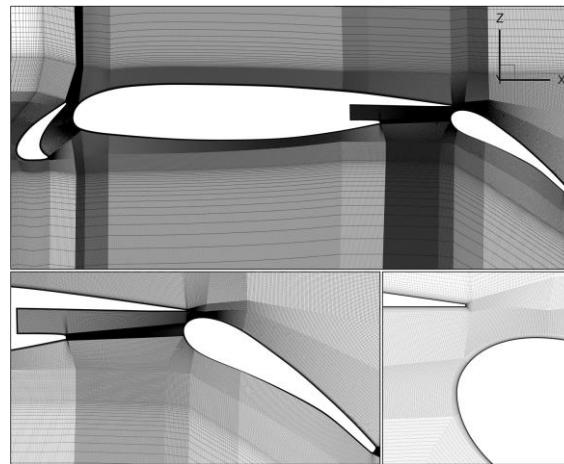
Figure 2: Block-structured grid with a detailed view of the refined mesh around the single-segment flap and the gap area.

Experimental data for oscillating trailing-edge flaps at high Reynolds numbers are not available in literature to the authors' knowledge. The intended insights contribute to an evaluation of how AFC via an oscillating ADHF contributes to lift enhancement improving future high-lift systems.

References

[1]   Flightpath 2050: Europe's vision for aviation: maintaining global leadership and serving society's needs. Luxembourg: Publications Office of the European Union, 2011. DOI: 10.2777/50266.

[2]   Ruhland, J. and Breitsamter, C. Numerical analysis of high-lift configurations with oscillating flaps. CEAS Aeronautical Journal 12.2, pp. 345–359, 2021. DOI: 10.1007/s13272-021-00498-7.

[3]   Dominik, C. J.; Lin, J. C. Parametric Investigation of a High-Lift Airfoil at High Reynolds Numbers. Journal of Aircraft 34.4, pp. 485–491, 1997. DOI: 10.2514/2.2217.

Acknowledgement

STAB

Mitteilung

Fachgruppe: Strömungsbeeinflussung

Aktive Böenlastabminderung am hochgestreckten Tragflügel mittels statischer und dynamischer Lastumverteilung

Marco Hillebrand, Thorsten Lutz
Universität Stuttgart, Institut für Aerodynamik und Gasdynamik
70563 Stuttgart, marco.hillebrand@iag.uni-stuttgart.de

Eine Reduzierung des CO_2-Verbrauchs von Flugzeugen kann durch die Erhöhung der Flügelstreckung erreicht werden. Im Rahmen des LuFo VI Projekts INTELWI wurde eine hochgestreckte, hocheffiziente Flügel-Rumpf-Konfiguration mit zwei Triebwerken mit sehr hohem Nebenstromverhältnis untersucht. Ein zentraler Aspekt beim Entwurf von Flügeln mit hoher Streckung sind die durch Böen und Manöver verursachten Lasten. Zur Reduktion dieser Lasten wurde die aerodynamische Wirksamkeit eines aktiven Böenlastabminderungssystem untersucht. Dieses System nutzt spannweitig segmentierte Vorderkantenklappen, modelliert als Droop Nose zur Torsionskontrolle, und spannweitig segmentierte Hinterkantenklappen zur Reduzierung des Biergemomentes. Bisher wurde das Böenlastabminderung-Potential mittels dynamischen Ausschlag untersucht. Eine weitere Methode zur Lastabminderung ist die statische Lastumverteilung (SLR) sowie eine Kombination von SLR und dynamischem Klappenausschlag. Dabei wird ein Klappen-Pre-Set definiert, das die aerodynamischen Lasten bei konstantem c_L zur Flügelwurzel hin verschiebt und somit das Biegemoment im horizontalen Reiseflug beim Durchflug von Turbulenzen reduziert.

Diese Arbeit untersucht das Lastabminderungspotential durch statische Lastumverteilung. Hierfür wurden URANS-Simulationen am starren sowie mit zeitechter Strukturkopplung am hochgestreckten Tragflügel durchgeführt. Für den elastischen Flügel wurden Fluid-Struktur-gekoppelte Simulationen basierend auf einem Modalmodell herangezogen, um die aeroelastischen Effekte während der Böenlastabminderung zu untersuchen. Die Lastumverteilung wird in zwei Hauptkonzepte unterteilt: die Verwendung von spannweitig segmentierten Hinterkantenklappen und die kombinierte Nutzung von Vorder- und Hinterkantenklappen. Für beide Konzepte wurde die Böeninteraktion sowohl bei statischen Klappen als auch mit zusätzlichem dynamischen Klappenausschlag analysiert. Abbildung 1 zeigt links den Verlauf des c_p sowie die maximalen Ausschlagswinkel für die Lastumverteilung mittels Hinterkantenklappen. Rechts ist das Konzept des kombinierten Vorder- und Hinterkantenklappenausschlags dargestellt. Die in Abbildung 1 dargestellten maximalen Klappenausschlagswinkel wurden mit zwei Ranbedingungen definiert. Der statische Klappenausschlag ist so konzipiert, dass keine Ablösung auftritt und der Auftriebsbeiwert im Reiseflug unverändert im Vergleich zum Zustand ohne
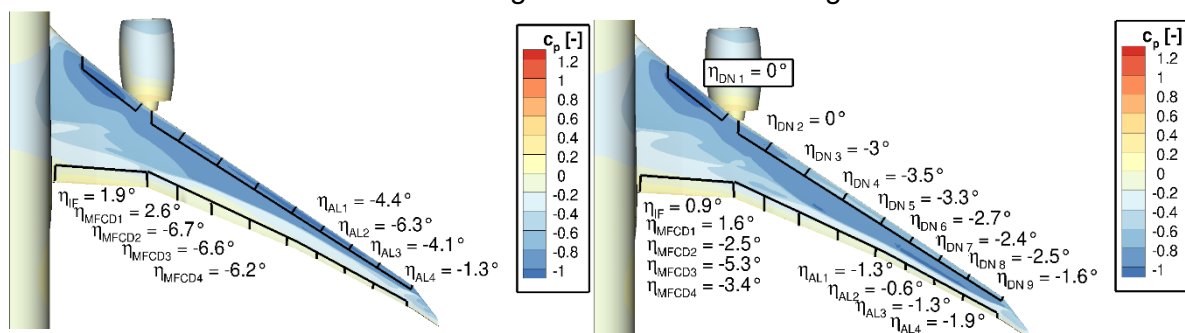

Abb. 1: Darstellung der Ausschlagswinkel für die Lastumverteilung. Auf der rechten Seite für das Konzept mit Hinterkantenklappen, links das Konzept mit kombinierten Ausschlag von Vorder- und Hinterkantenklappe

Klappenausschlag bleibt. Zwei limitierende Faktoren bestimmen die Lastumverteilung. Zum einen würde eine weitere Auslenkung der inneren Flügelklappe nach unten eine Hinterkanten-Ablösung erzeugen, die sich bei weiterem Ausschlag verstärkt. Zum anderen ist es nicht möglich, mehr Auftrieb am Außenflügel abzubauen, ohne im Bereich der Querruder eine stoßindu-zierte Ablösung zu verursachen. Infolgedessen verringert sich das Biegemoment an der Flü-gelwurzel ($M_{B,r}$) durch die Lastumverteilung mit Hinterkantenklappen um 11%, während das Torsionsmoment an der Flügelwurzel ($M_{T,r}$) um 5% erhöht wird. Bei kombiniertem Ausschlag von Vorder- und Hinterkantenklappen kann das $M_{B,r}$ um 8% und das $M_{T,r}$ um 24% reduziert werden.

Um das Potenzial der Lastabminderung während der Böeninteraktion zu quantifizieren, wer-den das $M_{B,r}$ sowie das $M_{T,r}$ herangezogen. Beide Verläufe sind in Abbildung 2 für alle Kon-zepte der Lastabminderung sowie für die Böeninteraktion ohne Lastabminderung (schwarz) dargestellt. Die rosa und lilafarbenen Kurven repräsentieren die SLR mit Hinterkantenklappen, während die orangefarbenen Verläufe die SLR mit einem kombinierten Ausschlag von Vorder- und Hinterkantenklappen (DN&TEF) darstellen. Hierbei repräsentieren die Volllinien den elas-tischen und die Strich-Punkt Linie den starren Flügel.
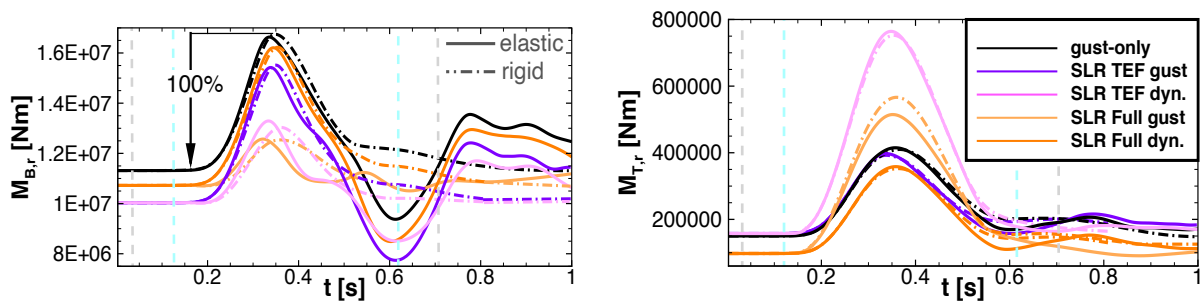

Abb. 2: Darstellung des $M_{B,r}$ sowie $M_{T,r}$ über die Zeit für die statische Lastumverteilung mittes Hinterkan-tenklappenausschlag (SLR TEF) und einem kombinierten Ausschlag von Vorder- und Hinterkantenklap-penausschlag (SLR Full). Zudem ist jeweils die Böeninteraktion mit dem statischen (gust) sowie mit ei-nem zusätzlichen dynamischen Klappenausschlag (dyn.) dargestellt.

Es zeigt, dass ohne zusätzlichen dynamischen Klappenausschlag das Potential zur Verringe-rung der Böenbelastung geringer als mit ist. Für die SLR mit DN&TEF wird das $M_{B,r}$ des elas-tischen Flügels um -9,8% reduziert. Beim starren Flügel beträgt die Verringerung -9,5%. Das $M_{T,r}$ kann für die SLR mit TEF für den elastischen Flügel um -5% reduziert werden. Die Verrin-gerung für die SLR mit DN & TEF beträgt -19,9%. Ein besseres Lastabminderungspotenzial ist für die SLR mit TEF zu entnehmen. Hier verringert sich das $M_{B,r}$ um 24% für den elastischen Flügel und um 23% für den starren Flügel. Das Lastabminderungspotential erhöht sich, wenn die Steuerflächen zusätzlich während der Böeninteraktion dynamisch ausgelenkt werden. So kann für den elastischen Flügel das $M_{B,r}$ um -76% für die SLR mit DN & TEF und um -54% für die SLR mit TEF reduziert werden. Bei der SLR mit TEF und zusätzlichem dynamischen Klap-penausschlag erhöht sich das $M_{T,r}$ für den elastischen Flügel um 117%. Für die SLR mit DN & TEF liegt eine Erhöhung des $M_{T,r}$ von 40.3% vor.

Somit wurde ein unterschiedliches Potential zur Böenlastabminderung zwischen SLR und der SLR mit dynamischen Klappenausschlägen gezeigt. Mit letzterem ist es möglich die böenin-duzierten Lasten hinsichtlich des $M_{B,r}$ stärker zu reduzieren als mit rein statischem Ausschlag. Zusätzlich wird im Paper der Einfluss der aeroelastik auf das Lastabminderungspotential dis-kutiert.

STAB

Mitteilung

Fachgruppe: Strömungsbeeinflussung

Finding an optimal control strategy to restrict flow separation in an experimental backward-facing ramp flow by means of reinforcement learning

Tobias Schesny, Viktoria Schilling, Alexandra Müller, Ben Steinfurth, Julien Weiss
TU Berlin, FG Aerodynamik, ben.steinfurth@tu-berlin.de

The field of active separation control (ASC), involving methods to prevent or delay flow separation by supplying external energy, has given rise to successful demonstrations for more than a century. These include Prandtl's cylinder experiment (1904), studies reported in Lachmann's seminal compilation (1961) and the work by Wygnanski, Greenblatt and co-authors (late 1990s). Despite the large body of literature, ASC has not reached a breakthrough in the aviation industry so far, which is arguably due to an excessive energy consumption. Specifically, common techniques involve the ejection of compressed air into the boundary layer such as to increase the near-wall momentum flux. The requirement for large amounts of mass flow, however, renders the approach unattractive.

Recent progress in the field of Deep Learning suggests that artificial neural networks can be used to great effect for the optimization of ASC parameters. In particular, reinforcement learning (RL) appears to be suited for this task. Irrespective of the specific application, an RL framework involves an *agent* that interacts with its *environment*. By performing *actions* and receiving feedback in the form of *observations* that allow for (partial) insight into the system *state*. By *rewarding* the agent for certain actions or combinations thereof, a strategy emerges to maximize the reward by learning optimal state-action pairs.

Using this approach, Rabault et al. (2019) demonstrated that the drag of a cylinder ($Re = 100$) can be reduced by controlling the flow rates of two jets ejected at opposite sides. In this scenario, actions are represented by adjusting the mass flow, and observations are provided by a numerical simulation.

The objective in the current study is to test the capabilities of RL subjected to experimental conditions online (i.e., during a wind tunnel measurement). In a closed-loop, low-speed wind tunnel, the flow over a backward-facing ramp ($Re_{\vartheta} = 1000$) is manipulated by an array of five pulsed-jet actuators, all of which driven by the same square-wave signal. The latter is defined by the pulse duration t_{p} and the time delay between successive pulses t_{off}. Since both the control authority and the mass-flow consumption depend on these time scales, their adjustment has significant implications with respect to the flow control performance (Steinfurth, 2022). Therefore, for a constant mass-flow, we let the action space of our RL framework span incremental changes of t_{p} and t_{off} The state of the system is returned by eight wall shear-stress sensors installed along the test section center line. Based on these sensors, the reward is defined such as to enforce actions that reduce the extent of the region of mean reverse-flow. The strategy is modified by means of proximal policy optimization over multiple episodes, each of which consist of five action-state pairs for which the cumulated reward is evaluated.

STAB

The adjustment of pulse parameters, namely t_{p} and t_{off}, is shown in Figure 1 (left) for one episode at the beginning and one at the end of training, respectively. The corresponding distributions of the forward-flow fraction (final timestep for each episode) are presented on the right-hand side of the same figure along with the unforced configuration.
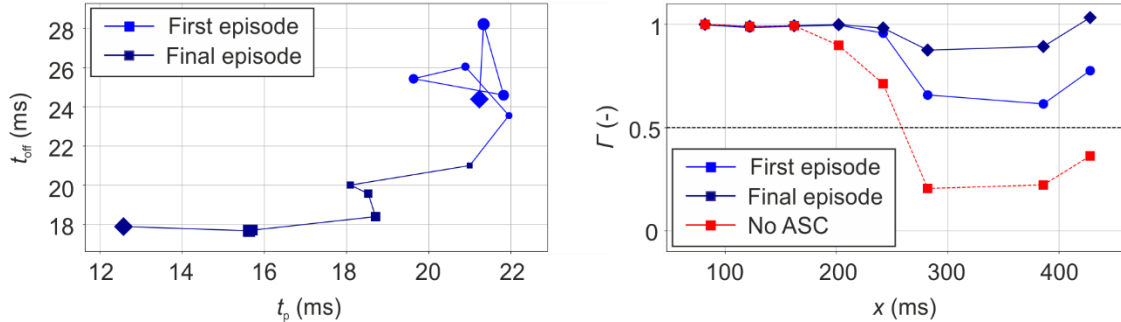

Figure 1: Adjustment of excitation parameters at the beginning and end of training (left) and corresponding forward-flow fraction distributions along the ramp (right)

It is important to retain in mind that the ejected mass-flow was the same for both ASC cases shown in Figure 1. Yet, larger forward-flow fractions are achieved at the end of training (dark blue curve). This is explained by an optimized adjustment of forcing time scales that are reduced from $\left(t_{\mathrm{p}}, t_{\mathrm{off}}\right) = (21,21)\,\mathrm{ms}$ where each episode was initiated to $\left(t_{\mathrm{p}}, t_{\mathrm{off}}\right) = (12,18)\,\mathrm{ms}$. This implicitly represents an increase of the actuation frequency and, more importantly, a reduction of the duty cycle ($t_{\mathrm{p}} < t_{\mathrm{off}}$). It was shown recently that the latter parameter effectively defines the control authority as a lower duty cycle results in an increased momentum input at a given mass-flow rate (Steinfurth, 2022).

Our full paper will contain an analysis regarding the influence of relevant hyperparameters pertaining to the chosen RL framework. Specifically, we plan to address the importance of the exploration rate, which propmts the agent to perform actions that are not deemed optimal according to the current strategy but allow to gather more information on state-action relations.

References

Greenblatt, D. and Wygnanski, I. J. (2000) *The control of flow separation by periodic excitation*, Prog. Aerosp. Sci 36(7).
Lachmann, G. V. (1961) *Boundary layer and flow control*, Pergamon Press, Oxford.
Prandtl, L. (1904) *Über Flüssigkeitsbewegung bei sehr kleiner Reibung*, Verhandlungen des III. Internationalen Mathematiker-Kongresses.
Rabault, J., Kuchta, M., Jensen, A., Réglade, U. and Cerardi, N. (2019) *Artificial neural networks trained through deep reinforcement learning discover control strategies for active flow control*, J. Fluid Mech. 865.
Steinfurth, B. (2022) *Flow physics of pulsed-jet actuation*, dissertation, TU Berlin.

STAB

Mitteilung

Fachgruppe: Strömungsbeeinflussung

<div align="center">

POD analysis of shock-wave / turbulent-boundary-layer interactions
under separation control

Deepak Prem Ramaswamy & Anne-Marie Schreyer
Institute of Aerodynamics, RWTH Aachen University, 52062 Aachen, Germany
d.ramaswamy@aia.rwth-aachen.de

</div>

Shock-wave / turbulent-boundary-layer interactions (SWBLIs) are complex flow phenomena, commonly encountered in many high-speed aerospace applications like transonic airfoils, supersonic air-breathing-engine inlets, etc [1]. A strong shock wave imposes a large adverse pressure gradient on the incoming boundary-layer and can lead to large-scale flow separation. To alleviate the associated detrimental effects, several flow-control techniques have been proposed and studied in literature. One effective approach is to use air-jet vortex generators (AJVGs), where small jets of air are injected into the incoming crossflow to generate streamwise vortices [2]. These vortices redistribute the momentum within the boundary layer, bringing high-momentum fluid close to the wall, and making the boundary layer more resistant to separation.

To assess the control effectiveness, we have performed streamwise/wall-normal and streamwise/spanwise PIV on AJVG-controlled SWBLIs of varying geometrical and flow parameters [3] [4] [5] [6]. In the present study, we apply proper orthogonal decomposition on the obtained datasets to identify the role of dominant coherent structures and consequently, improve the overall understanding of AJVG control mechanisms.
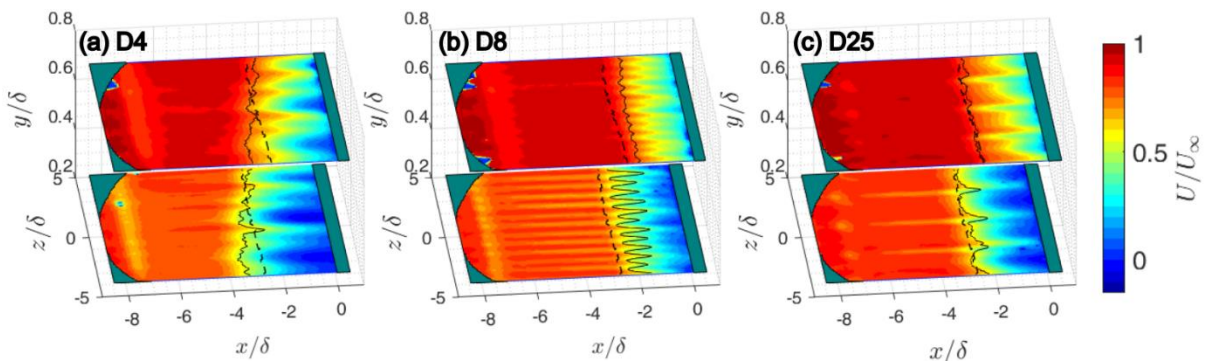

Fig 1. Mean streamwise velocity of AJVG-controlled SWBLI with (a) $D = 4d_{jet}$, (b) $D = 8d_{jet}$, and (c) $D = 25d_{jet}$ at $y = 0.24\delta$ and $y = 0.69\delta$ [5].

The experiments for this investigation were conducted on a 24° compression-ramp model in the trisonic wind tunnel facility at RWTH Aachen University at Mach 2.52 and $Re_\theta = 8225$. The incoming boundary-layer thickness (δ) at $x = -4.5\delta$ (upstream of the ramp corner at x=0) is 10.4mm. A single row of purely spanwise-injecting jets with a pitch angle of $\varphi = 45^o$ was placed at $x = -7.69\delta$. The tested AJVG parameters include (a) jet/jet spacings (D) [5], (b) jet-orifice shape [4], and (c) jet-injection-pipe length [6]. For the PIV analysis, two different setups were utilized: (a) a wall-parallel setup (WP-PIV) with the laser light sheet illuminating the streamwise/spanwise plane at $y = 0.24\delta$

and y = 0.69δ, and (b) a wall-normal setup (WN-PIV) with the laser light sheet in the streamwise/wall-normal plane at z = 0D and z = 1.5D. The WP-PIV images were acquired with a a Photron SA.5 highspeed camera (1024 px × 1024 px) and a Quantronix Darwin-Duo 100 Nd:YLF laser system (30mJ) at 1000 Hz. For WN-PIV, the images were acquired using four FlowSense EO 11M cameras (4008 px × 2672 px) and a Litron NANO-L pulsed Nd:YAG laser system (200mJ) operating at 6 Hz. For all cases, about 1000-1500 image pairs were acquired for data statistics. The acquired images were processed with an adaptive PIV algorithm with final interrogation window sizes of 32px by 32px at 75% overlap for WN-PIV and 16px by 16px at 50% overlap for WP-PIV. For further details on the experimental setups, see Refs [4] [5].

The obtained data quality is demonstrated using the mean streamwise velocity contour for three AJVG setups with jet-to-jet spacing of $D = 4d_{jet}$ (Fig. 1a), $D = 8d_{jet}$ (Fig. 1b), and $D = 25d_{jet}$ (Fig. 1c) at two wall-parallel planes: y = 0.24δ and y = 0.69δ. The black solid line depicts the location of the surrogate separation line, identified using the measured streamwise velocities. The dotted white line is the corresponding separation line for the uncontrolled baseline case.

With the injection of jets, a spanwise series of streamwise vortices is generated. The streamwise vortices induced by the AJVGs incited different control effects depending on the degree of interaction between adjacent vortices. The array with intermediate spacing (D8, see Fig. 1b) achieved the most favourable effects with reductions in separation length and area of about 25%. This reduction was brought about by the formation of stable, interacting streamwise-elongated coherent vortices downstream of jet injection and the associated entrainment of high-momentum fluid.

In the full article, we will discuss the results of snapshot-POD of the obtained PIV datasets to identify dominant structures of the flowfield and explain the differences in the control mechanism. POD is a statistical technique where ensembles of data are linearly decomposed into a series of spatially orthogonal modes, which are then ranked based on the turbulent kinetic energy. By combining the desired orders of the POD modes, the most energetic features of the flow field can be extracted. The outcomes will improve the understanding of AJVG parameters in controlling shock-induced separation.

References

[1] D. V. Gaitonde, „Progress in shock wave/boundary layer interactions," *Progress in Aerospace Sciences,* Bd. 72, pp. 80-99, 2015.

[2] R. Sebastian und A.-M. Schreyer, „Flow field around a spanwise-inclined jet in supersonic crossflow," *Aerospace science and technology,* Bd. 106, p. 106209, 2020.

[3] D. P. Ramaswamy und A.-M. Schreyer, „Control of Shock-Induced Separation of a Turbulent Boundary Layer Using Air-Jet Vortex Generators," *AIAA Journal,* Bd. 59, Nr. 3, 2021.

[4] D. P. Ramaswamy und A.-M. Schreyer, „Separation control with elliptical air-jet vortex generators," *Experiments in Fluids,* Bd. 64, Nr. 5, 2023.

[5] D. P. Ramaswamy und A.-M. Schreyer, „Effects of Jet-to-Jet Spacing of Air-Jet Vortex Generators in Shock-Induced Flow-Separation Control," *Flow, Turbulence and Combustion,* Bd. 109, pp. 35-64, 2022.

[6] D. P. Ramaswamy, R. Sebastian und A.-M. Schreyer, „Effects of jet-injection-pipe length on the flow-control effectiveness of spanwise-inclined jets in supersonic crossflow," *Physical Review Fluids,* Bd. 8, Nr. 11, 2023.

STAB

Mitteilung

Fachgruppe: Transportflugzeugkonfigurationen

Erweiterung des inversen 3D Flügel Entwurfsverfahrens für Anwendungen im Bereich der Verschneidung Flügel-Rumpf

Thade Gruner[1], Thomas Streit[2]

[1]TU Braunschweig, Universitätspl. 2, 38106 Braunschweig, Deutschland, t.gruner@tu-braunschweig.de
[2]DLR, Lilienthalplatz 7, D-38108 Braunschweig, Deutschland, th.streit@dlr.de

Das dreidimensionale inverse Entwurfsverfahren für transsonische Tragflügelgeometrien des DLR ermöglicht den Entwurf immer leistungsstärkerer und effizienterer Tragflügel. Nach der Vorgabe einer Zieldruckverteilung kann automatisiert zu einer dazugehörigen Geometrie gefunden werden. In der Prozesskette des Entwurfsverfahrens wird im inversen Modul aus der gegebenen Druckdifferenz zwischen der Druckverteilung der aktuellen Geometrie und der vorgegebenen Zieldruckverteilung die notwendige Geometriemodifikation iterativ berechnet [1],[2]. Die Druckverteilung der aktuellen Geometrie wird hier durch RANS-Lösungen bestimmt. Durch den starken dreidimensionalen Charakter der Strömung im Bereich des Übergangs vom Flügel zum Rumpf des Flugzeuges ist die Zieldruckverteilung nur durch Profilierung schwer zu erreichen. Es ist zu vermuten, dass auch Geometriemodifikationen der Verschneidungslinie von Flügel und Rumpf in spannweitiger Richtung zu der gewünschten Zieldruckverteilung führen können. Das inverse Entwurfsverfahren wird deshalb so erweitert, dass die berechneten Geometriemodifikation, zusätzlich zur Richtung innerhalb der Profilebene, anteilig in spannweitiger Richtung aufgeprägt werden können, um so im Bereich des Übergangs vom Flügel zum Rumpf eine Verbesserung im Entwurf von Flügelgeometrien zu erhalten.

Die Validierung der Verfahrensänderung erfolgt an einem konstruierten Beispiel. Es folgt ein Vergleich des originalen Verfahrens mit dem neu implementierten Verfahren.
Für alle Untersuchungen wurde eine strukturierte Diskretisierung der „ECOWING-Konfiguration" [3] des DLR verwendet und die Strömungslösung mit dem Strömungslöser „Flower" erzeugt.
Die Zieldruckverteilung für die Validierung wird durch eine vorgegebene Verschiebung der Verschneidungslinie von Flügel und Rumpf in spannweitiger Richtung erzeugt. Diese Verschiebung ist cosinusförmig und hat ihr Maximum an der Flügelvorderkante und wird in Richtung Hinterkante zu Null. Die Verschiebung der Verschneidungslinie und die Anpassung des Rechengitters sind in Abbildung 1a zu sehen. Abbildung 1b zeigt die Druckverteilungen der Ursprungsgeometrie und der modifizierten Geometrie bei 12,5% der Spannweite.
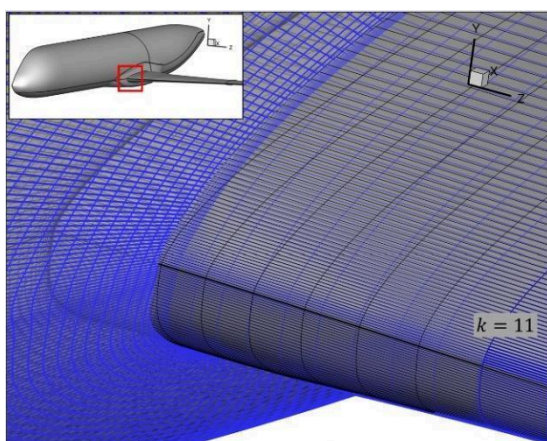

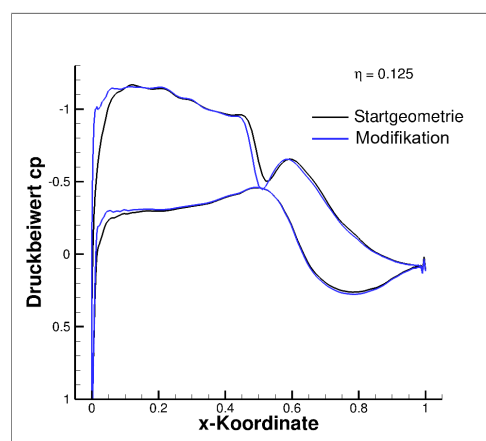**Abbildung 1a** Deformation der Diskretisierung für die konstruierte Zieldruckverteilung [4]

Abbildung 1b Druckverteilungen der Geometrien

Abbildung 2 zeigt das Ergebnis des modifizierten inversen Entwurfes nach Vorgabe der konstruierten Zieldruckverteilung, bei dem ausschließlich Geometriemodifikationen in spannweitiger Richtung zulässig waren. Bis auf einen kleinen Bereich an der Flügelvorderkante, ist das Verfahren in der Lage die vorgegebene Zieldruckverteilung sehr gut anzunähern. Auffällig ist, dass sich die erstellte Geometrie stark von der Geometrie der Zieldruckverteilung unterscheidet, obwohl sich die beiden Druckverteilungen stark ähneln.
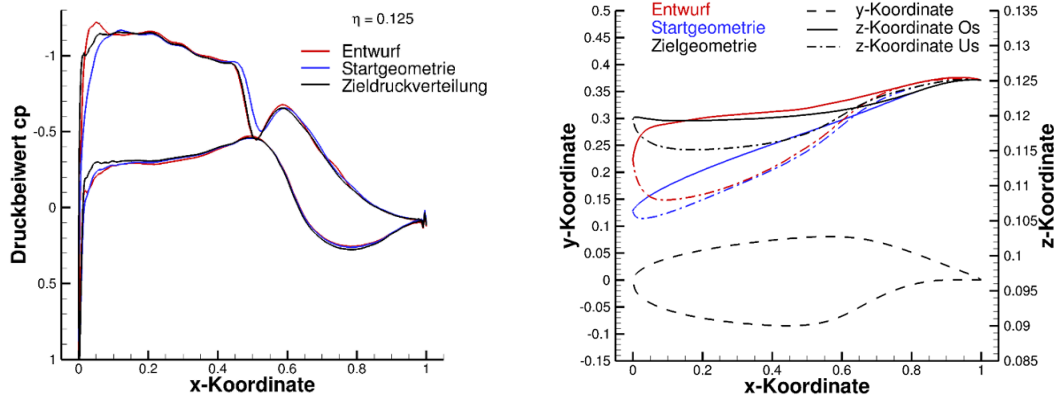
STAB

Abbildung 2 Ergebnis des Entwurfes in spannweitiger Richtung nach Vorgabe der konstruierten Zieldruckverteilung (links: Druckverteilung, rechts: Geometrie) [4]

Nachdem gezeigt wurde, dass das modifizierte inverse Entwurfsverfahren grundsätzlich konvergieren und Ergebnisse liefern kann, wird eine fiktive Druckverteilung als Zieldruckverteilung vorgegeben, die die Verdichtungsstoßposition im Bereich des Übergangs von Flügel zum Rumpf in Richtung Hinterkante verschiebt. Dabei werden die ursprüngliche Entwurfsmethode (Entwurf in y-Richtung), die modifizierte Entwurfsmethode (Entwurf in z-richtung) und eine gemischte Entwurfsmethode (in der die Geometriemodifikationen in beide Koordinatenrichtungen aufgeprägt werden) verglichen (siehe Abbildung 3).

Hier stellt sich heraus, dass der Entwurf in z-Richtung besonders gut den vorgegebenen Verdichtungsstoß abbildet. Das ursprüngliche Verfahren kann das Druckniveau bei 20% der Profiltiefe und auch die Nachexpansion nach dem Stoß besser abbilden. Der gemischte Entwurf kombiniert die Vorteile des ursprünglichen und des modifizierten Verfahrens und liefert insgesamt das beste Ergebnis.
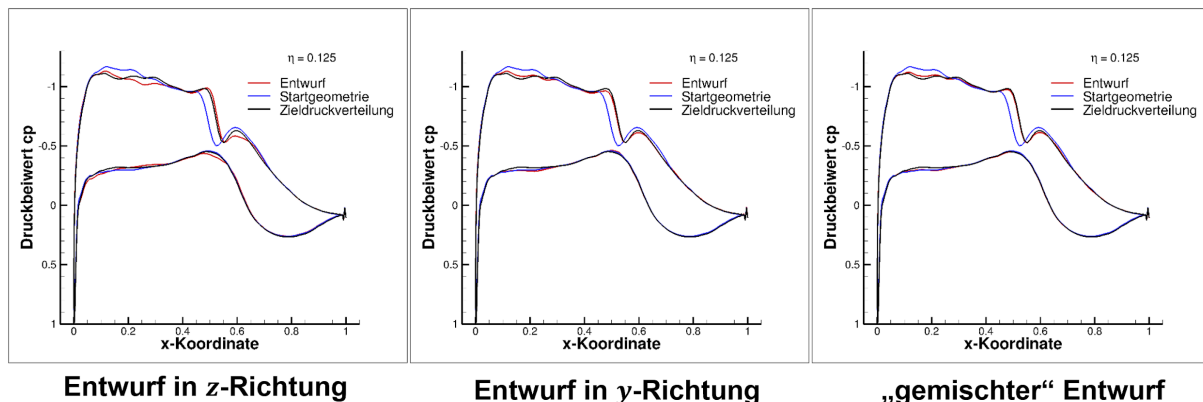

Entwurf in z-Richtung　　　**Entwurf in y-Richtung**　　　**„gemischter" Entwurf**

Abbildung 3 Vergleich der entworfenen Druckverteilungen nach Vorgabe einer Zieldruckverteilung mit anderer Verdichtungsstoßposition [4]

Neben den gezeigten Ergebnissen wurden weitere Beispiele untersucht und auch Untersuchungen bezüglich der Diskretisierung des Verfahrens durchgeführt. Hierzu werden Ergebnisse im Vollbeitrag gezeigt.

Es konnte gezeigt werden, dass eine Zieldruckverteilung im inversen Entwurf auch nur durch Modifikationen der Geometrie in spannweitiger Richtung erreicht werden kann. Das Ziel, das inverse Entwurfsverfahren des DLR zu erweitern, wurde damit erreicht und in Kombination mit dem ursprünglichen Verfahren konnte sogar eine Verbesserung in der Entwurfsqualität bewirkt werden.

Literatur
[1] Streit, T. and Hoffrogge, C., "DLR transonic inverse design code, extensions and modifications to increase versatility and robustness", Aeronautical J, 2017, **121**, (1245), pp 1733-1757, https://doi.org/10.1017/aer.2017.101
[2] Bartelheimer, W.: „Ein Entwurfsverfahren für Tragflügel in transsonischer Strömung". Dissertation. Köln: Deutsche Forschungsanstalt für Luft- und Raumfahrt, 1996
[3] Ruberte Bailo, J., Seitz, A., Streit, T, "Belly-Fairing Design Space Exploration for a Forward Swept Natural Laminar Flow Aircraft", 57th International Conference on Applied Aerodynamics, Bordeaux, France, March 1923.
[4] Gruner, T., "Erweiterung des inversen 3D Flügel Entwurfsverfahrens für Anwendungen im Bereich der Verschneidung Flügel-Rumpf", Studienarbeit, 2024, DLR-IB-AS-BS2024-52

Mitteilung

Fachgruppe: Transportflugzeugkonfigurationen

Gust Impact of a non-linear Folding Wing Tip

Andreas Molz, Christian Breitsamter
Chair of Aerodynamics and Fluid Mechanics, Technical University of Munich,
Boltzmannstr. 15, 85748 Garching bei München, andreas.molz@tum.de

Introduction

Within the scope of sustainable aviation, increasing the operational efficiency and diminishing pollutant emission is a key requirement for future transonic transport aircraft development. In an aerodynamic context, dynamic folding wing tips (FWT) show to possess great potential in the above mentioned requirements. One the on hand the folding wing tip enables higher wing spans, meanwhile meeting airport gate and runway limitations. On the other hand, attaching FWT to the main wing offers the potential to enhance the aircraft overall efficiency in combination with a potential gust load alleviation. Thus, extensive research is carried out on non-linear folding wing tips [1,2,3].

Based on the synergy effects of a folding wing tip, the LUFO VI-2 project GUSTAFO (Gust Load Alleviation by Folding non-linear Wing Tip) has been started in cooperation with RWTH Aachen and TU Berlin. The research focus is mainly set on the gust load alleviation potential with corresponding efficiency improvement.

Model Design

The focus of this work lies on the conduction of numerical investigations of non-linear folding wing tips under gust in cruise flight condition, considering wing tip deflections and their effect on the occurring wing loading. The following characterized wing configuration, called
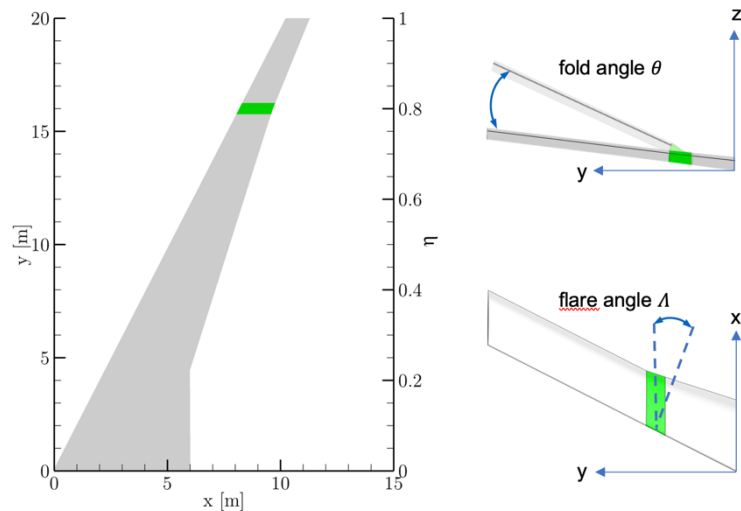

Figure 1: Geometry and hinge parameter of GUSTAFO 2.0 model

GUSTAFO 2.0, is part of the common research model (CRSM) 2020 designed for short and medium range operations. The utilized wing features a leading-edge sweep of $\varphi = 27°$ and a taper ratio of $\lambda = 0.166$. The wing features a root chord length of $c_r = 6\,m$, an aspect ratio of $AR = 14.7$ with a wing reference area $S_{ref} = 114.18\,m^2$. The hinge position is set to a wing span position of $\eta = 0.78$ and the angle between the hinge line and the aircraft longitudinal axis is called flare angle Λ. The deflection around the hinge line with respect to the wing tips initial position is defined by the fold angle θ. Figure 1 shows a sketch of the GUSTAFO 2.0 wing geometry, the hinge position and hinge angle definition.

Numerical Analysis

For the simulation procedure, the wing and wing tip are regarded as rigid and a geometrical rotation of wing tip around the hinge line is considered. As a result, URANS simulations are performed by utilizing ANSYS Fluent in conjunction with the Fluent inbuild Six Degree of Freedom solver (SDOF).

For the fluid dynamics setup, an URANS modeling approach is used. Specifically, the wing tip rotation is implemented by an User Defined Function (UDF). A pressure-based solution

method applies COUPLED pressure-velocity coupling to ensure mass conservation and to determine the pressure field. Spatial discretization is carried out using a second-order upwind scheme. The unstructured, tetrahedral mesh consists out of 31.3 mio elements($y^+ < 1$). The time step is limited by the dynamic mesh deformation of the FWT and is set to $t = 0.005\ s$. The differential movement equations of the FWT depending on the wing tip load are solved iteratively within the UDF, resulting in a fold angle θ. This coupling requires multiple consecutive exchange cycles between the wing loads and the UDF for each time step until the changes in the flow forces and wing tip movement converge. Subsequently, the corresponding nodes in the near field of the wing tip are shifted using the diffusion-based Dynamic Mesh approach.

Results

The studies are performed for a cruise Mach number $Ma = 0.78$ and a Reynolds number of $Re = 23.85 \cdot 10^6$, corresponding to an initial cruise altitude of $h = 35\,000\ ft$. The effect of different flare angles [0°, 25°, 45°] and spring stiffness for various gust frequencies and amplitudes are studied, focusing on the potential gust load alleviation and increase in aerodynamic efficiency.

Figure 2 and Figure 3 show exemplary results for a flare angle of $\Lambda = 25°$ at vertical gust impact featuring a frequency of $f_{gust} = 5\ Hz$ and amplitude of $A_{gust} = 0.1 U_\infty$. Figure 2 points out the potential root bending moment reduction of $\Delta C_{rwb} = 24.6\ \%$ of the nonlinear folding wing with respect to the initial wing tip under a fold angle $\theta = 0°$.
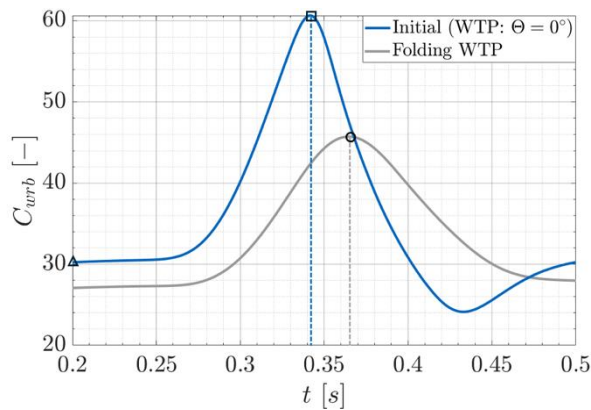

Figure 2: Gust load alleviation potential given by the root bending moment coefficient C_{wrb} for a flare angle $\Lambda = 25°$ compared to initial wing tip(fold angle $\theta = 0°$).
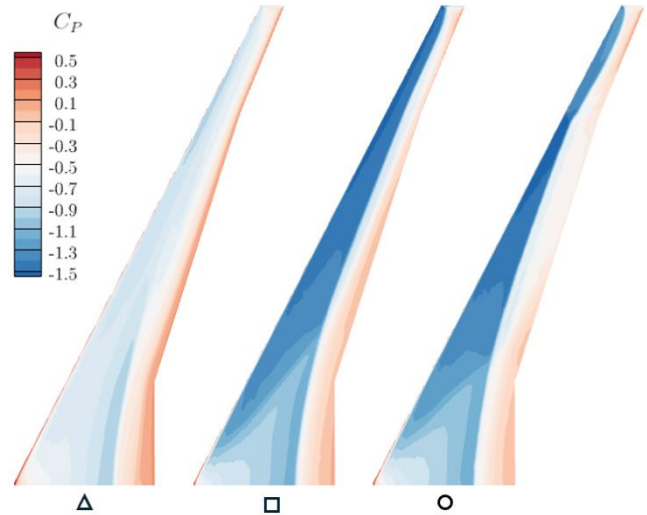

Figure 3: Pressure coefficient C_p distribution for cruise(t=0.2s) $\triangle$, initial wing($\theta = 0°, t = 0.342s$) $\square$ and gust impact of FWT ($\Lambda = 25°, t = 0.365s$) $\bigcirc$.

References

[1] A. Castrichini, T. Wilson, F. Saltari, F. Mastroddi, N. Viceconti, and J. Cooper. "Aeroelastics Flight Dynamics Coupling Effects of the Semi-Aeroelastic Hinge Device". In: Journal of Aircraft 57.2 (Mar. 2020), pp. 333–341. DOI: 10.2514/1.c035602.

[2] K. Chi-Wing Cheng, A. Cea Esteban, R. Palacios, A. Castrichini, and T. Wilson. "Nonlinear Gust Effects on Flexible Aircraft with Flared Hinged Wings". In: International Forum on Aeroelasticity and Structural Dynamics IFASD 2024. June 2024.

[3] T. Wilson, J. Kirk, J. Hobday, and A. Castrichini. "Small Scale Flying Demonstration of Semi Aeroelastic Hinged Wing Tips". In: International Forum on Aeroelasticity and Structural Dynamics IFASD 2019. June 2019

STAB

Mitteilung

Fachgruppe: Transportflugzeugkonfigurationen

On the Shifting of Wingtip Vortices due to Wingtip-Mounted Propellers

Michael Schollenberger, Thorsten Lutz, Ewald Krämer
Universität Stuttgart, Institut für Aerodynamik und Gasdynamik,
Wankelstraße 3 D-70563 Stuttgart, schollenberger@iag.uni-stuttgart.de

Motivation: Wingtip-mounted propellers (WTP) offer a way to increase the aero-propulsive efficiency of electric/hybrid-electric propeller driven aircraft. Different flow physical effects were proposed in literature as a reason of the WTP's abbilty to improve the efficiency. On the one hand the local effect of the wing's forward tilted force vector inside the area covered by the propeller slipstream (swirl recovery) and on the other hand the influence of the WTP on the wing-vortex system (vortex attenuation). In the literature, central WTP positions (thus with the propeller axis exactly aligned with the wingtip) have usually been investigated so far, through which a spanwise outward shift of the wingtip vortex core occurred. In Synyder and Zumwald [1, 2] it was therefore generally concluded for WTP that their effect on the aerodynamics of a wing is associated with an increase in the effective aspect ratio due to the larger vortex span (thus the spanwise distance between the left and the right vortex core). The aim of this study is thus to clarify whether this statement is generally valid and if the trajectory of the wingtip vortex core can be shifted depending on where the wingtip vortex rolls up relative to the quadrant of the propeller slipstream. Thus the impact of the quadrantal angle of the WTP position relative to the wing is examined, see Fig. 1.

Geometrical and Numerical Setup: A WTP in tractor configuration positioned at x/c prop = −1.2 upstream of a rectangular wing with a chord c = 0.5m and inclined with α = 5°. The local propeller position (propeller axis) relative to the roll-up trajectory of the wingtip vortex is varied, thus the wingtip vortex rolls up in different quadrants of the propeller slipstream. The velocity inside the propeller slipstream differs depending on where the wingtip vortex is located, see Fig. 1. In the I. and II. quadrant, the propeller slipstream has an outward directed spanwise velocity component in contrast to the III. and IV. quadrant, where the spanwise velocity component is inward directed. In the II. and III. quadrant the slipstream has a downward directed vertical velocity component and in the IV. and I. an upward one. For better visualization, a propeller position angle ϕ is introduced which describes the quantrantal propeller position relative to the center of the wingtip against the clockwise direction. For example, with a propeller position of ϕ = 45° the tip vortex core is in the I. quadrant and with ϕ = 90° it will be between the I. and II. quadrant of the propeller slipstream. URANS simulations were performed with the second order finite volume solver TAU [3], developed by the DLR. The propellers are modelled by an time accurate actuator line method (ACL), implemented into the TAU code by the author [4]. Structured cells are utilized in the boundary layer, the area of the slipstream, and the wing wake. Unstructured cells are utilized in the farfield. To ensure an accurate resolution of the vortex core, the domain around the wingtip vortex is refined.

Results: The influence of the quadrantal WTP position on the global coefficients is shown in Fig. 2. The quadrantal position of the propeller hub was selected so that the propeller radius in relation to the wingtip is constant at r/R = 0.75. In terms of aerodynamic efficiency c_L/c_D, there is a clear maximum when the hub is at the beginning of the third quadrant, at ϕ ≈ 200° - when the propeller is positioned vertically just above the wing and slightly inwards in spanwise direction. In contrast, the aerodynamic efficiency is minimized when the vortex roll up takes place in the I. quadrant, at ϕ = 45° - when the propeller is positioned vertical below and spanwise outwards of the wing. For comparison, the values of the isolated wing and the central WTP position are also shown. This shows that the influence of the very localized position around the wingtip has a considerable influence on the overall effect of the WTP. Even if all quadrantal propeller positions show an improvement compared to the isolated wing, the dif-

STAB

ference between the minimum and maximum is approximately the same as that between the isolated wing and the central position.

The wingtip vortex core position is also shown in Fig. 2 in terms of the "vortex span", thus the effective span calculated with the vortex core span (derived from the flow data at 1.9c downstream of the wing trailing edge). As expected, for a roll-up of the wingtip vortex in the I. and II. quadrant, the vortex span is increased due to a spanwise outwards shifted vortex, for a roll-up in the III. and IV. quadrant due to a spanwise inwards shift, the vortex span decreases. A vertical downward shift (not shown) takes place in the II. and III. quadrant, an upward shift in the I. and IV. quadrant. Depending on its relative quadrantal position, the WTP is therefore able to shift the wingtip vortex in any direction.

In contrast to literature [1, 2], the results show that a positive effect of the WTP on the aerodynamic efficiency is not necessarily associated with an increase in the vortex span. On the contrary, in the case considered here, the maximum efficiency increase occurs at $\phi \approx 200°$ when the vortex span is reduced and almost minimal. At those positions which are most effective for the vortex shift at $\phi = 0 - 180°$ a smaller part of the wing is covered by the propeller slipstream and the swirl recovery effect is thus lower. Even if the vortex displacement has a positive effect on the aerodynamic efficiency, at least in this case the direct influence of the area covered by the propeller slipstream due to swirl recovery was found to be dominant and the possible positive influence of a vortex core shift is negligible.
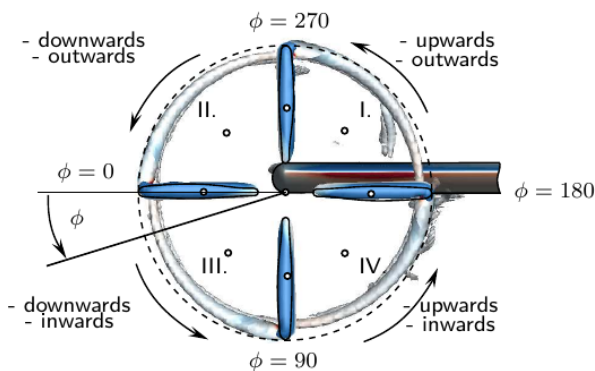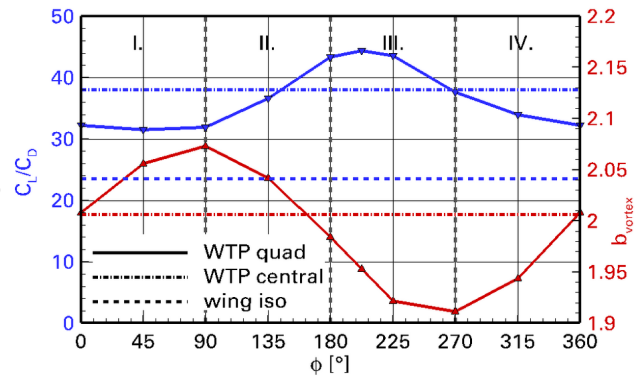

Fig. 1: Quadrantal position of the propeller   Fig. 2: Wing and propeller coefficients

Conclusion and Outlook: In conclusion, the quadrantal position of the propeller hub enables the wingtip vortex to be moved in the spanwise and vertical direction by a WTP. Depending on the quadrant of the propeller slipstream in which the roll-up of the wingtip vortex core takes place, the trajectory will be affected. The outward displacement of the wingtip vortex is not a general consequence of the increase in aerodynamic efficiency as stated by Snyder [1], but a relative effect of the quadrantal position. Contrary to expectations, the quadrantal position, in the case under consideration here, is optimal in terms of efficiency where the effective vortex span is even minimized. The increase in the effective vortex span associated with the shift of the wingtip vortex and correspondingly the effective aspect ratio (vortex attenuation) is of lesser importance here than the effect due the covering of the wing by the propeller slipstream (swirl recovery). The final paper will also discuss the influence of WTP inclination angles (inclined to the spanwise as well as the vertical axis) on the wingtip vortex core shifting.

References

[1] M. Snyder. Effects Of A Wingtip-Mounted Propeller On Wing Lift, Induced Drag, and Shed Vortex Pattern. PhD thesis, Oklahoma State University, Faculty of the Graduate College, 1967.
[2] M. Snyder and G. Zumwalt. Effects of Wingtip-Mounted Propellers on Wing Lift and Induced Drag. Aircraft Journal, 6(5):392–397, 1969. doi https://doi.org/10.2514/3.44076.
[3] D. Schwamborn, T. Gerhold, and R. Heinrich. The DLR TAU-Code, Recent Applications in Research and Industry. European Conference on Computational Fluid Dynamics ECCOMAS CFD 2006, 2006.
[4] M. Schollenberger, T. Lutz, and E. Krämer. Boundary Condition Based Actuator Line Model to Simulate the Aerodynamic Interactions at Wingtip Mounted Propellers. In A. Dillmann et al., New Results in Numerical and Experimental Fluid Mechanics XII, pages 608–618, Cham, 2020. Springer International Publishing. ISBN 978-3-030-25253-3. doi https://doi.org/10.1007/978-3-030-25253-3_58

STAB

Mitteilung

Fachgruppe: Transportflugzeugkonfigurationen

Numerical transonic buffet analysis for the XRF1 transport aircraft at forced wing oscillations

Vinzenz Völkl, Christian Breitsamter

Chair of Aerodynamics and Fluid Mechanics, Technical University of Munich

Boltzmannstr. 15, 85748 Garching b. München, vinzenz.voelkl@tum.de

Introduction

Providing flight safety and fuel efficiency over the whole flight envelope will be the most important factors in developing new transonic transport aircraft. For that an exact prediction of the loads, especially at the limit of the flight envelope, is needed in order to reduce structural weight. At high subsonic Mach number and beyond certain angle of attack a phenomenon called transonic buffeting is limiting the flight envelope. Transonic buffet is a self-sustained shock/boundary-layer instability. Shock induced flow separation is present associated with shock movement in chordwise direction as well as propagation of buffet cells in spanwise direction [1]. A severe unsteady pressure distribution impacts on the wing suction side. Typically, the wing structure is excited, with the coupled aerodynamic and structural phenomenon is called buffeting [2].

In order to investigate such transonic effects wind tunnel testing related to Mach and Reynolds number similarity and/or coupled fluid-structural simulations have to be conducted. For a first analysis of the mutual interaction of buffet-induced and motion-induced unsteady aerodynamic forces the present investigations focus on forced motion problems.

Reference Configuration and Numerical Setup

The forced motions are derived from the wing bending and torsion modes as the structure responds in its eigenmodes to the buffet induced aerodynamic excitation. Further, to investigate general trends and lock-in effects different eigenmodes and frequencies close and farther away from the buffet frequency of the unexcited structure are selected. URANS simulations have been carried out as a compromise of representing the dominant unsteady aerodynamic effects and computational effort. The numerical set-up is validated for the case without superimposed motions for which experimental data are available, obtained in the European Transonic Wind tunnel facility (ETW) [3, 4].

The XRF1 wind tunnel model is chosen as model geometry. Experimental results provided by the DFG research unit FOR 2895 are taken as conditions for the URANS simulations. A well resolved mesh with y+ < 1 is used as well as a timestep sensitivity study was conducted.

Results

The surface pressure coefficient c_p and modal content of the flow over the wing will be investigated thoroughly. This is done via different methods of modal analysis using the methods implemented in the Python-Library flowTorch [5]. Here, good alignment of the buffet modes with the experimental data can be seen. As well as for simulations with forced oscillations the influence of the motion onto the flow characteristics can be seen clearly.

STAB

Figure 1 depicts an exemplary result of the buffet flow over the XRF1 aircraft wing suction side. It shows the distribution of the pressure coefficient c_p on the upper side of left wing over a whole buffet cycle. The movement of the shock is visualized by the movement of the border between the blue and yellow area indicating areas of lower and higher c_p. The waves in the shock line are that called buffet cells and are typical for that phenomenon.
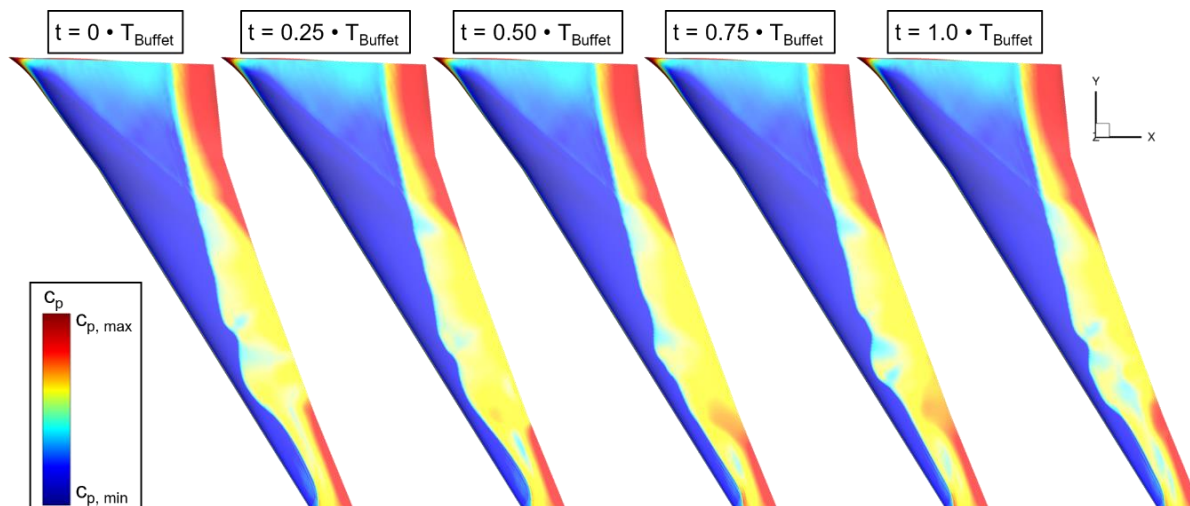

Fig. 1: Pressure coefficient (c_p) contour plots for one buffet cycle with the buffet period T_{Buffet} (Ma=0.84, Re=25•10^6, α=4.5°)

Acknowledgments

References

[1]   Iovnovich, M., and Raveh, D., "Numerical Study of Shock Buffet on Three-Dimensional Wings," *AIAA Journal*; Vol. 53, No. 2, 2015, pp. 449–463. doi: 10.2514/1.J053201.

[2]   Raveh, D., and Dowell, E., "Aeroelastic Responses of Elastically Suspended Airfoil Systems in Transonic Buffeting Flows," *AIAA Journal*; Vol. 52, No. 5, 2014, pp. 926–934. doi: 10.2514/1.J052185.

[3]   Lutz, T., Kleinert, J., Waldmann, A., Koop, L., Yorita, D., Dietz, G., and Schulz, M., "Research Initiative for Numerical and Experimental Studies on High-Speed Stall of Civil Aircraft," *Journal of Aircraft*, 2022, pp. 1–14. doi: 10.2514/1.C036829.

[4]   Waldmann, A., Ehrle, M., Kleinert, J., Yorita, D., and Lutz, T., "Mach and Reynolds Number Effects on Transonic Buffet on the XRF-1 Transport Aircraft Wing at Flight Reynolds Number," *Experiments in Fluids* [online], Vol. 64, No. 5, 2023, pp. 1–25, https://link.springer.com/article/10.1007/s00348-023-03642-7#citeas.

[5]   Weiner, A., "GitHub - FlowModelingControl/flowtorch: flowTorch - a Python Library for Analysis and Reduced-Order Modeling of Fluid Flows," https://github.com/FlowModelingControl/flowtorch, [retrieved 24 July 2024].

Mitteilung

Fachgruppe: Turbulenz und Transition

Numerische Untersuchungen zur selektiven Detektion charakteristischer Strömungsfeldmuster mittels Fasersensoren in einer turbulenten Grenzschichtströmung

L. Bagdenand, C. Wenzel, U. Rist

Institut für Aerodynamik und Gasdynamik der Universität Stuttgart

70569 Stuttgart, lisa.bagdenand@iag.uni-stuttgart.de

Fortschritte bei der Herstellung mikro-mechanischer Strukturen erlauben es heute, neue Sensoroberflächen herzustellen, durch die neue Formen der räumlichen und zeitlichen Signalerfassung möglich sind. Hierzu gehören mikro-mechanische Sensoren, wie z.B. die von Brücker et al. [1] vorgestellten flexiblen Micropillars zur Vermessung der Wandschubspannung. Nach dem Vorbild der Natur sind auch behaarte Oberflächen vorstellbar [2], auf der jedes Haar einen einzelnen Fasersensor darstellt. Hierbei ist jedoch noch unklar, welche besonderen Mechanismen der Signaldetektion und Analyse durch die bestimmte Anordnungen von diesen Einzelsensoren genutzt werden können. Abstrahiert setzt dies eine globale Interpretation von einzelnen lokalen Ereignissen voraus, eine Art Mustererkennung. Konkret bedeutet dies, in einer Menge von Daten Regelmäßigkeiten, Wiederholungen und Ähnlichkeiten zu erkennen. Beispielsweise kann hierfür künstliche Intelligenz als mögliches Hilfsmittel herangezogen werden. Guastoni et al. [3] zeigen, dass Deep Reinforcment Learning (DRL) für die aktive Strömungskontrolle genutzt werden kann. Durch ein neuronales Netz können sehr viele Daten gesammelt werden, um eine bessere Kontrollstrategie zu finden. So können komplexe Zusammenhänge basierend auf instantanen Geschwindigkeitsfluktuationen gesucht werden [4]. Die genauen Kontrollstrategien des DRL können aber noch nicht ausreichend quantifiziert werden, sodass auch das ein schwieriger aber dennoch vielversprechender Ansatz für die vorliegende Fragestellung ist. Die der Turbulenz naturgemäß zugrunde liegende chaotische Struktur des Strömungsfeldes macht es allerdings schwer, zeitlich und räumlich hochauflösende Messungen zu erstellen. Ein alternativer Ansatz wird beim Blick ins Tierreich deutlich. Dort ist eine Reihe von Insekten und Meeresbewohnern in der Lage, mithilfe von feinen Härchen auf ihrer Körperoberfläche Strömungen in dem sie umgebenden Fluid zu detektieren und entsprechend reagieren zu können [5]. Nach diesem Vorbild wäre es denkbar, mit ähnlichen Sensoren die turbulente Grenzschicht genau zu vermessen, um dann aktiv und gesteuert Maßnahmen zu deren Beeinflussung ergreifen zu können. Der chaotische Verlauf von turbulenten Strömungen und die große Bandbreite von Strukturen unterschiedlicher Größe erfordern jedoch Messungen an vielen verschiedenen Punkten. Die Erfassung und Klassifizierung von Wirbeln verlangt dabei, dass ein Strömungsfeld mit hoher lokaler und zeitlicher Auflösung erfasst wird. Zusätzlich ist eine Kopplung der verschiedenen Sensorsignale erforderlich, um die sich fortsetzenden Strukturen in den Antwortprofilen jedes betroffenen Sensors wiederfinden zu können. Inspiriert von den Ansätzen aus dem Tierreich und daran angelehnt wird ein borstenartiger Fasersensor als steifer Biegebalken betrachtet, auf den die ankommende Strömung als Streckenlast einwirkt, die dann ein Biegemoment an der Wurzel des Sensors hervorruft. Mit diesem Fasersensor können so momentane Geschwindigkeitssignale in Strömungs- und in Spannweitenrichtung detektiert werden. Die erhaltenden Momentenfelder korrelieren mit Werten von r > 0,9 sehr gut mit den Geschwindigkeitsfeldern. In den nachfolgenden Abbildungen sind die Konturdarstellungen der momentanen Momentenfelder mit den jeweiligen Geschwindigkeitsfeldern gegenübergestellt.
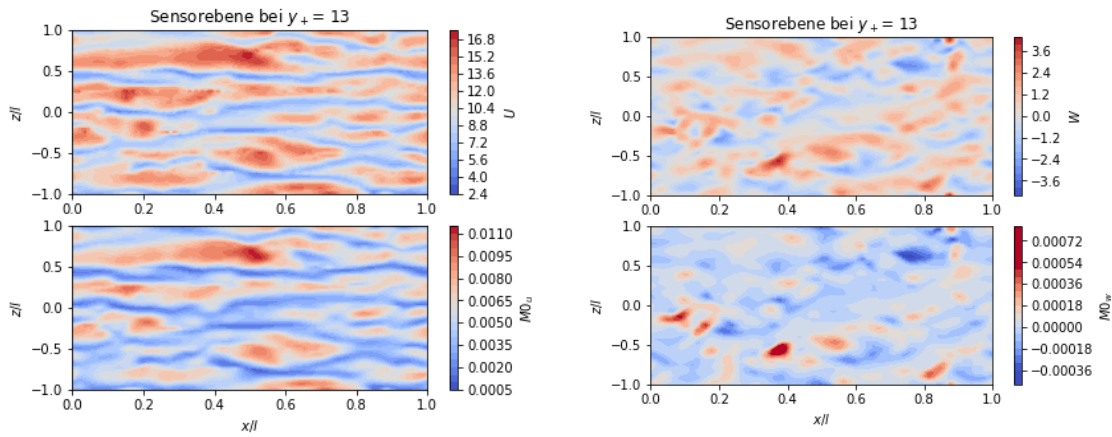
U-Geschwindigkeitskomponente in der wandparallelen Ebene bei $y^+ = 13$ im Vergleich zum berechneten Momentenfeld an der Wand

W-Geschwindigkeitskomponente in der wandparallelen Ebene bei $y^+ = 13$ im Vergleich zum berechneten Momentenfeld an der Wand

Um diese ermittelten Signale der Fasersensoren nutzen zu können, ist der State-of-the-Art Kontrollmechanismus die Opposition Control [6]. Dieser Mechanismus nutzt die wandnormale Geschwindigkeitskomponente und reduziert den Widerstand durch entgegengesetztes Absaugen und Ausblasen. Die Herausforderung ist nun, vom Sensorsignal, das die momentane Geschwindigkeit in Strömungsrichtung und in Spannweitenrichtung detektieren kann, auf die Geschwindigkeit in Wandnormalenrichtung zu schließen. So kann das Sensorsignal dem Kontrollmechanismus der Opposition Control Daten liefern und so die Strömung beeinflussen. Da ein Sensor einer einzigen Sensorlänge genau ein Momentenfeld liefert, das genau einem Geschwindigkeitsfeld zugeordnet werden kann, sollen Sensoren unterschiedlicher Länge genutzt werden, um die Gradienten der Geschwindigkeiten berechnen zu können und so von den Geschwindigkeitsfeldern in Strömungs- und Spannweitenrichtung auf das wandnormale Geschwindigkeitssignal schließen zu können.

Literatur

[1] Brücker C., Spatz J., Schröder W. Feasibility study of wall shear stress imaging using microstructured surfaces with flexible micropillars *Exp. Fluids*, 39, 464-474, 2005.

[2] Casas J., Steinmann T., Krjinen G. Why do insects have such a high density of flowsensing hairs? Insights from the hydromechanics of biomimetic MEMS sensors. *D J. R. Soc.*, Interface 7(51), 1487-1495, 2010.

[3] Guastoni, L., Rabault, J., Schlatter, P., Azizpour, H., Vinuesa, R. Deep reinforcement learning for turbulent drag reduction in channel flows. *European Physical Journal E*, 46(4), 2023.

[4] Sonoda, T., Liu, Z., Itoh, T., Hasegawa, Y. Reinforcement Learning for Reduction of Skin Friction Drag in a Fully Developed Turbulent Channel Flow. *Journal of Fluid Mechanics*, 960, A30, 2022.

[5] Klopsch, C., Kuhlmann, H. C., Barth, F. G. Airflow elicits a spider's jump towards airborne prey. I. Airflow around a flying blowfly. *Journal of the Royal Society Interface*, 9(75), 2591-2602 2012.

[6] H. Choi, P. Moin and J. Kim. Active turbulence control for drag reduction in wallbounded flows *Journal of Fluid Mechanics*, 262(4), 75-110., 1994.

STAB

Mitteilung

Fachgruppe: Turbulenz und Transition

COMPARING ASSIMILATION TECHNIQUES FOR PRESSURE AND TEMPERATURE FIELDS IN TURBULENT RAYLEIGH-BÉNARD CONVECTION

Robin Barta[1]*, Michael Mommert[1], Christian Bauer[1], Marie-Christine Volk[1], Claus Wagner[1][2]

[1] Institute of Aerodynamics and Flow Technology, DLR, Bunsenstraße 10, 37073 Göttingen, Germany
[2] Institute of Thermodynamics and Fluid Mechanics, TU Ilmenau, Helmholtzring 1, 98693 Ilmenau, Germany

* Corresponding author. E-mail: robin.barta@dlr.de

Velocity fields of flows can be measured precisely on temporal and spatial scales, e.g., by particle tracking velocimetry (PTV) [1,6]. Many interesting flows in scientific or industrial contexts, e.g., the ventilation of closed passenger cabins [5], are temperature-driven and it is a challenging task to also measure the temperature field with the same resolution as the velocity fields. Käufer et al. showed in [3] that it is indeed possible to measure the temperature field on the same scales as the velocity field by using thermo-liquid crystals as tracer particles for PTV. This method is intriguing but difficult to realize in general setups since a specific fluid medium is required to make the thermo-liquid crystals buoyancy neutral. Therefore, new methods – as described in [1,2,4] among others – attempt to infer unknown properties, such as the temperature or pressure fields of the flow, from the known velocity field using governing equations. We compare two of these methods – a physics informed neural network (PINN) approach [4] and the fractional step approach used by proPTV [1] – using ground truth data generated by a direct numerical simulation (DNS) of turbulent Rayleigh-Bénard convection in a cubic cell with system parameters, i.e., Prandtl and Rayleigh numbers:

$$Ra = 1 \cdot 10^6 \quad , \quad Pr = 0.7 \tag{1}$$

The governing flow equations are given by the incompressible Navier-Stokes equation in the Boussinesq approximation and the energy equation for the temperature:

$$\partial_t \vec{u} + (\vec{u} \cdot \nabla)\vec{u} = -\nabla p + \sqrt{\frac{Pr}{Ra}}\Delta\vec{u} + \mathrm{T} \cdot \vec{e_z} \tag{2}$$

$$\partial_t T + (\vec{u} \cdot \nabla)T = \frac{1}{\sqrt{Ra \cdot Pr}}\Delta T \tag{3}$$

$$\nabla \cdot \vec{u} = 0 \tag{4}$$

Here $\vec{e_z}$ is the unit vector in vertical direction along which gravity acts. The PINN tries to learn temperature and pressure fields to minimize the residuum of all three equations (2)-(4) for a given velocity field. proPTV uses a method based on the fractional step, typically applied in DNS to determine a pressure which is used to correct the velocity to be incompressible in each iteration. This method can only calculate an isothermal pressure field and a guess of the temperature is provided by rearranging equation (2) to solve for T. A direct comparison of the assimilated temperature and pressure is shown in figure 1. At the STAB conference we are going to present the comparison of the two methods in more detail as well as an extension of proPTV by combining both methods to assimilate a better tempera-
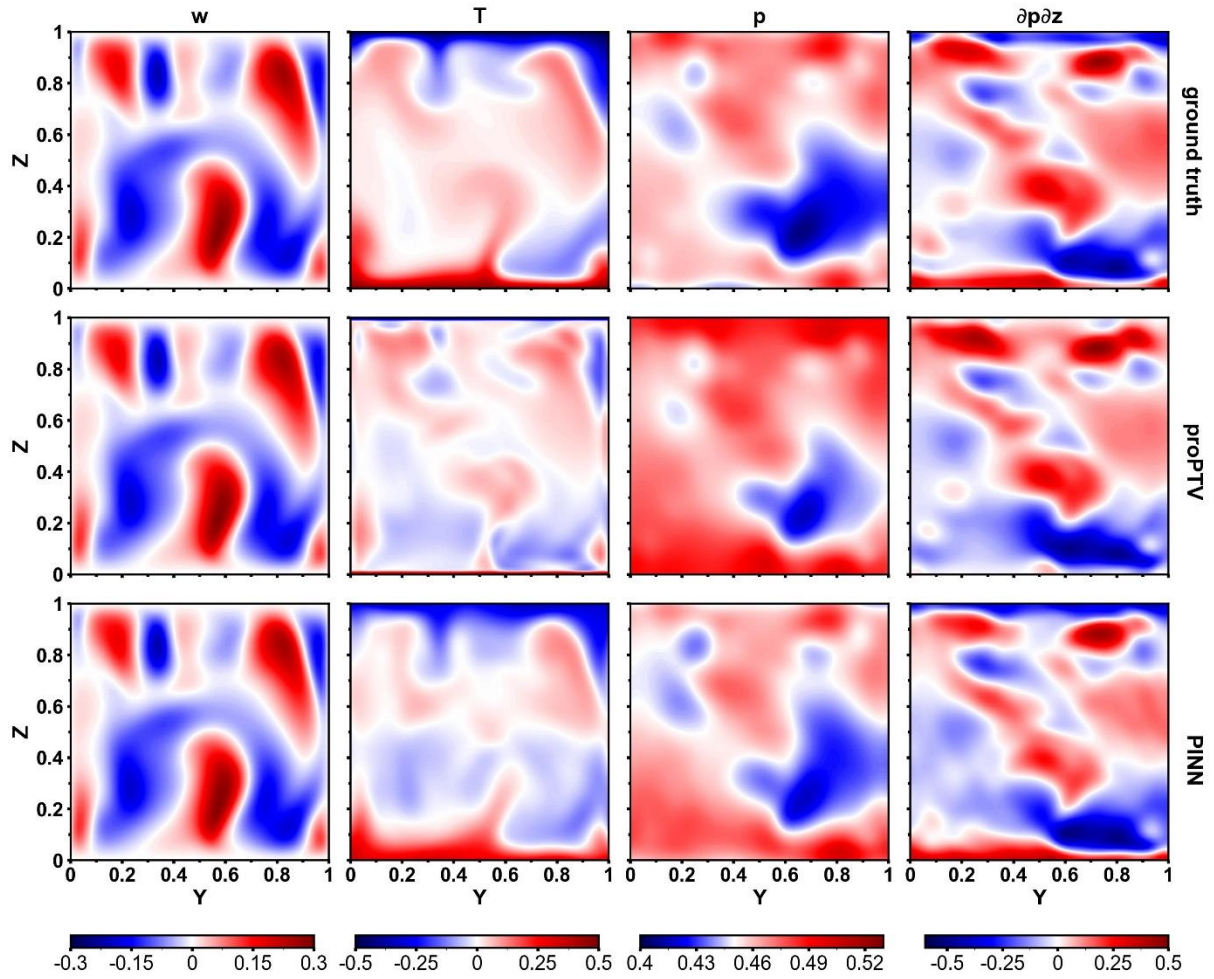
STAB

ture field.

Figure 1. Comparison of the assimilated temperature T and pressure p obtained using proPTV and PINN. The ground truth fields are shown in the top panels. The vertical velocity component w and the pressure gradient in the vertical direction $\partial p / \partial z$ are also shown.

References

[1] Barta R., et al.: proPTV: A probability-based particle tracking velocimetry framework. *Journal of computational physics* 113212, 2024.

[2] Bauer C. et al.: Assimilation and extension of particle image velocimetry data of turbulent Rayleigh–Bénard convection using direct numerical simulations. *Experiments in Fluids* 63:22, 2022.

[3] Käufer T., and Cierpka C.: Volumetric Lagrangian temperature and velocity measurements with thermochromic liquid crystals. *Measurement Science and Technology* 35.3:035301, 2023.

[4] Mommert M., et al.: Periodically activated physics-informed neural networks for assimilation tasks for three-dimensional Rayleigh-Benard convection. *arXiv preprint* 2403.02970, 2024.

[5] Schmeling D., et al.: Numerical and experimental study of aerosol dispersion in the Do728 aircraft cabin. *CEAS Aeronautical Journal* 14.2:509-526, 2023.

[6] Schröder A., and Schanz D.: 3D Lagrangian particle tracking in fluid mechanics. *Annual Review of Fluid Mechanics* 55.1:511-540, 2023.

STAB

Computational study of transient plasma actuator-induced wall-jet flow

Tarik ČORBO and Suad JAKIRLIĆ

Institute of Fluid Mechanics and Aerodynamics (SLA)

Peter-Grünberg-Straße 10, 64287, Technical University of Darmstadt

corbo@sla.tu-darmstadt.de, jakirlic@sla.tu-darmstadt.de

The turbulent flow induced by a plasma actuator mounted on a flat plate is simulated using the Improved Instability Sensitive Reynolds Stress Model (IISRSM) of Jakirlic and Maduta (2015), and novel approaches to modeling the unsteady plasma actuator (PA) force. Extending the work on the Scale-Adaptive Simulation (SAS) modeling strategy proposed by Menter and Egorov (2010), a Sensitized RANS-RSM is developed, which represents a grid-spacing free eddy-resolving turbulence model formulation based on the homogeneous dissipation concept of Jakirlić and Hanjalić (2002). The eddy-resolving capability of the model is ensured by an additional production term introduced in the length scale-supplying equation depending on the second derivative of the velocity field. By blending the $\overline{u_i u_j}$ turbulent stress tensor derived from the Boussinesq approximation and the background Reynolds stress model, the numerical robustness is improved and hence the connotation of "improved", Maduta et al. (2015). The geometry and boundary conditions of the considered flow configuration, representing a wall-jet induced at a flat plate in quiescent air, are based on the experimental and numerical investigation of Maden et al. (2013) and represent a box with dimensions of $0.45\,m$, $0.17\,m$, and $0.325\,m$ in the x, y, and z directions, respectively, where the exposed electrode of the plasma actuator ends at (0,0). Unlike the previous relevant works, two different approaches have been used here to model the transient PA force. The first approach is based on the measurements of Kuhnhenn et al. (2016), using the "exact" measurements of the force at the eight time sequences for an AC discharge cycle of the plasma actuator; this approach is denoted as EV (Exact time-varying Values). This approach uses a constant time step so that the time progression of the calculations matches that of the measurements. The second approach uses the eight measurements as well as additional temporally-interpolated force values to train a neural network to output the force value for any spatial and temporal position and is referred to as ML (Machine-Learning based force). This approach allows the use of a varying time step for the calculations. Preliminary calculations are also performed using the steady force for the plasma actuator from Kriegseis et al. (2013), averaged over the entire PA duty cycle. These baseline calculations, which also aim to study the influence of grid resolution, are performed on meshes of 4.7, 1.6, and 0.9 million cells, while the calculations with the transient PA force all use the 1.6 million cell mesh adopted by reference from the preliminary calculations. The calculations are performed with the finite volume method-based code OpenFOAM®, where all turbulence model equations and appropriate plasma actuator forces have been implemented.

Selected results of the simulations are illustrated in Figures 1 and 2. The time-averaged velocity fields obtained using the averaged steady plasma actuator force and the ML force are shown in Figure 1. It is obvious that the velocity field determined by using the ML-related force exhibits slightly lower values in the near field of the plasma actuator (from $x = 0 - 1\,mm$) than that obtained by using the steady PA force, and slightly higher values in the far field of the plasma actuator (from $x \geq 6\,mm$). This difference can also be seen in Figure 2, where the computational results are compared with the experimentally determined streamwise velocity profiles. The results using the EV force show a larger underestimation of the velocity maximum near the wall compared to the steady and ML-related PA forces within the entire PA-affected region. This can be explained by considering that the force was determined using only eight measurements, which are not sufficient to accurately represent the average force of the plasma actuator. On the other hand, the results obtained with the ML force moving away from $x = 0$ are much closer to the actual experimental results and the simulation with the constant force (note also the uncertainties in the experimental results, which exhibits a non-zero velocity value at the wall itself). These results demonstrate the validity of this approach for modeling

STAB

the transient force of the plasma actuator; accordingly, further improvements of the results are expected by refining the neural network algorithm.
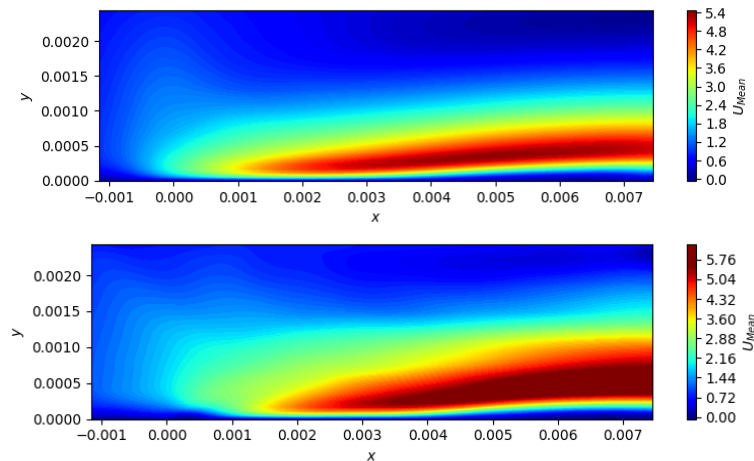

Figure 1: Time-averaged velocity fields determined with the averaged force of the plasma actuator (upper) and the force obtained from the neural network (lower).
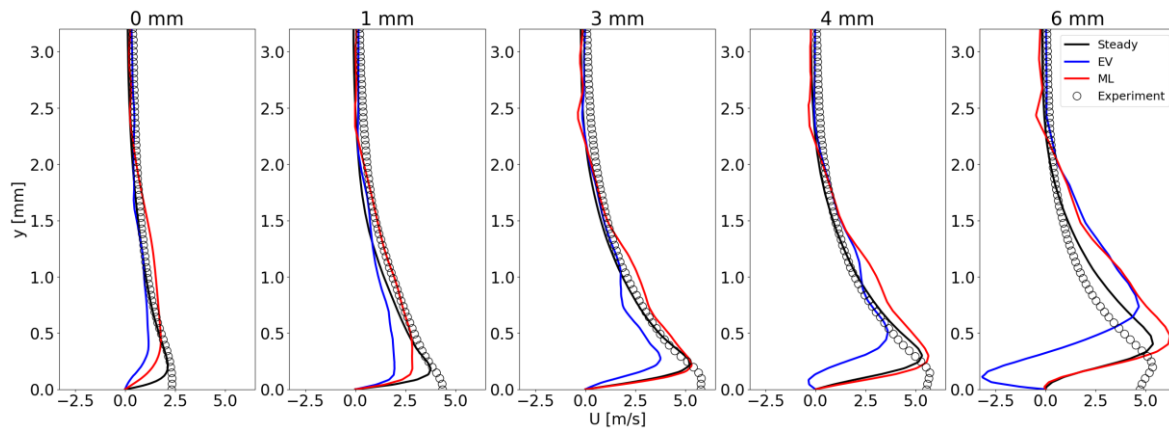

Figure 2: Mean velocity profiles in a range of locations using the average plasma actuator force (denoted as steady), the force using the exact time varying values (denoted as EV) and the force from the neural network (denoted as ML).

References

Jakirlic, S. and Maduta, R. (2015): Extending the bounds of "steady" RANS closures: towards an instability-sensitive Reynolds stress model. *Int. J. Heat and Fluid Flow* 51:175-194

Menter, F. and Egorov, Y. (2010): The Scale-adaptive Simulation method for unsteady turbulent flow predictions. Part 1: theory and model description. *Flow, Turbulence and Combustion* 85:113-138

Jakirlić, S. and Hanjalić K. (2002): A new approach to modelling near-wall turbulence energy and stress dissipation. *J. Fluid Mech.* 439:139-166

Maduta, R., Jakirlic, S., Ullrich, M. (2015). A numerically upgraded instability-sensitized Reynolds stress model for complex turbulent flow applications. In THMT-15. *Proceedings of the Eighth International Symposium on Turbulence Heat and Mass Transfer.* Begel House Inc.

Maden, I., Maduta, R., Kriegseis, J., Jakirlić, S., Schwarz, C., Grundmann, S., Tropea, C. (2013). Experimental and computational study of the flow induced by a plasma actuator. *Int. J. Heat and Fluid Flow* 41: 80-89

Kuhnhenn, M., Simon, B., Maden, I., Kriegseis, J. (2016). Interrelation of phase-averaged volume force and capacitance of dielectric barrier discharge plasma actuators. *J. Fluid Mech.* 809, R1

Kriegseis, J., Schwarz, C., Tropea, C., Grundmann, S. (2013). Velocity-information-based force-term estimation of dielectric-barrier discharge plasma actuators. *Journal of Physics D: Applied Physics* 46(5), 055202

STAB

Mitteilung

Fachgruppe: Turbulenz und Transition

A spectral investigation of the transitional boundary layer flow during free flight in the convective atmosphere

U. Deck and W. Würz

Institute of Aerodynamics and Gasdynamics, University of Stuttgart, 70569 Stuttgart, Pfaffenwaldring 21, ulrich.deck@iag.uni-stuttgart.de, wuerzwerner@gmail.com

During the flight in the lower earth atmosphere with active convection significant inflow turbulence is present. Both, high frequency disturbances and low frequency angle of attack fluctuations are causing an unsteady flow situation which is not comparable to calm conditions in higher flight altitudes or laminar wind tunnels [1, 2]. For wings or rotors with natural laminar flow (NLF) airfoils a significant effect on the transition process and location is expected and also investigated in previous studies. Low frequency angle of attack fluctuations are causing an unsteady pressure distribution and thus an unsteady boundary layer development [3, 4]. The velocity of the fluctuating transition front is depending on the gust wavenumber and is not identical for the up- and downstream direction [5]. Medium frequency disturbance of the inflow velocity resulting in streaky structures, these are able to interact with the Tollmien-Schlichting (TS) waves and finally cause turbulent spots or bursts [6]. High frequency disturbance directly affects the TS-wave transition process in the receptivity framework and thus leads to an additional upstream shifted transition location [7]. The present study uses inflow X-wire and surface hotfilm sensor signals of a free flight measurment data set, containing measurement sections in different weather conditions and a total amount of more than 100h flight test time. A spectral investigation of the boundary layer flow for different locations on the suction and pressure side of a NLF airfoil, a wide range of lift coeffcients and of course also distinguished inflow turbulence intensities is worked out.

All measurement data, which is sampled at f_S = 50kHz, is cut into small section of N_S = 1024 data points with an overlapping of 50%, resulting in an effective intervall length of 0,01s per section. Power spectral density is computed for the hotfilm sensor signals together with reference angle of attack, from CTA x-wire probe measurments, for each section. The short time intervalls are necessary to ensure proper reference angle of attack at least for the quasi-steady (low frequency) part of the angle of attack fluctuations. Statiscally averaging over all sections with identical inflow conditions results in an overview of spectral boundary layer behaviour:
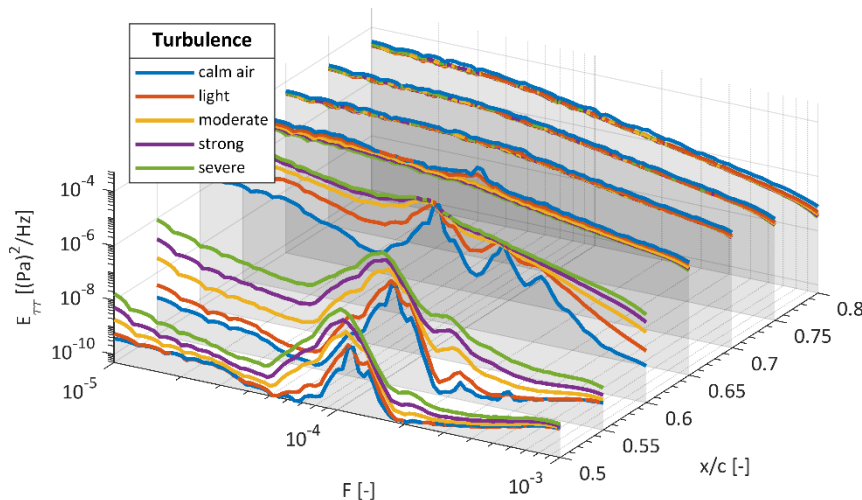

Fig. 1: Power spectral density for different chord locations on the suction side of a NLF airfoil for α = 3.6°. Displayed against the non-dimensional frequency parameter F.

STAB

For the first three chord positions in Fig. 1 a transitional boundary layer flow is identifiable due to the amplitude peaks in the expected TS-wave frequency range. For all regarded inflow turbulence categories this TS-wave amplitude peak is visible whereas the amplitudes in the whole frequency regime are higher for increased inflow turbulence. For a single sensor location the power spectral density can also be displayed for a wide range of angle of attacks :
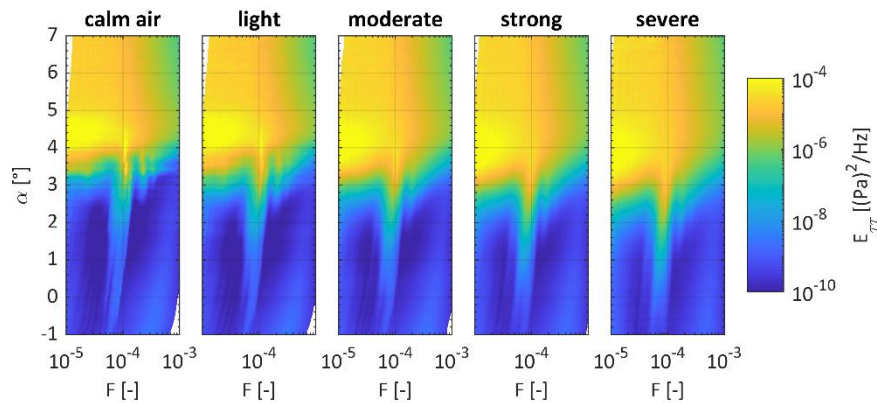

Fig. 2: Contour diagrams of the power spectral density at 60% x/c on the suction side for a range of angle of attacks and frequency parameters.

The TS-wave driven laminar-to-turbulent transition for all inflow turbulence categories is clearly visible. For higher inflow turbulences only the angle of attack where the boundary layer flow becomes a fully turbulent one is reduced. These results can be compared to laminar wind tunnel (LWT) measurements with artificial increased turbulence levels using three passive grids. Free flight measurement points are choosen to match LWT turbulence levels.
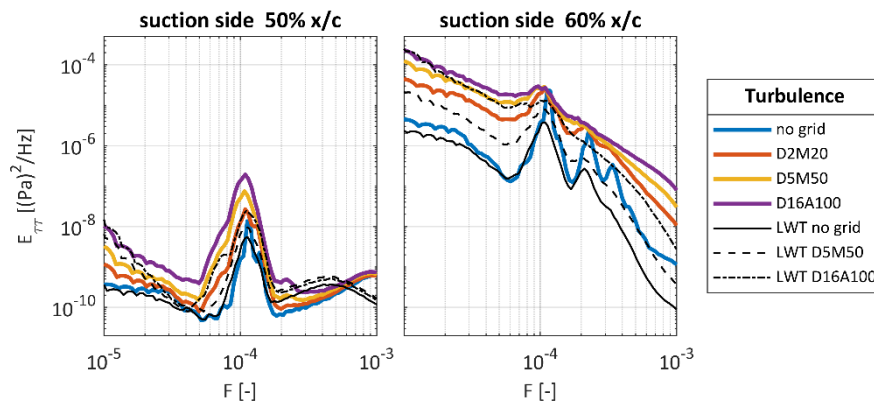

Fig. 3: Comparison of power spectral density, measured in the LWT (black lines) and free flight (colored lines) for different turbulence levels (D2M20 $\varepsilon_{40m/s} \approx 5 \cdot 10^{-5} m^2/s^3$, D5M50 $\varepsilon_{40m/s} \approx 5 \cdot 10^{-4} m^2/s^3$, D16A100 $\varepsilon_{40m/s} \approx 5 \cdot 10^{-3} m^2/s^3$).

In the final presentation and in the paper further detailed results, also for the pressure side, will be presented and discussed together with details of the measurement techniques. A thorough comparison of the flight data to wind tunnel measurements and to linear stability theory (LST) calculations, where applicable, is given and valuated.

[1] Greiner M., Würz W., (2022) "In-flight measurement of free-stream turbulence in the convective boundary layer", Experiments in Fluids, pp. 63:162
[2] Romblad J., Greiner M., Guissart A., Würz W. (2022): "Characterization of low levels of turbulence generated by grids in the settling chamber of a laminar wind tunnel" Experiments in Fluids, 2022, pp. 63-65
[3] Reeh A.D. (2014) "Natural laminar flow airfoil behavior in cruise flight through atmospheric turbulence". Dissertation, Technische Universität Darmstadt.
[4] Guissart A., Romblad J., Nemitz T., Tropea C. (2021) "Small-scale atmospheric turbulence and its impact on laminar-to-turbulent transition". AIAA Journal 59(9) pp. 3611–3621.
[5] Ohno D., Romblad J. Rist U. (2019) "Investigations of laminar to turbulent transition in an oscillating airfoil boundary layer", In IUTAM Laminar-Turbulent Transition, 9th IUTAM Symposium, London, UK, September 2-6, 2019, pp. 469-478, Springer
[6] Saric W., Reed H. L.; Kerschen E. J., (2002) "Boundary-layer receptivity to freestream disturbances", Annual Review of Fluid Mechanics, Vol. 34, pp. 291-319
[7] Kendall J.M., (1998) „Experiments on Boundary-layer Receptivity to Freestream Turbulence", 36th AIAA Aerospace Sciences Meeting and Exhibit, Reno, NV, USA, AIAA paper

STAB

Mitteilung

Fachgruppe: Turbulenz und Transition

Direct Determination of Intermittency Distribution with Fast-Response Temperature-Sensitive Paint

B. Dimond[1*], M. Costantini[1], C. Klein[1]

[1]DLR, Institute of Aerodynamics and Flow Technology, DLR, Bunsenstrasse 10, D-37073 Göttingen, Germany

*corresponding author: benjamin.dimond@dlr.de

Introduction and experimental setup

For many aerodynamical applications there is a great demand to describe, model and predict laminar-turbulent boundary layer transition, as the state of the boundary layer has a great impact on aerodynamic efficiency, performance, and thermal loads. Despite extensive research over the last decades, there is still a need for further research, especially in high Reynolds number flows, where both numerical and experimental studies on intermittency are limited. Laminar-turbulent transition is a very dynamic process that extends over a significant region, yet it is often practicable to define a single transition location to easily compare results. A sensible choice is the streamwise position of 50% intermittency, the intermittency factor γ being the proportion of laminar and turbulent boundary layer at one location ($\gamma = 0$ for a fully laminar and $\gamma = 1$ for a fully turbulent boundary layer). In many cases however it is not possible to directly determine the intermittency factors, thus requiring different definitions of the transition location depending on the measurement technique.

The focus of this work is the direct determination of intermittency with the help of a Ru(phen)-based fast response temperature-sensitive paint (iTSP) [1] for a high Reynolds number flow and the comparison with surface temperature distribution, average heat-flux and standard deviation of surface temperature σ_T that are often used to determine the transition location [2, 3]. The studies have been conducted in the low-turbulence ($Tu_{pu} \sim 0.06$ %) Cryogenic Ludwieg-Tube Goettingen (KRG) at a large chord Reynolds numbers ($7.5 \cdot 10^6$) and Mach number 0.8 with an angle-of-attack (AoA) of -2.1° (favourable pressure gradient λ_θ). A top plan view of the wind tunnel model (PaLASTra) [4], which was used in several previous measurements, can be seen in figure 1. The main part of the model is instrumented with iTSP on the port side and hot-films on the starboard side (18 hot-films staggered at 35°). The front part of the model is coated with conventional TSP (i.e. with limited temporal response). The model is also equipped with a row of pressure taps along the centre of the model. The iTSP observation area (32 x 55 mm²) is marked with a red rectangle and images are recorded at a frequency of 20 kHz. With the known thermal properties of the model and iTSP coating and the accurate time-resolved surface temperature measurement, the instantaneous heat-flux distribution can be determined. This in turn is then used to distinguish laminar and turbulent boundary layers at a given time and surface location and with it the intermittency distribution.
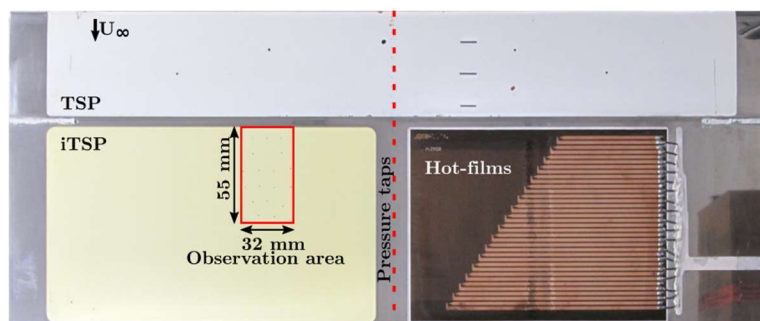

Fig. 1. Top plan view of the wind tunnel model (flow from the top). iTSP is visible as yellow coating on the left and hot-film array on the right.

STAB

Results

Figure 2 shows the time averaged results (for a time interval of 0.1 s) of surface temperature, intermittency, and standard deviation of the surface temperature σ_T for the observation area recorded with iTSP. Marked within figure 2 are the streamwise locations of the maximum gradient of the surface temperature distribution (orange), 50% intermittency ($\gamma = 0.5$ - blue), and of the maximum σ_T (red). There is a good agreement between the three different methods demonstrating that both the maximum temperature gradient and the maximum σ_T in streamwise direction are a good measure to estimate the location of 50% intermittency. The streamwise distribution of intermittency for $y = 0.169$ m is shown in figure 3 alongside the σ_T distribution and with the fitted Johnson intermittency model [5] $\gamma = 1 - e^{-0.0941\xi^3}$ with $\xi = \frac{x - x_t}{x_{75} - x_{25}}$, where x_{75} and x_{25} are the streamwise locations with intermittency values $\gamma = 0.75$ and $\gamma = 0.25$, respectively. The Johnson model shows a very good agreement throughout the whole distribution. Additionally, there is a good agreement between the streamwise extent of the intermittent region and increased values of σ_T. In the final contribution the detailed heat-flux and intermittency determination will be discussed and the transition location and distribution compared for various methods including the results obtained with the hot-film measurements.
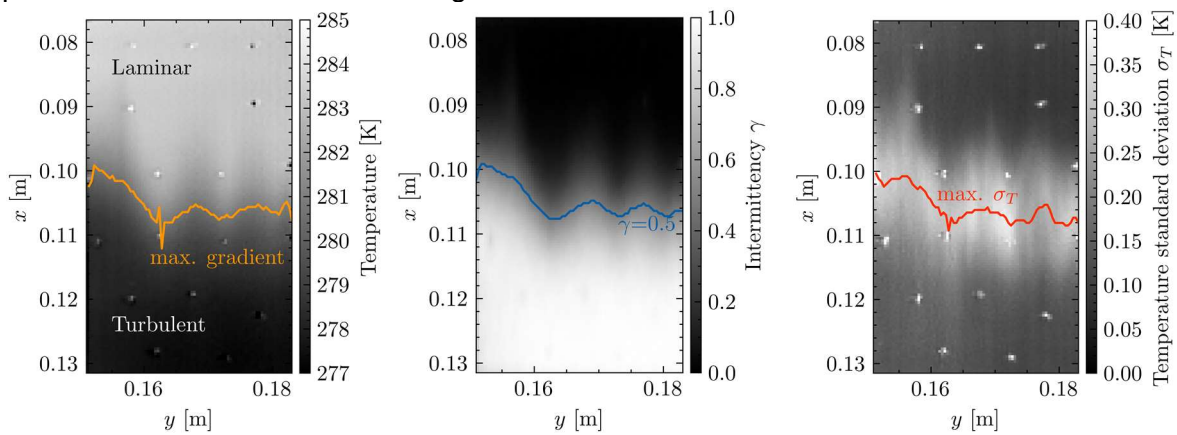

Fig. 2. Surface temperature distribution measured with iTSP (left) intermittency distribution (centre) and standard deviation of the instantaneous surface temperature values σ_T (right). Flow is from the top. Flow conditions are $Re_c = 7.5 \cdot 10^6$, M = 0.8, and λ_θ=12.9 × 10^{-3} (AoA = -2.1°).
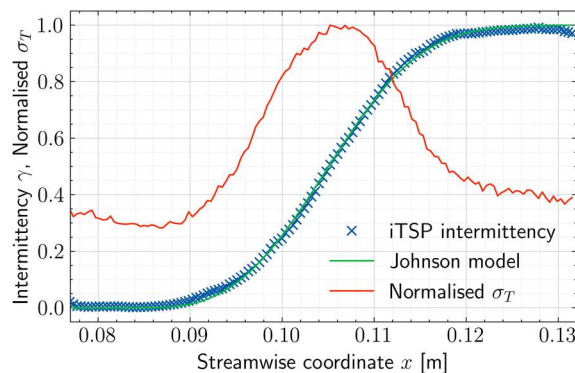

Fig. 3. Intermittency distribution determined with the iTSP in streamwise direction with the fitted Johnson intermittency model and normalised σ_T values.

References

[1] Dimond B. (2024): Investigation of boundary layer transition at high Reynolds numbers using time-resolved temperature-sensitive paint. PhD Thesis, Georg-August-Universität Göttingen.

[2] Miozzi M., Capone A., Costantini M., Fratto L, Klein C., Di Felica F. (2019) Skin friction and coherent structures within a laminar separation bubble., Experiments in Fluids Vol. 60.

[3] Costantini M., Henne U., Risius S., Klein C. (2021): A robust method for reliable transition detection in temperature-sensitive paint data. Aerospace Science and Technology Vol. 113.

[4] Costantini M., Hein, S., Henne, U., Klein, C., Koch, S., Schojda, L., Ondrus, V., Schröder, W. (2016): Pressure Gradient and Non-adiabatic Surface Effects on Boundary-Layer Transition. AIAA J. 54(11), 3465–3480.

[5] Johnson, M.W., Fashifar, A. (1994): Statistical properties of turbulent bursts in transitional boundary layers. Int. J. of Heat and Fluid Flow. Vol. 15.

STAB

Mitteilung

Fachgruppe: Turbulenz und Transition

Transition and Separation on a Spinning Projectile Subjected to Subsonic Flow at High Angles of Attack

B. Dutschke[1], Ch. Rey[1], Ch. Mundt[2]
[1]French-German Research Institute of Saint-Louis (ISL)
5 rue du Général Cassagnou, 68300 Saint-Louis, France
Bernd.Dutschke@isl.eu
[2]Universität der Bundeswehr München
Werner-Heisenberg-Weg 39, 85579 Neubiberg, Germany

Introduction

Spin-stabilized projectiles fired at large elevation angles above 70° are known to exhibit high angles of attack (AoA) up to 90° and higher at the apogee of the trajectory, while the flight velocity drops to subsonic values [1,2]. The aerodynamic behavior associated with these flow conditions has not been studied as extensively as regular low-AoA, high-velocity flight. In an attempt to characterize the high AoA aerodynamics of a spinning shell, subsonic wind tunnel tests were conducted at a free stream velocity of 30 m/s, corresponding to a diameter-based Reynolds number of $Re_D = 8{\times}10^4$. Aerodynamic forces and moments on a spinning projectile model were measured using a six-component force balance, and the flow fields in several transverse planes distributed along the length of the model were determined using classical 2D2C Particle Image Velocimetry (PIV).

This work focuses on the effect of spin on the separation position, and in particular the role of the laminar-to-turbulent transition.
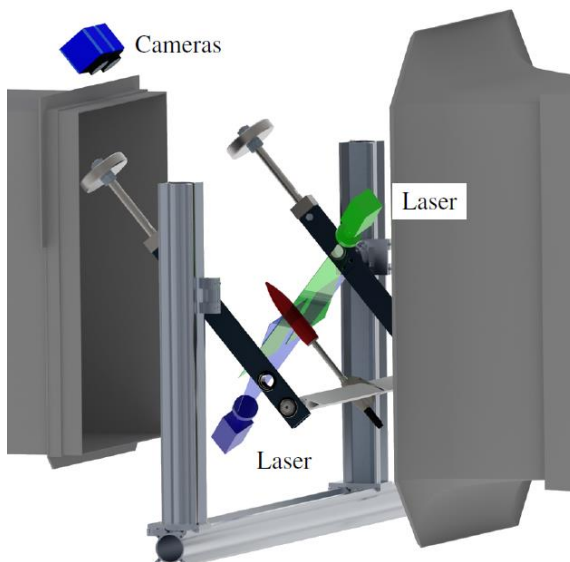
Experimental Setup

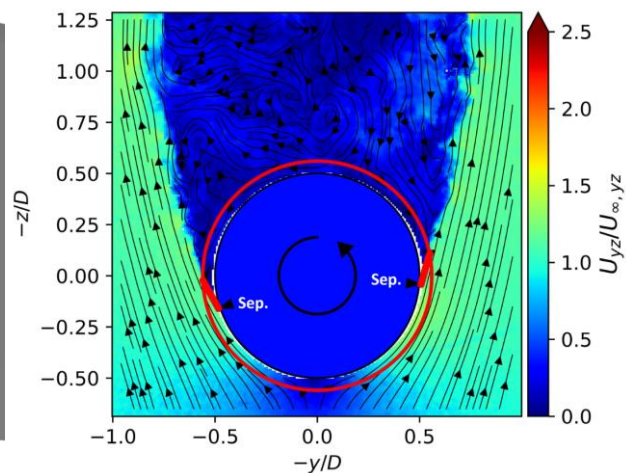Figure 1: PIV setup in the wind tunnel.

Figure 2: Instantaneous planar velocity field.

A generic projectile model, measuring 45 mm in diameter, was mounted on a spinning device driven by an electric motor, and spun up to frequencies between 70 Hz and 340 Hz. The spinning device was equipped with an internal force balance, and placed in the test section of the Göttingen-type wind tunnel using the high-AoA mount shown in Fig. 1. Two synchronized double-pulse lasers were used to create a continuous laser sheet perpendicular to the projectile axis. The flow was seeded with a glycol-based fog, and particle images were recorded with two sCMOS cameras mounted above the test section (cf. Fig. 1).

STAB

Results

From the force balance measurements, it was found that the magnitude of the normal force, i.e. the "in-plane drag", at high angles of attack exhibits a non-monotonous behavior with respect to the spin rate. At low spin rates it is reduced, but at higher spin rates it increases to values exceeding those of a non-spinning model. Inspection of the PIV-measured flow fields shows that the spin-induced reduction of the normal force is accompanied by a significant narrowing of the wake. To quantify the width of the wake, the circumferential positions of the flow separation are estimated from the PIV-measured velocity fields, as shown in Fig. 2. First, the positions of the shear layer are identified on a circle placed at some distance from the surface. In a second step, the streamlines are followed to the projectile surface. The particle images shown in Figures 3 and 4 show that the narrowing of the wake at higher spin rates is caused by a transition of the boundary layer on the side where the spin opposes the crossflow. An effective Reynolds number is defined, taking into account the effects of AoA and spin, and the range of values critical for the occurrence of transition is identified. The critical Reynolds numbers agree well with those reported in [3] for a non-rotating 2-D cylinder in crossflow.
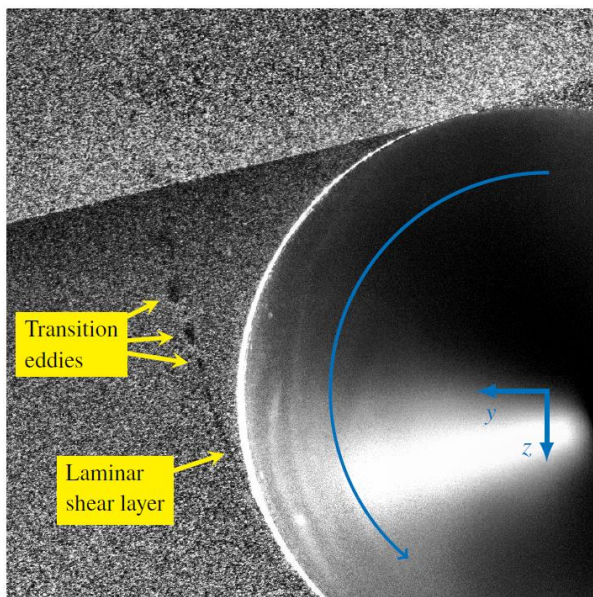

Figure 3: Low spin rate.
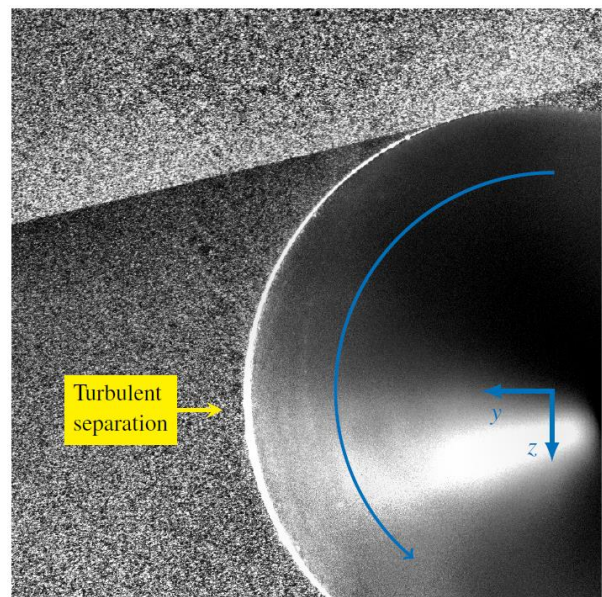
Figure 4: High spin rate.

References

[1]   Collings, W. Z., and Lieske, R. F., "Artillery Shell Drift at High Angles of Fire," *Journal of Spacecraft and Rockets,* Vol. 12, No. 3, 1975, pp. 169–173.

[2]   Dutschke, B., Weidner, S., Rey, Ch., and Mundt, Ch., "Aerodynamic Characterization, Flight Analysis and Limit-Cycle Stability for Artillery Shells Fired with High Elevation," *33rd International Symposium on Ballistics,* Vol. 1, Bruges, Belgium, 2023, pp. 32–48.

[3]   M. M. Zdravkovich, *Flow around Circular Cylinders: Volume 1: Fundamentals.* Oxford University Press, 1997.

STAB

Mitteilung

Fachgruppe: Turbulenz und Transition

Experimental Design for the Validation of Extended Hybrid Laminar Flow Control and Transition Prediction in Complex 3D Flows

Lajos Fohlmeister, Rolf Radespiel
Institute of Fluid Mechanics, TU Braunschweig, Germany, lajos.fohlmeister@tu-braunschweig.de
Sebastian Helm, Cornelia Grabe
Institute of Aerodynamics and Flow Technology, DLR Göttingen, Germany

The need for a Transition Experiment

Laminar Flow Control (LFC) and Hybrid Laminar Flow Control (HLFC) offer significant potential to reduce drag on aircraft, particularly by minimizing skin friction drag on lifting surfaces and fuselage [1]. This is critical for improving fuel efficiency and reducing emissions. However, successful implementation of LFC, especially HLFC, faces two primary challenges:

1. **Accurate Transition Prediction**: Predicting the transition from laminar to turbulent flow during the design process is essential but remains difficult for industrial applications [2]. This is especially true for complex three-dimensional flows involving Tollmien-Schlichting instabilities (TSI) and cross-flow instabilities (CFI), significant deviations from ideal pressure distributions as well as laminar flow control. Therefore, current models, often based on empirical data, require validation through experiments to test their capabilities and assumptions [2].

2. **Active Laminar Flow Control**: Laminar flow can be controlled through passive methods like optimizing airfoil geometry, active methods like suction (LFC), or hybrid approaches (HLFC) that combine both. Active methods typically involve trade-offs between system complexity and achievable laminar length [2]. The extended hybrid laminar flow control (xHLFC) concept proposed by Traub et al. [3] aims to extend laminar flow up to 80% of the chord length while reducing system complexity and improving off-design performance. Although the feasibility of this concept has been demonstrated on unswept wings at moderate Reynolds numbers [4], it has not yet been tested on a swept wing at higher Reynolds numbers.

To address these challenges, this paper presents an experimental setup that measures transition in three-dimensional flow scenarios and tests the xHLFC design on a single wing model.
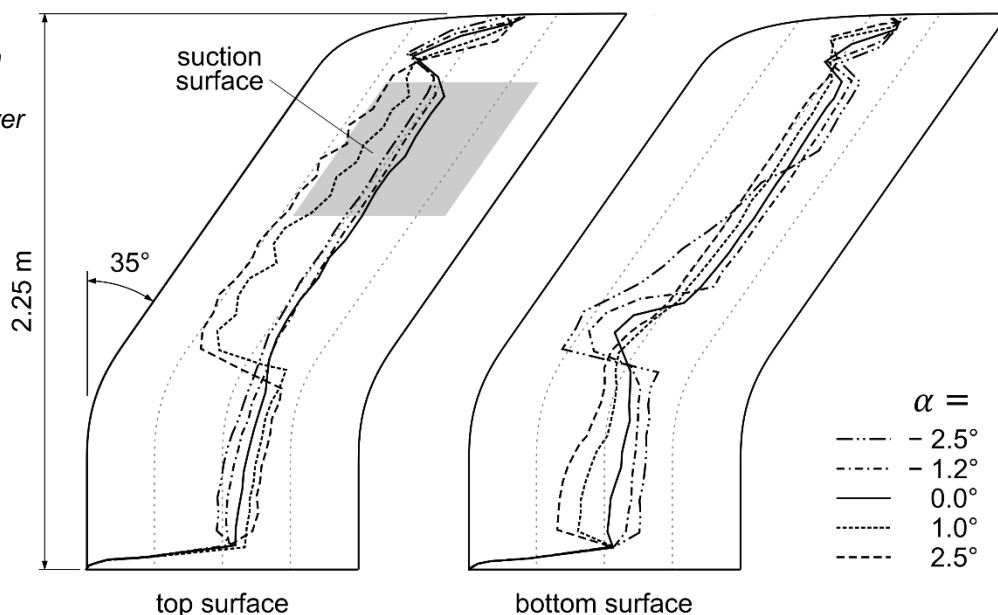
Validation Experiment Design

The experiment involves a 2.25-meter span untapered wing model with an unswept root section and a 35-degree swept outer section, see Figure 1. The sections are connected by a progressively increasing sweep angle, approximating a circular segment. The model is designed to be tested in the DNW-NWB low-speed wind tunnel. To enable testing at high Reynolds numbers, the model's airfoils are designed to be almost symmetrical. Combined with the restriction to small angles of attack (AoA), this reduces the lift generated at high chord lengths and, consequently, minimizes the wind-tunnel's influence. As a result, Reynolds numbers between 4.5 and 5 million are achieved at design speeds.

The model is divided into two sections:

1. **xHLFC Concept validation**: The outer wing section, which includes a suction chamber, simulates the amplifications present in free-flight conditions of a reference airfoil in the wind tunnel. The planform is designed to create nearly parallel isobars in this regime. Due to the significantly lower Reynolds number in the wind tunnel experiment, the used airfoil requires modifications to achieve similar levels of instability amplification. This is achieved by increasing the airfoil thicknesses and reducing the chord position of the maximum thickness to start the adverse pressure gradient earlier to amplify the TSI.

   A fully integrated suction chamber design, as suggested by Traub, is to be tested. In this design, the perforated skin surface and the suction chamber substructure are printed as a single part [3].

STAB

Figure 1 *Transition lines calculated with LILO based on the RANS boundary-layer data.*
Re = 4.45 Mio.,
Ma = 0.18

suction surface

2.25 m

35°

$\alpha =$
—·—·— − 2.5°
—··—··— − 1.2°
———— 0.0°
·········· 1.0°
— — — 2.5°

top surface   bottom surface

2. **Three-Dimensional Transition Study**: The inner wing section, with a progressively increasing sweep, creates complex transition scenarios where TSI and CFI are both significant. Using the AoA it can be controlled, which instability is causing transition. The bottom side features different airfoil sections to create a spanwise pressure gradient, further varying the transition position.

First numerical Results

The model geometry was recalculated under wind tunnel conditions using the DLR-TAU code comparing different transition prediction methods. These calculations do not yet incorporate suction or wind tunnel effects. The resulting transition lines for a calculation employing the e^N method based on the LILO stability code and three-dimensional boundary layer data extracted from the RANS solution are shown in Figure 1. It can be seen that the 2.5d conditions for the xHLFC validation are satisfied as the transition line is almost constant in the outer wing section on the upper surface. The forward movement of the transition line between an AoA of 0° and an AoA of 1° is caused by a change in the transition mode from TSI to CFI. In this way, the suction chamber can be tested with both transition modes.

On the bottom surface, the sudden movement of the transition line is created by the gradually increasing sweep angle. A more subtle change in the transition line, further outboard, is caused by the spanwise variation of the airfoils. To validate the numerical results the transition line will be determined experimentally using infrared thermography.

Conclusion

A wind tunnel model with a spanwise-varying sweep angle was designed to serve two purposes: to test an extended hybrid laminar flow suction concept under conditions comparable to free flight and to create complex transition scenarios for numerical model validation. This model provides an opportunity to study the interaction between Tollmien-Schlichting and cross-flow instabilities in the presence of suction, advancing the understanding and application of laminar flow control in aviation.

References

[1] Karpuk, S., Radespiel, R., & Elham, A. (2022). Assessment of future airframe and propulsion technologies on sustainability of next-generation mid-range aircraft. *Aerospace, 9*(5), 279. https://doi.org/10.3390/aerospace9050279

[2] Krishnan, K. S. G., Bertram, O., & Seibel, O. (2017). Review of hybrid laminar flow control systems. *Progress in Aerospace Sciences, 93*, 24–52 https://doi.org/10.1016/j.paerosci.2017.05.005

[3] Traub, H., Wolff, J., Jose, S., et al. (2021). Concept and design of extended hybrid laminar flow control suction panels. *PREPRINT (Version 1)*. Research Square. https://doi.org/10.21203/rs.3.rs-924184/v1

[4] Corelli, M., Sudhi, A., Scholz, P., Radespiel, R., & Badrya, C. (2022). Experimental study of a wing with hybrid laminar flow control application. *AIAA Aviation Forum*. https://doi.org/10.2514/6.2022-3770

STAB

Mitteilung

Fachgruppe: Turbulenz und Transition

Analysis of Separated Shear Flow and Reattachment over a Backward Facing Step using the DLR ADaMant Experiment

Maïté Guerin[1,2], Tobias Knopp[1], Cornelia Grabe[1], Marco Costantini[3], Andreas Schröder[3,4], Daniel Schanz[3], Reinhard Geisler[3]
[1]DLR, Institut für Aerodynamik und Strömungstechnik, Abteilung $C^2A^2S^2E$, Bunsenstraße 10, 37073 Göttingen,
[2]Laboratoire de Mécanique des Fluides de Lille, Université de Lille, Centrale Lille, Boulevard Paul Langevin, 59655 Villeneuve d'Ascq, France
(maite.guerin@centrale.centralelille.fr)
[3]DLR, Institut für Aerodynamik und Strömungstechnik, Abteilung EXV, Bunsenstraße 10, 37073 Göttingen
[4]BTU, Inst. für Verkehrstechnik, Siemens-v-Halske-Ring 15, 03046 Cottbus

In aerospace research and industry, computational fluid dynamics (CFD) and statistical turbulence models based on the Reynolds averaged Navier-Stokes (RANS) equations are a working-horse for design and analysis. Among the different flow features, it is important to correctly predict the size of separation regions and the reattachment point. In aerodynamic flows, different types of flow separation arise. Separation regions can be thin compared to the boundary thickness δ, i.e., incipient separation near trailing edges or shock-induced separation at transonic flow speed, but also thick, i.e., of the same order or larger than δ. The accuracy of RANS models to predict flow reattachment was a central topic at the ''The NASA's 40% Challenge and CFD Prediction Error Assessment Workshop 2018''. The question arose, as to whether and why some RANS models (e.g., SSG/LRR-ω) yield good agreement with experimental data for the validation case over a backward facing step (BFS), but predict reattachment too far downstream for the flow over the wall-mounted NASA hump [4].

In order to shed light on this question, a new BFS-flow experiment was performed within the DLR project ADaMant (see Fig. 1). The goals were (i) to provide highly resolved data for the mean velocity and for the Reynolds stresses using Lagrangian Particle Tracking (LPT) and for the wall-shear stress surface pattern using Temperature Sensitive Paint (TSP), (ii) to study the sensitivity of the reattachment line on the appearance of a secondary bubble by a variation of the step angle (25 deg, 45 deg, 90 deg), and (iii) to provide data from two test-facilities (the 1 Meter Tunnel Göttingen (1MG) and the Large Water Tunnel Braunschweig (GWB)).
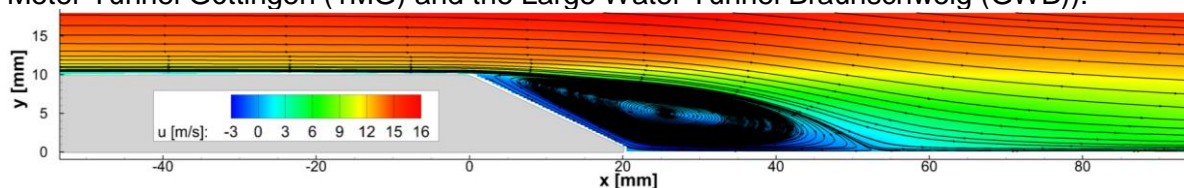

Figure 1: Backward-facing step (with 25° step angle) mean-velocity field from LPT (bin size 500 x 50μm²).

The aim of this experiment was to provide data for the validation and improvement of RANS and hybrid RANS/LES turbulence modelling and for the validation of the research hypotheses on the turbulence structure and the characterisation of the Reynolds stress anisotropies in separated shear flows proposed by Eisfeld [1,2]. Indeed, Eisfeld found a significant deviation in the turbulence structure (i.e., the Reynolds stress anisotropy a_{12}) in free-shear flows (e.g., the planar mixing layer) compared to attached turbulent boundary layer flows at zero pressure gradient. He reported values of $a_{12}=|\langle u'v'\rangle|/2k$ around 0.165 for free-shear flows, compared to $a=0.15$ for wall-bounded flows (with $\langle u'v'\rangle$ being the Reynolds shear stress and k being the turbulent kinetic energy). Such a larger value of a=0.15 for wall-bounded flows (with $\langle u'v'=0.165$ in free-shear flow regions see [1]. Hence, as the turbulent equilibrium state is observed to vary

accordingly with the flow type, locally adapted model coefficients are required to predict boundary layers and separated shear layers (and hence reattachment) correctly.

This hypothesis is studied in the present work by an evaluation of the bin-averaged 2D2C-LPT data for the 1MG with a spatial resolution of 50 µm in y- and 500 µm in x-direction. As the free-shear layer of the BFS flow is following the curved mean streamlines, the first step was to develop an automatized method to identify a suitable local coordinate system given by a locally changing unit vector basis of streamwise s-direction and normal n-direction. This flow-fitted local orthogonal basis was chosen to follow a suitable streamline. The streamline given by the peak turbulent kinetic energy in the center of the separated shear layer was selected.

The turbulent kinetic energy (TKE) of the separated shear layer was further studied. The TKE, Reynolds stress maximum and spreading rate (defined here by the 75%-maximum-TKE location) in the flow seem to also define three local regions (see Fig. 2), each associated with a different characteristic spreading rate of the turbulent kinetic energy. The spreading rate $d\delta/dx$ was found to be the largest for $x/H<3$, being $d\delta/dx\sim0.18$, then it stays roughly constant until the reattachment point near $x/H=5.5$. After flow reattachment, $d\delta/dx$ is around 0.03. The correlation coefficient $S_{uv} = |\langle u'v' \rangle|/(|u'^2|^{1/2}|v'^2|^{1/2})$ was found to be near 0.4 in the attached boundary layer, but significantly larger in the separated shear layer (i.e. between 0.55-0.6 for $x/H<3$, and around 0.5 for $x/H<5.5$). However, RANS models like the SSG/LRR model are calibrated to yield 0.4 (corresponding to an anisotropy a_{12} around 0.15, see [1]) Hence the present LPT data support the work by Eisfeld concerning the deviation of turbulence structure between attached and free-shear flows and the need for a flow-type-adapted modelling.

Then, the spreading of the separated shear flow and the TKE is studied in more detail. Different definitions for the spreading rate for planar mixing layer flows [3] were investigated. In [3], the scaling patch approach was used to show qualitative data collapse for the mixing layer. The present work attempts to likewise apply this approach to the BFS flow. Finally, the methods for data analysis are applied to the wall-resolved NASA hump flow LES data [4].
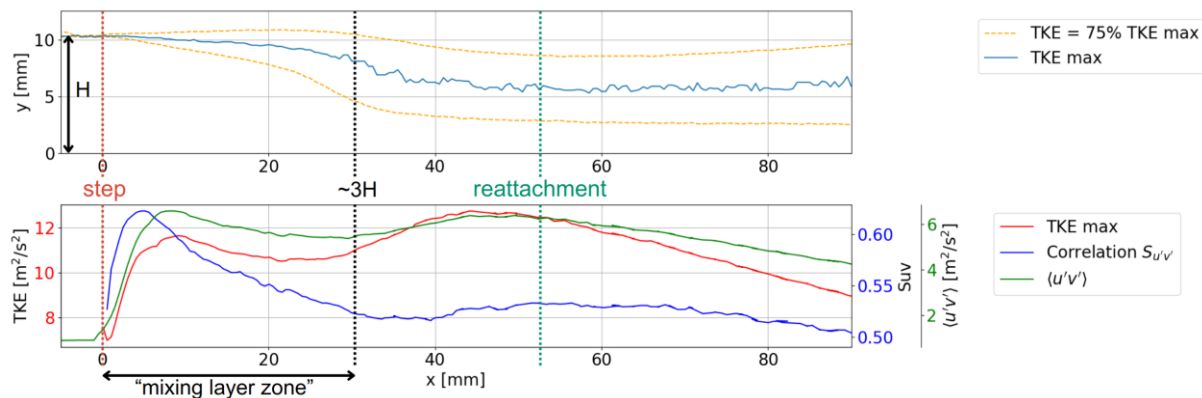

Figure 2: BFS turbulence study (for 90° step angle), step height H=10mm, entry velocity U=24.6 m/s.

To conclude, the LPT data for the ADaMant BFS flow experiment support the work by Eisfeld [2] suggesting that the local equilibrium state of turbulence is different between attached turbulent boundary layer flow and free shear flow. As an outlook, closer work on the similarity and scaling analysis of the planar mixing layer, the BFS flow, and the NASA hump flow could help to refine RANS models and to improve the understanding of turbulent free-shear flows.

References:

[1] Bernhard Eisfeld. "The importance of turbulent equilibrium for Reynolds-stress modeling". Physics of Fluids 34 (2022). DOI: 10.1063/5.0081157

[2] Bernhard Eisfeld, ''Characteristics of Incompressible Free Shear Flows and Implications for Turbulence modelling'', AIAA Journal, Vol. 59, (2021). DOI: 10.2514/1.J059654

[3] Tie Wei, Zhaorui Li and Daniel Livescu. "Scaling patch analysis of planar turbulent mixing layers". Physics of Fluids 34 (2022). DOI: 10.1063/5.0122494

[4] Ali Uzun and Mujeeb R. Malik. "Large-Eddy Simulation of Flow over a Wall-Mounted Hump with Separation and Reattachment". AIAA J., Vol. 56, 715-730 (2018). DOI: 10.2514/1.J056397

STAB

Mitteilung

Fachgruppe: Turbulenz und Transition

Modeling Approaches for Boundary-Layer Suction in Transition Transport Models

[1,4]Sebastian Helm, [1]Normann Krimmelbein, [1]Andreas Krumbein, [1,4]Cornelia Grabe, [2,4]Richard von Soldenhoff, [2,4]Heinrich Lüdeke, [3,4]Konstantin Thamm, [3,4]Peter Scholz

[1]DLR, Institut für Aerodynamik und Strömungstechnik, Bunsenstr. 10, 37073 Göttingen
[2]DLR, Institut für Aerodynamik und Strömungstechnik, Lilienthalplatz 7, 38106 Braunschweig
[3]Institut für Strömungsmechanik, TU Braunschweig, Hermann-Blenk Str. 37, 38108 Braunschweig
[4]Cluster of Excellence SE²A – Sustainable and Energy-Efficient Aviation, TU Braunschweig

sebastian.helm@dlr.de

Background

Laminarity is an important component of research for future sustainable and energy-efficient aviation and boundary-layer suction is a well-known active means of laminar flow control. As the design of laminar aircraft relies on CFD simulation the relevant physics of laminar-turbulent transition has to be included in the numerical model. In recent years transition transport models, such as the γ-$Re_{\theta t}$ model [1] or the DLR γ model [2], have been employed more frequently in aerodynamic shape optimization and also for the investigation of unsteady aerodynamic forces on laminar wings. However, to the authors' knowledge none of these models have been developed to capture the effect of boundary-layer suction.

Objective

The objective of this work is to derive and assess modeling approaches to capture the effect of boundary-layer suction in transition transport models. The focus of this work is on the DLR γ model.

Approach

The DLR TAU-Code is used for Reynolds-Averaged Navier Stokes (RANS) simulations. A mass flux boundary condition is applied to model boundary-layer suction [3]. Different models are considered to predict laminar-turbulent transition:

- The linear stability theory (LST) and e^N method are applied to generate reference solutions. This model framework has been validated for cases with boundary-layer suction [3].
- The γ-$Re_{\theta t}$ model is a widely-used model which founded the class of transition transport models [1]. It contains a transport equation for the transition criterion ($Re_{\theta t}$), which might be exploited to model the downstream effect of boundary-layer suction. However, unsatisfactory predictions were observed compared to wind-tunnel measurements of laminar-turbulent transition over a flat plate with boundary-layer suction [4].
- The DLR γ model was developed based on the γ-$Re_{\theta t}$ model with adaptations made for transport aircraft conditions [2]. It is currently our preferred transition transport model to predict laminar-turbulent transition in this particular context.

Results

For the ideal flat plate with homogeneous suction, a consistent delay of the transition location is observed for all transition prediction criteria (both for direct evaluation with boundary-layer data and as part of the transport equation approach) when the suction rate c_Q is increased (Fig. 1). However, the suction effect is significantly underes-

STAB

timated in comparison to the reference (LST). This discrepancy can be attributed to the fact that the stabilizing effect of suction on the boundary-layer profile is not considered by the transition criteria (LM2009 for the γ-$Re_{\theta t}$ model [1] and AHD simple for the DLR γ model [2]). The relatively small downstream displacement of the predicted transition location is caused by the reduction of momentum thickness when the rate of suction is increased. To address the current limitation of transition transport models the present work considers different approaches to correctly account for boundary-layer suction. This includes a correlation-based modification of transition criteria [5], the concept of equivalent pressure gradient [6] and different concepts to integrate the criteria into the transport model framework.

The different approaches are evaluated and assessed based on computations for the ideal flat plate with homogeneous and inhomogeneous suction. Furthermore, the measurement data of a real flat plate with finite thickness and blunt leading edge [4] are used for the validation of the modeling approaches.
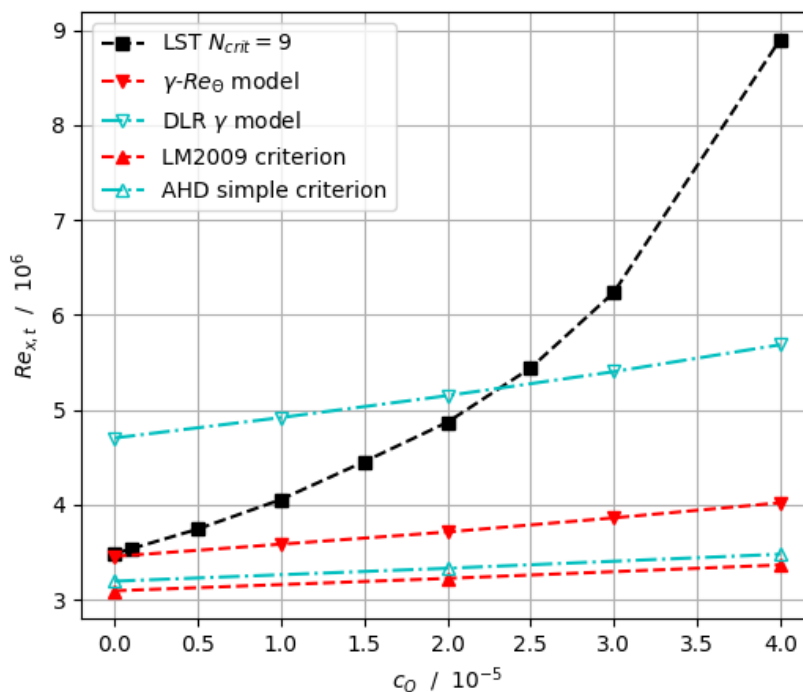

Fig. 1: Effect of homogeneous boundary-layer suction on the predicted transition location ($Re_{x,t}$) over an ideal flat plate at Mach number M=0.2 and turbulence intensity Tu=0.07% corresponding to N_{crit}=9

Acknowledgements

Literature

[1] Langtry, R. B., Menter, F. R.: Correlation-based transition modeling for unstructured parallelized computational fluid dynamics codes, AIAA journal, Vol. 47, No. 12, pp. 2894–2906 (2009)
[2] François, D. G., Krumbein, A., Krimmelbein, N., Grabe, C.: Simplified stability-based transition transport modeling for unstructured computational fluid dynamics, J. of Aircraft, Vol. 60, No. 6, p. 1-12 (2023)
[3] Krimmelbein, N., Krumbein, A.: Transition prediction for flows with suction using the e^N-method, AIAA Scitech Forum, No. AIAA 2021-0630 (2021)
[4] Helm, S., Grabe, C., Krumbein, A., von Soldenhoff, R., Lüdeke, H., Thamm, K., Scholz, P.: Wind-Tunnel Test with Boundary Layer Suction for the Validation of Transition Transport Models, AIAA Scitech (2024)
[5] Masad, J. A., Malik, M. R.: Transition correlation in subsonic flow over a flat plate, AIAA journal, Vol. 31, No. 10, p. 1953-1955 (1993)
[6] Stock, H.-W.: On laminar boundary layers with blowing and suction, Zeitschrift fur Flugwissenschaften und Weltraumforschung, Vol. 4, p. 93-100 (1980)

STAB

Mitteilung

Fachgruppe: **Turbulenz und Transition**

Correlating the internal encoding of boundary-layer profiles – Insights in neural networks used for boundary-layer stability prediction

Paul Hoffmann, Alexander Theiß, Stefan Hein
DLR – Institut für Aerodynamik und Strömungstechnik (AS)
Abteilung Hochgeschwindigkeitskonfigurationen
Bunsenstr. 10, 37073 Göttingen
paul.hoffmann@dlr.de

Motivation

The reduction of viscous drag plays a key role in the necessary reduction of carbon emissions in aviation and is heavily dependent on the boundary-layer state. Therefore, the location of laminar-turbulent transition is of crucial interest. A common way for its estimation is based on the analysis with local linear stability theory (LST), which typically requires expert-level knowledge. However, for a more accessible use of transition prediction, surrogate models for the LST have been of continuous interest for decades. In previous work [1], the authors presented an approach based on artificial neural networks (ANNs) for surrogate modelling of LST-based stability computation for three-dimensional compressible boundary layers.

In order for these surrogate models to be established in scientific application, a certain level of trust is indispensable. This holds particularly true for ANNs as they are effectively black box models. In this work, an approach inspired by the work of Zafar et al. [2] is made, where we try to get insights into the processing of boundary-layer profile data at an intermediate stage in the network by correlating neuron activations.

Methodology

The neural networks employed in a previous study [1] for the prediction of stability characteristics of planar Tollmien-Schlichting instabilities (TSI) and stationary crossflow instabilities (CFI) are further analysed, in particular the networks relying on velocity-profile information in their prediction process.

These networks have been trained on a database of stability results for compressible Falkner-Skan-Cooke basic flows for the two types of instabilities. Their network
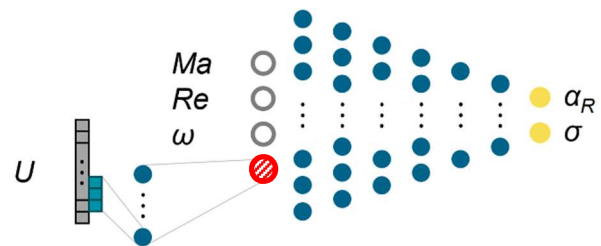

Figure 1: Schematic architecture of the CNN: the bottleneck neuron in red hatched, left of it the convolutional network part with the boundary-layer profile as the input, right of it the MLP part with further scalar inputs.

architecture is designed such that the boundary-layer profile information enters the network via a preceded convolutional network part, hence they are referred to as CNNs in the following. This first part is connected by only a single bottleneck neuron with the latter part of the network (see Fig. 1). The second network part is a multilayer perceptron (MLP), only comprising fully-connected layers, and performs the prediction of the boundary-layer stability quantities based on the processed profile information and further scalar inputs. By this design, the bottleneck neuron's activation effectively encodes the information from the boundary-layer profile in a single latent parameter Φ with respect to maximum significance for the stability characteristics of the profile.

STAB

In this work, we now aim at finding insights in what information the neural networks has learned to encode in these most meaningful, latent parameters by correlating them with best-fitting expressions, which are based on quantities describing the boundary-layer profile such as shape factors, etc.

Since for the approximation of Φ no assumption for an adequate ansatz-function can be made, as the network parts have to be seen as arbitrary, nonlinear mappings, symbolic regression (SR) is used to find fitting equations. The symbolic regression is a regression analysis method from the field of evolutionary algorithms, which finds expressions from a pool of candidate variables best fitting given data. In this problem, selected physical boundary-layer quantities and properties are chosen as the candidates.

To account for the possibly highly nonlinear character of the relations, we do not look for a correlation of the neuron activation directly. Instead, we try to find an adequate expression for the normalised activation in a first step, which exclusively shows the term of linear dependency. The corresponding scaler and bias terms to obtain the fit in the unnormalised form can then simply be determined via curve fitting in a second step.

Results

For both instability types, we search for correlations of the latent parameters of the respective ANN's bottleneck neuron based on the original training data samples. Exemplarily, the correlation between the latent parameter of the ANN with the found fit $\widetilde{\Phi}_{\mathrm{SR}}$, a function linearly dependent on the incompressible shape factor $H_{32,\,\mathrm{inc}}$, is shown for the TSI case in Fig. 2. Further, it is then examined if the found correlations also hold for selected cases from the ATTAS flight experiment dataset [3], which have previously been used to evaluate the models' prediction performance and can be regarded as test cases with realistic boundary-layer profiles faced in application.

Albeit the agreement between the fitted expressions is fairly good, correlation does not imply causation herein. Therefore, it can only be taken as an indication and not as a proof that the ANNs indeed learn to extract sensible physical representations of the boundary-layer profile.
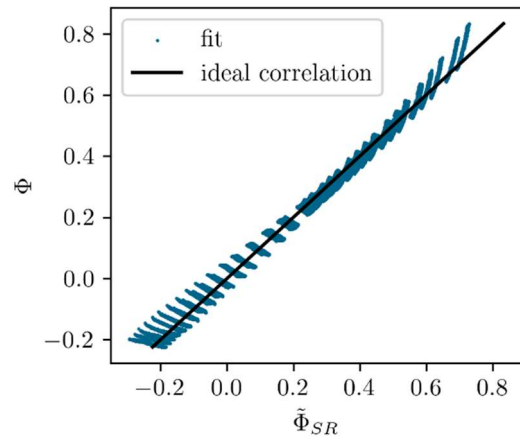

Figure 2: Correlation between the activation of the ANN's bottleneck neuron and the SR-found fit for the data samples of the training dataset for the TSI case.

References

[1] Hoffmann, J.P., Theiß, A., Hein, S.: Neural networks as a surrogate model for linear stability analysis of three-dimensional compressible boundary layers. AIAA SCITECH 2024 Forum, 2024-2684, (2024)

[2] Zafar, M. Xiao, H., Choudhari, M.M., Li, F., Chang, C.L., Paredes, P., Venkatachari, B.: Convolutional neural network for transition modeling based on linear stability theory. Phys. Rev. Fluids, **5**(11), 113903 (2020)

[3] Horstmann, K., Redeker, G., Quast., A., Dressler, U., Bieler, H.: Flight tests with a natural laminar flow glove on a transport aircraft. Flight Simulation Technologies Conference and Exhibit, 385-392 (1990)

Mitteilung

Fachgruppe: Turbulenz und Transition

Preliminary validation and stabilization of Reynolds stress models using the CFD Software by ONERA, DLR, Airbus (CODA)

Keerthana Chandrasekar Jeyanthi[1], Johannes Löwe[1], Matthias Lühmann[2], Tobias Knopp[1], Andreas Krumbein[1]

[1]DLR, Institut für Aerodynamik und Strömungstechnik, Abteilung C²A²S²E
Bunsenstraße 10, 37073 Göttingen, keerthana.chandrasekarjeyanthi@dlr.de
[2]Flight Physics, Airbus, Airbus-Allee 1,28199 Bremen

Most industrial applications of Computational Fluid Dynamics (CFD) rely on the Reynolds-averaged Navier-Stokes (RANS) equations and turbulence modelling. Irrespective of their popularity, eddy viscosity models (EVMs) such as the Spalart-Allmaras [1] and the Shear Stress Transport model (SST) by Menter [2] can be insufficient in terms of accuracy for certain flow regimes like three-dimensional (3D) separation on aircraft wings, junction flow separation, flows over curved surfaces, and vortical flows. This has led to further development of other turbulence models on the basis of second moment closure termed as the Reynolds Stress Models (RSMs). Several RSMs have been proposed ([3] [4]) yet they are reported to be not as robust and stable as the EVMs in some CFD solvers. RSMs contain seven additional equations, six for Reynolds stresses and one for the length-scale variable (e.g.

Fig 1 Grid convergence of skin friction coefficient for 2D zero pressure gradient flat plat in CODA and other legacy codes

ω) which makes its implementation into a CFD solver and the numerical solution quite challenging, in particular, if an implicit solution strategy is employed.
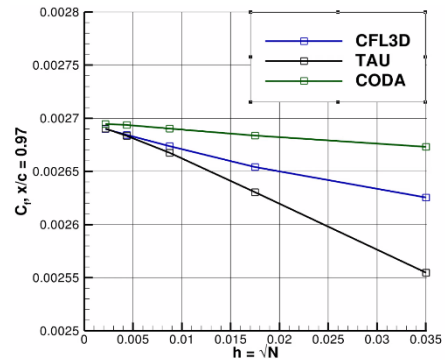
In the present work, implementation, testing and validation of the SSG/LRR-ln(ω) [5] model into the next generation flow solver CODA are considered. CODA [6] is the CFD software being developed as part of a collaboration between the French Aerospace Lab ONERA, the German Aerospace Center (DLR), Airbus, and their European research partners. CODA is jointly owned by ONERA, DLR and Airbus. For a finite volume discretization, CODA solves the RANS equations using a cell centred approach with strong implicit methods. A steady state problem is solved by marching in
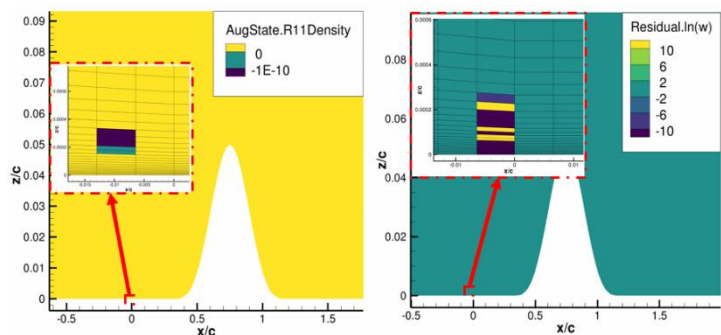

Fig 2 As the realizability gets violated in a few cells, the residuals around these cells remain high while the rest of the field has much lower residuals

fictitious pseudo time using an implicit Euler scheme and a Newton-type iteration method within each time step. The RANS equations are solved in a fully coupled manner where a single block of mean flow equations (density, momentum and energy) are solved along with the turbulent equations (Reynolds stresses and length scale variable).
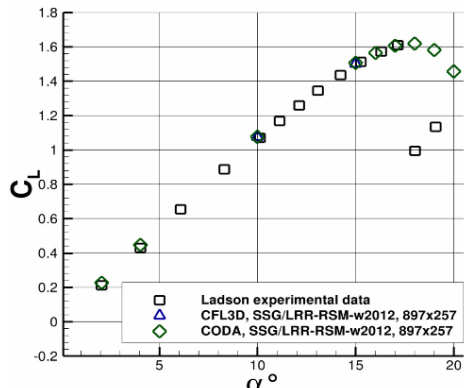
STAB

Fig 3 Validation of NACA0012

The robustness of the solver depends not only on the numerical solution method (linearization and iteration scheme, implicit/explicit treatment of turbulence model source terms, discretization scheme for the convective fluxes and the gradients), but also on details of the turbulence model. An issue arises during the solution process as the model may enter into physically unrealizable regimes [7]. We describe in detail the challenges that are faced to ensure the robustness of the implementation. The validation of the model for the 2D zero pressure gradient flat plate (2DZP) case (Fig 1) showed promising results. However, convergence issues were encountered for 2D bump in channel (Fig 2) case using the generalized gradient diffusion (GGD) model. Investigating the convergence problems for this case led to studies on realizability constraints and their violation. The usual clipping approach [8] failed for an implicit solution strategy as it affects the differentiability of the residual operator. We present the validation studies performed for some 2D airfoil cases (RAE2822, NACA0012, DLR F15, NHLP) (Fig 3) using different approaches to enforce the realizability constraints. These cases show the presence of unrealizable Reynolds stresses in the converged solution (Fig 4). Enforcing the realizability constraints removed these unphysical values and improved the robustness and
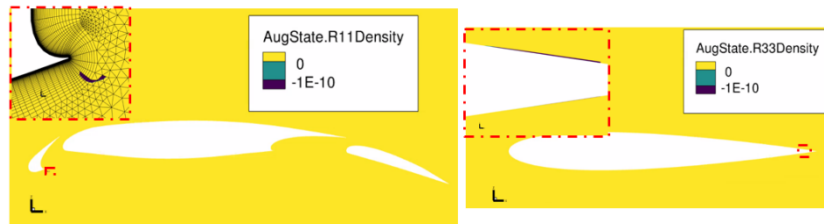

Fig 4 Presence of negative normal stresses in the converged solution of a 3-element air foil (NHLP) on the left and NACA0012 (AoA=10°) on the right.

convergence behaviour.

Bibliography

[1] P. Spalart and S. Allmaras, "A One-Equation Turbulence Model for Aerodynamic Flow," *AIAA Paper,* no. 92-0439, 1992.

[2] F. R. Menter, "Two-equation eddy-viscosity turbulence models for engineering applications," *AIAA Journal,* vol. 32, pp. 1598-1605, 1994.

[3] C. G. Speziale, R. Abid and P. A. Durbin, "On the realizability of reynolds stress turbulence closures," *Journal of Scientific Computing,* vol. 9, no. 4, pp. 369-403, 1994.

[4] B. Launder, G. Reece and W. Rodi , "Progress in the Development of a Reynolds Stress Turbulence Closure," *Journal of Fluid Mechanics,* vol. 68, pp. 537-566, 1975.

[5] B. Eisfeld and O. Brodersen, "Advanced Turbulence Modelling and Stress Analysis for the DLR-F6 configuration," *AIAA Paper,* 2005-4727.

[6] T. Leicht, D. Vollmer, J. Jägersküpper, A. Schwöppe, R. Hartmann, J. Fiedler and T. Schlauch, "DLR-Project Digital-X: Next generation CFD solver 'Flucs'," *Deutscher Luft- und Raumfahrtkongress 2016, Braunschweig,* no. 420027, 2016.

[7] U. Schumann, "Realizability of Reynolds-stress turbulence models," *The Physics of Fluids,* vol. 20, no. 5, pp. 721-725, 1977.

[8] J. C. André, G. D. Moor, P. Lacarrère and R. D. Vachat, "Turbulence Approximation for Inhomogeneous Flows: Part I. The Clipping Approximation," *Journal of Atmospheric Sciences,* vol. 33, no. 3, pp. 476-481, 1976.

STAB

Mitteilung

Fachgruppe: Turbulenz und Transition

Towards physics-based nowcasting of the instantaneous wind velocity profile using a stochastic modeling approach

Marten Klein · Juan A. Medina Méndez · Mark Simon Schöps · Heiko Schmidt

Lehrstuhl Numerische Strömungs- und Gasdynamik, Brandenburgische Technische Universität (BTU) Cottbus-Senftenberg, Siemens-Halske-Ring 15A, 03046 Cottbus
E-Mail: marten.klein@b-tu.de

Christoph Glawe

wpd Onshore GmbH & Co. KG, Borsigstraße 8, 74321 Bietigheim-Bissingen

Prediction of available wind power is continuing to gain importance with the incorporation of volatile renewable sources in the power grid. Wind power is one of the sources reducing the inertia of the power grid. Fluctuations occur on short time scales necessitating the ability to predict wind speeds on very short time horizons at a given location. A key problem in this regard is that wind fields are governed by the local atmospheric conditions in the atmospheric boundary layer (ABL). In order to improve power grid stability, control is required that can crucially benefit from nowcasting site-specific inflow velocity profiles. It is established that there are various challenges that are associated with the time-resolved prediction of the available wind power. These challenges are fundamentally related to the capturing of ABL inflow conditions (e.g. [1, 2]), but also wind farm effects (e.g. [3]), which yield further complications.

Forecasting operates on the timescale of hours, providing means for resource allocation on a day-ahead basis utilizing probabilities of undesired and desired events such as power ramps. Nowcasting, by contrast, aims to get hands on the currently available wind power sources. The challenge is to predict wind speeds in the ABL in response to constantly changing conditions. Advances in nowcasting can therefore notably benefit from advanced standalone simulation tools that are able to economically predict wind speeds by autonomously evolving the ABL over a short time horizon.

The day-ahead allocation of resources is generally limited by the predictive capabilities and resolution of the available numerical weather prediction (NWP) models. Taking ICON-D2 [4], the present operational NWP model of the German Weather Service (DWD), the spatial resolution is 2.2 km in the horizontal direction and 20 m in the vertical direction in the vicinity of the surface. Grid cells expand in height to 1.4 km toward the stratosphere so that 65 vertical mesh cell layers compose the lower atmosphere, resolving a typical wind park with only a few grid cells. The time step is usually about 30–90 sec and hence insufficient for nowcasting (on the time scale of up to a few minutes). NWP enables statistical day-ahead estimates of the available wind energy (e.g. [5]), but a detailed time-resolved and operational prediction as required for power grid control is not possible. Additional modeling (e.g. [6]) or a deconvolution strategy for NWP (e.g. [7–10]) or other computational fluid dynamics simulation (e.g. [11]) data is thus needed in order to obtain the instantaneous inflow wind velocity profiles that are specific to a site at which a wind turbine is located. Irrespective of

the technical details of the approach taken, it needs to be applicable for a variety of atmospheric flow conditions and able to capture the transient evolution of the atmospheric boundary layer.

Some of the standing challenges in modeling atmospheric boundary-layer turbulence may be addressed by considering the momentarily available energy in the flow. This is feasible to do when instantaneous flow profiles are evolved. Map-based advection modeling provides the necessary means to distinguish turbulent advection from diffusive transport processes. This approach is readily utilized in the so-called one-dimensional turbulence (ODT) model [12]. It has been demonstrated previously that ODT possesses relevant predictive capabilities for ABL flows. Application cases encompass the neutral and stratified ABL [13], surface roughness [14], stratification effects [15], and time-dependent boundary conditions [16]. The standalone model application is exemplified for the neutral ABL over a smooth surface in Fig. 1 below.

The primary objective of this contribution is to provide an overview of the regime-spanning forward modeling capabilities offered by the stochastic ODT model. The focus is on the applicability of the model and its validation for neutral and stable ABL flows as a prerequisite for future applications to challenging atmospheric conditions.
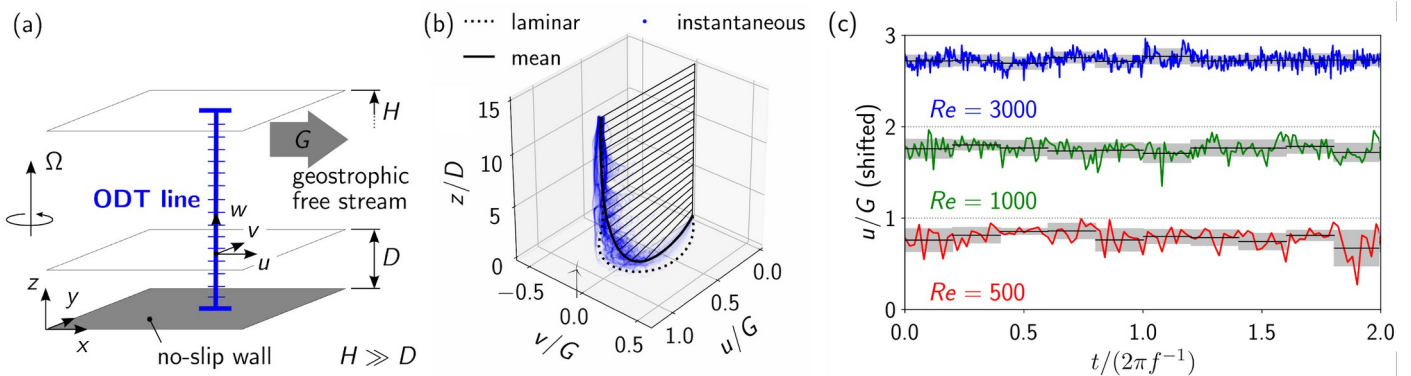

Fig. 1: (a) Sketch of the standalone ODT application to the atmospheric boundary layer (ABL). (b) 200 snapshots of the instantaneous horizontal wind velocity profile are shown together with the turbulent mean and the laminar Ekman flow solution demonstrating wind turning and wind variability effects across a notional wind turbine. (c) Stochastically simulated time series and window-based averages of the streamwise velocity u at a notional hub height $z = D$ for various turbulence intensities labeled by the Reynolds (Re) number. The hub height is taken as the Ekman length scale D to yield time series from the log region of the turbulent boundary layer [15]. $f = 2\Omega$ is the local Coriolis parameter.

References

[1] Holtslag A A M, Svensson G, Baas P *et al.* 2013 *Bull. Am. Meteorol. Soc.* **94** 1691–1706
[2] Haupt S E, Kosović B, Berg L K *et al.* 2023 *Wind Energ. Sci.* **8** 1251–1275
[3] Porté-Agel F, Bastankhah M and Shamsoddin S 2020 *Bound.-Lay. Meteorol.* **174** 1–59
[4] Reinert D, Prill F, Frank H *et al.* 2021 *DWD Database Reference for the Global and Regional ICON and ICON-EPS Forecasting System, Version 2.2.2* (Offenbach am Main, Germany: DWD)
[5] Muschinski T, Lang M N, Mayr G J *et al.* 2022 *Wind Energ. Sci*. **7** 2393–2405
[6] Ehsani R, Heisel M, Li J *et al.* 2024 *J. Fluid Mech.* **979** A12
[7] Kelley N D and Jonkman B J 2007 *Overview of the TurbSim stochastic inflow turbulence simulator* Tech. Rep. NREL/TP-500-41137 National Renewable Energy Laboratory
[8] Boyko V and Vercauteren N 2023 *Q. J. R. Meteorol. Soc.* **149** 2125–2145
[9] Sommerfeld M, Dörenkämper M *et al.* 2023 *Wind Energ. Sci.* **8** 1153–1178
[10] Yassin K, Helms A, Moreno D *et al.* 2023 *Wind Energ. Sci.* **8** 1133–1152
[11] Glawe C, Klein M and Schmidt H 2023 *Proc. Appl. Math. Mech.* **23** e202300055
[12] Kerstein A R 1999 *J. Fluid Mech.* **392** 277–334
[13] Kerstein A R and Wunsch S 2006 *Bound.-Lay. Meteorol.* **118** 325–356
[14] Freire L S and Chamecki M 2018 *Agric. For. Meteorol*. **250/251** 9–23
[15] Klein M and Schmidt H 2022 *Adv. Sci. Res.* **19** 117–136
[16] Klein M and Schmidt H 2023 *Adv. Sci. Res.* **20** 55–64

STAB

Mitteilung

Fachgruppe: Turbulenz und Transition

Modification of the SSG/LRR-ω Model for Separated Shear Flows Using Boundary-Layer Sensors

Tobias Knopp[1]
[1]DLR, Institut für Aerodynamik und Strömungstechnik, Abteilung C²A²S²E
Bunsenstraße 10, 37073 Göttingen

One paradigm for transport-equation-based statistical turbulence modeling in computational fluid dynamics (CFD) is the restriction to local flow quantities. All terms in the turbulence model equations should depend only on the local solution of mean-flow gradients and turbulence quantities (as well as their gradients). The paradigm of locality is applied not only to RANS turbulence modeling, but also to hybrid RANS/LES modeling (in particular for the design of blending functions to switch from the attached-boundary-layer-flow RANS region to the outer LES region).

An extension of the paradigm was initially proposed in [5]. For the unstructured CFD solver TAU, an additional data structure was developed which provides, for each surface point, the field points on a wall-normal line. Another data structure allows to map, for each surface point, the values of surface quantities to all field points on this wall-normal line. This enables the evaluation of the boundary layer thickness δ_{99}, integral boundary layer parameters such as displacement thickness δ^*, momentum thickness θ and the shape factor $H_{12}=\delta^*/\theta$, and pressure gradient parameters in the inner scaling $\Delta p_s^+=v/(\rho u_\tau^3)(dP/ds)$ and in Rotta-Clauser scaling $\beta_{RC}=\delta^*/(\rho u_\tau^2)(dP/ds)$. Here, u_τ denotes the friction velocity and v is the kinematic viscosity.

The boundary layer quantities can be used to define blending functions for boundary layers, which remedy shortcomings of existing blending functions [5]. Such blending functions have a value of one inside the boundary layer and decay to zero in the outer flow. There are wide-spread blending functions based on the paradigm of locality, e.g., the function F_1 used in the SST model and the function f_d used in the SA model. However, the boundary layer thickness predicted by f_d was found to be too small in turbulent boundary-layer flows in a strong adverse pressure gradient [5]. Moreover, the functions F_1 and f_d often yield unwanted behaviour near stagnation points and for the wake flow regions downstream of stagnation points and upstream-located parts of multi-element airfoils and wings.

The modification of RANS turbulence models for separated shear layer is another application of such boundary layer sensors, which is presented in this work. As described in [1], ''one of the fundamental dilemmas in turbulence modeling'' is that ''model constants are not physical constants''. The constant α_ω of the production term of the ω-equation used in the SSG/LRR-ω model controls the growth rate of shear layers. The value used in the outer layer is 0.44, which is suitable for attached boundary layers. However, a lower value of 0.30 is more suitable for free-shear slows like the mixing layer. (An alternative view for an RSM was given by Eisfeld in [9], who found that the Reynolds stress anisotropy a_{12} changes from a value around 0.15 in attached boundary layers to 0.165 in mixing layers, which can be accounted for by a flow-specific adjustment of the pressure-strain correlation model). In the present work, a sensor function is proposed which allows to change the value of α_ω between attached boundary layers and free shear layers (see Fig. 1 (left)). The modification yields a significant improvement for the reattachment of the flow over the NASA wall-mounted hump [8] (see Fig. 1 (middle)).

Another flow phenomenon for which the SSG/LRR-ω model was found to require modification is wake flow in a significant APG. Two versions to modify the dissipation rate locally in the wake subjected to APG are used. The first modification is the so-called $S_{\omega 4}$ term by Probst & Radespiel, based on previous works by Hanjalic & Leschziner. The second modification is extending an APG modification for turbulent boundary-layer flows based on the half-power law [6]. Both modifications increase the dissipation in the wake at APG [7], hence reduce the Reynolds stresses and increase the model tendency for flow reversal in the wake, i.e. to predict a region of negative values of the centerline velocity U_{CL} (see figure 1 (right)). The use of the

STAB

modification for wake flow in an APG also requires a sensor to identify the wake flow region and to characterise the strength of the pressure gradient in the free shear flow.

Besides the presentation of modifications for separated shear flows and reattachment, the potential of boundary layer sensors for the improvement of RANS turbulence models is outlined. The boundary layer sensors also allow to identify different sub-regions of attached boundary layers. RANS models are based on a generalized law of the wall [4], which does not account for Reynolds number effects. Re-effects have been observed for zero-pressure gradient boundary layer flows, e.g., the beginning of the log law in the mean velocity is near $y^+ = 2.6(\delta^+)^{1/2}$ [2], where δ^+ is the Reynolds number based on the friction velocity. The influence on the predictive accuracy for zero-pressure gradients has not been studied. However, Re-effects were found to be important in adverse pressure gradients [3,6].

The boundary layer sensors are also useful for the assessment of the reliability of aerodynamic predictions. The prediction of the separation point using present RANS models is known to be not fully reliable. As a remedy, empirical criteria to characterise the state of the boundary layer are useful. This could be threshold values for the shape factor ($H_{12} > 2.5$-2.6) and for the pressure gradient β_{RC}, above which the reliability of RANS models decreases due to not yet understood effects of strong adverse pressure gradients. Such threshold values could also be trained from large databases (and refined for special airfoil geometries and flow conditions).
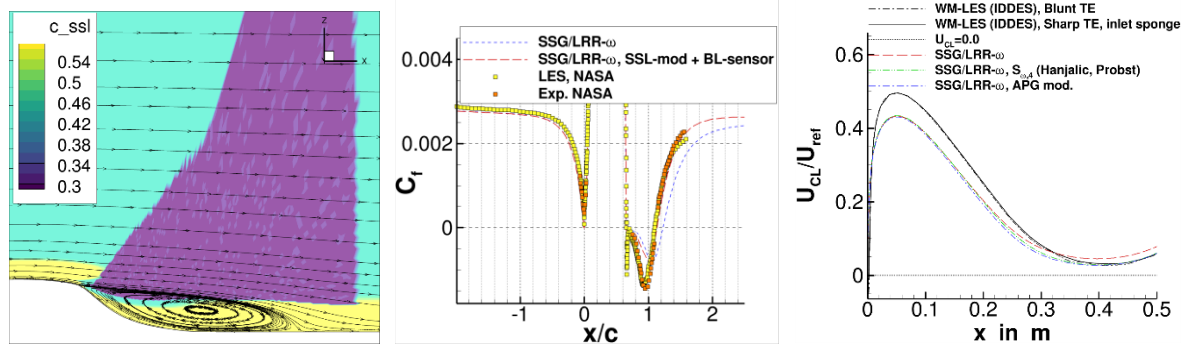

Figure 1: Flow-adapted adjustment of the coefficient α_ω (denoted by c_ssl in the legend) of the SSG/LRR-ω model in the separated shear layer (SSL) (left). Prediction for skin-friction coefficient and flow reattachment for the NASA hump flow (middle). Turbulent wake flow at adverse pressure gradient using two modifications of the SSG/LRR-ω model in the wake for the improved prediction of the tendency for flow reversal of the centerline velocity U_{CL} (right) compared to the reference LES [7].

Finally, the flow sensors for attached flow and separation are well suited to be used for turbulence model augmentation terms obtained by machine-learning methods, e.g., the field-inversion/ machine learning (FI/ML) and the gene-expression programming (GEP) approach.

References:

[1] Durbin, P.A., Petterson Reif, B.A., Statistical Theory and Modeling for Turbulent Flows, Wiley, 2000.

[2] Klewicki, J.C., Fife, P., Wei, T.: On the logarithmic mean profile. J. Fluid Mech. **638**:73–93, 2009.

[3] Yaglom, A.M.: Similarity laws for constant-pressure and pressure-gradient turbulent wall flows. Annu. Rev. Fluid Mech. **11**:505, 1979.

[4] Spalart : The Conjecture of a General Law of the Wall for Classical Turbulence Models, Implying a Structural Limitation. Flow Turbul Combust, **112**:443-457, 2023.

[5] Knopp, T.: A modification of DDES based on a detection of attached boundary layers and separation, In: 17. DGLR-Fach-Symposium der STAB, 9. – 10. Nov. 2010, Berlin, Deutschland, 2010.

[6] Knopp, T. : An Empirical Wall Law for the Mean Velocity in an Adverse Pressure Gradient for RANS Turbulence Modelling, Flow Turbul Combust, **109**:571-601, 2022.

[7] Guseva, Strelets, Travin, Shur: LES-based Computation of Evolution of Turbulent Wakes Subjected to Adverse Pressure Gradient. Math. Models Comput. Simulation **13**:91-105, 2021.

[8] Uzun, A., Malik, M.R.: Large-Eddy Simulation of Flow over a Wall-Mounted Hump with Separation and Reattachment. AIAA J. **56**:715-730, 2018.

[9] Eisfeld, B. : The importance of turbulent equilibrium for Reynolds-stress modeling. Phys. Fluids **34**, 2022.

STAB

Mitteilung

Fachgruppe: Turbulenz und Transition

Assessment and Adaptation of Transition Criteria for Non-Self-Similar Flows

[1]Normann Krimmelbein, [2]Sebastian Helm, [2]Andreas Krumbein
DLR, Institut für Aerodynamik und Strömungstechnik, [1]Lilienthalplatz 7, 38108
Braunschweig, normann.krimmelbein@dlr.de, [2]Bunsenstr. 10, 37073 Göttingen

Background

With the establishment of transport equation approaches for transition prediction a revival of simple transition criteria is accompanied. Some of the transition criteria used in transport equation approaches are derived based on linear stability theory (LST) results for self-similar flows. In this regard, one transition prediction method available in the DLR TAU code is the DLR-γ transition transport model that utilizes a simplified form of the AHD criterion [1].

Objective

Ideally, the LST based transition criteria emulate the behavior of LST computations not only for self-similar flows but also for non-self-similar flows. Generally, flows around general aerodynamic configurations deviate from having a self-similar character. This deviation is especially pronounced if the considered flow undergoes more or less strong local variations, e.g. the flow is subject to (strong) pressure gradients or to (local) suction/blowing. The objective of the work is to assess transition criteria based on reference LST computations and, if necessary, to adapt and/or reformulate these criteria to improve their prediction capability for non-self-similar flows, especially with focus on flows with suction.
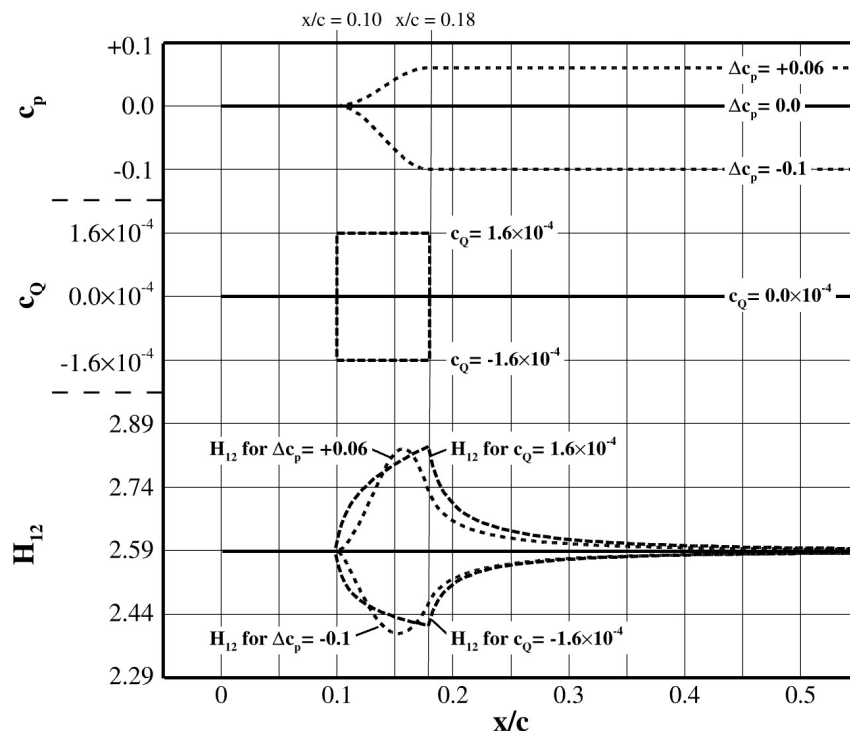

Fig.1: Flow conditions and boundary layer development

Approach

For Falkner/Skan flows the envelope of computed N-factors can be approximated as a straight line if the envelope is considered to be a function of the momentum loss Reynolds number Re_θ [2]. Based on different specific external velocity distributions different Falkner/Skan solutions can be obtained, each characterized by having a constant shape factor H_{12} and a constant pressure gradient parameter Λ_θ.

STAB

The AHD criterion [2] has been derived based on these characteristics and the parameters to determine the N-factor envelope are then based on Re_θ and Λ_θ. A general distinction of the original AHD criterion to the simplified version used in the DLR-γ model is that the original criterion utilizes Λ_θ, averaged in streamwise direction, whereas the simplified version just uses a local Λ_θ. To consider also blowing and suction, for the present work an effective pressure gradient parameter $\Lambda_{\theta,eff}$ has been established, that makes use of a certain equivalence of pressure gradient and blowing/suction for Falkner/Skan flows [3].

Results

Based on a Blasius flow at a velocity of u = 40m/s and a unit Reynolds number of 2.6×10^6 1/m, non-self-similar solutions have been established by locally imposing cosine-shaped positive and negative pressure gradients (Δc_p = +0.06 and Δc_p = -0.1) and locally introducing constant blowing/suction (c_Q = v_{wall}/u = +/-1.6×10^{-4}), see figure 1. Computations for the different flow conditions have been performed using a laminar boundary layer code. The different developments of the laminar boundary layer, expressed by the shape factor H_{12}, are shown in figure 1. LST analyses have then been undertaken to compute reference N-factor envelopes. For the simplified AHD criterion with $\Lambda_{\theta,eff}$ in its original local formulation (i.e. usage of the non-averaged $\Lambda_{\theta,eff}$) the computed N-factor envelopes more or less resemble the LST results for the Blasius flow upstream and also immediately downstream of the region with pressure gradient respectively with suction/blowing (not shown here). Additionally, an exceptionally large deviation to the LST results exists in the region with pressure gradient respectively suction/blowing (not shown here). However, using an averaged $\Lambda_{\theta,eff}$ for the simplified version of the AHD criterion significantly improves the predicted N-factor envelopes and gives results in good agreement with LST for the considered flow conditions (Fig. 2).
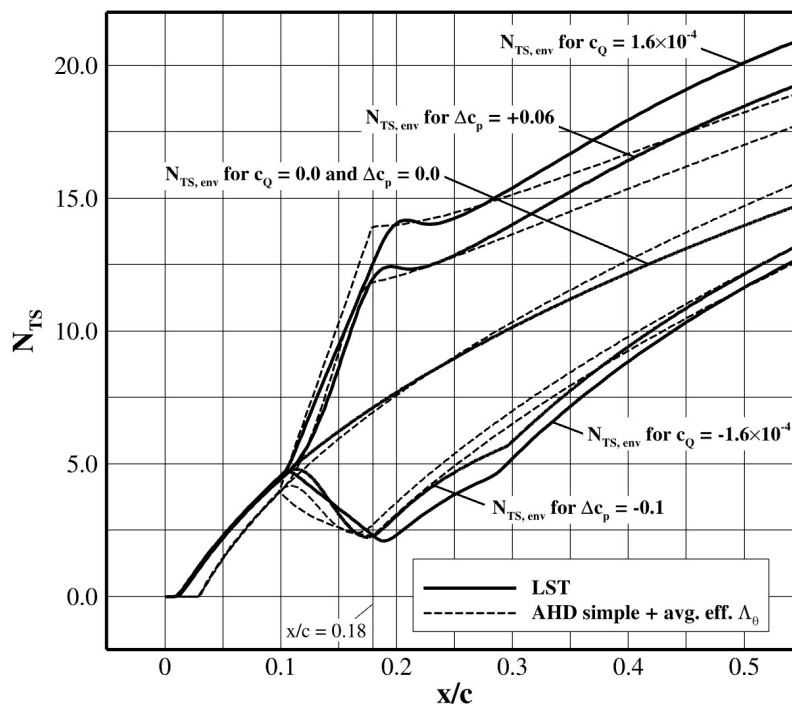

Fig. 2: Predicted N-factor envelopes

Literature

[1]   François, D. G., Krumbein, A., Krimmelbein, N., and Grabe, C., "Simplified Stability-Based Transition Transport Modeling for Unstructured Computational Fluid Dynamics," Journal of Aircraft, 2023, pp. 1–12.

[2]   Habiballah, M., Analyse de l'instabilité des couches limites laminaires et prévision de la transition de régime laminaire au régime turbulent, Ph.D. thesis, École nationale supérieure de l'aéronautique et de l'espace, 1981.

[3]   Stock, H. W., "On Laminar Boundary Layers with Blowing and Suction," Zeitschrift für Flugwissenschaften und Weltraumforschung, Vol. 4, No. 2, 1980, pp. 93–100.

STAB

Mitteilung

Fachgruppe: Turbulenz und Transition

Verhalten kritischer N-Faktoren bei Laminarhaltung durch Absaugung

Heinrich Lüdeke (Heinrich.Luedeke@dlr.de),
Paul Weigmann (Paul.Weigmann@dlr.de),
R. von Soldenhoff (Richard.vonSoldenhoff@dlr.de)

DLR, Institut für Aerodynamik und Strömungstechnik,
Lilienthalplatz 7, 38108 Braunschweig

Für die Entwicklung neuartiger, verbesserter Absaugoberflächen werden am DLR Windkanalversuche mit Absaugung an einer modular aufgebauten ebenen Platte durchgeführt. Die ersten Versuche an diesem Modell fanden 2019 statt, es folgte eine Kampagne in 2021, sowie weitere in 2022 bis 2024. Das Windkanalmodell besteht aus einer aerodynamisch geformten Nase, einem 4 m langen ebenen Bereich sowie einer verstellbaren keilförmigen Klappe an der Hinterkante. Es ist modular aufgebaut, sodass sich einzelne Elemente durch Absaugflächen oder instrumentierte Traversen austauschen lassen. Absaugpanels können im 500 mm breiten mittleren Bereich eingesetzt werden (vgl. Abb. 1). Deren Maße betragen in der Basiskonfiguration wahlweise 200 x 500 mm oder 400 x 500 mm und lassen sich beliebig positionieren sowie aneinanderreihen [1]. Aktuelle Untersuchungen zur Rumpf-Laminarisierung mit gestaffelter Absaugung erlauben weiterhin im Stromaufbereich auch 1,3m breite Panels und ermöglichen somit eine verbesserte optische Auswertung der Transition.

Die Druckverteilung entlang der Oberfläche lässt sich durch Anstellwinkelvariation sowie den Hinterkantenwinkel einstellen, sodass die Transition ohne Absaugung für alle Anströmgeschwindigkeiten von 20 m/s bis 60 m/s ausschließlich den ebenen Bereich des Modells umfasst und nicht stromauf der eingesetzten Absaugbereiche auftritt. Der Volumenstrom der Absaugung variiert zwischen $\dot{V} = 0 \ldots 10$ l/s und wird im sogenannten Laminar Flow Meter über den Druckverlust in laminar durchströmten Röhrchen mit hoher Genauigkeit gemessen. Auf diese Weise lassen sich Volumenstrombeiwerte bis $c_Q = 1 \cdot 10^{-3}$ realisieren.

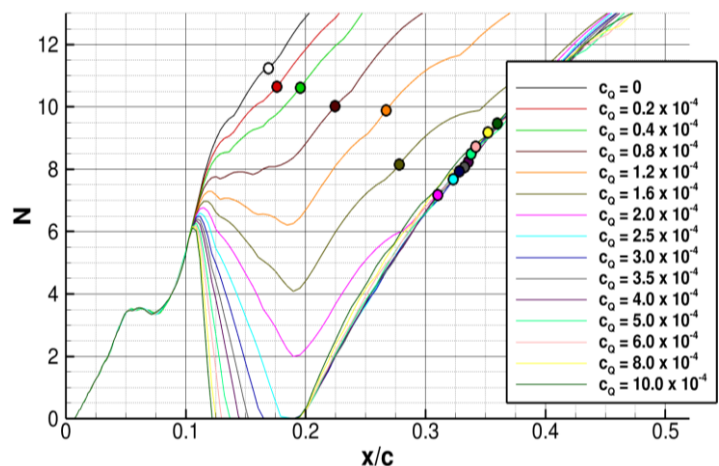**Abb. 1: Modell im DNW-NWB, aus [1]**

Abb. 2: Kritische N-Faktoren bei Absaug-Variation

Im Rahmen der vergangenen Kampagnen konnten diverse Absaugoberflächen im Bezug auf Laminarhaltung untersucht werden. Hierzu zählen u. a. klassische lasergebohrte Bleche, geätzte 50 µm starke Folien des so genannten TSSD Konzepts [3] mit unterliegendem, mehrlagigem Drahtgewebe sowie verschiedene geschlitzte Bleche oder Folien. Die Poren und Schlitze variieren im Durchmesser zwischen 50 und 60 µm. Die Porösität dieser Oberflächen liegt jeweils im Bereich von 0,8 % [2] und ist in Einzelfällen räumlich variabel gewählt.

STAB

Die Bestimmung der Transitionslinie mit Hilfe von Infrarotkameras und beheizten Panels zur Kontrasterhöhung zeigt, dass sich alle untersuchten Oberflächen, zur Erweiterung des laminaren Bereichs stromab der Absaugpanels eignen. Andererseits zeigt sich auch, dass eine Verschiebung der Transitionslinie geringer ausfällt, als durch die klassische Anwendung der Linearen Stabilitätstheorie (LST) unter Vorgabe eines einheitlichen kritischen N-Faktors N_{Krit} vorhergesagt. Dieses Verhalten wurde unter anderem in Flugversuchen mit klassischen Absaugflächen am Leitwerk beobachtet und lässt sich im Folgenden mit Hilfe der umfangreichen Datensätze für die verschiedenen Absaugflächen detailliert untersuchen.

Aus den Infrarotmessungen zur Bestimmung der Transitionslage werden mit Hilfe von LST Simulationen kritische N-Faktoren bei einer Variation der Absaugraten ermittelt. Es ergibt sich für alle betrachteten Fälle eine Reduktion von N_{Krit} bei ansteigender Absaugung, solange Instabilitäten entlang der Absaugflächen reduziert werden. Sobald entlang der Absaugung sämtliche relevanten Moden gedämpft sind, wächst N_{Krit} erneut an allerdings bei vergleichsweise geringen Erweiterungen des laminaren Bereichs (Siehe Abb. 2).

Eine zusätzliche Auswertung von Hitzdrahtdaten bezüglich des genannten Transitionsverhaltens und der Anfachung von Störmoden soll parallel in einem weiteren STAB-Artikel vorgestellt werden, um sowohl die Grenzschichtprofile als auch zeitlich aufgelöste Störmoden zu betrachten.

Verbesserte LST Vorhersagen lassen somit in Zukunft auch Optimierungen der Absaugung und folglich erweiterte Laminarhaltungs Eigenschaften erwarten. Dazu sollen in der vorgestellten Untersuchung kritische N-Faktoren bei Absaugung näher betrachtet und deren Verhalten anhand unterschiedlicher denkbarer Einflussfaktoren erläutert werden. Parallel durchgeführte DNS-Studien der Absaugung erlauben zusätzlich Einblicke in die Bedeutung solcher Faktoren wie der Aerodynamischen Rauigkeit oder Interaktionen mit der Absaugkammerung.

Literatur:

[1] R. von Soldenhoff: Overview of the Wind Tunnel Tests with Suction in the DNW-NWB, in New Results in Numerical and Experimental Fluid Mechanics XIV - Contributions to the 23rd STAB/DGLR Symposium, Berlin. Springer Verlag, 2023

[2] H. Lüdeke, C. Breitenstein: Experimental investigation of hybrid laminar flow control by a modular flat plate model in the DNW-NWB. CEAS Aeronautical Journal, 2021

[3] M. Horn, A. Seitz, M. Schneider: Cost-effective HLFC design concept for transport aircraft. DLRK, 2019

STAB

Turbulence Model Impact on the Vortices shed by one IEA10MW Blade under Large Angles of Attack

Neeraj Paul Manelil[1], Johannes Nicolaas Theron[1], Leo Höning[1],Bernhard Stoevesandt[1],Aqeel Ahmed[2], Felix Houtin Mongrolle[2] , and Bastien Duboc[2],

neeraj.paul.manelil@iwes.fraunhofer.de

[1] *Fraunhofer Institute for Wind Energy Systems, Küpkersweg 70, 26129 Oldenburg, Germany*

[2] *Siemens Gamesa Renewable Energy, 685 Avenue de l'Université,Saint-Étienne-du-Rouvray 76801, France*

Keywords: Wind turbine, Turbulence, Vortex Induced Vibration

This study investigates the impact of different turbulence models on the shed vortices emanating from one blade of the IEA 10MW [1] under extreme angles of attack. Understanding the fully detached flow behavior is crucial for estimating a potential vibration risk when wind turbines are not operating. Such a scenario can occur during maintenance periods when the turbine brake is on and is unable to spin under large yaw misalignment. Literature indicates that certain combinations of relative angles between the wind turbine blade and the incident wind could setup blade oscillations that grow [2, 3]. We use computational fluid dynamics (CFD) simulations to analyze how various turbulence models influence the wake's structure, the induced frequencies and the blade loading.The results provide insights into the accuracy and reliability of turbulence models in predicting wake dynamics and blade pressure distribution. This research offers guidance for selecting appropriate turbulence models in aerodynamic studies of large-scale wind turbines when the flow around the blade is fully detached.

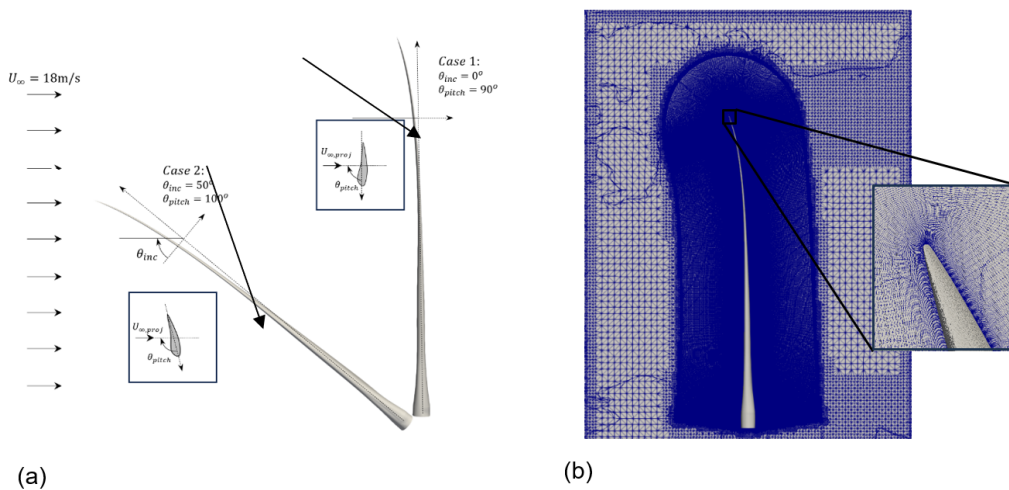The accuracy of turbulence models is particularly challenged when the flow

Figure 1: a)Schematic of cases considered, b) Body-fitted structured mesh

becomes strongly three-dimensional and is subject to separation. To investigate this, two flow scenarios (Case 1 and Case 2) have been identified and illustrated in figure 1a). In Case 1, the wind impacts the turbine blade normally on the suction side, with an inclination angle of 0° and a pitch angle of 90° as defined
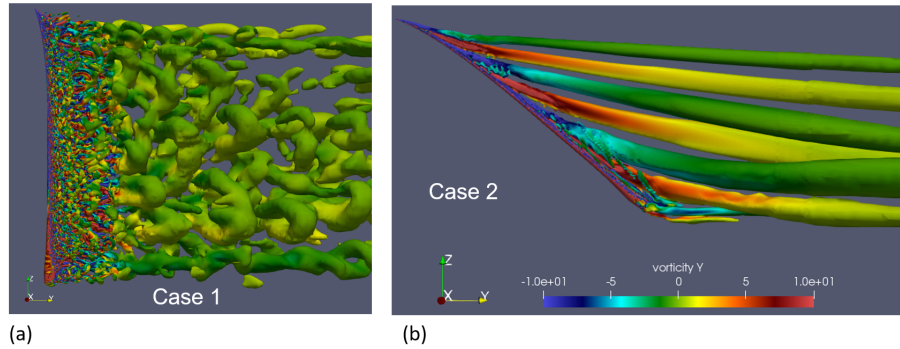
Figure 2: Iso-lambda2 surfaces coloured by vorticity in the Y plane for a)Case 1 b) Case 2

in [2]. In contrast, the second case involves the blade being inclined towards the wind, generating a span-wise flow along the blade length, with an inclination angle of 50° and a pitch angle of 100°. A uniform flow velocity of 18 m/s is applied along the Y-axis (see Fig. 1a)). Simulations are conducted using Open-FOAM V2306 with turbulence models including k-omega SST, k-omega SST LM, Spalart-Allmaras, SA-DDES, k-omega DDES, and a k-omega DDES blend used for comparison. The wake characteristics were found to be sensitive to the near-blade grid parameters such as first layer spacing, expansion ratio and radial distance of near-blade mesh. Figure 1 b) depicts the structured body-fitted mesh used in the present investigation.

Figure 2 illustrates the coherent structures in the wake of the turbine blade predicted by the k-omega SST model. The findings from this study stress the critical need for a detailed sensitivity analysis to assess the influence of turbulence models and grid resolution on wake characteristics. Some turbulence models, such as Spalart-Allmaras, tend to provide averaged wake information, missing out on small-scale fluctuations. While these models are faster and more stable, allowing for longer time steps, they lack the precision of high-fidelity models like DDES. For scenarios involving vortex-induced vibrations, DDES simulations are promising, as they effectively capture the full range of forcing frequencies that could lead to phenomena such as lock-in and subsequent tip displacement growth.

Acknowledgement

References

[1] Pietro Bortolotti, Helena Canet Tarres, Katherine Dykes, Karl Merz, Latha Sethuraman, David Verelst, and Frederik Zahle. Iea wind task 37 on systems engineering in wind energy – wp2.1 reference wind turbines. Technical report, International Energy Agency, 2019.

[2] Christian Grinderslev, Felix Houtin-Mongrolle, Niels Nørmark Sørensen, Georg Raimund Pirrung, Pim Jacobs, Aqeel Ahmed, and Bastien Duboc. Forced motion simulations of vortex-induced vibrations of wind turbine blades–a study of sensitivities. *Wind Energy Science Discussions*, 2023:1–23, 2023.

[3] SG Horcas, NN Sørensen, F Zahle, GR Pirrung, and T Barlas. Vibrations of wind turbine blades in standstill: Mapping the influence of the inflow angles. *Physics of Fluids*, 34(5), 2022.

Mitteilung

Fachgruppe: Turbulenz und Transition

A tracer particle's path through the turbulent energy spectrum

Michael Mommert[1], Theo Käufer[2], Christian Cierpka[2], Claus Wagner[1,2]

[1] German Aerospace Center (DLR), Institute of Aerodynamics and Flow Technology, Department Ground Vehicles, Bunsenstr. 10, 37073 Göttingen, michael.mommert@dlr.de

[2] Technische Universität Ilmenau, Institute of Thermodynamics and Fluid Mechanics, 98693 Ilmenau,Germany

The energy cascade is a model concept that describes the transfer of energy in turbulent flows from larger to smaller scales [1]. It is usually associated with energy spectra reflecting an inertial subrange bounded by injection and dissipation ranges. Respective energy spectra are typically generated by applying a Fourier transform to the data reflecting the flow.
In an alternative approach [2] such energy spectra can also be computed based on the joint distribution of the kinetic energy $\boldsymbol{u} \cdot \boldsymbol{u}$ and the curvature of the velocity vector field $\kappa = \left\| \frac{\boldsymbol{u} \times ((\boldsymbol{u} \cdot \nabla)\boldsymbol{u})}{\|\boldsymbol{u}\|^3} \right\|$ [3].

The advantages of this approach are the avoidance of spurious effects of Fourier transforms in non-periodic spatial domains and the persistence of links between local flow states and the energy spectrum.
A drawback of this method is the reliance on the computation of partial derivatives, which requires a high sampling resolution of the flow fields. However, this dependence can be alleviated by the use of physics-informed neural networks (PINNs) [4,5].

PINNs provide a continuous approximate solution function $[\boldsymbol{u}, T, p] = \boldsymbol{f}([t, x, y, z])$ of the governing system of differential equations, allowing gaps in the data to be filled and providing access to derivatives of $\boldsymbol{f}$ via automatic differentiation.

In our contribution, we use PINNs to enhance a dataset of Rayleigh-Bénard convection consisting of Lagrangian particle tracks with additional information from particle image thermometry [6]. Based on the resulting neural representation of the flow, we analyze the particle tracks and the distribution of temperatures within the $\boldsymbol{u}^2$-κ-plane.
The top of figure 1 shows how a curvature-based spectrum is generated: It depicts the distribution of $\boldsymbol{u}^2$ and κ for for an equidistant sampling of the PINN within the studied flow domain. From this distribution the spectrum (black line) is computed by averaging $\boldsymbol{u}^2$ for each κ-bin. Further, the path of an exemplary tracer particle is added to the $\boldsymbol{u}^2$-κ-plane, while its physical path is depicted in the bottom of figure 1.
Based on this connection, we aim to investigate links between certain regions of the flow and the $\boldsymbol{u}^2$-κ-plane.
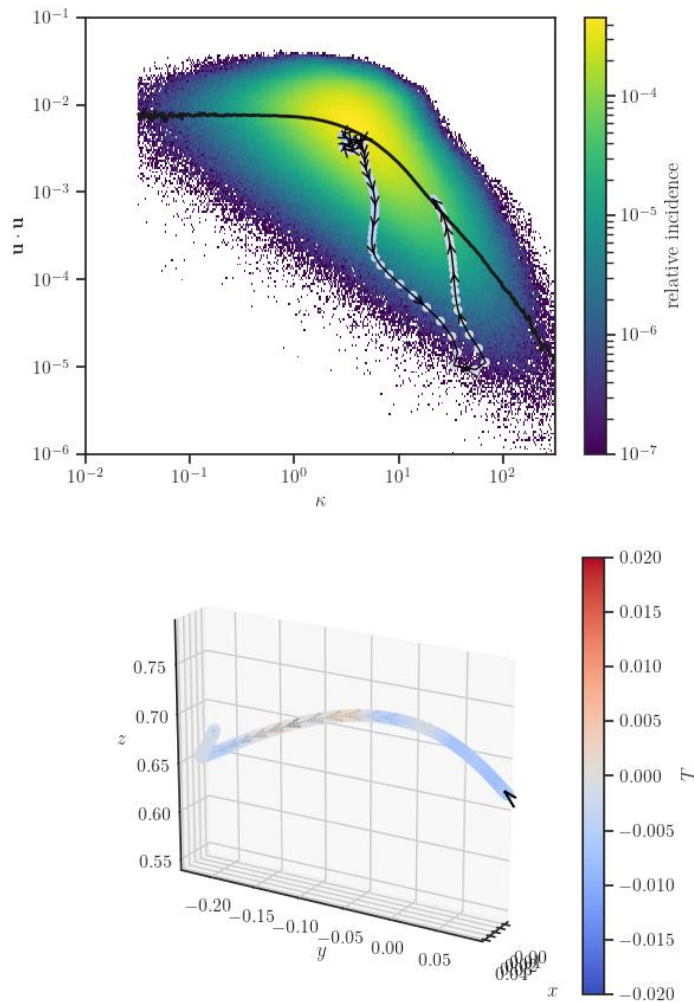
STAB

Figure 1: Top – Distribution of $\mathbf{u}^2$ and κ for the investigated flow domain, with the black line representing the derived curvature-based energy spectrum and an added path of an exemplary tracer particle. Bottom – Physical path of the tracer particle investigated above.

[1] Richardson, L.F. (1922) Weather prediction by numerical process. Q.J.R. Meteorol. Soc 203 pp. 282-284.

[2] Mommert, M., Bauer, C., Wagner, C.(2024) Curvature-based energy spectra from neural representations of turbulent Rayleigh-Benard convection. ICTAM 2024.

[3] Theisel, H. (1996) Vector Field Curvature and Applications. Diss. Universität Rostock.

[4] Raissi, M., Perdikaris, P., Karniadakis, G.E. (2019) Physics-informed neural networks: A deep learning framework for solving forward and inverse problems involving nonlinear partial differential equations. J. Comput. Phys. 378 pp. 686-707.

[5] Mommert, M., Barta, R., Bauer, C., Volk, M.-C., Wagner, C. (2024) Periodically activated physics-informed neural networks for assimilation tasks for three-dimensional Rayleigh-Benard convection. arXiv.

[6] Käufer, T., Cierpka, C. (2024) Volumetric Lagrangian temperature and velocity measurements with thermochromic liquid crystals. Meas. Sci. Technol. 35 035301

STAB

Mitteilung

Fachgruppe: Turbulenz und Transition

Revisiting near-wall modeling of fully developed turbulent flow in concentric annuli

Nishidh Shailesh Naik Burye, Juan A. Medina Méndez, Marten Klein, Heiko Schmidt
Lehrstuhl Numerische Strömungs- und Gasdynamik, BTU Cottbus-Senftenberg
Siemens-Halske-Ring 15A, 03046 Cottbus
E-Mail: naikbnis@b-tu.de, medinjua@b-tu.de

The large body of research over the years supporting Reynolds-Averaged Navier-Stokes (RANS) and Large Eddy Simulation (LES) models facilitates their application today in the optimization of many relevant industrial applications or processes. Despite the fact that canonical wall-bounded turbulent flows have been the subject of several reviews, models and theories, we revisit the topic of turbulent flows in concentric annuli. These are relevant canonical flows for several industrial applications such as coaxial heat exchangers, jet engine annular flows, wire-tube electrostatic precipitators, among many others. Our interest in the topic arises in the context of an exploratory study using a popular open source CFD solver [1]. Validation data for consideration, to that extent, was taken from Direct Numerical Simulation (DNS) results published in the literature [2, 3]. Since [1], we have carried out a more systematic analysis of the canonical system, utilizing the most readily available and well-known RANS and LES models in OpenFOAM. In all cases, the focus is on the available near-wall closure from the perspective of an industrial computational fluid dynamics (CFD) engineer. To simplify the discussion, we only report on the case of RANS models. Figure 1 shows the obtained mean velocity profile in a turbulent annular pipe flow using OpenFOAM. The radius ratio is $r_a/R = 0.1$, where r_a is the radius of the annulus and R is the outer wall radius; the Reynolds number based on the mean friction velocity as in [2], is $Re_{\tau^*} = 600$. In order to understand these results, we comment first on the correct application of near-wall closure models. Specialized literature in RANS [4] clearly distinguishes between so-called high Reynolds number (HRN) models, and low Reynolds number (LRN) models for wall-bounded RANS flows. LRN and HRN models refer in fact to the considered near-wall resolution, implying simulations with either viscous sublayer or logarithmic layer resolution, respectively. HRN RANS models rely on the use of classical laws of the wall, most notably, logarithmic laws of the wall. These are traditionally derived in the context of planar geometry, and modifications for cylindrical coordinates are not as well understood as their planar counterparts. We refer to [5] for a dated, yet clarifying discussion on the topic. It is expected that application of HRN RANS models in OpenFOAM is most accurate for the near-outer cylinder wall flow resembling a classical pipe flow. These models, however, are inconsistent for small r_a/R in the near-inner cylinder wall flow, which is more formally related to a cylindrical boundary layer [5]. Conversely, LRN RANS models rely on the use of damping functions in order to make the closure equations asymptotically consistent with near-wall behavior. Examples are the mixing length model using the van Driest damping function, or the modified ε-equation and v_t formulation in the Jones and Launder k-ε model [4]. Notwithstanding the inconsistent use of planar HRN RANS models in near-inner cylinder wall behavior, there is the more general issue faced by the average CFD engineer when choosing among near-wall closures, or "wall functions" in OpenFOAM. The average user is able to select wall functions for both HRN and LRN RANS models without any word of caution. However, here are only some RANS turbulence models in OpenFOAM effectively implementing LRN asymptotically consistent equations or damping functions. The use of the OpenFOAM k-ε implementation with viscous layer resolution and wall functions is theoretically inconsistent, given that no logarithmic law of the wall should be used, and no damping functions exist in said implementation, despite [4]

STAB

showing one implementation of k-ε with damping functions. This situation makes the choice of some "combinations" in OpenFOAM nonsensical. From the more theoretical point of view, it is also debatable whether the use of "planar" damping functions in LRN RANS cylindrical flows is suitable, e.g., the use of a planar derivative for the calculation of the dissipation at the wall in the Jones-Launder model [4]. To the best of our knowledge, no specialized research has been carried out on this topic. In order to evaluate this issue, we have developed a 1-D RANS finite volume method (FVM) solver in cylindrical coordinates implementing the classical Launder-Sharma LRN model for turbulent concentric annular pipe flows. Figure 2 shows the 1-D simulation results compared to DNS for the same case discussed before. The results seem to suggest that planar damping functions can still work in LRN RANS flows, although further research at different radius ratios and Reynolds numbers is still needed.
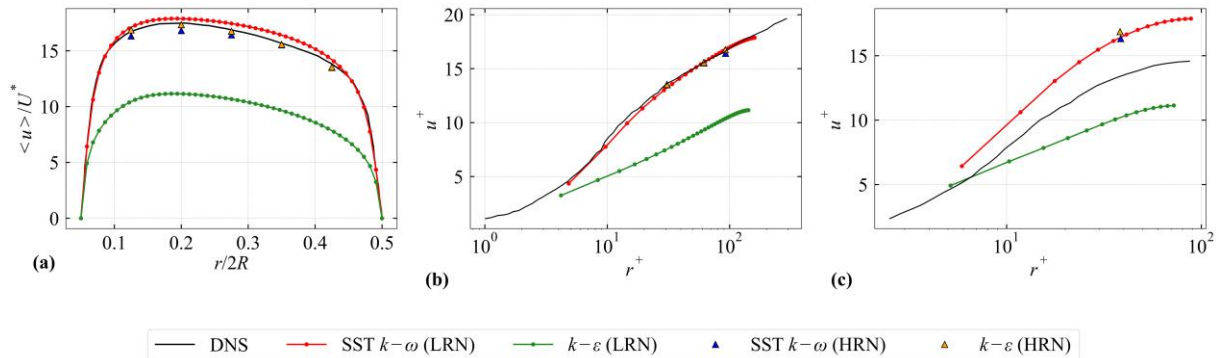
Figure 1: (a) Mean velocity profile obtained with LRN and HRN application of k-ε and k-ω models in OpenFOAM. (b) Viscous-scaled velocity profile in the near-outer wall region. (c) Viscous-scaled velocity profile in the near-inner wall region. DNS results from [2] are shown for comparison.
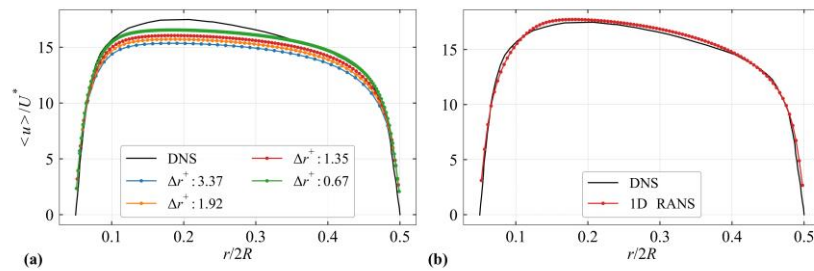
Figure 2: Mean streamwise velocity profiles: (a) Grid convergence analysis using the developed 1-D FVM RANS solver. (b) Best solution obtained with the 1-D FVM RANS solver.

References

[1] M. Klein, P.-Y. Tsai, and H. Schmidt. Stochastic modeling and large-eddy simulation of heated concentric coaxial pipes, *New Results in Numerical and Experimental Fluid Mechanics XIV,* 154: 435–444, 2024.

[2] B. J. Boersma and W.-P. Breugem. Numerical simulation of turbulent flow in concentric annuli. Flow, Turbulence and Combustion, 86(1):113–127, 2011.

[3] E. Bagheri and B.-C. Wang. Effects of radius ratio on turbulent concentric annular pipe flow and structures. International Journal of Heat and Fluid Flow, 86:108725, 2020.

[4] D.C. Wilcox. Turbulence Modeling for CFD. DCW Industries, Inc., 2006.

[5] F. M. White. The axisymmetric turbulent boundary layer on an extremely long cylinder. (AD0700246), 1969.

STAB

Mitteilung
Fachgruppe: Turbulenz und Transition
100 years of Prandtl's Mixing Length: falling short for aerodynamic analysis?

Cord Rossow, 38100 Braunschweig, cord.rossow@dlr.de

Problem Statement:

In aerodynamic flows, viscous effects are concentrated in thin boundary layers along solid surfaces. Numerical simulation at high Reynolds numbers requires the turbulent boundary layer to be correctly described, and the modeling of turbulence is still an indispensable prerequisite. Modern turbulence modeling involves one to seven additional equations with deliberately formulated source terms. The high computation times to solve the resulting stiff system of flow and turbulence equations makes the efficient integration into fast wing design cycles challenging. Therefore, one way to reduce the high numerical effort is to address the stiffness problem directly at its root, i.e. how the influence of turbulence is modeled.

Objective:

Classically, solution to the turbulent closure problem relies on Boussinesq's eddy-viscosity assumption, and the respective models are called Eddy Viscosity turbulence Models (EVM). Various types of EVM exist with increasing complexity, from algebraic or zero-equation models like the Baldwin-Lomax model, to the Spalart-Almaras one equation model, and two-equation models such as the Wilcox *KW*-model and the Menter *KW_sst*-variant. To overcome the inherent limitations of EVM, so-called differential Reynolds stress models (RSM) are proposed, where for 3D problems seven additional equations have to be solved.

Despite decades-long efforts, up to now no "universal" turbulence model has evolved which can be applied with reasonable reliability to various types of flows, related to numerical robustness as well as to predictive quality. To the contrary, depending on the problem at hand, the "most suitable" model has to be selected, where "suitable" depends to a large extend on the specific experience of the corresponding user community.

With respect to algebraic EVM however, since about the 1990s there is unanimous consensus that models like the Cebeci-Smith or the Baldwin-Lomax model are not sufficiently accurate, and thus these models are not in routine use anymore.

On the other hand, concerning numerical compatibility with the flow equations, algebraic turbulence models are very efficient, since no additional equations with source terms are introduced. Thus, if the predictive quality of algebraic turbulence models can be enhanced towards applicability for airfoil and wing design, very fast and efficient design cycles which directly embed the solution of the Navier-Stokes equations may become feasible. The objective of the present contribution is to advance algebraic modeling towards this purpose.

Strategy:

Algebraic turbulence models mainly rely on the "Mixing Length" hypothesis, which Ludwig Prandtl first proposed almost 100 years ago at the 1925 GAMM conference in Dresden [1]. Based on this Mixing Length hypothesis and further modifications, algebraic turbulence models like the Cebeci-Smith and the Baldwin-Lomax model [2] were derived and in use until the 1990s. The Baldwin-Lomax model avoided the computation of boundary layer properties such as displacement thickness and edge velocity, making it more applicable to methods solving the Navier-Stokes equations. Algebraic turbulence models were numerically robust, but for more complex airfoil and wing flows with shock-boundary layer interaction and/or flows being close to separation, these models proved to be inadequate by predicting shock locations too far downstream and/or too large regions of attached flow.

During the 1990s, Granville [3] and others reformulated certain terms and coefficients for the Baldwin-Lomax model. In the present contribution, first the influence of these "new" coefficients will be evaluated. Second, a revised formulation close to the original approach of Prandtl will be proposed by using experimental evidence from Escudier [4]. Third, the new formulation will be augmented with a sensor function based on shear stress relations [5] to enhance prediction of shock location and flows close to separation. The resulting model provides predictive properties close to the one equation *SA* or the two equation *KW_sst* EVM.

Results:

Figures 1 and 2 show computational and experimental results for the well known RAE2822 airfoil CASE 9 and 10 onflow conditions, where computations were performed with the Spalart-Almaras (*SA*) one equation model as reference, the algebraic original Baldwin-Lomax (*BL_org*) formulation, the Baldwin-Lomax model with "new" Granville coefficients (*BL_nc*), and an algebraic model based on Prandtl's original mixing length formulation with present revisions (*PR_ml*). As can be seen, the presently revised mixing length model *PR_ml* matches the results of the *SA* model quite well. Computations of the NACA4412 airfoil close to separation (not shown here) exhibit similar trends, also w.r.t. velocity profiles.

Figures 3 and 4 show 3D results of the DLR FLOWer code for the ONERA M6 wing with angles of attack (AoA) of 3.06 degrees and 6.06 degrees for the *SA*, *BL_org*, Menter's *KW_sst*, the present *PR_ml*, and the *PR_ml* model with shear stress sensor (*PR_ml+*). For the 3.06 degrees AoA case, the flow is attached and all models give similar results. For the 6.06 degrees AoA case with strong shock boundary layer interaction, the *SA* model, the *KW_sst*-model and both algebraic *PR_ml* models are closer to experimental results, whereas the original Baldwin-Lomax model *BL_org* predicts the shock wave further downstream.

Literature:

[1]Prandtl, L.: "Bericht über Untersuchungen zur ausgebildeten Turbulenz", ZAMM 5, pp.136-139, 1925.
[2]Baldwin, B.S., Lomax, H.: "Thin Layer Approximation and Algebraic Model for Separated Turbulent Flow", AIAA Paper 78-257, 1978.
[3]Granville, P.S.: "Baldwin-Lomax Factors for Turbulent Boundary Layers in Pressure Gradients", AIAA Journal, Vol.25, No. 12, pp.1624-1627, 1987.
[4]Escudier, M.P.: "The Distribution of Mixing Length in Turbulent Flows near Walls", Imperial College, Heat Transfer Section Report TWF/TN/12, 1966.
[5]Perry, A.E., Schofield, W.H.: "Mean Velocity and Shear Stress Distributions in Turbulent Boundary Layers", The Physics of Fluids, Vol. 16, No.12, pp.2068-2074, 1973.
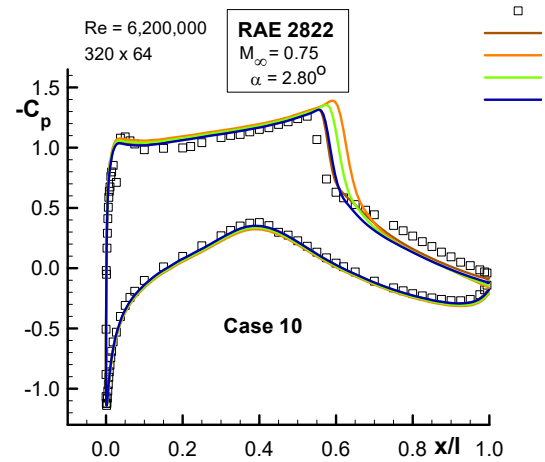
Figures:
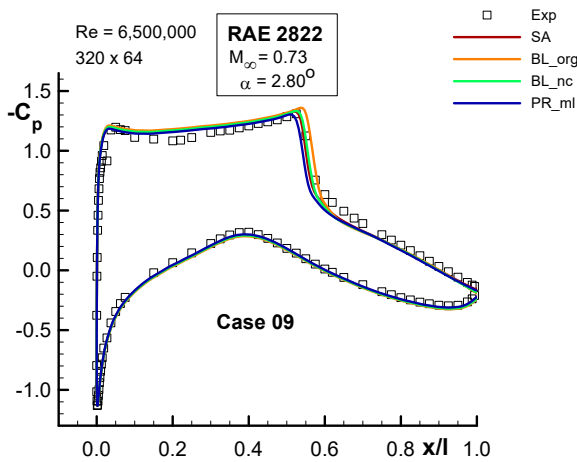
Figure 1: RAE2822 airfoil, Case 09

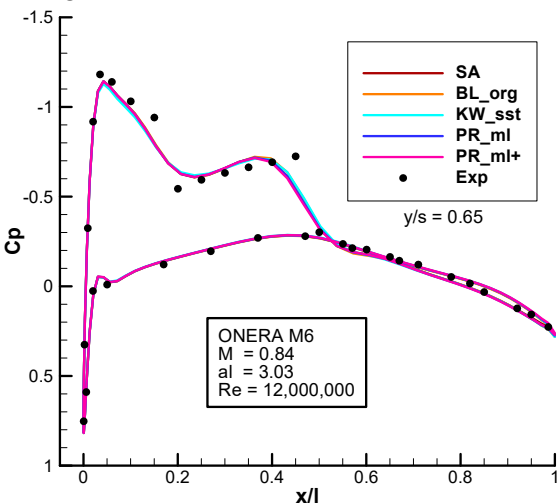Figure 2: RAE2822 airfoil, Case 10
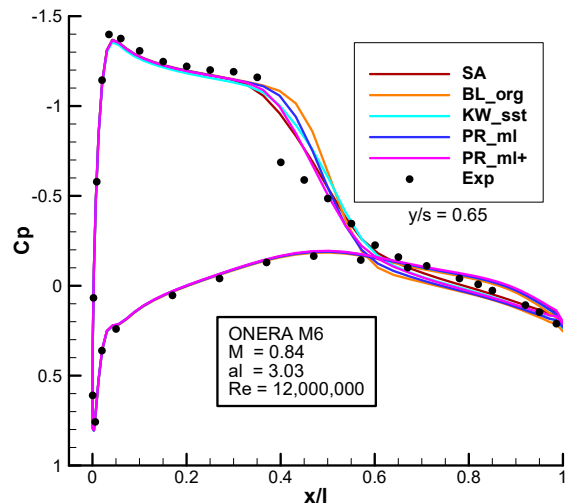

Figure 3: M6 wing, AoA=3.03 degrees

Figure 4: M6 wing, AoA=6.06 degrees

STAB

Mitteilung

Fachgruppe: Turbulenz und Transition

Investigation of different transition models with distributed propulsion over a laminar wing

Berk Sarikaya[1], Cornelia Grabe[2], Thorsten Lutz[1]

[1]University of Stuttgart, Institute for Aerodynamics and Gas Dynamics
Wankelstraße 3, 70563 Stuttgart

[2]Institute of Aerodynamics and Flow Technology, DLR
Bunsenstraße 10, 37073 Göttingen

berk.sarikaya@iag.uni-stuttgart.de

Introduction

Efficiency of propeller-driven aircraft is strongly influenced by the interactions between wing and the propellers. The distributed propulsion concept could be effective in increasing the lift and delaying flow separation. However, the past studies focus on fully turbulent CFD solutions that do not take the local unsteady effects such as interactions between the propeller wake and wing-boundary layer into account. Considering a tractor propeller upstream of an NLF wing, the helical tip vortex and the trailing edge vortices shed by the propeller interact with the boundary layer periodically and boundary layer relaxation phenomenon [1] occurs. Relaxed boundary layers are more resilient to separation, and can delay transition onset. Relaxed boundary layers (also known as calmed region) have slightly elevated levels of shear stress than undisturbed laminar flow, but lower than that of turbulent flow.

Method

At the Institute for Aerodynamics and Gas Dynamics, joint numerical and experimental studies on the impact of distributed tractor propellers on the laminarity of the wing boundary layer are conducted in the frame of the SynTrac collaborative research center. In the present study, a test case from literature [2] is replicated numerically. In the experimental case, a 9.5 mm diameter circular rod of length 0.41 m is rotated at 0.1c upstream and 0.25c down relative to the leading edge. The wing is 0.61 m wide and has a chord of 0.25 m. The wake street shed by the rod convects downstream and interacts with the wing periodically. In [2], despite the flowfield being 3-D, the crossflow components is found to be about 10% of the streamwise mean. Thus, for a basic understanding of the effects of the wake packets and streamwise boundary layer interactions, the simulations are reduced to 2-D (as experiments) with a circular rod passing in front of an airfoil (Figure 1). The rod grid starts its movement approximately 75mm above the leading edge and moves down at a constant velocity of 9.8175 m/s based on rotational frequency. DLR-TAU code is used in this study to numerically solve the URANS equations. TAU is a cell-vertex based, finite-volume solver that can solve transition transport equations and utilize overset grids in the process [3], [4]. Menter's SST model is used in conjunction with DLR 1-equation γ model and the Langtry/Menter 2-equation γ- Re_θ model [5].

Results

The streamwise evolution of the skin friction coefficients and velocity profiles at x/c = 32% for different instances of time are plotted for DLR 1-eq. transition model in Figure 2. The skin friction coefficient plots indicate that the transition point when rod is far away from the airfoil is at around 45% (timestep 1). At timestep 83, the rod is nearly in line with the leading edge, and the large wake from the rod impinges the leading edge and increases the C_f. After that, steady

STAB

movement of the shed wakes are observed as peaks that move downstream. At timestep 135, the boundary layer after 20% of chord seems to be fully turbulent which indicates early transition caused by the wake. However, the shear stress decreases rapidly as this wake passes and the point of transition moves downstream (timesteps 170 and 198). The laminarity is retained as much as 60% of the chord at timestep 198 with slightly elevated shear stress levels, which is an indicator of the relaxation. The transition point moves downstream, and the extended laminar flow benefit is realized from that timestep on. Different boundary layer profiles also suggest different temporal behavior. It is seen that the boundary layer profiles with no disturbance from the rod (e.g. timestep 1) show an inflection point (as it is close to the clean transition point) and a 'weak' boundary layer, whereas timestep 135 shows a turbulent-like shape with the steepest velocity gradient at the wall. At timestep 170, laminar-like behavior is seen, with slightly steeper gradient than the clean airfoil (timestep 1), also similarly obtained at timestep 198, with a profile that is in-between timesteps 170 and 1. The boundary layer at timestep 170 is believed to be in a relaxing state (calmed region). In the full paper, additional results for the Langtry/Menter 2-equation γ- Re_θ model will be presented as well as a comparison and analysis of the two transition transport models.
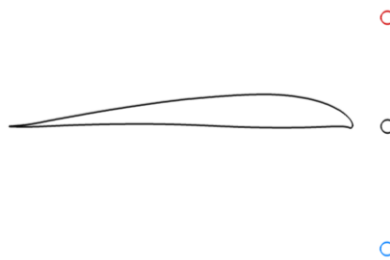
Figure 1 Airfoil and trajectory of the rod (timestep 1: red, timestep 81: black, timestep 170: blue)
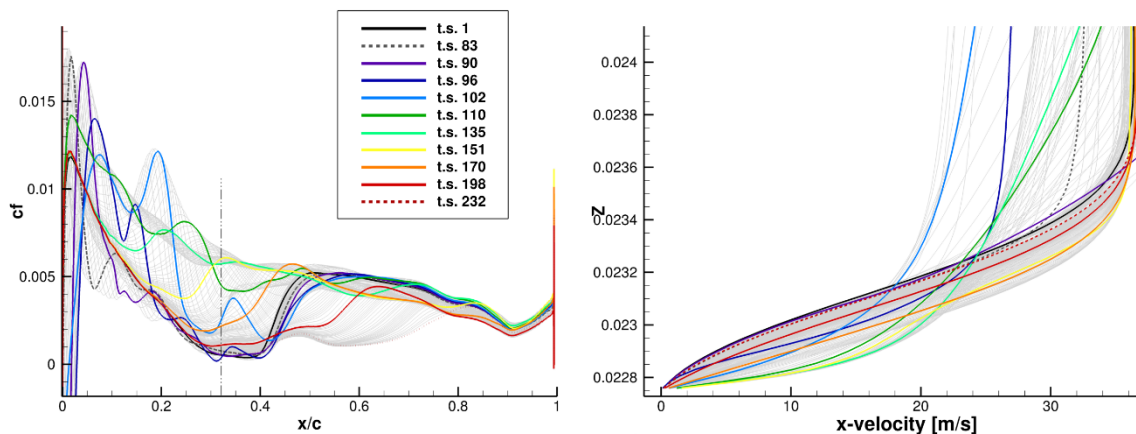
Figure 2 Skin friction coefficient (left) and velocity profiles (right) at x/c = 32%

References

[1]   R. M. Howard and S. J. Miley, "Time-dependent boundary-layer response in a propeller slipstream," J. Aircraft, vol. 26, no. 9, pp. 863–869, Sep. 1989, doi: 10.2514/3.45852.
[2]   R. W. Renoud and R. M. Howard, "Airfoil boundary-layer response to an unsteady turbulent flowfield," AIAA J., vol. 28, no. 11, pp. 1894–1900, Nov. 1990, doi: 10.2514/3.10496.
[3]   D. Schwamborn, T. Gerhold, and R. Heinrich, "THE DLR TAU-CODE: RECENT APPLICATIONS IN RESEARCH AND INDUSTRY," in ECCOMAS CFD 2006 Conference, Sept. 2006.
[4]   D. G. François, A. Krumbein, N. Krimmelbein, and C. Grabe, "Simplified Stability-Based Transition Transport Modeling for Unstructured Computational Fluid Dynamics," in AIAA SCITECH 2022 Forum, San Diego, CA & Virtual, Jan. 2022. doi: 10.2514/6.2022-1543.
[5]   R. B. Langtry and F. R. Menter, "Correlation-Based Transition Modeling for Unstructured Parallelized Computational Fluid Dynamics Codes," AIAA J., vol. 47, no. 12, pp. 2894–2906, Dec. 2009, doi: 10.2514/1.42362.

Acknowledgments

STAB

Mitteilung

Fachgruppe: Turbulenz und Transition

Numerical analysis of boundary-layer transition on a high-aspect ratio backward-swept laminar wing considering different mass cases

Martin Schmalz, Markus Ritter, Michael Fehrs

DLR Institute of Aeroelasticity, Bunsenstr. 10, 37073 Göttingen

Martin.Schmalz@dlr.de

Motivation:

In the interest of sustainable and ecologically friendly aviation, the design process of future aircraft generations must incorporate a contribution to reduce global greenhouse gas emissions. One way of reducing the fuel consumption of aircraft is to increase their aerodynamic efficiency by modifying the shape of the wing. Using a laminar wing design, the transition location on the wing can be pushed further downstream increasing the amount of laminar boundary flow and therefore minimizing frictional drag. In addition, the use of a particular leading edge shape according to a crossflow attenuated laminar flow (CATNLF) design strategy [1-3] decreases the risk of crossflow instabilities even for large leading edge sweep angles compared to other design approaches.

The design robustness might be a major challenge in the structural optimization process. According to CS-25 regulations, many different load cases have to be considered for the structural sizing within the preliminary design process of the aircraft. Furthermore, different mass cases must be taken into account based on varying fuel mass and different payload during cruise flight, which eventually have a significant influence on the elastic behavior of the wing. At the moment, it is not known how robust this kind of laminar wing design is in specific flight scenarios with varying wing deflection under loading. To ensure aerodynamic performance of the laminar wing for each individual mass case, the impact of the wing deformation on the transition characteristics must be considered.

Objective:

This work assesses an aircraft wing with natural laminar flow design in consideration of different mass scenarios using transitional CFD simulations. Each mass case is defined by a distinct amount of payload and fuel mass, thus modifying the centre of gravity and the deformation of the wing structure. It should be identified to what extent the transition location of the boundary layer flow on the wings surface is preserved in relation to each individual mass case.

Methods:

The LuFo-VI-2 project ULTIMATE (**ul**tra high efficien**t** **wi**ng and **m**ove**a**bles for nex**t** **ge**neration aircraft) investigates new concepts and strategies for improving the aerodynamic performance of future generation aircraft. Based on a derivative of the DLR-F25 configuration, a short/medium-range aircraft developed within the LuFo-VI-2 project VirEnfREI [4], an aircraft model is designed with a high-aspect ratio and backward-swept wing. The aerodynamic design of the flight shape follows a CATNLF-design for the leading edge [5]. The final design shape of the wing is used as an input for a structural optimization process as part of the DLR in-house parametric model generator cpacs-MONA [6], in which different gust and maneuver load cases are considered together with four different mass cases regarding payload and fuel mass. A hybrid CFD-mesh is created for the flight shape of the wing. In order to consider different mass cases, the CFD-mesh of the flight shape is deformed according to the particular wing deformation obtained for a specific case using radial basis functions. RANS-simulations are performed using the TAU transition module with the e^N-method for transition prediction. Here, a combination of the boundary layer solver COCO and the linear stability solver LILO is used [7].

STAB

Results:

The maximum-take-off-weight (MTOW) mass case has the largest deformation of all the mass cases considered with a maximum structural deflection of roughly 6% with respect to the semi span of the wing. It is defined by 100% payload and 49% fuel. Figure 1 shows the deformation of the wing structure for this mass case compared to the flight shape. The influence on the laminar-turbulent transition is illustrated in Figure 2 which shows a contour plot of the distribution of the wall friction coefficient c_f on the upper surface of the wing at transonic flow conditions. Due to intellectual property rights, the surface data are projected onto a rectangular planform. Neglecting the region close to the fuselage at the wing root as well as at the wing tip, it can be seen that laminar flow (low c_f values) is present almost everywhere on the upper side of the wing for the flight shape. In the case of the MTOW configuration, almost no change of the transition location is detectable in spite the large deflection at the wing tip. In this region, laminar flow is even promoted for the MTOW configuration. It can be stated that the design of the presented laminar wing provides a robust behavior against wing deformation for the particular conditions considered.

In the full paper, further mass cases with different elastic structural deformations will be considered and the impact on the performance will be analyzed.
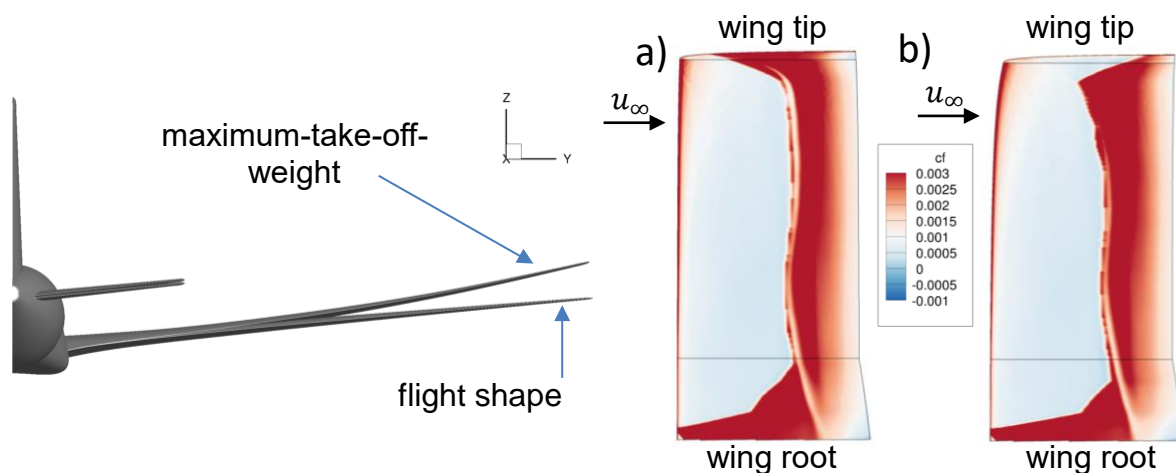
Figure 1: Deformed wing shape of mass case MTOW compared to the flight shape

Figure 2: Distribution of the wall friction coefficient c_f on the upper surface of the wing at transonic flow conditions (rectangular wing projection): a) flight shape b) mass case MTOW

References

[1] Lynde , M.N. and Campbell, R.: Computational Design and Analysis of a Transonic Natural Laminar Flow Wing for a Wind Tunnel Model. 35th AIAA Applied Aerodynamics Conference, Denver, Colorado, 2017.

[2] Campbell, R. L. and Lynde, M. N.: Natural Laminar Flow Design for Wings with Moderate Sweep. 34th AIAA Applied Aerodynamics Conference, Washington, D.C., 2016.

[3] Streit, T. et al.: NLF Potential of Laminar Transonic Longe-range Aircraft. AIAA Aviation 2020 Forum, USA, virtual event, 15th-19th June 2020.

[4] Schulze, M. et al.: The Effect of Aspect Ratio Variation on the Preliminary Aeroelastic Assessment of a Mid-Range Transport Aircraft. International Forum of Aeroelasticity and Structural Dynamics (IFASD), The Hague, The Netherlands, 2024.

[5] Streit, T., Ruberte Bailo, J. and Seitz, A.: Design of a Highly Efficient Transport NLF Aircraft with a Backward Swept Wing and a Long Single-Aisle Fuselage. 34th International Council of the Aeronautical Sciences (ICAS), Florence, Italy, 2024.

[6] Klimmek T. et al.: cpacs-MONA – An Independent and in High-Fidelity Based MDO Tasks Integrated Process for the Structural and Aeroelastic Design of Aircraft Configurations. International Forum of Aeroelasticity and Structural Dynamics (IFASD), Savannah, USA, 2019.

[7] Krumbein, A., Krimmelbein, N. and Schrauf, G.: Automatic Transition Prediction in Hybrid Flow Solver, Part 1: Methodology and Sensitivities. *Journal of Aircraft*, 46(4), 1176-1190, 2009.

STAB

Mitteilung

Fachgruppe: Turbulenz und Transition

Quantitative comparison of results from DNS and nonlinear parabolized stability equations for the subharmonic transition process

Francesco Tocci[1], Stefan Hein[1] and Philip Ströer[2]

[1]DLR, Institut für Aerodynamik und Strömungstechnik (AS),
Abteilung Hochgeschwindigkeitskonfigurationen (HGK), Bunsenstr. 10, 37073 Göttingen, Germany
francesco.tocci@dlr.de

[2]University of Twente, Department of Thermal and Fluid Engineering, Group of Engineering Fluid Dynamics, Drienerlolaan 5, 7522 NB Enschede, The Netherlands

Background and Motivation

The laminar-turbulent transition process in a flat plate boundary layer can be viewed as a sequence of instabilities, beginning with the spatial growth of two-dimensional (2D) Tollmien-Schlichting (TS) waves. As these waves amplify to certain finite amplitudes, they evolve into a three-dimensional (3D) vortical structure, forming distinct Λ-shaped vortices. These three-dimensional disturbances rapidly grow to large amplitudes, finally causing the breakdown to turbulence. Among the possible transition mechanisms, the experiments conducted by Kachanov and Levchenko [1] provided a detailed understanding of the subharmonic resonance process, also known as the H-type transition. In this scenario, disturbances arise with twice the period and twice the wavelength of the fundamental 2D TS waves, leading to a staggered pattern of Λ-vortices (see Figure 1). The H-type transition has already been extensively studied numerically, with both direct numerical simulations (DNS) (e.g., [2]) and the more computationally efficient nonlinear parabolized stability equations (NPSE) (e.g., [3]) yielding closely aligned results in the weakly nonlinear regime. However, a detailed quantitative comparison between these two methods in the more strongly nonlinear stage of the transition process has not yet been thoroughly presented. This contribution aims to address this gap, with a particular focus on identifying the limitations of NPSE—specifically, investigating the location prior to transition where NPSE ceases to deliver accurate results.

Methodology and Results

Direct simulations were carried out using the incompressible spectral element method (SEM) code Nek5000 [4]. The SEM decomposes the physical domain into spectral elements, where the flow field solution is represented by a sum of Lagrange interpolants defined by an orthogonal basis of Legendre polynomials within each element. All parameters were chosen to match the conditions of the wind-tunnel experiments conducted by Kachanov and Levchenko [1]. The disturbances were introduced via a blowing and suction strip where the wall-normal velocity was prescribed to model the effect of vibrating ribbon-induced disturbances. As in the experiments [1], the transition scenario is referred to as 'controlled,' since the initial disturbance wavelengths and frequencies are fixed such that only the fundamental 2D TS (reduced frequency $\mathrm{F} = 124 \times 10^{-6}$) and the oblique subharmonic waves (reduced frequency $\mathrm{F} = 62 \times 10^{-6}$) are introduced without any random components. The amplitudes of these two harmonics were chosen to achieve subharmonic resonance between 2D and 3D disturbances, closely following the experimental setup [1]. Figure 1 shows an instantaneous snapshot of the vortical structures developing inside the boundary layer for the H-type transition, where the characteristic staggered arrangements of the Λ-vortices are visible. This subharmonic breakdown was also investigated using compressible NPSE, which enables the study of the nonlinear evolution and interaction of 2D TS waves and 3D oblique waves, potentially up to the breakdown stage where significant changes in skin friction occur. The NPSE results were obtained with the NOLOT code (see [3]). The spatial development of selected time- and spanwise-Fourier components of the disturbances from the DNS simulation was extracted to provide a benchmark for direct comparison with NPSE. Figure 2 shows an excellent agreement between DNS and NPSE results for both the initialised and some selected nonlinearly generated harmonics, up to a streamwise location where nonlinear effects remain weak. Note that deviations observed further upstream are due to differences in mode initialization between the two approaches, leading to varying transients. However, after these initial transients have decayed, the agreement between DNS and NPSE becomes excellent. This agreement, facilitated by using a common base flow in both DNS and NPSE—thereby minimizing inaccuracies due to base flow differences rather than methodological discrepancies—provides a strong foundation for further analysis. Specifically, the final contribution will focus on identifying the point at which NPSE begins to lose accuracy in the highly nonlinear regime closer to the transition point, where deviations from DNS become significant and NPSE may ultimately fail to converge.
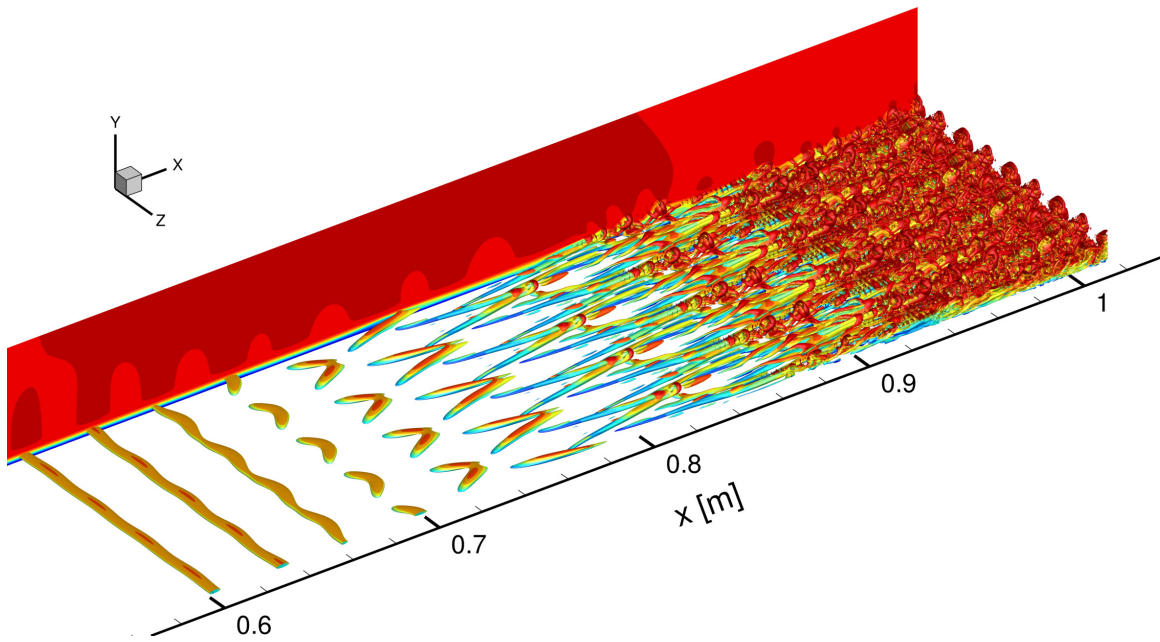
STAB

Figure 1: Instantaneus isosurfaces of the Q-criterion coloured by the streamwise velocity, showing the staggered Λ-vortices.
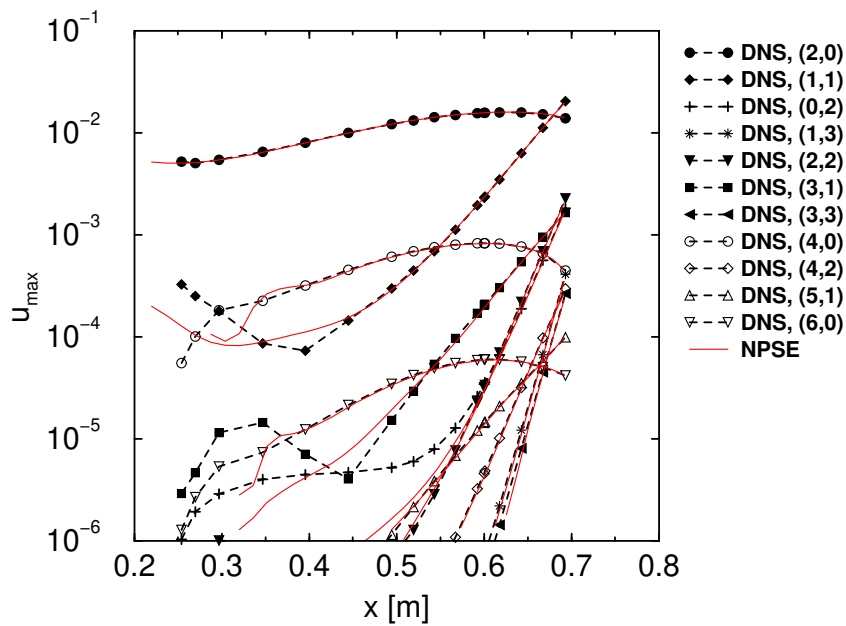

Figure 2: Comparison of amplification curves for the streamwise velocity component between DNS (symbols) and NPSE (solid red lines) across various harmonics commonly considered in the literature. The initialised 2D and 3D TS waves are denoted by $(2,0)$ and $(1,1)$, respectively, with the nonlinearly generated harmonics labeled as (m,n), where m and n represent multiples of the frequency and the spanwise wavenumber of the oblique TS mode $(1,1)$, respectively.

References

[1] Y. S. Kachanov and V. Y. Levchenko. The Resonant Interaction of Disturbances at Laminar-Turbulent Transition in a Boundary Layer. *Journal of Fluid Mechanics* 138 (1984), pp. 209–247.

[2] H. F. Fasel, U. Rist, and U. Konzelmann. Numerical Investigation of the Three-Dimensional Development in Boundary-Layer Transition. *AIAA Journal* 28.1 (1990), pp. 29–37.

[3] S. Hein. "Nonlinear Nonlocal Transition Analysis". DLR Forschungsbericht 2005-10. PhD thesis. University of Stuttgart, 2005.

[4] P. F. Fischer, J. W. Lottes, and S. G. Kerkemeier, 2008 *Nek5000 Web page*. http://nek5000.mcs.anl.gov

STAB

Mitteilung

Fachgruppe: Turbulenz und Transition

Validation and Analysis of the Reynolds-Stress Model SSG/LRR-ω for Wall-Bounded Flows with Mean-Streamline Curvature

Srinivas L. Vellala[1,2] and Tobias Knopp[1]

[1]DLR, Institut für Aerodynamik und Strömungstechnik, Abteilung C²A²S²E
Bunsenstraße 10, 37073 Göttingen

[2]Friedrich-Alexander Universität Erlangen-Nürnberg, LSTM, Cauerstr. 4
91058 Erlangen (srinivas.l.vellala@fau.de)

The present work is dedicated to validation and analysis of the Reynolds-stress model (RSM) SSG/LRR-ω for turbulent boundary layer flows along walls with concave and convex surface curvature. During the last decade, only a few new test cases of wall-bounded flow with curvature have been studied, most of them using DNS/LES. This is in contrast to the importance of the surface curvature effects on the lower side of modern transonic airfoils. Moreover, this is in contrast to the large number of experimental and numerical studies that have been performed for the improvement and validation of turbulence models (RANS, hybrid RANS/LES, wall-modeled LES) for turbulent boundary layer flows subjected to pressure gradient, separation and reattachment.

RANS turbulence modeling for flows with significant streamline curvature was mainly pursued for models based on the Boussinesq hypothesis. Linear eddy-viscosity models cannot capture the mean-streamline curvature effect where convex curvature reduces turbulence and concave curvature amplifies it. Empirical modifications have been proposed to alter the growth rate of turbulence, e.g., for the Spalart-Allmaras model (SA) and for the SST model (see [5,6]). For a RSM, which remedies the need for the Boussinesq hypothesis, the need for curvature correction(s) is still open. The production tensor of the Reynolds stresses is exact and able to capture the effects of mean-streamline curvature. However, there are other tensorial terms involving modelling, viz., (i) the turbulent transport of the Reynolds stresses due to velocity and pressure fluctuations, (ii) the pressure-strain-correlation (i.e., redistribution), and (iii) dissipation. The different model contributions of the SSG/LRR-ω model are studied. Regarding (i), different models for the turbulent transport, the generalised gradient diffusion hypothesis (GGDH) and the simple gradient diffusion hypothesis (SGDH) are considered. Analytical investigations highlight the importance of the Reynolds stress anisotropy to capture curvature effects [5]. Moreover, a sensitisation to curvature using the idea by Zeman [8] is investigated. Concerning (ii), the different redistribution models LRR, SSG, and blended SSG/LRR model are considered.

The present work reviews existing test-cases from the 1970s and 1980s and gives an assessment regarding their suitability for the validation of curvature effects. The selected cases are the flows by Gillis & Johnston (1983) and by So & Mellor (1975). Moreover, the case by Monson & Seegmiller (1992) is also used, as this case was used for the design of the rotation-correction for the Spalart-Allmaras model (SA-RC) by Shur et al. (2000).

For the selected cases, a computational set-up (geometry/boundary of the computational domain, boundary conditions) is developed based on the information given in the corresponding publications. For this purpose, the position of the inflow boundary is determined to match the boundary layer properties (boundary layer thickness, shape factor, skin-friction coefficient C_f) at different reference positions upstream of the curvature region. Moreover, the shape of the wall opposite to the curved wall of interest is designed to match the streamwise distribution of the pressure coefficient C_p measured in the experiment. For this, a gradient-based optimisation method was developed and applied. The re-design of the opposite wall was necessary to account for three-dimensional effects in the wind tunnel experiment (e.g., corner vortices, boundary layers on the spanwise wind-tunnel side walls) and to account for local effects due to special devices used in the wind-tunnel like suction boxes, which cannot be described by an exact boundary condition in a CFD solver.

STAB

The results for the convex-curvature turbulent boundary-layer flow by [1] are shown in figure 1. The model ingredients of the SSG/LRR-ω (GGDH, blended SSG/LRR redistribution model) were found to yield best agreement with the experimental data among the possible options. The GGDH is superior to SGDH, which is plausible as it benefits from the wall-normal fluctuation v'^2 and the importance of the different Reynolds normal stresses in curved flows (see [5]). The blended SSG/LRR redistribution model was found to give better agreement with the experimental data than SSG and LRR model alone. Additionally, a sensitisation of GGDH on curvature (denoted CC-1) based on the work by Zeman [8] was developed, which was found to yield a small improvement for the predicted Reynolds stresses in the outer boundary layer.
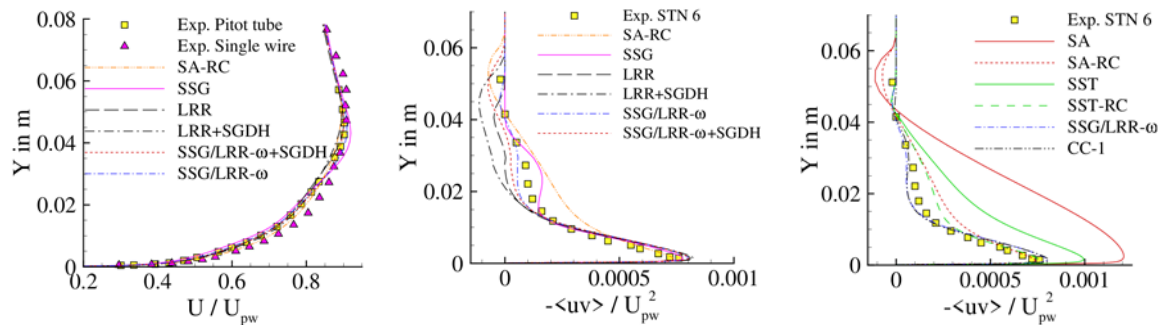
Figure 1: Convex-curvature turbulent boundary-layer flow by Gillis & Johnston (1983) [1]: Study of effect of redistribution model (LRR, SSG, SSG/LRR) and turbulent transport model SGDH, GGDH (left and middle) and curvature sensitisation of GGDH inspired by Zeman [8] (denoted by CC-1).

Moreover, for the flow by Gillis & Johnston, the SSG/LRR-ω model was found to yield a superior agreement with the experimental data compared to SA-RC and SST-RC. For the test-case by Monson [3], similar results were obtained. For the concave-curvature case by So & Mellor [2], the SSG/LRR-ω model was also found to yield good agreement with the experimental data, except for effects due to the presence of Görtler vortices, which could not be captured.

To conclude, the SSG/LRR-ω model was found to yield overall good agreement with experimental data for different validation cases of turbulent boundary-layer flows with convex and concave streamwise surface curvature.

References:

[1] Gillis, J.C., Johnston, J.P., Turbulent boundary-layer flow and structure on a convex wall and its re-development on a flat wall. Journal of Fluid Mechanics, Vol. 135, pp. 123-153, 1983.

[2] So, R.M.C., Mellor, G.L., Experiment on Turbulent Boundary Layers on a Concave Wall. Aeronautical Quarterly 76, 1975.

[3] Monson, D.J., Seegmiller, H.L., An experimental investigation of subsonic flow in a two-dimensional U-duct. NASA TM 103931, 1992.

[4] Shur, Michael L., Michael K. Strelets, Andrey K. Travin, and Philippe R. Spalart. Turbulence modeling in rotating and curved channels: assessing the Spalart-Shur correction. AIAA Journal, Vol. 38, pp. 784-792, 2000.

[5] Durbin, P., Adapting Scalar Turbulence Closure Models for Rotation and Curvature. Journal of Fluids Engineering, Vol. 133, pp. 061205-1-8, 2011.

[6] Durbin, P., Some recent developments in turbulence closure modeling. Annual Review of Fluid Mechanics, Vol., 50, pp. 77-103, 2018.

[7] Bradshaw, P., Effects of streamline curvature on turbulent flow. AGARDograph No. 169, 1973.

[8] Zeman, O., The persistence of trailing vortices: A modeling study. Phys. Fluids 7, 135-143, 1995.

[9] Vellala, S.L., Sensitisation and Analysis of the Differential Reynolds Stress Modell SSG/LRR-omega for flows with mean-streamline curvature using local Richardson number. Master thesis, Friedrich-Alexander-Universität Erlangen, 2024.

STAB

Mitteilung

Fachgruppe: Turbulenz und Transition

Robust dynamic mode decomposition for the analysis of coherent flow structures

Andre Weiner, Janis Geise
TU Dresden, Chair of Fluid Mechanics, George-Bähr-Str. 3c, 01062 Dresden,
andre.weiner@tu-dresden.de, janis.geise@tu-dresden.de

The spectral decomposition of time-resolved snapshots is a common approach to understand and model coherent structures in fluid flows. K. Taira et al. [1] provide a comprehensive overview of several methods and applications. The proper orthogonal decomposition (POD) is straightforward to compute and also forms the foundation for many derived algorithms [2]. An analysis of the POD mode coefficients sheds light on the frequency content of the corresponding spatial modes. However, for complex flows, a single mode often contains mixed frequency content from multiple, possibly unrelated flow patterns. The spectral POD (SPOD) avoids this mixing by filtering multiple overlapping blocks of the snapshot data before computing the POD for each filter frequency individually [3]. The partitioning into multiple blocks smoothens the resulting spectra at the cost of reduced frequency resolution. A drawback of the SPOD is the enormously increased computational cost and memory consumption compared to the POD. A third common algorithm is the dynamic mode decomposition (DMD) introduced by P. Schmid [4], where a linear relationship between pairs of consecutive snapshots is assumed. The standard DMD operator is easy to compute and interpret. The temporal dynamics of each spatial mode are described by exactly one pair of frequency and growth rate. A significant obstacle in the practical DMD analysis is the pronounced sensitivity to noise and nonlinearity, which is why a plethora DMD variants have been developed to improve robustness [5]. As first noted by J. H. Tu et al. [6], the standard DMD is not limited to snapshots from a single recording (trajectory). Combining snapshots from multiple runs is an effective noise reduction measure that does not require any algorithmic modifications. In the optimized DMD [7], the original operator definition is replaced by a nonlinear least-squares definition that accounts for the error propagation over the entire sequence of snapshots. Another powerful idea is the consistency between forward and backward propagation [8]. The inverse of the forward operator, computed in the standard DMD, relates pairs of snapshots backward in time. Typically, the backward error will be much larger than the forward error due to a bias introduced by noise. The consistent DMD [8] balances both errors. Optimized DMD and consistent DMD require tailored solutions of nonlinear, nonconvex optimization problems. Therefore, the different ideas are algorithmically not compatible. Moreover, the optimized DMD is not applicable to ensembles of snapshots, i.e., snapshots recorded in multiple runs.

Our contribution presents an alternative approach to compute the DMD [9], which provides enormous flexibility in the operator definition. The key idea is to exploit advanced libraries and optimization techniques developed by the deep learning community. Specifically, we employ automatic differentiation and empirically enhanced gradient descent algorithms to combine and solve for multiple, user-defined constraints (forward-backward consistency, error propagation). The approach also enables learning from multiple trajectories and other powerful machine learning techniques, e.g., early stopping to prevent overfitting and batch training for accelerated learning. The figure below demonstrates the robustness of the proposed method for the flow past a cylinder. Even for severely corrupted snapshot data, the flow dynamics can be extracted reliably thanks to the additional constraints placed on the operator.

In the full manuscript, we present additional results for turbulent flows, discuss further algorithmic extensions, and compare the results to those obtained with related methods, i.e., POD and SPOD. The presented algorithms and examples are available via FlowTorch [10], an open-source Python library for flow analysis.

STAB

Leading five eigenvalues λ of the DMD operator for the canonical flow past a cylinder at Re=100. Each square contains a zoom view of a dedicated portion of the unit circle (inner circle area shaded). γ denotes the noise level. The results are averaged over 10 runs. Legend: ref. – exact DMD applied to clean data, exact – exact DMD, ADAM/POD – proposed algorithm, varPro – optimized DMD via variable projection.

[1] K. Taira et al.: "Modal analysis of fluid flows: an overview", AIAA Journal (2017)

[2] J. Weiss: "A tutorial on the proper orthogonal decomposition", AIAA Journal (2019)

[3] A. Towne et al.: "Spectral proper orthogonal decomposition and its relationship to dynamic mode decomposition and resolvent analysis", Journal of Fluid Mechanics (2018)

[4] P. J. Schmid: "Dynamic mode decomposition of numerical and experimental data", Journal of Fluid Mechanics (2010)

[5] P. J. Schmid: "Dynamic mode decomposition and its variants", Annual Review of Fluid Mechanics (2022)

[6] J. H. Tu et al.: "On dynamic mode decomposition: theory and applications", Journal of Computational Dynamics (2014)

[7] T. Askham, J, N. Kutz: "Variable projection methods for an optimized dynamic mode decomposition", SIAM Journal on Applied Dynamical Systems (2018)

[8] O. Azencot et al.: "Consistent dynamic mode decomposition", SIAM Journal on Applied Dynamical Systems (2019)

[9] A. Weiner, R. Semaan: "Backpropagation and gradient descent for an optimized dynamic mode decomposition", ArXiv (2023)

[10] A. Weiner, R. Semaan: "FlowTorch – a Python library for analysis and reduced-order modeling of fluid flows", Journal of Open Source Software (2021)

STAB

Mitteilung

Fachgruppe: Versuchsanlagen

Aspekte zur Auslegung des High-Speed-Diffusors und der Umlenkecken des neuen
Windkanals der Fakultät für Maschinenbau an der UniBw M

Oliver Meyer[1]
Benjamin Heine[2]
Daniel Romann[3]

[1] Institut für Aerodynamik und Flugsimulation, Universität der Bundeswehr München, Werner-Heisenberg-Weg 39, 85577 Neubiberg, oliver.meyer@unibw.de
[2] PARI GmbH, Moosstrasse 3, 82319 Starnberg
[3] aem-GmbH, Maria-Probst-Str. 3, 80939 München

Der neue Windkanal des Fachgebietes Strömungsmechanik der Fakultät für Maschinenbau der UniBw M hat nach der Messstrecke einen vergleichsweise steilen Diffusor, der zum Ablösen neigt. Die gegebenen räumlichen Randbedingungen sowie das Ziel, den Windkanal möglichst mit eigenen Mitteln zu realisieren, führen schließlich zu dem kritischen, relativ kurzen Hochgeschwindigkeitsdiffusor, siehe Abb. 1. Verschiedene Maßnahmen zur Vermeidung von Strömungsablösungen werden untersucht und anhand des Gesamtdruckverlustes über den Diffusor bewertet. So werden z.B. Turbulatoren am Diffusoreintritt sowie auf halber Diffusorlänge eingesetzt, eine Aufteilung des Diffusors in vier Teildiffusoren zur Verringerung der relativen Diffusor Öffnung vorgenommen und ein Konus auf der Mittelachse des Diffusors eingesetzt, der letztlich den Öffnungswinkel des Diffusors stark verringert und die Strömung direkt auf den Ringquerschnitt des Gebläses lenkt, siehe Abb. 2.

Darüber hinaus werden die Ergebnisse einer numerischen Untersuchung des Ablöseverhaltens von dreidimensionalen quadratischen Diffusoren vorgestellt, die während des Baus des Windkanals durchgeführt wurde, siehe Abb. 3. Das Ablöseverhalten von quadratischen Diffusoren wird in einem Stabilitätsdiagramm zusammengefasst und damit die vorhandenen Lösungsansätze hinsichtlich ihrer Ablösungsneigung eingeordnet. Damit können die experimentellen Ergebnisse zur Validierung der Berechnungen herangezogen werden.

Dem Bau des Windkanals ging zudem eine umfangreiche numerische Studie zur Auslegung der Umlenkecken voraus. Bei der Auslegung eines anderen Windkanals hatte sich gezeigt, dass mit herkömmlichen Umlenkblechen, die weitgehend nach dem Stand der Technik ausgelegt waren, die Strömung nicht ausreichend umgelenkt wurde und die Gefahr einer ungleichmäßigen Gebläseanströmung bestand. Um dennoch eine gleichmäßige Gebläseanströmung zu gewährleisten, wurden verschiedene geometrische Parameter der Umlenkecken variiert und anhand verschiedener aerodynamischer Kriterien bewertet. So wurden der relative Radius, der relative Abstand, eine Vorder- und Hinterkantenverlängerung sowie der Anstellwinkel der Vorderkante der Umlenkbleche variiert. Die Qualität der Strömung nach der Umlenkung wurde anhand der radialen Geschwindigkeitskomponente, des Druckverlustbeiwertes ζ, der globalen Homogenität der Strömung sowie der lokalen Homogenität, d.h. dem Einfluss der Nachläufe hinter den Umlenkblechen, bewertet. Die hier im Windkanal realisierten Umlenkbleche wurden schließlich nach den Ergebnissen dieser Studie ausgelegt.
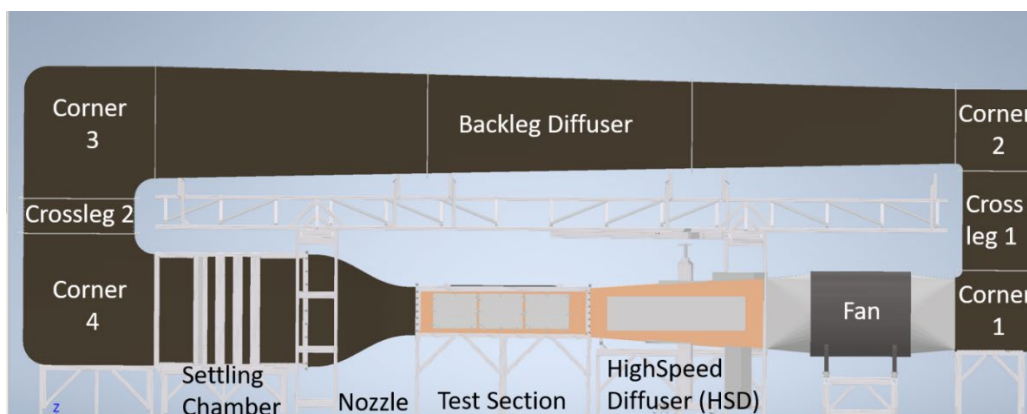
Abb. 1: Seitenansicht des Neuen Windkanals mit dem untersuchten High Speed Diffusor
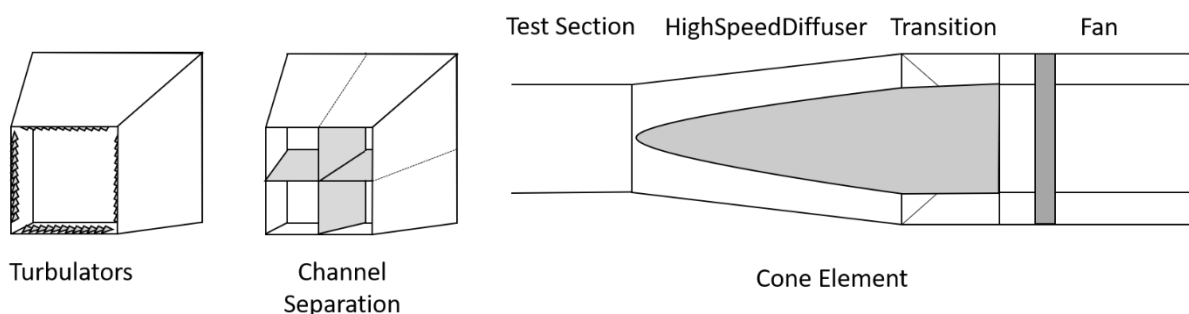
Abb. 2: Maßnahmen zur Reduktion der Ablöseneigung des High Speed Diffusors (s.o.)
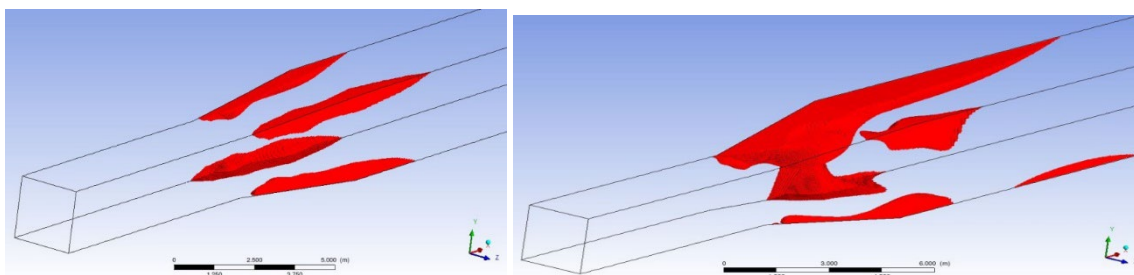

Abb. 3: Numerische Darstellung wachsender Ablösegebiete bei zunehmendem Öffnungswinkel in einem quadratischen Diffusor [1]
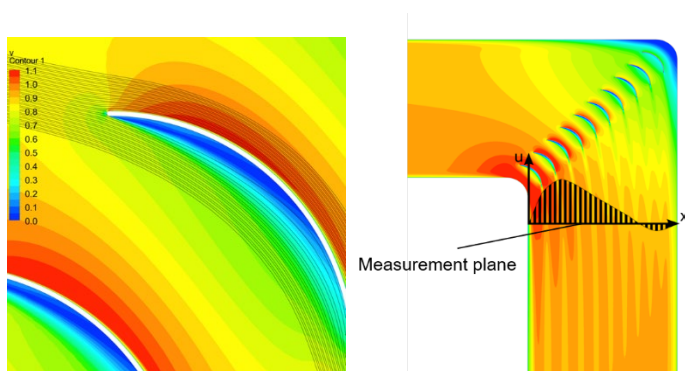

Abb. 4: Detail der Durchströmung einer Umlenkecke (links) und die Darstellung der Strömungs-Bewertungsebene nach einer Umlenkecke (rechts)

Referenzen

[1]   Kipek, Matthäus: *Numerical Analysis of Three Dimensional Quadratic Diffusers*, Master Thesis at UniBw M, Munich, Germany, 2016

STAB

Mitteilung

Fachgruppe: Versuchsanlagen

Entwicklung eines Kleinwasserkanals zum Einsatz optischer Messtechnik für Lehrzwecke

Steffen Risius[1], Alois P. Schaffarczyk[1], Jost Kemper[1], William Thielicke[2]

1. Kiel University of Applied Sciences (FH Kiel), Grenzstraße 3, 24149 Kiel
2. Optolution Messtechnik GmbH, Gewerbestraße 18, 79539 Lörrach
Email: steffen.risius@fh-kiel.de

Basierend auf dem Wasserkanal von Prandtl präsentieren wir einen Kleinwasserkanal mit ähnlichen Abmessungen, der zum Einsatz von optischer Strömungsmesstechnik, insbesondere für Lehrzwecke entwickelt wurde. Fast 150 Jahre nach der Geburt Ludwig Prandtls und 120 Jahre nach Prandtls berühmten Veröffentlichung zur Grenzschichttheorie und zur Strömungsablösung, sind deren Tragweite für Schüler und Studierende noch heute schwer zu erfassen. Ebenso fristet die Erklärung der Physik des Fliegens, zu der Prandtls Tragflügeltheorie entscheidende Beiträge geliefert hat [2], in Schulen und Hochschulen noch heutzutage ein eher kärgliches Dasein [3]. Ziel der hier vorgestellten Arbeit ist es zu beschreiben, wie moderne optische Strömungsmessverfahren in einem kleinen Wasserkanal verwendet werden, um diese Inhalte an Studierende zu vermitteln.

Der präsentierte Kleinwasserkanal (ca. 1200 x 150 x 300 mm) ist ähnlich aufgebaut, wie der Originalwasserkanal, den Prandtl für seine ersten strömungsphysikalischen Untersuchungen nutzte. Als Antrieb wird ein Strömungsgenerator mit 200 W verwendet, dessen feinregulierbare Drehzahl die Einstellung einer Strömungsgeschwindigkeit zwischen ca. 0.05 und 0.40 m/s ermöglicht. Durch Gleichrichter und Siebe wird die Strömung vom Antrieb auf der Unterseite mehrfach begradigt und in den oberen Teil des Kanals, in dem sich die Messstrecke (ca. 140 x 125 x 200 mm) befindet, umgelenkt. Der Kanal wird für den Einsatz der optischen Messtechnik *Particle Image Velocimetry (PIV)* [4] genutzt, dessen Aufbau im Folgenden näher beschrieben wird.

Zur Aufnahme der Strömungsgeschwindigkeiten mittels PIV wird ein 500 mW Pulslaser (der Klasse 2M) verwendet und ein Lichtschnitt mit 0.5 mm Breite und einer Wellenlänge von 638 nm erzeugt, der über eine Lichtschnittoptik von oben in die Messstrecke eingekoppelt wird (Optolution LD-PS/0.5). Die Aufnahme der PIV Daten erfolgt über eine CMOS Kamera mit 2.35 Megapixel, die seitlich in die Messstrecke gerichtet ist und eine maximale Aufnahmefrequenz von 80 Doppelbildern pro Sekunde, bei einem minimalen Bildabstand von 60 µs ermöglicht (Optolution OPTOcam 2/80). Die Kamerabelichtung und die Laserpulse werden mit einem im Laser integrierten Synchronizer gesteuert. Zur Sichtbarmachung der Strömung werden 50 µm große Seeding-Partikel aus Polyamid verwendet. Die Aufnahme und Auswertung der PIV-Daten erfolgt über PIVlab, eine freie MATLAB Toolbox.

Die beschriebene Versuchsanlage ermöglicht es unterschiedliche Strömungskörper zu untersuchen und deren Umströmung mittels PIV quantitativ zu erfassen. Beispielsweise können Zylinderumströmungen sichtbar gemacht werden und die Ablösefrequenzen der Kármánschen Wirbelstraße bei unterschiedlichen Strömungsgeschwindigkeiten und Zylinderdurchmessern untersucht werden. Ebenso können Tragflächenprofile innerhalb des Kanals untersucht werden und deren Auftriebsbeiwerte bei unterschiedlichen Anstellwinkeln mit Hilfe der Zirkulationsbestimmung ermittelt werden.
Gute Erfahrungen wurden mit der Verwendung transparenter Strömungskörper gemacht, die eine Abschattung des Lichtschnitts auf der vom Laser abgewandten Seite vermeiden.

STAB

In dieser Arbeit beschreiben wir beispielhaft Ergebnisse von Untersuchungen eines Tragflügelprofils bei niedrigen Reynolds-Zahlen (Re ~ 20000). Die Daten werden mit numerischen Ergebnissen verschiedener RANSE-Löser verglichen. Der hier gezeigte Vergleich illustriert die beobachteten Phänomene und verdeutlicht die Chancen und Herausforderungen eines kombinierten experimentell-numerischen Untersuchungsansatzes.

Die aktuelle optische Messmethoden ermöglicht es auch mit vergleichsweise einfachen experimentellen Aufbauten wertvolle Ergebnisse zu erzielen. Durch die PIV-Messtechnik bietet der präsentierte Kleinwasserkanal eine Möglichkeit die historisch einschneidenden Erkenntnisse Prandtls in der Lehre erfahrbar zu machen. Dadurch bietet der Versuchsaufbau einen niedrigschwelligen Zugang zu essenziellen experimentellen Daten, die mit entsprechenden numerischen Rechnungen verglichen werden.
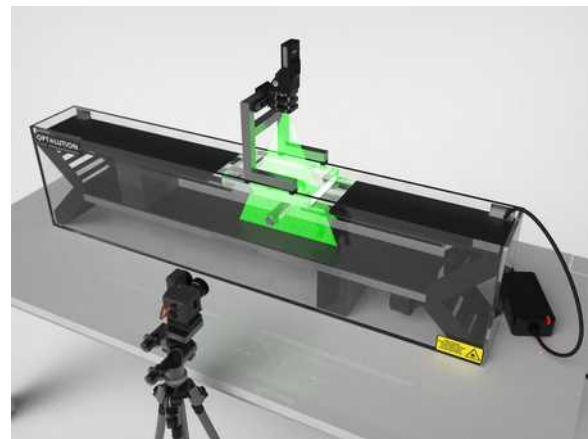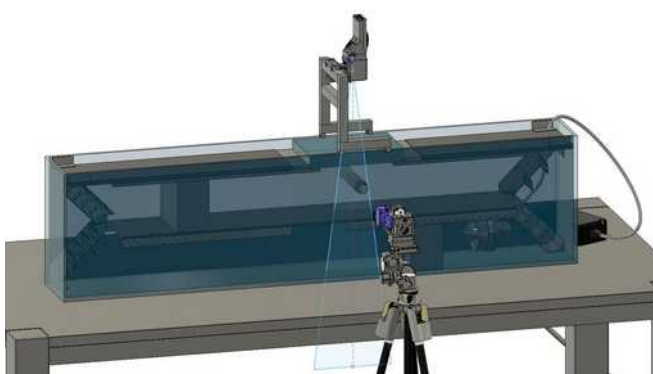
Bild 1: Aktuelle moderne Version von Prandtls Wasserkanal, der für die Lehre an Hochschulen eingesetzt wird (Quelle: optolution.com).
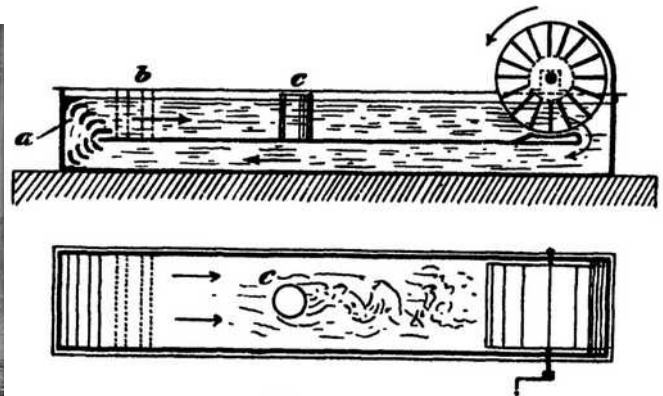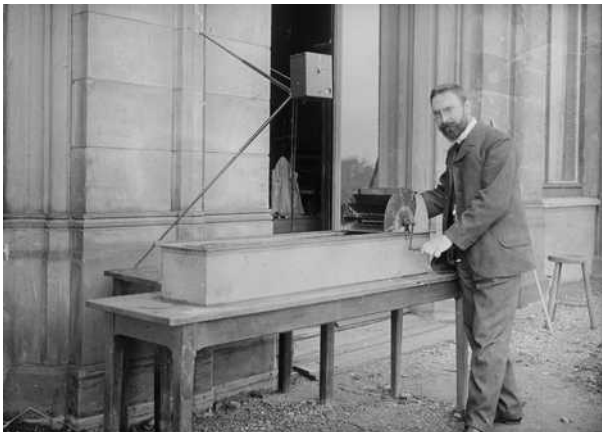
Bild 2: Historischer Aufbau des Wasserkanals von Ludwig Prandtl (Quelle: dlr.de).

[1] L. Prandtl: *Über Flüssigkeitsbewegung bei sehr kleiner Reibung*. Verhandlungen III, Intern. Math. Kongress. Heidelberg, 1904, S. 484

[2] L. Prandtl: *Tragflügeltheorie*. 1., Mitt. Ges. Wiss. Gött., Math.-phys. Kl., 151 (1918). Tragflügeltheorie. 2., dto., 107 (1919)

[3] W. Send: *Physik des Fliegens* (The Physics of Flying), Physikalische Blätter (6/2001), 51-58

[4] M. Raffel, C. Willert, S. Wereley, J. Kompenhans (2007): *Particle Image Velocimetry: A Practical Guide* Springer Berlin, Heidelberg

STAB

Mitteilung

Fachgruppe: Versuchsanlagen

Windkanal mit Sensor – Vergleich Experiment und CFD-Rechnung

Wind Tunnel with Sensor – Comparison Experiment and CFD-Computation

Wolfgang Send
ANIPROP GbR, Sandersbeek 20, 37085 Göttingen
wsend@aniprop.de
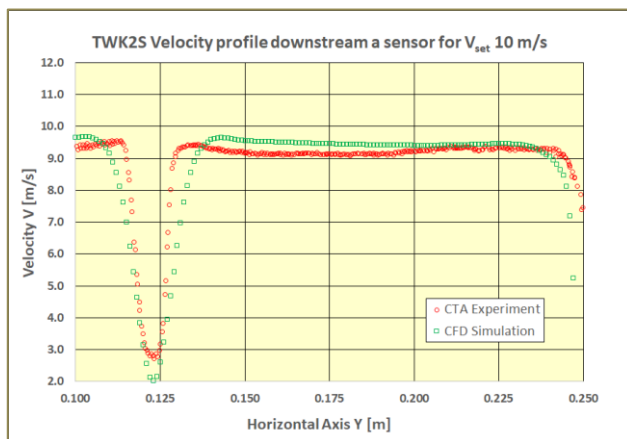
Bild 1. Vergleich Messung und CFD-Rechnung.

Gegenstand der Arbeit ist die experimentelle Untersuchung des Einflusses eines zylinderförmigen Sensors (d = 8 mm) und die numerische Nachbildung des Experiments in gleichem Maßstab. Bild 1 vergleicht eine Messung und eine CFD-Rechnung. Die y- und die z-Komponente der Wirbeldichte in Bild 2 zeigen das Ausmaß der Störung stromab. Die x-Position der Querschnitte ist die gleiche wie in Bild 1. Geometrie und Rechennetz sind Bild 3 zu entnehmen. Stromauf von der Sensorposition zeigt sich bei der Wirbeldichte keinerlei Störung mehr. Die Strömung bleibt stromab jedoch instationär, wie ein Strömungsfilm zeigt. Die blauen und roten Ränder in Bild 2 gehören zur Grenzschicht des Kanals TWK2S. Dessen Ausführung ist an anderer Stelle bereits beschrieben [1].

Das vertikale Geschwindigkeitsfeld v_z im Nachlauf des Sensors zeigt in der CFD-Modellierung eine komplexe Struktur, deren Details im Experiment nicht vergleichbar erfasst werden können. Der Anstieg der vertikalen Komponente ist allerdings gemessen worden. Anders als v_x wird v_z im

Ausgangspunkt der Arbeit war der Vergleich verschiedener Sensoren in ein- und demselben Windkanal [1]. Die neue Anordnung sollte nun die Frage klären, wieweit ein Sensor das Geschwindigkeitsfeld in seiner Umgebung beeinflusst. Dazu wurde der Windkanal für eine CFD-Rechnung maßstäblich nachgebildet und in die Messkammer ein Sensor eingelassen. Die Rechnung ist mit der Software STAR-CCM+ von Siemens ausgeführt.
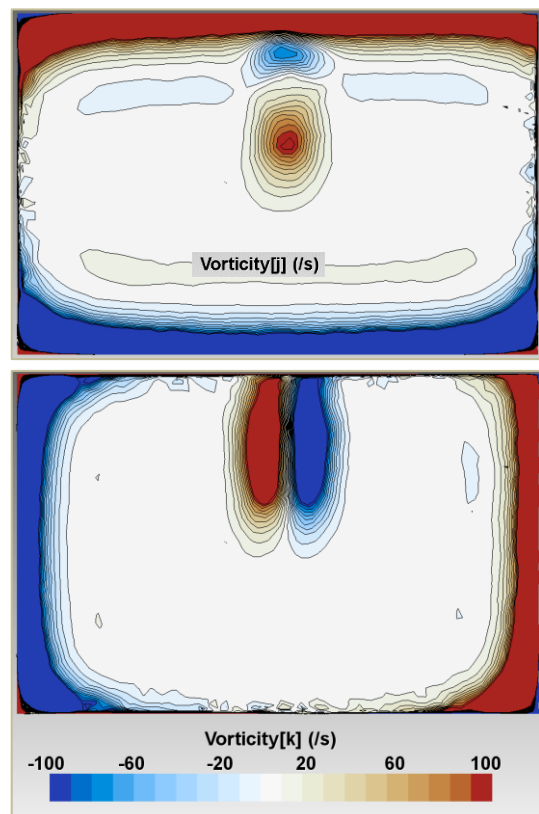
Bild 2. Wirbeldichte j_y und j_z bei x_S.

Bereich des Sensors größer und nicht kleiner. Der Sensor wird dazu möglichst parallel zur Strömung ausgerichtet. Bild 4 zeigt die z-Komponente im Experiment und in der Modellierung.
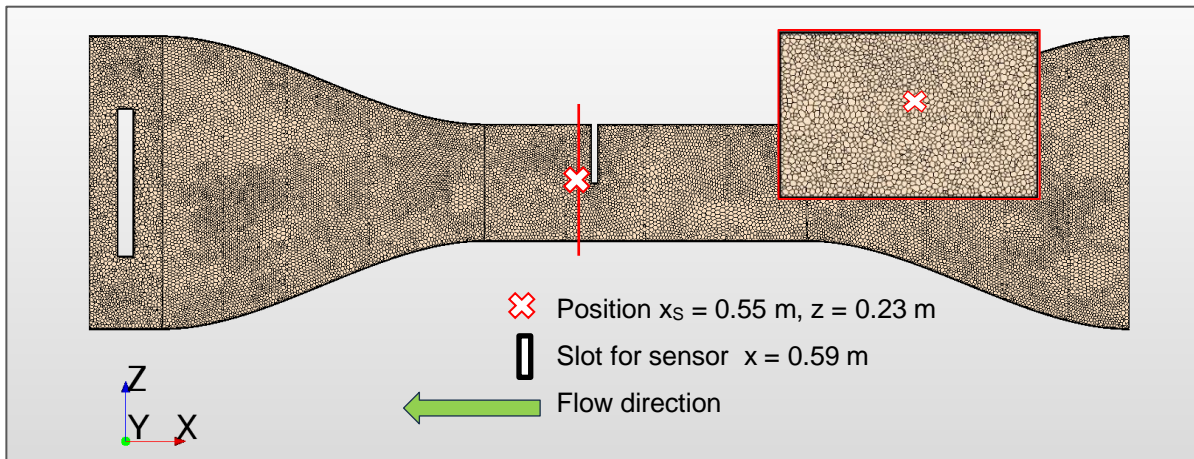
Bild 3. Testwindkanal TWK2S von ANIPROP GbR (Eiffelkanal) – Geometrie und CFD Netz.

Ziel der Arbeit ist neben der Darlegung des schon Erreichten auch die Aufklärung eines Phänomens, das während der Untersuchungen aufgetaucht ist in Messungen und CFD-Modellierungen des Geschwindigkeitsprofils V_x von verschiedenen Windkanälen. Bei genauerer Analyse der Strömung hat sich nämlich herausgestellt, dass die Längsgeschwindigkeit im Querschnitt der jeweiligen Messstrecken keineswegs ihren maximalen Wert in der geometrischen Mittelachse hat. Die wenigen dem Verfasser bislang bekannten Ergebnisse zeigen vielmehr einen kleinen, wulstähnlichen Anstieg zum Rand hin, bevor die Geschwindigkeit in der Wandgrenzschicht absinkt. Zu erwähnen sind das Ergebnis aus der Modellierung des transsonischen Windkanals TWG beim DLR Göttingen bei Mach 0.3 im Rahmen einer experimentellen Untersuchung und eine Mes-
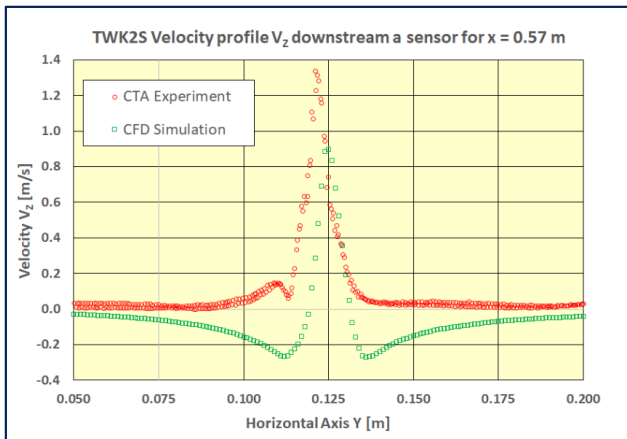
Bild 4. Vergleich Messung und CFD-Rechnung.

sung mit LDA bei der österreichischen Firma E+E, letztere bei 10 m/s in einem Kanal Göttinger Bauart mit offener Messstrecke. Selbst die Messung in Bild 1 zeigt diesen Anstieg. Die Ergebnisse dieser Arbeiten werden vorgestellt.

Bild 5 zeigt das Geschwindigkeitsprofil des Kanals im vorderen Teil der Messkammer bei x = 0.75 m. Die Farbgebung lässt den Bereich der Grenzschicht weiß erscheinen. Offensichtlich liegt das Minimum der Geschwindigkeit außerhalb der Grenzschicht im Zentrum des Kanals. Zum Rand hin zeigt sich in alle Richtungen ein Anstieg der Geschwindigkeit.
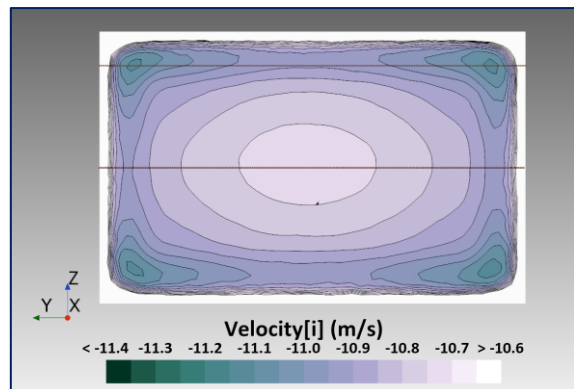
Bild 5. Geschwindigkeitsprofil V_x bei x = 0.75 m.

[1] Send W., *Geschwindigkeit eines Windkanals nach Betz mit Lasertriangulation - vergleichende Messungen*, DLRK2021, Document-ID: 550282. https://www.dglr.de/publikationen/2021/550282.pdf

STAB

Mitteilung

Fachgruppe: Windenergie

LES Investigation on Wind Turbine Trailing Edge Noise Modelling Parameters
of the TNO-based Prediction Tool IAGNoise+

Sabrina Haubold, Thorsten Lutz, Andrea Beck
University of Stuttgart, Institute for Aerodynamics and Gas Dynamics
Wankelstraße 3, 70563 Stuttgart, Germany
sabrina.haubold@iag.uni-stuttgart.de

Wind energy as a renewable resource continues to gain importance as the societal focus shifts further towards green energy. However, noise regulations restrict both the placement and operation of wind turbines. A reduction of noise emissions at the source would open the way for further expansion of this energy sector. Currently, the major contributions to wind turbine noise result from aeroacoustic sources such as turbulent boundary layer trailing edge interaction noise (TBL-TEN). Various measures to reduce this primary noise source either actively or passively are subject of current research. The proper design of these systems and devices requires prediction tools with favorable characteristics, both in terms of accuracy and computational efficiency. The RANS-TNO-based prediction tool IAGNoise+ [1] is able to fulfill both these requirements to a satisfactory degree, making it a good fit for parameter studies and industrial design of rotor blades. The current version of the TNO-model employed in the IAGNoise+ tool has already been extended by Kamruzzaman [1] and Hornung [2] to provide more accurate predictions for a wider range of cases. One area that has been noted to lack accuracy in all TNO-based-models so far is in the prediction of wall pressure fluctuations (WPF) on the pressure side of the airfoil. Also a recent study on the capabilities of the IAGNoise+ tool in its current version [2] to predict noise reduction via boundary layer suction [3] showed an underprediction of the impact of suction massflow on the noise reduction. This paper aims to explore remaining shortcomings of the current model by comparing the predictions to detailed flow and aeroacoustic data gained from Large Eddy Simulations (LES). These simulations are performed as Direct Noise Computations (DNC) by adjusting spatial and temporal resolution to capture the acoustic fluctuations that are naturally part of the Navier-Stokes equations.

The wall-resolved LES were performed using the High-Order Discontinuous-Galerkin Solver FLEXI [4] for a NACA64-418 airfoil at a Reynolds Number of $Re = 5E5$ and a Mach number of $Ma = 0.2$. The spanwise extent of the computational domain was chosen as twice the boundary layer thickness at the trailing edge. The mesh resolution was chosen to satisfy $x^+ \approx z^+ \approx 20$ and $y^+ \approx 1$ as the simulations were run as implicit LES without a subgrid scale model, resulting in stricter resolution requirements. The flow was tripped at $x/c = 0.05$ on both suction and pressure side to ensure comparable conditions near the trailing edge. In total, the mesh was made up of $N_E \approx 730\,000$ cells. A polynomial degree of $N = 7$ was chosen for the simulations, resulting in $375E6\ DOF$ for the given mesh. Time resolved data was collected at specified locations within the flow field. An evaluation point for far field acoustic data was placed 1.2 chord lengths above the trailing edge just outside the acoustic near field, as the mesh resolution up to the point had to be kept fine enough to resolve the acoustics signal up to the highest relevant frequency of $5kHz$. Finally, the boundary layer near the trailing edge and further upstream up to 70 percent chord was mapped by 16 spanwise planes with 40 points in wall normal direction and about 130 points in streamwise direction. This allows for an examination of the development of boundary layer properties and the resulting wall pressure fluctuations along the airfoil surface, as well as the influence of the distance between the evaluation position and the trailing edge. Once the flow had fully developed and reached a quasi stationary state, it was simulated and recorded for 5 convective time units, which is sufficient to capture the lowest relevant frequencies of trailing edge noise for the present case at $500Hz$. The sampling frequency for the recorded pressure fluctuation data was chosen as $40kHz$.

STAB

The IAGNoise+ prediction data for comparison with the LES results was generated from 2.5D RANS flow solutions at the same Reynolds Number, performed using the flow solver FLOWer [5]. The computational grid is comprised of an very fine O-grid topology around the extruded airfoil and a corser background mesh, spanning 180 chord lengths in x- and y-direction. The grids are overlapped using the Chimera overset grid technique. Within the O-grid, the near-wall resolution is chosen to satisfy a $y^+ \approx 0.2$, in order to obtain high quality data for the IAGNoise+ prediction.

In the TNO-prediction, suction side and pressure side boundary layer data are evaluated separately and the WPF spectra and resulting sound spectra of each side are calculated before the contributions are added up to form the full TE noise spectra. This allows for comparisons at this early stage of the prediction with WPF data directly extracted from the LES, as shown in Figure 1. At locations further upstream of the TE (left plot) the spectra match relative well, but begin to deviate for locations further downstream (right plot). One potential explanation for pressure and suction side spectra being much closer to each other than in the prediction model may be cross-talk between suction and pressure side. As this is a feedback phenomenon of acoustics and flow, it can only be captured in direct noise computations and not in decoupled two-step predictions, but would also have an impact in real-life noise measurements. Therefore one focal point of the final paper will be a deeper investigation into this behavior, also looking into other potential causes. Boundary layer properties such as velocity profiles, turbulence kinetic energy, but also more specific quantities such as the distribution of integral length scales of the vertical velocity fluctuations and the convection velocity of these scales, particularly relevant for the trailing edge noise prediction are extracted for various streamwise as well as spanwise locations from the LES to obtain a complete picture of the development of these properties and further identify shortcomings in the prediction. The goal is for this investigation to lay the foundation for further improvement of the prediction method.
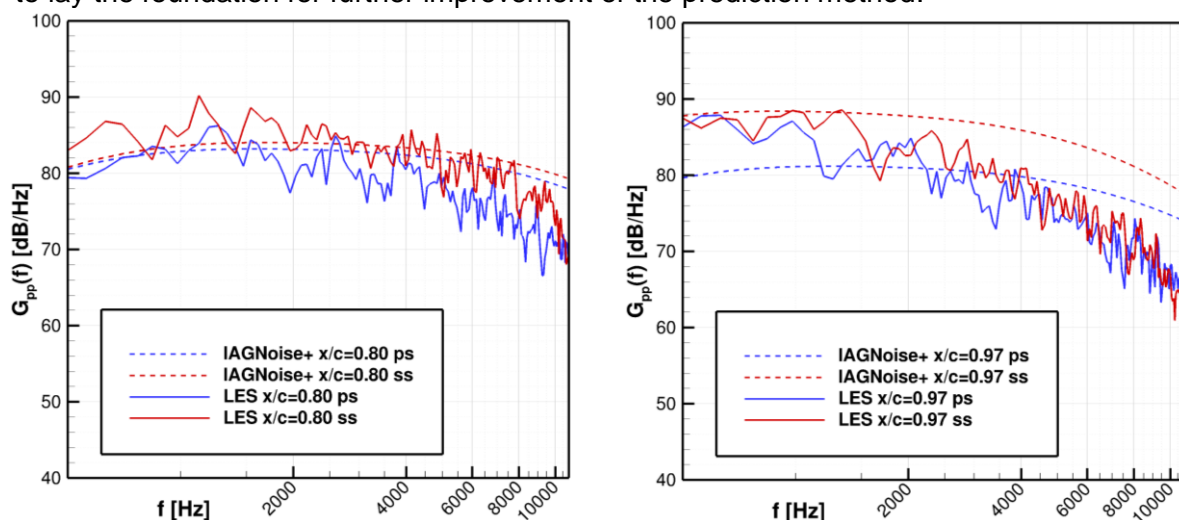
Fig 1: Comparison of wall pressure fluctuation spectra between RANS-TNO-based prediction and direct extraction from time-accurate LES data close to the trailing edge at 97 percent chord (left) and further from the trailing edge at 95 percent chord (right).

Literatur :
[1] M. Kamruzzaman, D. Bekiropoulos, A. Wolf, T. Lutz, E. Krämer, Rnoise: a RANS based airfoil trailing-edge noise prediction model, AIAA Conf. (2014) 1e22, https://doi.org/10.2514/6.2014-3305.
[2] C. Hornung, T. Lutz, E. Krämer: "A model to include turbulence-turbulence interaction in the prediction of trailing edge far field noise for high angles of attack or slightly separated flow", Journal of Renewable Energy, 136, 945–954, 2019. http://doi.org/10.1016/j.renene.2018.12.093.
[3] S. Haubold, F. Seel, T. Lutz, A. Beck and E. Krämer, "Study on the Capabilities of a TNO-Based Trailing Edge Noise Prediction Tool Applied to Boundary Layer Suction on a NACA 64-418 Airfoil," , Proceedings of the 10th International Conference on Wind Turbine Noise, Dublin, 2023.
[4] N. Krais et al.: FLEXI: A high order discontinuous Galerkin framework for hyperbolic–parabolic conservation laws, Computers & Mathematics with Applications, 2020. https://doi.org/10.1016/j.camwa.2020.05.004
[5] N. Kroll, C. Rossow, D. Schwamnorn, K. Becker and G.Heller, "MEGAFLOW – a Numerical Flow Simulation Tool for Transport Aircraft Design, " Proceedings of the 23rd International Congress of Aeronautical Sciences, Toronto, 2002. https://doi.org/10.1016/S1270-9638(00)00131-0.

STAB

Mitteilung

Fachgruppe: Wind Energy

Surface measurements in a pressure-induced flow separation around a 3D printed Gaussian bump in an open test section wind tunnel

Fabian Reuschling[a], Philipp Seelemeyer[b], Arnaud Le Floc'h[b] and Michaela Herr[b]
Departments of Technical Acoustics[a] and Wind Energy[b]
DLR Institut für Aerodynamik und Strömungstechnik, Lilienthalplatz 7, 38108 Braunschweig

Giuseppe Di Labbio
Département de génie mécanique, École de technologie supérieure
1100 Rue Notre-Dame Ouest, Montréal, Québec H3C 1K3, Canada

Jérôme Vétel
Département de génie mécanique, Polytechnique Montréal
2500 Chemin de Polytechnique, Montréal, Québec H3T 1J4, Canada
arnaud.lefloch@dlr.de

At high angles of attack, the boundary layer near the trailing edge of a wind turbine blade can experience flow separation, leading to detrimental performances for the wind park and an increase in noise emission (Suryadi 2015). The complex unsteady nature of separated flows remains an active field of research as the mechanisms driving the wall-pressure response remain poorly understood. However, long term objectives for wind energy at DLR include an improved prediction of such adverse conditions with the use of on-board sensors and AI-led real time monitoring. In an effort to pursue that goal, a recent study investigated the analogies of wall pressure signatures between separated flows on a flat plate *versus* near the trailing edge of two distinct airfoils (Le Floc'h 2024). Of particular interest, the onset of separation (upstream of the mean detachment) presented unique features including a positive skewness and a strong low-frequency activity in wall pressure linked to the so-called breathing cycles of the recirculation region. However, to date, the relevance of the breathing motion to noise emissions is still being debated in spite of being the dominant contributor to turbulent kinetic energy for separated flows. Moreover, it was also observed in (Le Floc'h 2024) that each dataset suffered from limitations that prevented from acquiring the full range of frequencies associated with flow separation, from the low-frequency breathing all the way up to small scales of backflow.

Aiming at overcoming such limitations, the present study investigates comprehensive surface measurements in a pressure-induced flow separation around a smooth bump following the same geometry as given in the recent Boeing Gaussian Bump case study that was specifically desgined at NASA for repeatable smooth-body flow separation conditions (Gray 2023). Indeed the parametric functions that defined the outline of the 3D surface were given as a function of L, the side length of the bump square base whereas h is the apex :

$$y(x,z) = h\,\frac{1+\mathrm{erf}\left(\frac{\frac{L}{2}-2z_0-|z|}{z_0}\right)}{2}\exp^{-\left(\frac{x}{x_0}\right)^2} \text{ with } x_0/L = 0.195, z_0/L = 0.06, \text{ and } h/L = 0.085.$$

The experiments are planned in the Acoustic Wind Tunnel in DLR Braunschweig (AWB) where the open test section consists of a rectangular nozzle that is 1.2m high per 0.8m wide. The bump is to lay horizontal on a flat plate that is located just a few cm downstream of the nozzle at half height. Similarly to the NASA close test section experiments, caution was given to the extent of secondary flow that stems from the side walls of the nozzle, limiting our selection of the bump length L=0.5m instead of 0.9144m (e.g. 3 ft) from (Gray 2023). Such dimensions were deemed adequate to avoid any possible interaction with the shear layers. The apex of the bump is set at x=0.77m from the flat plate leading edge, where we calculated the ratio height of the bump over boundary layer thickness $h/\delta \approx 3.5$. In Fig.1a we present the eight different parts that together form the bump. Each part is 3D-printed and the part with the sensors installed for the recirculation region is presented in details in Fig.1b.
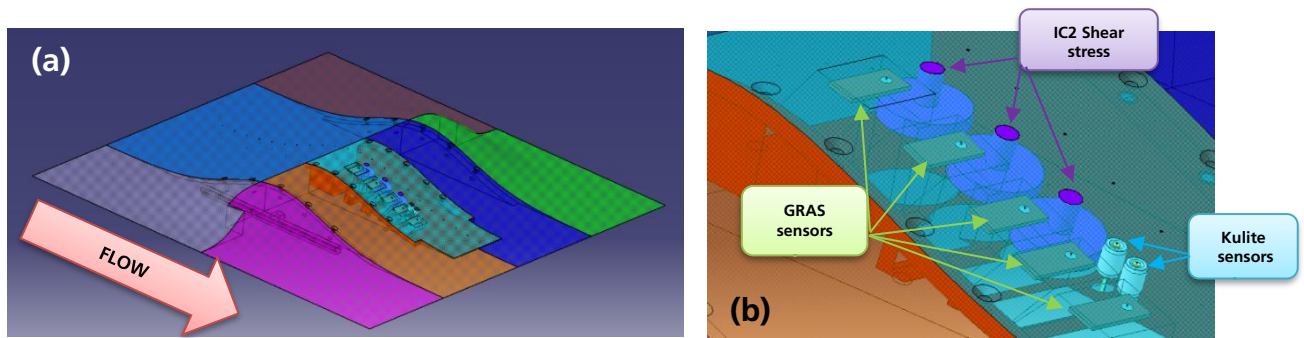
Figure 1 (a) 3D view of the smooth bump.   (b) zooming on the instrumented patch with both pressure and shear-stress sensors

Our objective here is to cover low-, mid- and high-frequency activities using a combination of both Gras and Kulite sensors over the curved surface. Five consecutive Gras sensors are distributed along the streamwise axis starting at the onset of separation, where we want to resolve the low-frequency as well as the convection motion inside the expected recirculation bubble. Located in the vicinity of the fifth Gras sensor, a couple of Kulite sensors will also be used to detect backflow motion on top of the regular vortex shedding (Le Floc'h 2024).

Last not but least in our experimental setup, one original contribution is that synchronized measurements of wall shear stress will be performed as well using IC2 shear stress capacitive sensors to further document the link between wall-pressure and wall-shear.Typically we aim to investigate the coherence values between the two phsysical quantities, track and detect either a lagging or leading parameter, and even use modal decomposition (POD) to build reduced order models for such flow.

In order not to attenuate the high-frequency content of the wall-pressure signature, the pressure sensors (Gras and Kulites) are pinhole mounted as shown in Fig.2 using a strip of aluminum (0.3mm thick) in which we drill a 0.4mm diameter hole. The idea is then that the sensing elements are put in contact directly over the metal strip and smooth curvature is preserved thanks to surface treatments including rounds of filling and sanding.
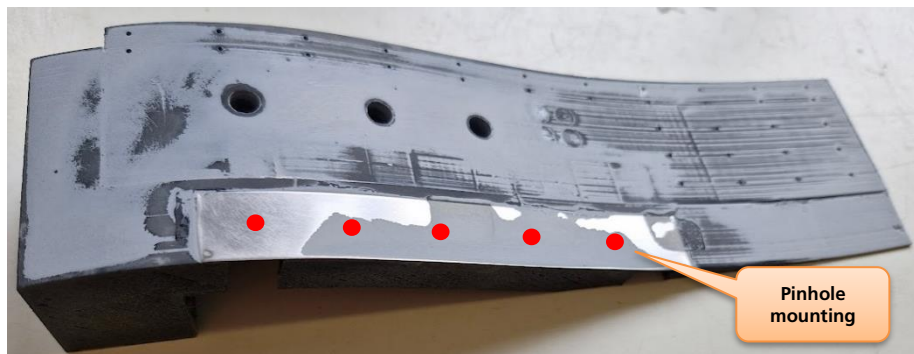
Figure 2 - 3D printed part of the test piece for instrumentation evaluation. Insert of a metal strip with Ø 0.4mm pinholes located at the red dots.

In the final paper, a detailed analysis of mean and unsteady wall quantities (pressure and shear) will be provided with a focus on mean flow statistics compared to the original NASA setup, as well as on flow separation unsteadiness, including the locations where the low frequency breathing and high frequency backflow (upstream convection) can be identified.

References

Gray, Corke, Thomas, Gluzman, Straccia. 2023. "Turbulence Model Validation through Joint Experimental / Computational Studies of Separated Flow Over a Three-Dimensional Tapered Bump." NASA report.

Le Floc'h, Suryadi, Hu, Herr, Wang, Ghaemi, Di Labbio, Dufresne, Vétel. 2024. "Wall pressure signature of separated flows: A comparison between flat plate and airfoil}." *TSFP13.*

Suryadi, Herr. 2015. "Wall pressure spectra on a DU96-W-180 profile from low to pre-stall angles of attack." *AIAA conference.*

STAB

Mitteilung

Fachgruppe: Windenergie

FSI simulations of IEA-15MW wind turbine under gust conditions

Neeraj Paul Manelil[1], Johannes Nicolaas Theron[1], Leo Höning[1], Bernhard Stoevesandt[1]

neeraj.paul.manelil@iwes.fraunhofer.de

[1] *Fraunhofer Institute for Wind Energy Systems, Department Aerodynamics, CFD and stochastic Dynamics, Küpkersweg 70, 26129 Oldenburg, Germany*

[2] *Institute of Physics and ForWind, University of Oldenburg, Küpkersweg 70, 26129 Oldenburg, Germany*

Keywords: Wind turbine, Gust, DDES, FSI

Meteorological data confirms the occurrence of extreme climatic events in the atmospheric boundary layer, characterized by regions with significant spatio-temporal acceleration and relatively high velocities compared to their surroundings. These events, commonly known as gusts according to the International Electrotechnical Commission (IEC) definition [6], typically last around 10 seconds and exert substantial dynamic loads on wind turbine structures. These loads cause significant displacements at the tips of wind turbine blades, leading to considerable stresses and bending moments. The importance of these factors has increased due to the trend of larger wind turbine rotor diameters over the past decade, driven by the goal of reducing the levelized cost of energy (LCOE). Consequently, turbine manufacturers are now required to demonstrate the structural integrity and resilience of their turbine designs under extreme gust scenarios as defined by IEC certification standards[6].
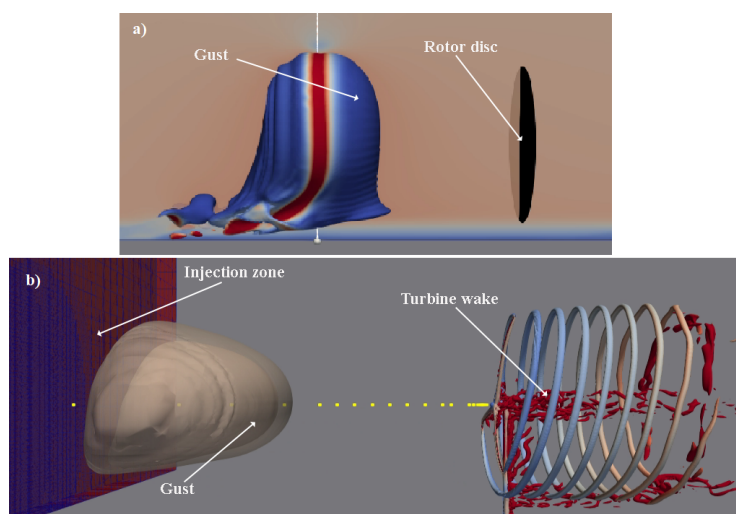
Figure 1: Comparison of spatial description (represented by iso-velocity surface) of gust a) from present study (simulation without turbine) with b) [7] (simulation with IEA 15MW turbine)

The current assessment of aero-elastic loads on large wind turbines (greater than 15 MW) during wind gusts faces two primary shortcomings. First, the determination of loads and bending moments on turbine blades relies on low-fidelity Blade Element Momentum (BEM) simulations [1], which fail to fully capture the three-dimensional complexities of blade geometry, a factor that becomes increasingly significant in larger turbines. Second, the description of gusts in the IEC

STAB

standards is based on simple deterministic models that do not accurately reflect real-world observations from field measurements [2]. To address these challenges, the present study aims to improve the understanding of aero-elastic loads by conducting blade-resolved large eddy simulations (LES) to quantify these loads on the IEA 15MW wind turbine under the influence of a wind gust defined based on measurements.

The blade resolved simulation in this study is carried out with in-house framework for fluid-structure coupled computational fluid dynamics (CFD) simulations, detailed in [4]. The structural solver and the mesh deformation module are integrated into the open-source CFD toolbox OpenFOAM. Delayed-Detached Eddy Method is used to solve the fluid domain and the Geometrically Exact Beam Theory (GEBT) based structural solver is used to simulate structural deformation of the turbine blade. The robustness of this comprehensive framework for fluid-structure coupling has been previously validated in prior works, as documented in [3] and [5]. Figure 1 a) presents the propagation of gust under boundary layer effects. The gust has a maximum velocity that is $50\% >$ the mean rated wind velocity. The gust in introduced into the computational domain in such a way that center of gust coincides with the hub height of the 15MW turbine. It is noted that in both the scenarios the gust is strongly influenced by the boundary layer. This is evidenced by the deformation of gust near the ground shown in Fig 1 a). Figure 1 b) presents preliminary results from such a simulation clearly indicate, the gust, injection zone and wind turbine wake. These simulations are ongoing and results would indicate the influence of the two different gust description on the aero-elastic loads of the wind turbine. Initial results suggest indicate deformation of the gust as it approach the induction of the WT indicating possibilities of load variations even before impact.

References

[1] Galih Bangga and Thorsten Lutz. Aerodynamic modeling of wind turbine loads exposed to turbulent inflow and validation with experimental data. *Energy*, 223:120076, 2021.

[2] Wim Bierbooms and Po-Wen Cheng. Stochastic gust model for design calculations of wind turbines. *Journal of Wind Engineering and Industrial Aerodynamics*, 90(11):1237–1251, 2002.

[3] B Dose, H Rahimi, I Herráez, B Stoevesandt, and J Peinke. Fluid-structure coupled computations of the nrel 5mw wind turbine blade during standstill. In *Journal of Physics: Conference Series*, volume 753, page 022034. IOP Publishing, 2016.

[4] B Dose, H Rahimi, B Stoevesandt, and J Peinke. Fluid-structure coupled investigations of the nrel 5 mw wind turbine for two downwind configurations. *Renewable energy*, 146:1113–1123, 2020.

[5] Bastian Dose, Hamid Rahimi, Iván Herráez, Bernhard Stoevesandt, and Joachim Peinke. Fluid-structure coupled computations of the nrel 5 mw wind turbine by means of cfd. *Renewable energy*, 129:591–605, 2018.

[6] IEC-Standard. *61400-21. Measurement and Assessment of Power Quality of Grid Connected Wind Turbines.* 2002.

[7] Stuart Edward Norris, John Edward Cater, Karl Alexander Stol, and CP Unsworth. Wind turbine wake modelling using large eddy simulation. In *Proceedings of the 17th Australasian Fluid Mechanics Conference. University of Auckland*, 2010.

Mitteilung

Fachgruppe: Windenergie (Wind energy)

Evaluating the effect of a leading-edge slat on the aerodynamics of the NACA0018 airfoil

Johannes N. Theron
Fraunhofer Institut für Windenergiesysteme, Oldenburg
johannes.theron@iwes.fraunhofer.de

Abstract
This study dedicated to studyning the effect of two leading-edge slat design on the aerodynamics of the NACA0018 airfoil with rounded trailing edge at Reynolds number between 1^e5 and 1^e6. In addition to the static polars, a number of dynamic stall simulations were performed to evaluate the effect of the slats on inhibiting / postponing dynamic stall effects.

Computational grids and CFD solver
The NACA0018 airfoil coordinates were generated using XFOIL, and the trailing edge subsequently opened up to xx% of the chord. A circular section was manually constructed and blended into the opened-up trailing edge. Two leading-edge slats were designed; the first slat was constructed by cutting the leading edge of the airfoil along a line cloned from a NACA61A10 airfoil (Ref. i,ii) and simulated with two gap sizes and the second consisting of a simplified extraction of the leading edge converted into a constant-thickness slat representing a sheetmetal part. The two slat design are shown in Figure 1.
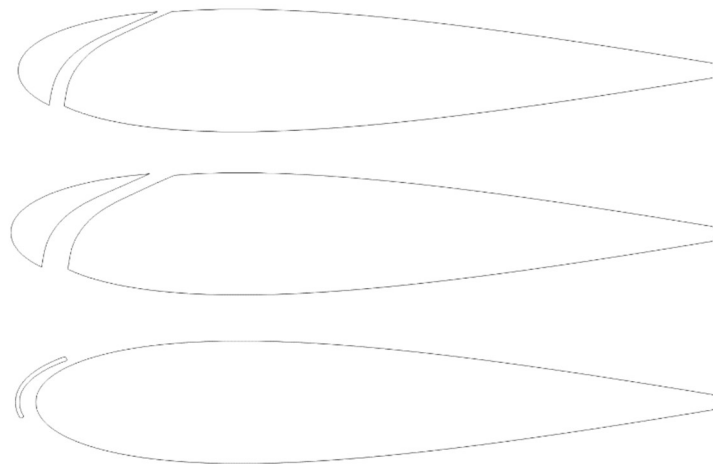
Figure 1 Slat design tested

The three slats and unmodified NACA0018 airfoil were simulated in the Reynolds number range from 1^e5 to 1^e6. For the case of Re=1^e6, the effect of the slats on increasing the stall angle as well as maximum CL, is shown in Figure 2 below.

STAB
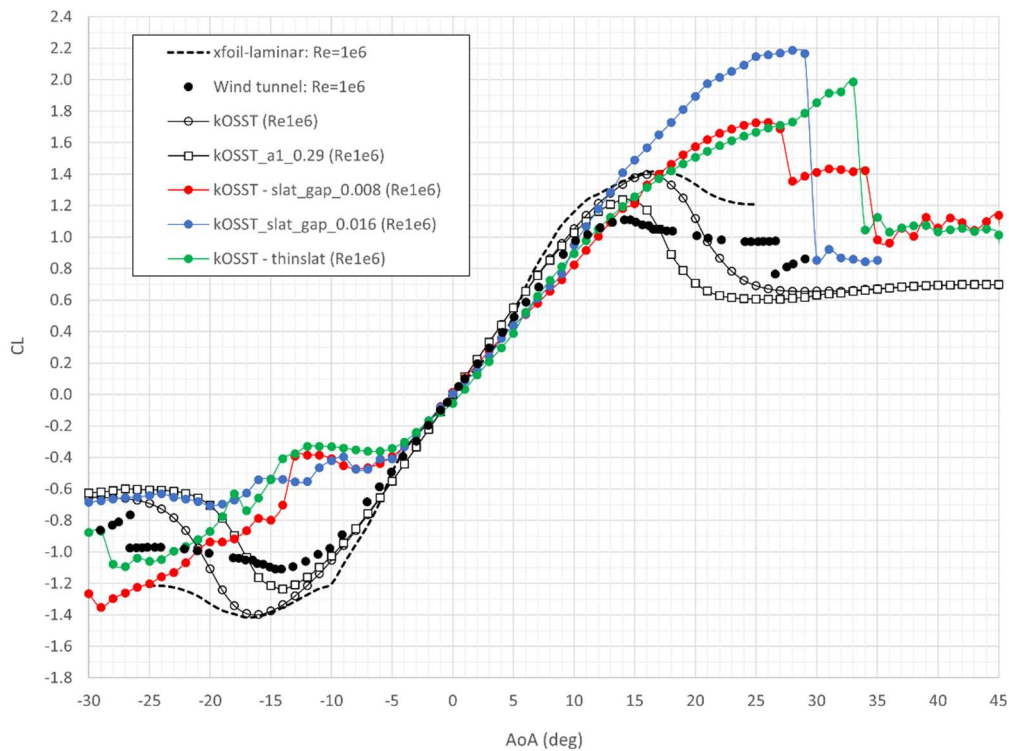
Figure 2 Lift coefficient at Re=1e6

All configurations were also subjected to deep stall conditions to evaluate the slat designs' ability to suppress dynamic stall. One example at reduced frequency of 0.263 is shown below. Here the supopression of dynamic stal lis clearly évident for all three slat designs tested.
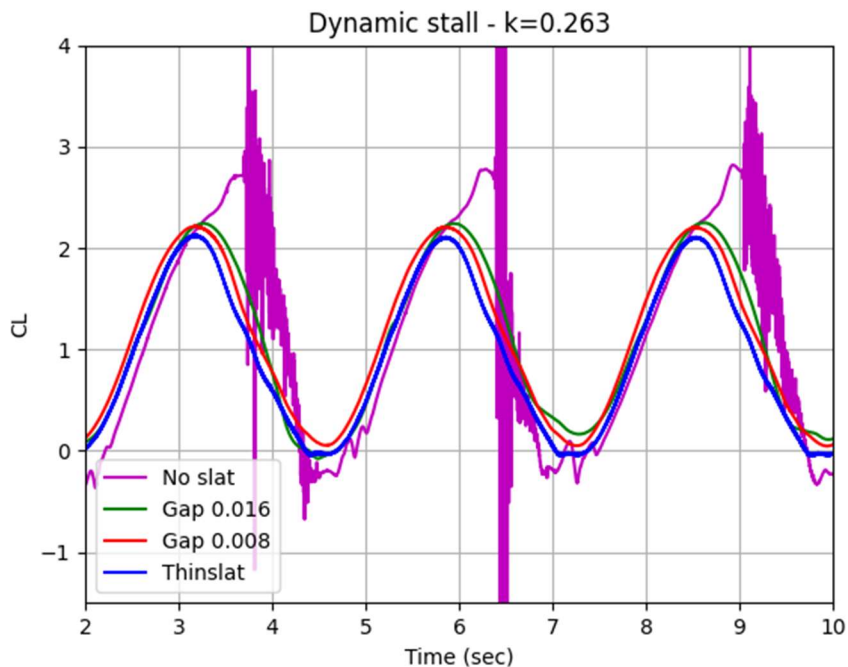
Figure 3 Dynamic stall at Re=3e5 (15deg ±15°)

---

[i] *Two-dimensional wind-tunnel investigation of two NACA 6-series airfoils with leading-edge slats*, Stanley M. Gottlieb, Langley Aeronautical Laboratory, National advisory commitee for aeronautics, 1949

[ii] *Aerodynamic loads on a leading-edge flap and a leading-edge slat on the NACA 64A10 airfoil section,* John A. Kelly and George B. Mc Collogh, Ames Aeronautical Laboratory, National advisory commitee for aeronautics, 1954

STAB

Mitteilung

Fachgruppe: Windenergie

Numerical investigation of the tower influence on the tip vortices of a model wind turbine

Tobias Weislein, Thorsten Lutz
University of Stuttgart, Institute of Aerodynamics and Gas Dynamics,
Wankelstraße 3, 70563 Stuttgart, tobias.weislein@iag.uni-stuttgart.de

1. Introduction

The continued growth of the wind energy sector as a source of renewable energy leads to increasing demands for space-efficient wind park layouts. Nevertheless, a reduction in the distance between wind turbines gives rise to more pronounced wake interaction effects A wind turbine located in the wake of another wind turbine must deal with substantially higher fatigue loads due to the increased inflow turbulence [1]. Furthermore, the inflow velocity is reduced compared to the unperturbed inflow resulting in a potential power loss of up to 40% [2]. This highlights the necessity of research into decreasing near wake length. It is well known that the near wake length is determined by the tip vortices. These prevent the turbulent mixing of the outside flow with the low velocity in the wind turbine wake [3]. Therefore, research into speeding up the tip vortex decay and thus wake decay should improve wind park power output and reduce the spatial extent of wind parks.

Investigations of tip vortex decay on a model wind turbine, designed by [4], are conducted in joined research between the University of Stuttgart and the "Technische Universität" Berlin (TUB). The high-fidelity numerical investigations performed at the IAG are defined to mimic the conditions of experiments in an underwater towing tank performed at TUB. Preliminary investigations are focused on the influence of supporting structures besides the rotor blades themselves. The influence of the turbine nacelle was shown in [5] to be negligible. However, literature by [6 and 7] suggests that the tower has a more significant impact on the wake dynamics, especially in the tip vortices. These showed that the tower promotes earlier tip vortex breakdown but did not provide a detailed analysis on these disturbances. Therefore, this paper aims to examine how the disturbances are caused by the tower, how they propagate and how they interact with the tip vortex by means of high-fidelity numerical simulations.

2. Numerical method and setup description

Fully turbulent delayed detached eddy simulations (DDES) are performed using the compressible finite volume solver FLOWer [8]. In RANS mode the two equation Menter-SST turbulence model is used. To minimize numerical dissipation caused by the grid resolution, a 5th order weighted essentially non-oscillatory (WENO) scheme is applied in meshes containing vortical structures. For improved numerical stability, a second order scheme is used for the geometry bound meshes, as these contain cells with a high aspect ratio, in order to maintain $y^+ \leq 1$ to resolve the boundary layer. The meshes of the different components are overset using the chimera overlapping technique. One rotor revolution is captured with 1440 time steps resulting in a CFL number of less than one in the vortex containing meshes. Uniform inflow without inflow turbulence is used and the water tunnel walls, and the water surface is modelled as a slip wall.

3. Results and Conclusion

The DDES were conducted for a TSR of 6 and the results are presented in Figure 1. The plot on the left depicts the λ_2 iso-surface that visualize the vortical structures in the turbine wake. To improve the visibility of the relevant structures, every λ_2 iso-surface below r/R=0.9 is blanked out. The tip vortices travel downstream and interact with the tower of the model turbine, thereby forming a Karman vortex street. This results in a deformation of the tip vortices. The perturbations on the tip vortices propagate in circumferential direction as the tip vortices travel further downstream.

STAB

The plot in the top right illustrates the velocity in the plane normal direction. It can be noted that there is an axial velocity component in the centre of the tip vortices. This axial component increases after the interaction with the tower of the turbine. Additionally, when considering the circumferential vorticity in the plot on the bottom, the interaction leads to a displacement of the tip vortex core. This deformation of the vortex core can potentially lead to elliptic instabilities which cause an earlier tip vortex breakdown.
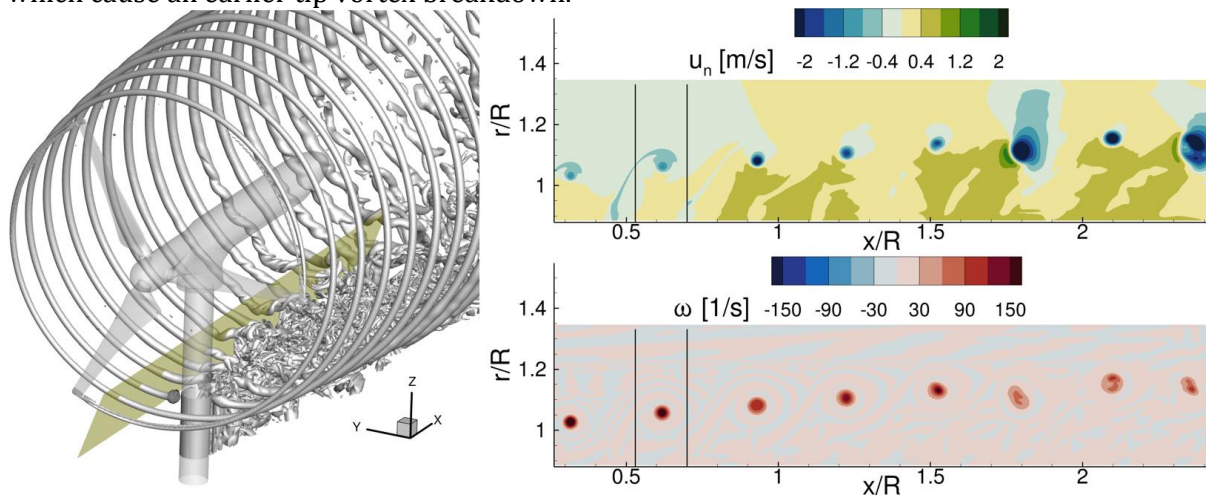
Figure 1 *(left): λ_2 iso-surface plot of turbine wake, cutplane marked in yellow; (right): velocity in plane normal direction (top), vorticity in circumferential direction (bottom); For both plots on the right, the black lines inicate the position of the tower*

The presented results highlight the interaction between the tip vortices and the tower of a model turbine. This results in a perturbation of the tip vortices, which in turn causes a variation in the axial vortex core velocity and vortex core displacement. These disturbances travel in circumferential direction leading to earlier breakdown of the tip vortices. To fully understand the interaction of the different vortical structures shed by the blades and tower, detailed discussion of the flow physics is presented in the full paper. Additionally, the results will be compared to a simulation without the tower.

[1] Jens N Sørensen et al., 'Determination of Wind Turbine Near-Wake Length Based on Stability Analysis', *Journal of Physics: Conference Series* 524 (16 June 2014): 012155, https://doi.org/10.1088/1742-6596/524/1/012155.

[2] Joseph C. Y. Lee and M. Jason Fields, 'An Overview of Wind-Energy-Production Prediction Bias, Losses, and Uncertainties', *Wind Energy Science* 6, no. 2 (5 March 2021): 311–65, https://doi.org/10.5194/wes-6-311-2021.

[3] L. E. M. Lignarolo et al., 'Tip-Vortex Instability and Turbulent Mixing in Wind-Turbine Wakes', *Journal of Fluid Mechanics* 781 (25 October 2015): 467–93, https://doi.org/10.1017/jfm.2015.470.

[4] S. Krumbein et al., 'The Underwater Berlin Research Turbine: A Wind Turbine Model for Wake Investigations in a Water Towing Tank', *Journal of Physics: Conference Series* 2767, no. 4 (1 June 2024): 042011, https://doi.org/10.1088/1742-6596/2767/4/042011.

[5] Tobias Weislein et al., 'Numerical Investigation of the Vortical Structures in the near Wake of a Model Wind Turbine', *Journal of Physics: Conference Series* 2767, no. 2 (1 June 2024): 022008, https://doi.org/10.1088/1742-6596/2767/2/022008.

[6] Giovanni De Cillis et al., 'POD-based Analysis of a Wind Turbine Wake under the Influence of Tower and Nacelle', *Wind Energy* 24, no. 6 (June 2021): 609–33, https://doi.org/10.1002/we.2592.

[7] Xiaocheng Zhu et al., 'Numerical Investigation of the Effect of Towers and Nacelles on the near Wake of a Horizontal-Axis Wind Turbine Model', *Energy* 238 (January 2022): 121782, https://doi.org/10.1016/j.energy.2021.121782.

[8] N Kroll et al., 'MEGAFLOW - A NUMERICAL FLOW SIMULATION TOOL FOR TRANSPORT AIRCRAFT DESIGN', *AIRCRAFT DESIGN*, n.d.

STAB

Namensverzeichnis der Autor(inn)en und Koautor(inn)en